NORTHWESTERN UNIVERSITY

Marine Sulfur and Strontium Cycling During the Transition from a Cool to Warm Greenhouse in the Early Cretaceous

A DISSERTATION

SUBMITTED TO THE GRADUATE SCHOOL

IN PARTIAL FULFILLMENT OF THE REQUIREMENTS

for the degree

DOCTOR OF PHILOSOPHY

Field of Earth and Planetary Sciences

By

Brian Michael Kristall

EVANSTON, ILLINOIS

December 2016

Abstract

Marine Sulfur and Strontium Cycling During the Transition from a Cool to Warm Greenhouse in the Early Cretaceous

Brian Michael Kristall

This dissertation develops and applies coupled marine sulfur and strontium cycle modeling to the highly dynamic Early Cretaceous demonstrating the value of increased model constraint from linkage of biogeochemical cycles with shared forcing factors. A foundation for this work is first provided by review of relevant geochemical, sedimentological, and paleontological evidence for the climatic shift from a cool to warm greenhouse in the Early Cretaceous, along with information about the timing (Geologic Time Scale 2012) of emplacement for several large igneous provinces, and the deposition of South Atlantic basinal evaporites. The coupling of the strontium and sulfur cycles first relies on a new iterative method developed here for modeling the Phanerozoic composite marine radiogenic strontium isotope record. Unlike previous strontium cycle models, variable strontium isotope ratios for the total weathering and diagenetic input fluxes are used instead of assuming that modern ratios were constant throughout the Phanerozoic. Despite the dominance of the linked hydrothermal and weathering input fluxes driving changes in both isotope records, this coupling enables a more detailed examination of the sulfur cycle, indicating that a complex interplay of changes to multiple sulfur cycle parameters is necessary to reproduce the seawater sulfate sulfur isotope record of the Early Cretaceous. Coupled strontium-sulfur modeling enables clear distinction of the Aptian-Albian (~20 Ma) isotopically light sulfate ocean as an alternate state requiring changes to multiple sulfur cycle parameters instead of the persistence of a negative excursion. The geologically rapid return to more ^{34}S enriched sulfate values following the newly observed

minor negative excursion at the Albian-Cenomanian boundary is thought to be caused by fluctuations in the pyrite burial flux driven by sea level changes in a low sulfate ocean. The model results presented here also suggest a distinctly different range of values for the sulfur isotope composition of the weathering flux, weathered evaporite:pyrite ratios, pyrite burial fraction and integrated fractionation associated with pyrite burial compared to previous models as well as the importance of estimating major changes in concentration for both strontium and sulfur.

Acknowledgements

I would like to begin by thanking my advisor, Matt Hurtgen, who was willing to give me a second chance in the academic world. I will always be grateful for his willingness to take a chance on me and reaffirming that I am a capable scientist and researcher. I would also like to thank Matt for his support, encouragement, flexibility, understanding, and guidance both professionally and personally throughout my time at Northwestern. It has been enjoyable working together and challenging one another over the years.

As a member of my committee I would also like to thank Brad Sageman for all his support, encouragement and guidance along with being a great scientific mentor, professor, and department chair. I always appreciated his direct and constructive criticism. All of our conversations whether scientific or personal were always enlightening, enjoyable, and helpful.

As the third and final member of my committee I would like to thank Andy Jacobson for all his valuable input, editing, and support throughout my time here. Especially in the final several months when I gave him an extreme headache with all the revised strontium equations.

During my time here at Northwestern I have learned much from the faculty. I would like to thank Yarrow Axford, Trish Beddows, Craig Bina, Neal Blair, Dan Horton, Steve Jacobsen Cesca McInerney, Maggie Osburn, Matt Rossi, and Suzan van der Lee for all that I have learned from each and every one of you both in and out of the classroom as well as scientifically and personally. An additional special thank you to Trish Beddows for leading amazing field trip to the Yucatan. Similarly, an additional special thank you to Craig Bina for letting us all tag along on an amazing field trip to the UP and especially for indulging me in trying to find the Sudbury ejecta layer.

A special thank you to the lab managers and technicians in the IRMS and SedGeo labs over the years that have made this work possible – Petra Sheaffova, Kelly Peeler, Alexa Socianu, Koushik Dutta, and Grace Schellinger.

I would like to thank the administrative staff for all that they have done in keeping this department running and organizing all of our events. Thanks to Reid Wellensiek, Shelley Levine, Alison Witt-Jansen, Ben Rice, Lisa Collins, Gina Allen and Alexis McAdams. A special thank you to Ben, Lisa, Alexis, and Gina for keeping me stocked in free candy as I would stress eat while writing my thesis, publications, and proposals.

I must give a special big thank you to all the past graduate students in the Hurtgen-Sageman group that helped me out in the beginning providing fruitful scientific discussions, guidance, advice, support, lab training, and answered all my questions small and big even when they were furiously trying to finish up – Richard Barclay, Derek Adams, Young Ji Joo, Maya Gomes, and Jeremy Gouldey. I would also like to thank current Hurtgen-Sageman graduate students Matt Jones and Jiuyuan Wang for their support and discussions both scientific and non-scientific. In addition, I would like to give a special thank you to Greg Lehn and Grace Andrews for all their helpful discussions regarding isotopes and geochemistry as well as expanding our research group by dragging Andy back in time even if it was kicking and screaming a little. Of course there were many other graduate students that came before and after me that helped, supported, provided insight both scientifically and personally, and challenged me along the way that deserve my gratitude and thanks: Allie Baczynski, Rosemary Bush (everyone's favorite paleobotanist), Dan Li, Laurel Childress, Josh Townsend, Ashley Gilliam, Jamie McFarlin, Miguel Merino, Emily Wolin, Trevor Bollmann, Renee French, Jessica Lodewyk, Michelle

Wenz, Yun-Yuan Chang, Kim Adams, Simon Lloyd, Carl Ebeling, Xiaoting Lou, Amir Salaree, Nooshin Saloor, Mike Witek, John Lazarz, Eddie Brooks, Everett Lasher, and Fei Wang.

A very big special thank to all of my family and friends new, old, gone, big and small for all their love and support over the years as none of this could have been done without them. Especially my parents who have supported and encouraged me no matter what through all the ups and downs on this long journey.

Finally, the biggest and most important thank you to my wonderful wife, Rebecca. Thank you for all your loving support, encouragement, understanding, and tolerance especially these last few months. But most of all thank you for saying yes and being my original silly girl willing to join me on this crazy adventure.

Table of Contents

Table of Figures

Table of Tables

CHAPTER 1

INTRODUCTION

1.1 Introduction

The oceans, and biota contained within, play a critical role in regulating Earth surface conditions. In particular, couplings and feedbacks amongst the key global biogeochemical cycles operate to regulate the Earth system, and these depend critically on the chemical and biological composition of the ocean [Kump and Garrels, 1986; van Cappellen and Ingall, 1994, 1996; Colman et al., 1997; Colman and Holland, 2000; Huston et al., 2001; Grenne and Slack, 2003; Kump and Seyfried, 2005; Konhauser et al., 2007; Meyers, 2007; Hurtgen et. al., 2009; Adams et al., 2010; Meyer et al., 2016]. While it has long been recognized that the major ion chemistry of the Precambrian oceans varied considerably, it is only recently that scientists have appreciated the extent to which Phanerozoic ocean chemistry has fluctuated [Horita et al., 2002; Grenne and Slack, 2003; Lowenstein et al., 2003; Coogan, 2009; Bots et al., 2011; Gothmann et al., 2015]. Therefore, understanding the evolution of ocean chemistry through time as it relates to changes in the major biogeochemical cycles plays a critical role in our ability to reconstruct the dynamics of changing climatic conditions of the geologic past and understand the evolution of life within the oceans.

With the high abundance of sulfate (~28 mmol/L) in the modern ocean, the key role of the sulfur cycle (Fig. 1-1) in determining the redox state of the oceans and influencing the climatic state throughout Earth history has often been overlooked – until recently [van Cappellen and Ingall, 1994, 1996; Huston and Logan, 2004; Kump and Seyfried, 2005; Hurtgen et al., 2009; Shen et al., 2009; Adams et al., 2010; Farquhar et al., 2010; Newton et al., 2011]. Even

though concentrations have been low for much of Earth's history, sulfate has always been an important oxidant within the oceans, especially after the evolution of microbial sulfate reduction [Jorgensen, 1982; Huston et al., 2001; Kah et al., 2001, 2004; Canfield, 2004; Huston and Logan, 2004; Kump and Seyfried, 2005; Shen and Buick, 2004; Canfield and Farquhar, 2009; Shen et al., 2009; Adams et al., 2010; Jamieson et al., 2013; Bowles et al., 2014]. With the intimate connections between the sulfur, iron, phosphorus, carbon, and oxygen cycles (Fig. 1-1), especially at low sulfate concentrations, recent works have highlighted the very important role the marine sulfur cycle plays in regulating seawater nutrient availability, the marine carbon cycle and ultimately climate [van Cappellen et al., 1996; Kurtz et al., 2003; Hurtgen et al., 2009; Adams et al., 2010; Gomes et al., 2016]. Within this context, a better understanding of the chemical evolution of the ocean, and in particular marine sulfate concentrations and S cycling, is crucial for understanding how the oceans, life, and the entire planetary system have evolved.

In this dissertation, I reconstruct the sulfur isotope composition of Early Cretaceous seawater sulfate (as recorded in marine barite) and employ a coupled geochemical box model of the sulfur and strontium cycles to better understand the mechanisms responsible dor driving sulfur isotope variation during this time. The Early Cretaceous was an extremely dynamic time period characterized by excessive volcanism (Byran and Ernst, 2008; Bryan and Ferrari, 2013; Mackenzie et al., 2016), increased tectonic activity (Seton et al., 2012), and fluctuations in the climate state [Frakes et al., 1992; Leckie et al., 2002; Jenkyns, 2010; Boucot et al., 2013]. In Chapter 2 I review the growing evidence for cooler climate conditions during the Early Cretaceous, preceding the warm greenhouse conditions that typify the Mid- to Late-Cretaceous, along with the timing of relevant major geologic events in light of the recently revised Geologic

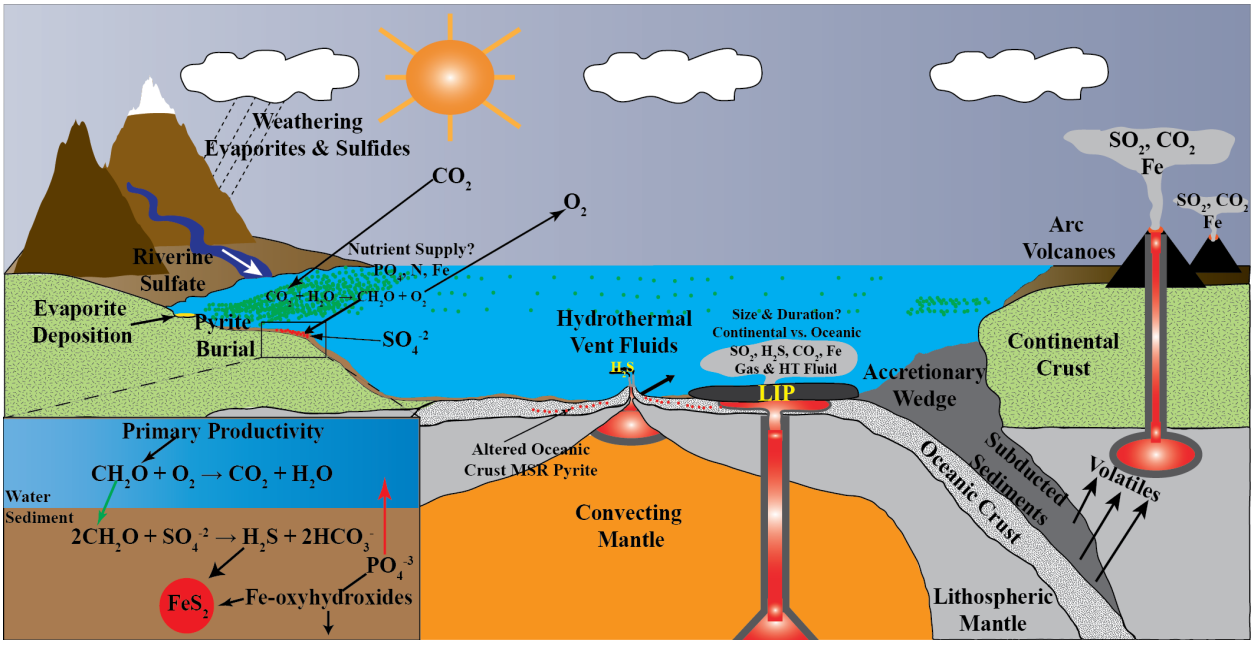

Figure 1-1 Marine sulfur cycle cartoon

Marine sulfur cycle cartoon displaying the input fluxes – subaerial volcanic gases, weathering of evaporates and sulfides, venting of hydrothermal fluids at mid-ocean ridges, and large igneous province (LIP) gas emissions – along with output fluxes – evaporite deposition and pyrite burial in the sediments and altered oceanic crust. Also demonstrates the connections between the S, C, Fe, P, and O cycles through photosynthetic primary productivity producing organic matter that feeds microbial sulfate reduction in the sediments, which leads to pyrite (FeS_2) formation and burial that releases phosphate adsorbed to iron oxyhydroxides back to the water column.

Time Scale 2012 [Gradstein et al., 2012]. In Chapter 3 I review the modern marine strontium cycle and present an iterative method for modeling the radiogenic strontium isotope composition ($^{87}Sr/^{86}Sr$) of seawater utilizing the composite seawater $^{87}Sr/^{86}Sr$ record of McArthur et al. (2012) to determine estimates for the Sr isotope composition of input fluxes in the geologic past. In Chapter 4 I expand the marine barite S isotope record for the Early Cretaceous and add an open ocean pyrite sulfur isotope record. In addition, I further develop a coupled Sr-S cycle box model in order to examine the impact of variation in S cycle parameters other than the two dominant

input fluxes – weathering and hydrothermal. In the final chapter, I summarize the conclusions of this work, which indicate the importance of variation in the isotopic composition of input and output fluxes for both the Sr and S cycles in the geologic past along with the influence that changes in seawater concentrations have on both elemental cycles.

1.2 Sulfur Cycle Overview

There are four naturally occurring stable isotopes of S with masses 32, 33, 34, and 36. The two most abundant isotopes, ^{32}S (~95.0%) and ^{34}S (~4.2%), are used to report the isotopic composition of a substance as a ratio of the minor versus dominant isotope that is standardized against the Vienna Canyon Diablo Troilite (VCDT) and expressed in permil (‰) notation:

$$\delta^{34}S_{smp} = \left[\frac{\left({}^{34}S/{}^{32}S \right)_{smp}}{\left({}^{34}S/{}^{32}S \right)_{VCDT}} - 1 \right] \times 1000 \qquad (1\text{-}1)$$

A variety of physical and chemical processes such as diffusion, phase changes, UV photolysis, microbial reactions, and mineral precipitation can result in depletion or enrichment of the heavier isotope in a S-bearing product relative to either another S-bearing product or the residual S pool. The largest fractionations in the S cycle occur during microbial sulfate reduction (MSR):

$$SO_4^{-2} + 2CH_2O \Rightarrow H_2S + 2HCO_3^- \qquad (1\text{-}2)$$

This metabolic process plays a key role in the consumption and preservation of organic matter (represented as CH_2O above) in sediments and anoxic deep waters thereby linking the S, carbon (C), and oxygen (O) cycles (Fig. 1-1). Similar to organic matter, an increase in the burial of MSR-produced hydrogen sulfide via pyrite (FeS_2) formation can contribute to a rise in

atmospheric oxygen (Fig. 1-1) [van Cappellen et al., 1996; Canfield and Farquhar, 2009; Hurtgen et al., 2009]. The magnitude of fractionation induced during MSR varies widely depending on the organism, initial sulfate concentration, availability and type of organic matter, metabolic pathway, and metabolic rate, which results in fractionations ranging from nearly zero to 70‰ [Detmers et al., 2001; Habicht et al., 2002; Brunner and Bernasconi, 2005; Adams et al., 2010; Bradley et al., 2011, 2016; Sim et al., 2011a,b; Leavitt et al., 2013; Wing and Halevy, 2014].

The burial of MSR-related pyrite is a major contributor to one of the four primary reservoirs in the global marine S cycle – crustal sulfide [Holser et al., 1988, 1989; Berner and Berner, 1996; Arthur, 2000; Canfield, 2004]. The other three primary reservoirs involved in the global marine S cycle with sufficient size and residence time to influence both the mass and isotopic composition when analyzed on geologic time scales are the ocean, mantle and crustal sulfate [Holser et al., 1988, 1989; Berner and Berner, 1996; Arthur, 2000; Canfield, 2004]. Potential reservoirs like the atmosphere are not included in global S cycle models that examine long geologic time scales because gaseous outputs of S from the mantle reservoir via subaerial volcanoes go directly to the oceans on timescales shorter than what is considered in these models. The crustal sulfate reservoir is primarily viewed as sulfate bearing evaporitic sediments and sedimentary rocks with minor contribution from sulfate minerals dispersed in other sediment types and altered oceanic crust [Maynard and Okita, 1981; Kump and Garrels, 1986; Holser et al., 1988, 1989; Paytan and Kastner, 1996; Arthur, 2000; Greinert et al., 2002; Alt et al., 2003; Hansen and Wallmann, 2003; Canfield, 2004; Huston and Logan, 2004; Hein et al., 2007; Johnson et al., 2009; Halevy et al., 2012; Zhou et al., 2015]. Similarly, the crustal sulfide reservoir is primarily viewed as microbially mediated sedimentary pyrite mostly found in shales

while igneous and metamorphic sulfides, massive sulfide deposits and MSR sulfides in altered oceanic crust and serpentinites are not considered current major contributors to this reservoir [Holser et al., 1989; Canfield, 2004; Calmels et al., 2007; Farquhar et al., 2010; Alt and Shanks, 2011; Alt et al., 2012, 2013]. These secondary contributors to the crustal sulfate and sulfide reservoirs and fluxes to the mantle during subduction are receiving more attention recently [Canfield, 2004; Alt and Shanks, 2011; Alt et al., 2012, 2013]. During subduction these secondary contributors to the crustal sulfate and sulfide reservoirs could be volatilized and possibly contribute to the isotopic contamination of arc volcano magma chambers and the subaerial volcanic gas flux [Alt et al., 1993, 2012, 2013].

The exchanges between these four reservoirs via weathering, hydrothermal circulation through the oceanic crust, volcanic gas emissions (subaerial and subaqueous), along with sulfate and sulfide mineral deposition controls the S isotopic composition and sulfate concentration of the oceans (Fig. 1-1). Even though the S isotope composition of the input fluxes to the oceans have been less than that of seawater sulfate for most of Earth history, it has been the MSR fractionation and burial of even more ^{34}S-depleted pyrite that maintains the ^{34}S-enriched values in sulfate [Holser et al., 1988, 1989; Canfield, 2004; Kampschulte and Strauss, 2004; Wu et al, 2010; Halevy et al., 2012]. Amongst the marine S cycle input fluxes, the one with the lowest $\delta^{34}S$ value has varied through time as each flux represents a mixture of variable proportions except for uncontaminated mantle gas emissions via plumes [Torssander, 1989; Alt et al., 1993, 2012; Berner and Berner, 1996; Arthur, 2000; Shanks, 2001; Ono et al., 2007]. The S in hydrothermal fluids is a variable mixture dominated by leached mafic S with thermochemically reduced seawater sulfate resulting in $\delta^{34}S$ values slightly greater than the mantle value (~0‰) that depends on the mid-ocean ridge spreading rate and S isotope composition of seawater sulfate at

the time [Arthur, 2001; Shanks, 2001; Canfield, 2004; Ono et al., 2007; Peters et al., 2010]. Gas emissions from volcanoes at convergent margins, which dominate the total subaerial volcanic gas flux, are a mixture of mantle S with volatilized, subducted minerals and pore waters that generally results in enrichment of ^{34}S [Ueda & Sakai 1984; Woodhead et al 1987; Alt et al 1993, 2012, 2013; Herzig et al 1998; de Hoog et al 2001]. The isotope composition of the weathering flux depends on the variable proportions of available evaporites and sedimentary sulfides for weathering with their distinct $\delta^{34}S$ values along with differing weathering rates for sulfide and sulfate minerals [Holser et al., 1988, 1989; Berner and Berner, 1996; Wu et al., 2010].

In this study I aim to improve our understanding of the complex interplay of the marine S cycle fluxes and their variable isotope compositions. To do so I develop coupled marine strontium-sulfur cycle box modeling and apply it to the dynamic Early Cretaceous where the rock record exhibits two large excursions in the S isotope composition of seawater sulfate [Paytan et al., 1998, 2004; Kamschulte and Strauss, 2004]. With the two cycles linked by constant scalars through their common hydrothermal and weathering fluxes the potential variability in the strontium cycle constrains these dominant input fluxes for the sulfur cycle. This enables me to examine a range of initial condition values along with fluctuations within S cycle parameters other than the two primary input fluxes.

CHAPTER 2

UPDATING THE TEMPORAL FRAMEWORK OF THE EARLY CRETACEOUS: REVIEW OF MAJOR GEOLOGIC EVENTS AND UPDATED AGE MODELS FOR THE SEAWATER SULFATE ISOTOPIC RECORD

2.1 INTRODUCTION

The Early Cretaceous is a time of significant transition in Earth's history. While Pangea began to breakup during the Jurassic, it accelerated during the Cretaceous as much of Gondwana was still connected and began to separate within the Early Cretaceous (Fig. 2-1) [Larson, 1991; Seton et al., 2009; 2012; Torsvik et al., 2009; Moulin et al., 2010; McKenzie et al., 2016]. In some areas this breakup of Gondwana was initiated by the eruption of large igneous provinces (LIPs) [Bryan and Ernst, 2008; Bryan and Ferrari, 2013]. As Pangea separated new oceanic gateways slowly opened and basins began to form producing significant changes within oceanic circulation [Poulsen et al., 2001, 2003; Hotinski and Toggweiler, 2003; Hay et al., 2006; Hay, 2008, 2009; Trabucho Alexandre et al., 2010]. Some of the newly formed ocean basins also provided regions for major evaporite deposition impacting seawater concentrations [Davison, 2007; Chaboureau et al., 2012, 2013]. These tectonic changes along with the increased volcanism from both continental arcs and LIPs is thought to have driven a major shift in the climatic state from a cool greenhouse (or icehouse) to the warm-hot greenhouse that characterizes the Late Cretaceous [Frakes et al., 1992; Boucot et al., 2013; McKenzie et al., 2016; Tucker et al., 2016].

The temporal alignment of major geologic events with geochemical, paleontological, and sedimentological records is critical for understanding the impact of these events and the

Figure 2-1 Late Jurassic-Early Cretaceous paleogeographic maps

Paleogeographic maps by Ron Blakely (cpgeosystems.com) for the **A**) Late Jurassic (150 Ma), **B**) Early Cretaceous (120 Ma), and **C**) Mid-Cretaceous (105 Ma) showing the continued breakup of Pangea, in particular the opening of the South Atlantic Ocean. The location of ODP drill holes used by Paytan et al. (2004) to generate a Cretaceous marine barite S isotope record are displayed. 305 – Shatsky Rise; 417D & 418B – Bermuda Rise; 551 – Gobun Spur; 765C & 766A – Exmouth Plateau and Gascoyne-Argo Abyssal Plain; 1049C – Blake Nose

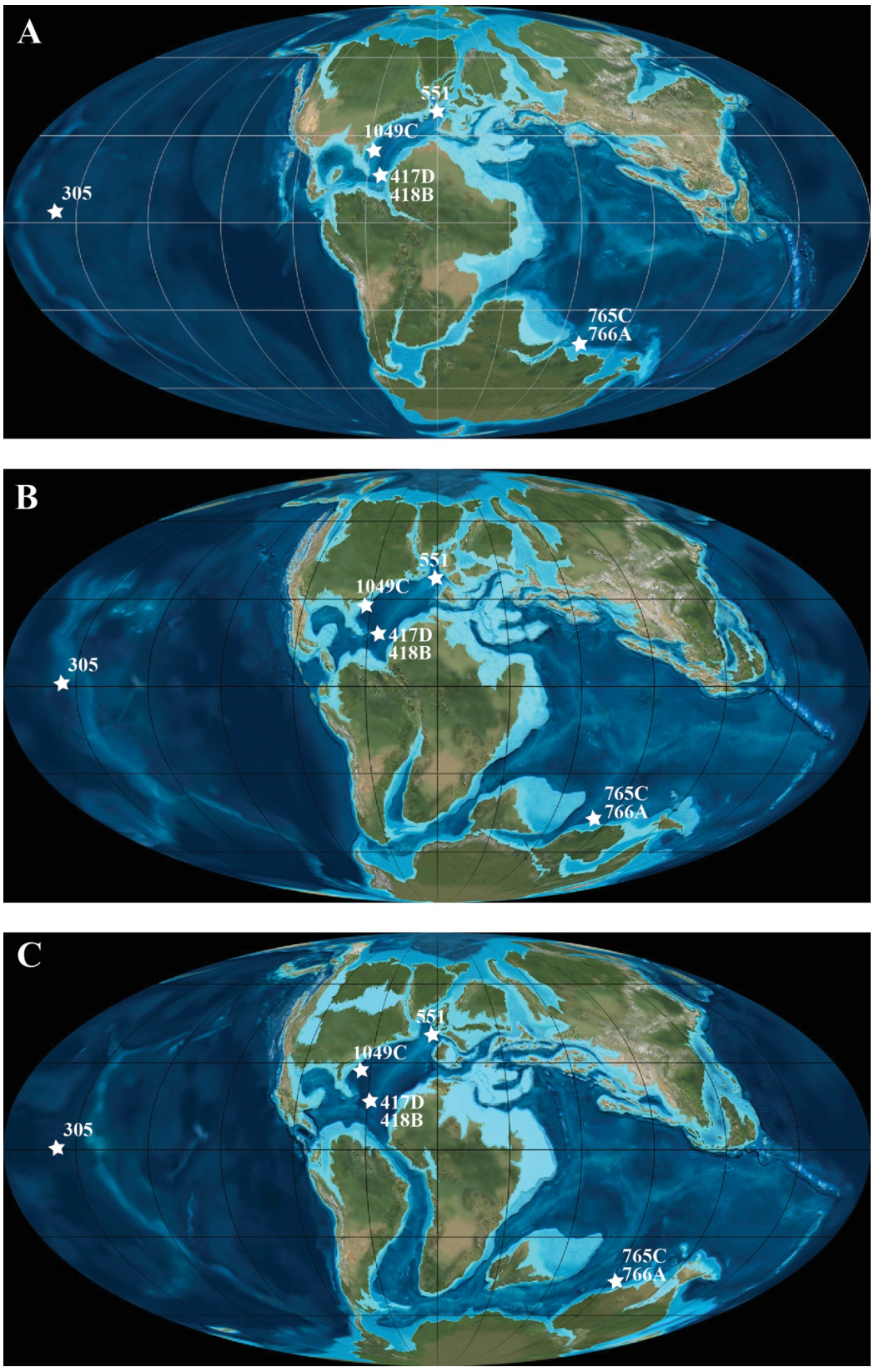
A
551
1049C
417D
418B
305
765C
766A
B
551
1049C
417D
418B
305
765C
766A
C
551
1049C
417D
418B
305
765C
766A

mechanisms driven by them that change Earth's climate. With improvements in radioisotopic and astrochronological dating techniques incorporated into the recently updated Geologic Time Scale (GTS2012) it is important to reassess age assignments and correlations of these major geologic events with the geochemical, paleontological, and sedimentological records. In light of the recent GTS, this chapter presents a review of evidence for a cool greenhouse (icehouse) climatic state along with the timing of several LIPs, deposition of the South Atlantic Salts, oceanic anoxic events (OAEs) and positive carbon isotope excursions (CIEs) during the Early Cretaceous. In addition, the age models necessary for the existing composite marine barite S isotope record for the Cretaceous will be updated as the remainder of this thesis focuses on the sulfur cycle during the Early Cretaceous [Paytan et al., 1998, 2004].

2.2 A COOL EARLY CRETACEOUS AND POSSIBLE GLACIAL EVENTS[1]

Over the last 30 years there has been growing evidence for the possible presence of short term, episodic continental ice and cold snaps during the Cretaceous greenhouse climate especially within the Early Cretaceous [e.g. Frakes and Francis, 1988; Frakes et al., 1992, 1995; Alley et al., 2003; Price and Nunn, 2010; Price and Passey, 2013; Pagani et eal., 2014]. Much of the sedimentological evidence for the presence of glaciers and cold episodes during the Early Cretaceous is concentrated in Australia, which was located near the southern pole as part of Eastern Gondwanaland along with Antarctica and the Indian subcontinent at this time (Fig. 2-1) [Frakes et al., 1995; Constantine et al., 1998; De Lurio and Frakes, 1999; Alley et al., 2003;

[1] Since the Thaumarchaeota are not marine surface dwellers, but instead reside at intermediate water depths and within the sediments they therefore cannot record sea surface temperatures. This along with the numerous uncertainties in the temperature calibration curves due to the lack of cultured species leads to all TEX_{86} data and related claims of cooling to be ignored [Ho and Laepple, 2016].

Seton et al., 2012]. Southeastern Australia (New South Wales, Victoria, South Australia) is believed to have spanned paleolatitudes ranging from ~60°-70°S during the Early Cretaceous [Frakes et al., 1995 references within]. Paleomagnetic analysis of Early Cretaceous (Hauterivian to mid Aptian) volcanoclastic sandstones in the Tethyan Himalaya deposited along the northern passive margin of Greater India indicate a paleolatitude of ~55.5°S supporting these higher paleolatitude estimates [Frakes et al., 1995; Li and Powell, 2001; Price et al., 2012; Du et al., 2015; Huang et al., 2015]. In the southwestern Eromanga and western Carpentaria Basins of Australia, pebble to boulder sized clasts that produce penetration structures in the laminae of the

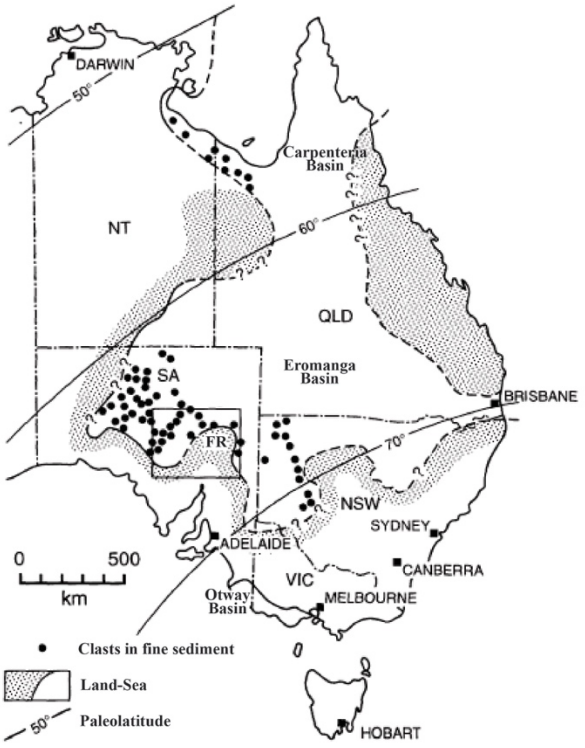

Figure 2-2 Early Cretaceous drop stones from Australia

Regional map of eastern Australia from Frakes et al. (1995) showing Early Cretaceous seaways (Eromanga and Carpentaria Basins) and the location of clasts within fine grained sediments (filled circles). Paleolatitudes from Embleton (1984). FR = Flinders Ranges

Table 2-1. Early Cretaceous sedimentological features indicative of glacial to periglacial conditions or near freezing marine temperatures

Location	Basin/Formation /Strat member	Glacial indicator feature	Age estimate	Refs.
Australia – northern South Australia & southwestern New South Wales	Eromanga Basin (1) Bulldog Shale (2) Cadna-owie Fm	Ice rafted dropstones, clasts up to 3 m dia, exhibit high degree of rounding, penetration structures in laminae	(1)Barremian/ Aptian-Albian; (2) Valanginian-Barremian/Aptian	1, 2
Australia – Flinders Ranges South Australia	Eromanga Basin Bulldog Shale Petermorra Creek	glendonites	Late Aptian	3
Australia – Flinders Ranges South Australia	Eromanga Basin Cadna-owie Fm Trinity Well	Max ~2 m thick diamictite called Livingston Tillite Member, laterally continuous over ~500 m of available outcrop, up to boulder sized clasts, smooth polished and facet clasts,	Berriasian(?)-Valanginian	4
Australia – Flinders Ranges South Australia	Eromanga Basin Cadna-owie Fm Trinity Well	Periglacial deposits, fossil ice wedges, congeliturbation	Berriasian(?)-Valanginian	4
Australia – southeast Victoria	Gippsland Basin Wonthaggi Fm	Cryoturbation structures –Type 3a & 3b involutions	Aptian	5
Svalbard	Carolinefjellet Fm Dalkjegla Mb	glendonites	Aptian	6
Svalbard	Rurikfjellet Fm Ullaberget Mb(?)	glendonites	Late Valanginian	7
Axel Heiberg Island, Nunavut, Canada	Sverdrup Basin Christopher Fm Invincible Point Mb	glendonites	Late Aptian – Early Albian	8
NE Alaska – Brooks Range	Colville Basin Kongakut Fm Pebble Shale Unit	Outsized pebbles of chert + quartzite in shale interpreted as ice rafted drop stones	Hauterivian-Barremian	2, 9

References: 1 – Frakes et al., 1995; 2 – Frakes and Francis, 1988; 3 – De Lurio and Frakes, 1999; 4 – Alley and Frakes, 2003; 5 – Constantine et al., 1998; 6 – Maher et al., 2004; 7 – Price and Nunn, 2010; 8 – Herrle et al., 2015; 9 – Molenaar, 1983

hosting fine-grained sediments have been found in large clusters and as lonestones (Table 2-1 and Fig. 2-2) [Frakes and Francis, 1988; Frakes et al., 1995; Alley and Frakes, 2003]. These clasts can be up to 3 m in diameter and have variable shapes ranging from angular to well-rounded with some displaying smooth, polished and faceted surfaces characteristic of transport within a glacial environment [Frakes and Francis, 1988; Frakes et al., 1995; Alley and Frakes, 2003]. These clasts are located throughout the fine sediments of the Cadna-owie Formation (Parabarana Sandstone and Pelican Well equivalents) and the overlying Bulldog Shale, which

have a combined age range of Valanginian to Albian [Frakes and Francis, 1988; Frakes et al., 1995; Alley and Frakes, 2003]. While there had been debate on the origin of these dropstones, discovery of a glacial diamictite near the Flinders Ranges in South Australia provides definitive proof for the presence of some glaciers during the Early Cretaceous (Table 2-1) [Frakes and Francis, 1988; Frakes et al., 1995; Alley and Frakes, 2003]. In addition, periglacial deposits with fossil ice wedges and congeliturbation features were found in outcrops within a few kilometers of the exposed diamictite [Alley and Frakes, 2003]. This diamictite, the Livingston Tillite Member of the Cadna-Owie Formation, has been assigned an age of Berriasian-Valanginian based on local palynoflora, while the majority of Cadna-Owie Formation located further northward is dated Valanginian-Aptian [Alley and Frakes, 2003].

A single glacial diamictite at a point during the Early Cretaceous does not indicate the presence of long-lived massive continental ice sheets throughout the Early Cretaceous. However, it does prove that notable and significant ice accumulation at high paleolatitudes (or high altitudes) was possible during parts of the Early Cretaceous and that the greenhouse climate system was quite dynamic and variable, especially at high latitudes [Frakes et al., 1992; Dera et al., 2011; Korte and Hesselbo, 2011; Boucot et al., 2013]. Oxygen isotope records and Mg/Ca ratios from low to mid latitude belemnites and bulk rock carbonate during the Late Valanginian indicate that the cooling/glacial episode was global and not restricted to Eastern Gondwanaland (Table 2-2) [van de Schootbrugge et al, 2000; Price et al., 2000; Kessels et al., 2006; McArthur et al., 2007]. This Late Valanginian cooling trend is further evident in the transition from a "tropical carbonate factory" to a "cool-water carbonate factory" observed on carbonate platforms throughout the Tethyan and Atlantic realms [Greselle et al., 2011 and references within]. The presence of glendonites in Svalbard indicating near freezing marine temperatures and the

migration of Boreal ammonites and calcareous nannofossils into southern Europe and the Central Atlantic Ocean during the Late Valanginian indicates that the Arctic climate was equally dynamic at this time (Tables 2-1 and 2-2) [Kessels et al., 2006; McArthur et al., 2007 and references within; Price and Nunn, 2010]. A 4-5‰ positive excursion in $\delta^{13}C$ of plant organic matter from Crimea during the Upper Valanginian indicates a significant decrease in atmospheric pCO_2 further supporting a major cooling trend during this time [Grocke et al., 2005]. Assuming the younger end of the assigned age range for the Livingston Tillite Member is correct, than it is highly probable that the glacial diamictite coincided with the previously identified global climatic cooling event during the Late Valanginian [van de Schootbrugge et al, 2000; Price et al., 2000; Alley and Frakes, 2003; Grocke et al., 2005; Kessels et al., 2006 McArthur et al., 2007; Price and Nunn, 2010; Greselle et al., 2011]. A Late Valanginian glacial environment with a global effect is further supported by strongly asymmetrical sea level fluctuations reaching a maximum in amplitude within the Vocontian Basin (Tethys Ocean) at this time [Greselle and Pittet, 2010]. Estimates of $\delta^{18}O_{sw}$ derived from clumped isotope thermometry (Δ_{47}) of Late Valanginian belemnite rostra from the Yatria River in Siberia are enriched in ^{18}O relative to the assumed ice free value, potentially indicating the presence of notable continental ice at this time [Price and Passey, 2013]. The coincidence of these sedimentalogical, paleontological, and isotopic data can be taken to represent a distinct glacial episode that may have lasted a few million years during the Early Cretaceous supporting the notion of a "cool greenhouse" and a very dynamic climate system during parts of the Mesozoic (Tables 2-1 and 2-2) [Frakes et al, 1992; Dera et al., 2011; Korte and Hesselbo, 2011].

Table 2-2. Early Cretaceous isotopic, chemical and biotic evidence indicative of cooling trends, glacial conditions, or near freezing marine temperatures

Location	Basin/Formation/ Strat member	Isotopic, chemical & biotic evidence	Age estimate	Refs.
Svalbard	Rurikfjellet Fm Ullaberget Mb(?)	$\delta^{18}O_c$ glendonites & belemnites imply high latitude near freezing marine temperatures	Late Valanginian	1
Australia – Flinders Ranges South Australia	Eromanga Basin Bulldog Shale Petermorra Creek		Late Aptian	2
Gulf of Mexico Central Atlantic NW Tethys (France & Spain) SW Boreal (UK)	DSDP 535 ODP 638 Vocontian Basin Provence Platform SE Spain Speeton Clay FM	$\delta^{18}O_c$ belemnites + bulk rock, Mg/Ca belemnites indicate cooling trend ~4°C in NW Tethys, SW Boreal & Central Atlantic Oceans paleolatitudes ~17-45°N	late Early Valanginian to Late Valanginian/Early Hauterivian	3-6
NW Tethys (France & Spain)	Vocontian Basin Provence Platform SE Spain	0.8-1.0‰ positive change in calculated relative $\delta^{18}O_{sw}$ implies possible substantial ice-caps	Late Valanginian to Early Hauterivian	6
Siberia	Yatria River	Positive $\delta^{18}O_c$ belemnites + Δ_{47} calculated $\delta^{18}O_{sw}$ positive indicate cool temperatures + possible ice growth	Late Valanginian	7
Wombat Plateau, NW Australia	ODP 761C	$\delta^{18}O_c$ belemnites indicate near freezing (~5C) intermediate depth waters	Berriasian-Valanginian	8
Southern Boreal (Germany)	Lower Saxony Basin (A39)	$\delta^{18}O_c$ belemnites indicate cooling trend ~8°C	late Early Barremian to Late Barremian	9
Western Australia	Carnarvon Basin Windalia Radiolarite Gearle Siltstone	Belemnite $\delta^{18}O_c$ and Mg/Ca indicate cool temperatures followed by ~6°C warming trend	Late Aptian to Early Albian	10, 11
Central Atlantic & North Sea Basin	ODP 638 BGS borehole 81/43	Southward migration cold water calcareous nannofossil *Crucibiscutum salebrosum*	late Early Valanginian to Late Valanginian/Early Hauterivian	5
NW Tethys (France & Spain)	Vocontian Basin Provence Platform SE Spain	Southward migration boreal ammonites	Early-Late Valanginian to Late Valnaginian	6
Eastern North Atlantic Ocean NW Tethys	DSDP 545 Vocontian Basin	Increased abundances boreal calcareous nannofossil *Repagulum parvidentatum*	Late Aptian-Early Albian	12, 13
Eastern North Atlantic Ocean	DSDP 545	Decline deep-dwelling *Nannoconus spp*.	Late Aptian-Early Albian	13

References: 1 – Price & Nunn, 2010; DeLurio & Frakes, 1999; 3 – van de Schootbrugge et al., 2000; 4 – Price et al., 2000; 5 – Kessels et al., 2006; 6 – McArthur et al., 2007; 7 – Price and Passey, 2013; 8 – Bralower, 1992; 9 – Mutterlose et al., 2009; 10 – Pirrie et al., 1995; 11 – Price et al., 2012; 12 – Herrle and Mutterlose, 2003; 13 – McAnena et al., 2013

This proposed Late Valanginian glacial episode would have overlapped in part and possibly entirely with the positive carbon isotope excursion of the Weissert Event [van de

Schootbrugge et al, 2000; Price et al., 2000; Alley and Frakes, 2003; Grocke et al., 2005; Kessels et al., 2006 McArthur et al., 2007; Price and Nunn, 2010; Greselle et al., 2011; Charbonnier et al., 2013; Martinez et al., 2013]. A positive carbon isotope excursion is most often taken to be indicative of an increased burial of organic carbon, which would coincide with a drawdown of atmospheric CO_2 producing a cooling of the climate [Arthur et al., 1988]. However, despite the clear positive carbon isotope excursion the Weissert Event is known for its limited amount of organic carbon-rich black shale deposition compared to the widespread black shale deposition characteristic of other oceanic anoxic events [Hennig et al., 1999; Bersezio et al., 2002; Brassel et al., 2004; Westermann et al., 2010 and references within]. A cold glacial climate state such as proposed for the Late Valanginian would result in well oxygenated deep ocean waters that would inhibit the deposition of black shales and enrichment of redox sensitive elements [Westermann et al., 2010; Kujau et al., 2012]. The coincidence of this glacial state with the Weissert Event could help explain biomarker and redox sensitive trace element data that support well oxygenated bottom waters in multiple locations during this purported oceanic anoxic event (OAE) [Westermann et al., 2010; Kujau et al., 2012].

The presence of numerous glendonite beds in the Arctic Sverdrup Basin and the Australian Eromanga Basin spread across the Late Aptian into the Early Albian indicate a long lasting global cool period at this time (Table 2-1) [De Lurio and Frakes, 1999; Maher et al., 2004; Herrle et al., 2015]. This cold episode is further supported by belemnite $\delta^{18}O_c$ and Mg/Ca values from the Carnarvon Basin in western Australia and the migration of the boreal calcareous nannofossil *Repagulum parvidentatum* into the Tethys and proto-North Atlantic Oceans (Table 2-2) [Pirrie et al., 1995; Herrle and Mutterlose 2003; Price et al., 2012; McAnena et al., 2013]. The presence of cryoturbation structures in fluvial-lacustrine deposits of the Gippsland Basin in

southeastern Australia during the Aptian indicate that high latitude glaciers may have been present during this cold snap (Table 2-1) [Constantine et al., 1998]. The drawdown of atmospheric CO_2 from the increased weathering and deposition of organic carbon during and following the Early Aptian OAE 1a along with numerous black shale horizons comprising OAE 1b at the Aptian-Albian boundary likely contributed to the relative cooling of the climate [Arthur et al., 1988; Menegatti et al., 1998; Poulsen et al., 2001; Leckie et al., 2002; Weissert and Erba, 2004; Wagner et al., 2007; Browning and Watkins, 2008; Jenkyns et al., 2010; Trabucho Alexandre et al., 2011; McAnena et al., 2013; Herrle et al., 2015] This prolonged cool period that would result in the demise of ocean stratification along with increased nutrient availability and productivity has been suggested to be a major driving force in the major changes observed in planktonic foraminiferal assemblages across the Aptian-Albian boundary [Huber and Leckie, 2011; McAnena et al., 2013].

The sedimentological, isotopic, and biotic evidence summarized above and in Tables 2-1 and 2-2 clearly support the presence of at least two distinct cold periods during the Early Cretaceous – mid Valanginian to Early Hauterivian and Late Aptian to Early Albian. This growing body of evidence has pushed reconciliation of the potential existence of episodic, short term cold periods during greenhouse climate states along with an awareness of the dynamic variability and nuances present in such conditions [Dera et al., 2011; Korte and Hesselbo, 2011; Pagani et al., 2014].

2.3 EARLY CRETACEOUS LARGE IGNEOUS PROVINCES

Advances in the study of large igneous provinces (LIPs) have led to the definition moving beyond size characteristics to instead focus on the intraplate tectonic setting along with

the transient and pulsed nature of these systems further emphasizing their anomalous nature [Bryan and Ernst, 2008]. This revised definition now requires that >75% of the total igneous volume (>0.1 Mkm^3) must be emplaced during one or more short-lived igneous pulses (1-5 Ma) emphasizing high magma emplacement rates [Bryan and Ernst, 2008]. The low emplacement rates and long-lived nature of spreading centers/mid-ocean ridges (MOR) contrasts with the characteristics of a LIP event, despite several LIPs being rifted apart leading to the development of MORs (e.g. North Atlantic Igneous Province, Central Atlantic Magmatic Province, Parana-Etendeka). This distinction between the end of a LIP event and the development of a MOR is further emphasized in the intraplate tectonic setting requirement in the revised definition [Bryan and Ernst, 2008]. The initial intraplate tectonic setting highlights the point of the mantle melt region feeding the LIP as being anomalous and away from concurrently active plate boundaries with active magmatism. However, not all LIPs are rifted apart leading to the development of MORs such as the Columbia River flood basalts and the Siberian Traps highlighting the anomalous nature of these large, mantle melt regions. Geochemically related intrusive and extrusive magmatic activity can precede and follow the main pulse(s) of a LIP with the maximum lifespan of a LIP event being ~50 Ma [Gibson et al., 2006; Bryan and Ernst, 2008]. Most of the LIPs with long lifespans (>15 Ma), though, have multiple pulses [Bryan and Ernst, 2008]. A complication to determining the lifespan of a LIP event is the slower, continual magmatic activity during the rifting of a LIP and the development of spreading centers may appear continuous and geochemically related to the LIP event [Mahoney et al., 1993; Tejada et al., 1996, 2002; Taylor, 2006; Bryan and Ernst, 2008]. While LIPs are not evenly distributed through the geologic record they are clearly related to the supercontinent cycle with several LIPs

clustering during the Early- to Mid-Cretaceous related to the continued breakup of Pangea [Bryan and Ferrari, 2013]. The following is a review of the timing of Early Cretaceous LIPs.

The Parana-Etendeka LIP, located today primarily in Brazil along with Paraguay, Argentina, Uruguay, and Namibia, preceded the opening of the South Atlantic Ocean during the Early Cretaceous [Gibson et al., 2006; Moulin et al., 2010; Janasi et al., 2011; Chaboureau et al., 2013]. The extrusive volcanics of the Paranae-Etendeka LIP were dominated by tholeiitic basalts, but also contained significant silicic (rhyolite and dacite) eruptions [Peate et al., 1990; Bryan et al., 2002; Gibson et al., 2006]. Recent reanalysis and recalculated (FC 28.201 Ma) ^{40}Ar-^{39}Ar dates along with U-Pb dates (zircon and baddeleyite) from extrusive samples constrain the main phase of the Parana-Etendeka LIP beginning at ~135 Ma and ending around 131.5 Ma (Table 2-3 and Appendix I Table A1-1) [Turner et al., 1994; Stewart et al., 1996; Wigand et al., 2004; Thiede and Vasconcelos, 2010; Janasi et al., 2011; Pinto et al., 2011]. While smaller alkaline eruptions and emplacement of dykes related to the Parana-Etendeka LIP preceded the Late Valanginian to Late Hauterivian main phase by up to 10 Ma, the main phase postdates the onset of the Weissert C isotope event (mid-Valanginian) [Gibson et al., 2006; McArthur et al., 2007; Janasi et al., 2011; Charbonnier et al., 2013; Martinez et al., 2013]. Based on current estimates for the start of the Weissert C isotope event (136.8 Ma Martinez et al., 2013) and its duration (~2 Ma Charbonnier et al., 2013) the main phase of the Parana-Etendeka LIP began just as the Weissert event was nearing its end. This timing therefore calls into question the claim of Pb isotopic signatures representative of main phase Parana-Etendeka silicic eruptions coincident with the onset and peak of the C isotope excursion of the Weissert Event within ODP Hole 1149B [Chavagnac et al., 2008; Peate et al., 2009].

One of the least constrained and poorly understood large igneous provinces is the Early-Mid Cretaceous High Arctic LIP. The High Arctic LIP is primarily expressed in the giant radiating dyke swarm that encompasses Franz Josef Land, Svalbard, the Queen Elizabeth Islands (Sverdrup Basin Magmatic Province), and southern Alpha Ridge [Buchan and Ernst, 2006; Dossing et al., 2013]. Extrusive volcanic rocks from the High Arctic LIP are found subaerially in the Queen Elizabeth Islands, Svalbard (Kong Karls Land), Bennett Island (De Long Islands, Russia) and Franz Josef Land [Embry and Osadetz, 1988; Harland, 1997; Buchan and Ernst, 2006; Drachev and Saunders, 2006; Dossing et al., 2013]. While the array of the radiating dyke swarm across the Arctic region implies relatedness, chemical and isotopic similarities of the Early Cretaceous tholeiitic basalts from Svalbard, Franz Josef Land, and the Queen Elizabeth Islands further indicate a common origin [Harland, 1997; Maher, 2001; Estrada and Henjes-Kunst, 2004; Buchan and Ernst, 2006; Dossing et al., 2013]. Although it remains highly debated, many authors have suggested that the Alpha-Mendeleev Ridge (also referred to as Alpha-Mendeleev LIP) is an oceanic plateau that was a major extrusive component of the High Arctic LIP [Maher, 2001; Gaina et al., 2011 Grantz et al., 2011; Saltus et al., 2011; Dossing et al., 2013]. Despite this controversy most authors agree on a proposed plume center for the High Arctic LIP located on the elevated southern end of the Alpha Ridge that appears to have been the center of the giant radiating dyke swarm [Maher, 2001; Buchan and Ernst, 2006; Dossing et al., 2013]. Reliable radioisotopic ages for the High Arctic LIP originate primarily from intrusive volcanic rocks, as readily accessible extrusive volcanic rocks, in particular the Alpha-Mendeleev Ridge, are limited (Appendix I Table A1-2) [Silantyev et al., 2004; Buchan and Ernst, 2006; Villeneuve and Williamson, 2006; Nejbert et al., 2011; Shipilov and Karyakin, 2011; Tegner et al., 2011; Corfu et al., 2013]. Sedimentological constraints from the four transgressive-

Table 2-3. Lifespan and major pulses of Early- to Mid-Cretaceous LIPs. See text for references and corresponding tables in Appendix I compiling published radioisotopic dates.

LIP	Major Pulse(s) (Ma)	Total Lifespan (Ma)	Geologic Stage of Major Pulse(s)
Parana-Etendeka	135-131.5	145-127.5	Late Valanginian-Hauterivian
High Arctic LIP	~128-123 (Isachsen Fm), ~106-97 (Strand Fiord Fm)	138-92	Late Barremian-Early Aptian, Late Albian-Cenomanin
Ontong Java-Manihiki-Hikurangi Plateau + Nauru Basin & East Mariana Basin flood basalts	~130-125	~130-125	Barremian-Early Aptian
Comei-Bunbury	134-129.5	134-129.5	Late Valanginian-Early Barremian
Kerguelen Plateau-Broken Ridge Rajmahal-Bengal-Sylhet Traps	119-115.5, 112-107, 100, 95-94	120-94	Late Aptian, Early-Late Albian, Late Albian, Cenomanian
Southeast Africa LIP	123-121, 101-99	130-94	Early-Late Aptian, Late Albian-Early Cenomanian

regressive cycles that mark Valanginian to Maastrichtian stratigraphy throughout the Arctic region are also used to help constrain the timing of volcanic activity for the High Arctic LIP [Embry and Osadetz, 1988; Harland, 1997; Buchan and Ernst, 2006]. Intrusive volcanic activity is thought to have begun in the early Valanginian (~138 Ma) coincident with regional rifting followed by three main periods of extrusive and intrusive activity: Hauterivian-Barremian (133-128 Ma), Late Barremian-Aptian (128-112 Ma), and Late Albian-Early Cenomanian (106-97 Ma) (Strand Fiord Formation on Axel Heiberg Island) (Table 2-3) [Embry and Osadetz, 1988; Buchan and Ernst, 2006; Villeneuve and Williamson, 2006; Nejbert et al., 2011; Shipilov and Karyakin, 2011; Dossing et al., 2013]. Zircons from a felsic tuff/bentonite on Svalbard have been dated with U-Pb to 123.3 ± 0.2 Ma in line with age estimates for the Isachsen Formation volcanics on the Queen Elizabeth Islands and the Late Barremian-Early Aptian pulse [Embry and Osadetz, 1988; Buchan and Ernst, 2006; Corfu et al., 2013; Dossing et al., 2013]. The near stepwise transition in sandstone composition from quartz arenites to sublitharenites in the Late

Barremian Helvetiafjellet Formation on Svalbard coincident with the arrival of marine facies is further support for significant extrusive activity from the High Arctic LIP starting earlier in the Barremian [Maher et al., 2004]. The ~20 Ma duration of sublitharenite sandstones containing volcanic lithics and plagioclase grains in Svalbard (Carolinefjellet Formation) is indicative of the massive volume of these extrusive volcanics consistent with the Barremian-Aptian initial major pulse of the High Arctic LIP (Table 2-3) [Maher et al., 2004]. Late Cretaceous alkaline volcanics in the Arctic region, such as the Hansen Point volcanics on NW Ellesmere Island, are thought to represent a change to continental rift-related magmatism and therefore beyond the defined LIP phase [Estrada and Henjes-Kunst, 2004, 2013; Bryan and Ernst, 2008; Tegner et al., 2011].

Similarities in elemental compositions, isotopic ratios, velocity structure, and chronologies have led to the suggestion that the Early Cretaceous Ontong Java, Manihiki, and Hikurangi Plateaus located in the southwestern Pacific Ocean originated from the same mantle source as a singular plateau [Mahoney et al., 1993; Tejada et al., 1996, 2002, 2004; Taylor, 2006; Hoernle et al., 2010; Timm et al., 2011; Chandler et al., 2012; Hochmuth et al., 2015]. Recent surveys of the basins, fracture zones, and relict spreading centers surrounding the plateaus have enabled reconstructions of a singular Ontong Java-Manihiki-Hikurangi Plateau (OJMHP) (Fig. 2-3) [Taylor, 2006; Chandler et al., 2012; Hochmuth et al., 2015]. The reconstructions of a singular OJMHP place the initiation of rifting and therefore the end of the LIP event near the start of the Cretaceous magnetic superchron (Chron 34, 125.93-83.64 Ma, GTS2012) [Taylor, 2006; Chandler et al., 2012; Ogg, 2012; Hochmuth et al., 2015].

These reconstructions imply that the majority of the emplacement of the OJMHP should have occurred prior to 123 Ma and probably by ~126 Ma [Taylor, 2006; Chandler et al., 2012;

Figure 2-3 Ontong Java-Manihiki-Hikurangi Plateau maps

A) Augmented bathymetric map from Taylor (2006) showing the location (red outline) of Ontong Java Plateau (OJP), Manihiki Plateau (MP), Hikurangi Plateau (HP), and Robbie Ridge (RR) along with tectonic and geophysical features. White lines – abyssal hill seafloor fabric; Coarse dashed green lines – fracture zones; Fine dashed green lines – triple junction traces; Fine dashed red line – zigzag rift boundary; Black lines with barbs – trenches; Dashed black lines – sutures. Select magnetic lineations are color-coded and labeled 34 and M0 through M29. Small black numbers indicate DSDP and ODP drill sites. Australia (Aust.), Chatham Rise (CR), Clipperton Fracture Zone (CFZ), Ellice Basin (EB), East Mariana Basin (EMB), Gilbert seamounts (GS), Nauru Basin (NB), New Zealand (NZ), Osbourn Trough (OT), Solomon Islands (SI), Stewart Basin (SB), Tokelau seamounts (TS), Wishbone Scarp (WS). **B**) Reconstruction of the Ontong Java-Manihiki-Hikurangi Plateau at M0 time (~125 Ma) by Taylor (2006), just before its break up and the end of the Pacific (PAC)-Phoenix (PHO) spreading.

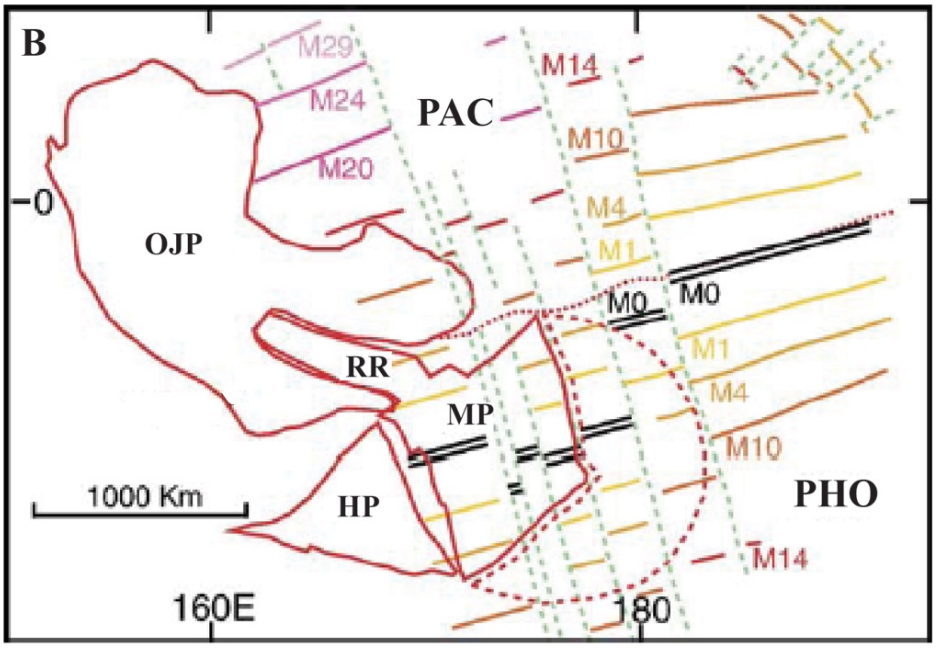
B
M29
M24
M20
M14
M10
M4
M1
M0
M0
M1
M4
M10
M14
PAC
PHO
0
OJP
RR
MP
HP
1000 Km
160E
180

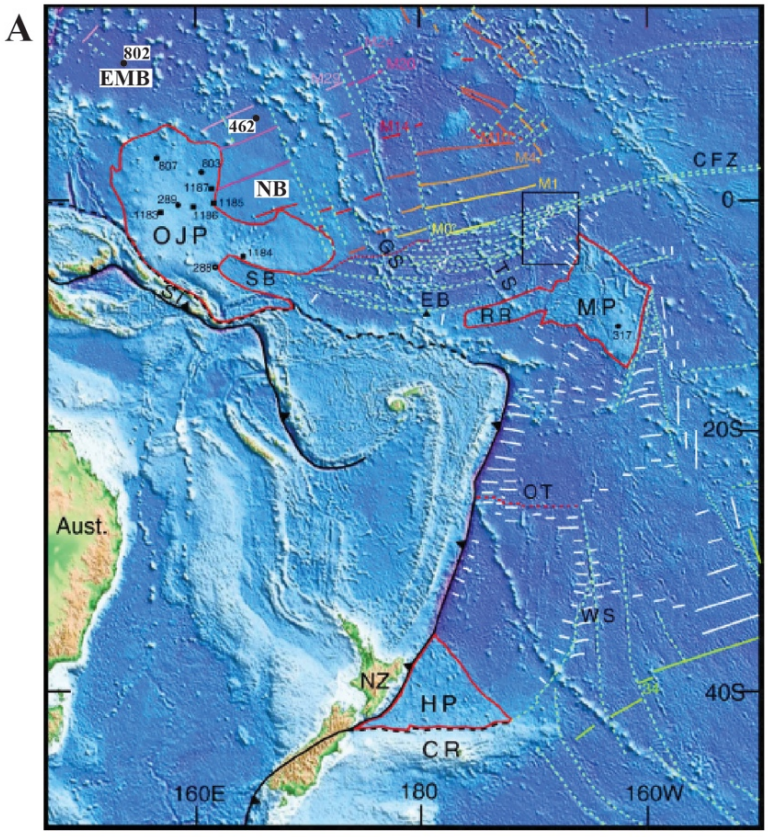
A
802
EMB
462
807
603
1187
289
1185
1183
1186
NB
OJP
1184
288
SB
EB
RR
MP
317
CFZ
0
20S
40S
OT
WS
Aust.
NZ
HP
CR
160E
180
160W

Hochmuth et al., 2015]. Assigning the termination of the main phase for OJMHP to ~126 Ma is at the older end of the typical published age range (119-125 Ma) given for formative, voluminous volcanism and slightly older than the typical mean age (122-123 Ma) for OJMHP (Appendix I Table A1-3) [Mahoney et al., 1993; Tejada et al., 1996, 2002; Chambers et al., 2004; Taylor, 2006, Hoernle et al., 2010; Timm et al., 2011]. The discrepancy between most of the published ages and the timing of the tectonic reconstructions for OJMHP could result from sampling rift stage volcanics istead of main phase volcanics, an updated value for the Fish Canyon Tuff (FCT) standard used to calculate $^{40}Ar/^{39}Ar$ radioisotope ages, changes in the GTS Barremian-Aptian boundary age, and/or potential argon recoil [Renne et al., 1998, 2010, 2011; Ogg et al., 2004; Fitton et al., 2005 and references within; Taylor, 2006; Bryan and Ernst, 2008; Kuiper et al., 2008; Chandler et al., 2012; Ogg and Hinnov, 2012 and references within; Hochmuth et al., 2015]. The presence of the Early Aptian planktonic foraminifera zone *Leupoldina cabri* in sediments on Ontong Java just above the basalt in ODP Holes 1183A and 1186A requires the termination of the main phase of OJMHP to have occurred no later than the Early Aptian [Sikora and Bergen, 2004; Ogg and Hinnov, 2012]. The updated value for the FCT used in determining $^{40}Ar/^{39}Ar$ radioisotope ages along with astronomical tuning of large sections of the Cretaceous time period has resulted in the Barremian-Aptian boundary being pushed older, from ~121 Ma in GTS1995 to 125 ± 1.0 Ma in GTS2004 to the current 126.3 Ma in GTS2012 [Ogg et al., 2004; Ogg and Hinnov, 2012 and references within]. Therefore, the Early Aptian foraminiferal zone on top of Ontong Java further supports termination of the main phase at ~126 Ma according to GTS2012. The decline in marine $^{87}Sr/^{86}Sr$ values beginning in the Late Barremian Boreal ammonite zone *Paracrioceras elagans* (lower part Tethyan *Ancyloceras vandenheckei*) following a steady, near linear increase in values that began in the Late Jurassic

supports an earlier initiation for the OJMHP [MacArthur et al., 2004, 2007, 2012]. This implied older age for the majority emplacement of OJMHP is better aligned with the GTS2012 age of ~125.5 Ma for the initiation of OAE1a, as many authors connect the eruption of Ontong Java as a potential triggering factor for OAE1a [Jenkyns, 1995, 2010; Jenkyns et al., 1995; Menegatti et al., 1998; Jones and Jenkyns, 2001; Leckie et al., 2002; Tejada et al., 2009; Malinverno et al., 2010; Bottini et al., 2012; Herrle et al., 2015; Gomes et al., 2016]. With the tectonic reconstructions indicating rifting began early within the Cretaceous superchron (Chron 34 125.93-83.64 Ma, GTS2012) marking the end of the LIP construction it is likely that many of the younger ages including claims of late minor pulses are related to rifting or separate, distinct events [Taylor, 2006; Bryan and Ernst, 2008; Chandler et al., 2012; Hochmuth et al., 2015]. For example, some younger seamounts on the Hikurangi Plateau (99-67 Ma) are thought to represent distinct separate magmatic events related to the plateau's collision with Zealandia [Taylor, 2006; Hoernle et al., 2010; Chandler et al., 2012] Assuming the singular OJMHP hypothesis is correct, then the main phase of major emplacement must have ended around 126-125.5 Ma prior to the initiation of its breakup and coincident with the onset of OAE1a [Jenkyns, 1995, 2010; Jenkyns et al., 1995; Menegatti et al., 1998; Leckie et al., 2002; Taylor, 2006; Tejada et al., 2009; Malinverno et al., 2010; Chandler, 2012; Ogg and Hinnov, 2012; Hochmuth et al., 2015; Gomes et al., 2016]. While chemically related volcanism likely continued during the initial stages of breakup of the OJMHP, determining a precise termination age of the LIP phase (high effusive rate, intraplate setting) and initiation of rift volcanism during the Cretaceous magnetic superchron is quite difficult [Tejada et al., 1996, 2002, 2004; Taylor, 2006; Bryan and Ernst, 2008; Chandler et al., 2012].

Consolidation of OJMHP to a single LIP makes it the most voluminous LIP known, yet there are indications that the event may have been even larger including ocean basin flood basalts in the Nauru and East Mariana Basins surrounding the Ontong Java Plateau (Fig. 2-3A) [Castillo et al., 1991, 1994; Tejada et al., 2002, 2004; Mochizuki et al., 2005; Taylor et al., 2006; Hoernle et al., 2010]. The Nauru and East Mariana Basins along with nearby Pigafetta Basin are the oldest ocean basins containing Jurassic-Early Cretaceous oceanic crust based on magnetic anomalies [Nakanishi et al., 1992; Nakanishi and Winterer, 1998]. However, the Naura and East Mariana Basins are unusual in that later Cretaceous basaltic sills, flows, pillows, and volcaniclastic sediments cover this crust [Moberly and Jenkyns, 1981; Tokuyama and Batiza, 1981; Castillo et al., 1991, 1994]. Drilling ~1200 mbsf into the Naura Basin (DSDP Hole 462) recovered ~100 m of Cretaceous volcaniclastic sediment and ~650 m of Cretaceous basalt, but never reached Jurassic oceanic crust [Moberly and Jenkyns, 1981; Tokuyama and Batiza, 1981; Mochizuki et al., 2005]. The chemical composition and isotopic ratios of the basalts and volcaniclastic sediments in Nauru Basin along with the basalts in East Mariana Basin have a Kwaimbaita-type tholeiitic lava signature, which is the dominant basaltic type found throughout the OJMHP [Tokuyama and Batiza, 1981; Castillo et al., 1991, 1994; Tejada et al., 1996, 2002, 2004; Castillo, 2004; Hoernle et al., 2010; Timm et al., 2011].

The typical age range of ~111-115 (± 5) Ma given for the Nauru and East Mariana Basin Cretaceous basalts is based on whole rock ^{40}Ar-^{39}Ar measurements from samples from the upper portions of the basalt section from DSDP Hole 462 and ODP Hole 802 (Appendix 1 Table A1-3) [Ozima et al., 1981; Pringle, 1992; Castillo et al., 1994]. This age range overlaps with some of the younger ages given for OJMHP samples, but could be the result of argon recoil and therefore represent minimum ages [Tejada et al., 1996, 2002; Chambers et al., 2004; Fitton et al., 2005;

Taylor, 2006; Hoernle et al., 2010]. A basalt sample from the bottom of the recovered section from DSDP 462 gave a whole rock ^{40}Ar-^{39}Ar age of 129.7 ± 4.6 Ma based on two consecutive fractions in the step heating process [Takigami et al., 1986]. Despite the significant error range, limited confidence from only two fractions forming the data plateau, and potential issues of whole rock Ar-Ar dating, this age is more aligned with the majority of OJMHP being emplaced by ~126 Ma based on reconstructions of a singular plateau [Taylor, 2006; Chandler et al., 2012; Hochmuth et al., 2015]. Regardless of the issues aligning ages, the lack of a structural boundary demarcating the Ontong Java Plateau from the Nauru Basin and their similarities in basaltic composition and isotopic ratios support the hypothesis that they are related and originate from a singular event [Castillo et al., 1991, 1994; Tejada et al., 1996, 2002, 2004; Castillo, 2004; Mochizuki et al., 2005; Taylor, 2006; Hoernle et al., 2010]. With the Late-Oligocene Caroline Ridge separating the East Mariana Basin from the Ontong Java Plateau today, a connection between the two during the Early Cretaceous was likely to be structurally uninhibited similar to the Nauru Basin supporting their relatedness [Castillo et al., 1994; Altis, 1999].

Using the reconstructions of the singular OJMHP, strontium isotope stratigraphy, the presence of Early Aptian planktonic foraminifera zone *L. cabri* on OJP and the whole rock ^{40}Ar-^{39}Ar "plateau-like" age from the bottom of DSDP Hole 462 the estimated main phase of the OJMHP-Naura Basin-East Mariana Basin LIP is from 130-126 Ma (Table 2-3) [Takigami et al., 1986; Sikora and Bergen, 2004; McArthur et al., 2004, 2007, 2012; Taylor, 2006; Chandler et al., 2012; Hochmuth et al., 2015]. As noted previously, the rifting of OJMHP complicates determination of the end of the high effusive rates associated with the LIP phase and the start of the slower but more continuous rifting volcanism. If the younger ages (111-115 Ma) at the top of the flood basalt sections in the Nauru and East Mariana Basins along with those from OJMHP

are correct it is difficult to identify them as part of an all encompassing LIP phase while the Manihiki and Hikurangi Plateaus had already significantly rifted away [Ozima et al., 1981; Pringle, 1992; Castillo et al., 1994; Taylor, 2006; Hoernle et al., 2010; Chandler et al., 2012; Hochmuth et al., 2015]. Therefore, it is possible that the main phase of the OJMHP-Nauru Basin-East Mariana Basin LIP represents the total lifespan of the LIP according to the revised definition of Bryan and Ernst (2008). However, this implies that volcanism chemically similar to the LIP phase did continue through the rifting phase of OJMHP for several to tens of millions of years, if the younger ages are correct. In the rifting of an oceanic plateau LIP the chemistry of the LIP phase and rifting phase basalts are likely to be more similar than the basalts in a continental LIP and the resultant mid-ocean ridge (Parana-Etendeka and southern Mid-Atlantic Ridge). It is possible that the elevated spreading rates that characterize the Mid-Cretaceous could have allowed for notable addition to the OJMHP-Nauru Basin-East Mariana Basin LIP during its rifting phase accounting for the younger ages (125-110 Ma) [Larson, 1991; Tejada et al., 1996, 2002; Rowley, 2002; Chambers et al., 2004; Fitton et al., 2005; Taylor, 2006; Hoernle et al., 2010].

The Kerguelen hotspot is thought to be one of the longest lived volcanic centers producing the Comei-Bunbury LIP (~132 Ma), the Rajmahal-Bengal-Sylhet Traps (~118 Ma), and the Kerguelen Plateau-Broken Ridge (~120-95 Ma) during the Early- to Mid-Cretaceous [Coffin et al., 2002; Kent et al., 2002; Ingle et al., 2002, 2004; Ray et al., 2005; Zhu et al., 2009]. Late Cretaceous to Paleogene activity from the Kerguelen hotspot produced the Ninetyeast Ridge and the most northern portions of the Kerguelen Plateau [Coffin et al., 2002]. The Bunbury basalts of southwestern Australia were subarieal eruptions during the Early Cretaceous into a fault graben located between the Archean Yilgarn Craton and the Proterozoic Leeuwin Complex

[Frey et al., 1996; Ingle et al., 2004]. ^{40}Ar-^{39}Ar dating of plagioclase separates from Bunbary basalts provide an age of 132.2 ± 0.3 Ma similar to earlier whole rock ^{40}Ar-^{39}Ar age of ~130 Ma (Appendix I Table A1-4) [Frey et al., 1996; Coffin et al., 2002]. Recent analysis of dismembered mafic lava flows, sills, dykes, and gabbroic intrusions along with subordinate ultramafic and silicic rocks within the eastern Tethyan Himalayan sequence in southeastern Tibet identified these components as deposits of the Early Cretaceous Comei LIP [Zhu et al., 2009 and references within]. U-Pb zircon dating of the range of igneous rock types in southeastern Tibet provide an age range of 129.5-134.1 Ma with a weighted mean age of 131.5 ± 0.8 Ma (n=15) (Appendix Table A1-4) [Zhu et al., 2009]. The coincident ages for the Bunbary basalts and the Comei LIP along with reconstructions of Gondwanaland during the Early Cretaceous imply that they represent a singular LIP event (Comei-Bunbary) (Table 2-3) [Coffin et al., 2002; Zhu et al., 2009; Bryan and Ferrari, 2013].

Geochemical and isotopic similarities link the Bunbary basalts of southwestern Australia to the Rajmahal-Bengal-Sylhet Traps (RBS Traps) of eastern India and parts of the Kerguelen Plateau, indicating a common source in the Kerguelen hotspot [Ingle et al., 2002, 2004; Ghatak and Basu, 2011]. The oldest date within the southern Kerguelen Plateau and the RBS Traps, however, is 118.99 ± 2.11 Ma (Appendix I Table A1-5) [Coffin et el., 2002; Duncan, 2002; Kent et al., 2002; Ray et al., 2005]. This ~10 Ma gap in volcanic activity in conjunction with the chemical linkages to the Kerguelen hotspot can result in the Comei-Bunbary LIP and the Kerguelen Plateau-Broken Ridge-RBS Traps being considered either separate LIP events or distinct major phases of a single long lived LIP [Coffin et al., 2002; Ingle et al., 2002, 2004; Ray et al., 2005; Zhu et al., 2009; Ghatak and Basu, 2011]. For the purpose of this study the Early Cretaceous Comei-Bunbary LIP and the Early- to Mid-Cretaceous Kerguelen Plateau-Broken

Ridge-RBS Traps LIP are considered separate events [Coffin et al., 2002; Duncan, 2002; Ingle et al., 2002, 2004; Zhu et al., 2009]. In addition, the Late Cretaceous to Paleogene Ninetyeast Ridge, Skiff Bank and northern Kerguelen Plateau are excluded from the Kerguelen Plateau-Broken Ridge-RBS Traps LIP despite also being related to the Kerguelen hotspot [Coffin et al., 2002; Duncan, 2002]. The Kerguelen Plateau-Broken Ridge-RBS Traps LIP was primarily constructed during 4 major pulses. The RBS Traps and part of the southern Kerguelen Plateau were formed from the first pulse (119-115.5 Ma) while the remainder of the southern Kerguelen Plateau and Elan Bank were produced during the second pulse (112-107 Ma) (Table 2-3 and Appendix I Table A1-5) [Coffin et al., 2002; Duncan, 2002; Kent et al., 2002; Ray et al., 2005]. The third pule at ~100 Ma produced the central Kerguelen Plateau while the final pulse and end of the LIP phase at 95-94 Ma resulted in Broken Ridge [Coffin et al., 2002; Duncan, 2002].

Recent seismic analysis off the southeastern coast of Africa and plate-kinematic reconstructions of the Cretaceous breakup of Gondwanaland has led to the recognition of a Southeast African LIP [Parsiegla et al., 2008; Gohl et al., 2011]. The current rifted remnants of this LIP include the Mozambique Ridge-Transkei Rise-Agulhus Plateau, Maud Rise, Northeast Georgia Rise, and northern Astrid Ridge [Gohl et al., 2011]. Seismic studies have resulted in both the Mozambique Ridge and Agulhus Plateau being characterized as over-thickened, seismically homogenous, lower crustal units with elevated seismic velocities (7.0-7.6 km/s) indicative of the addition of large volumes of mantle derived magma [Gohl et al., 2011]. The Transkei Rise is a corridor of thicker oceanic crust connecting the Mozambique Ridge and Agulhus Plateau that is 500-1000 m shallower than the surrounding Indian Ocean crust [Gohl et al., 2011]. It is suspected that the Transkei Rise represents ~20 Ma of a lower level of excessive volcanic activity separating the two major pulses of the Southeast African LIP [Gohl et al.,

2011]. The initial pulse of the Southeast African LIP produced the Mozambique and Astrid Ridges while the second major pulse formed the Agulhus Plateau-Maud Rise-Northeast Georgia Rise complex [Gohl et al., 2011]. Unfortunately, currently there are no radioisotope dates from any of the components of the Southeast African LIP. Therefore, the lifespan of the LIP and the timing of its major pulses are relatively constrained by plate-kinematic reconstructions and geophysical measurements. The inability to date the Transkie Rise by magnetic spreading anomalies is taken to indicate its formation during the Cretaceous magnetic superchron (125.93-83.64 Ma) [Gohl et al., 2011; Ogg, 2012]. Magnetic data from the Mozambique Ridge and Mozambique Basin to the northeast of the rise constrain the formation of the ridge to between 140-122 Ma [Konig and Jokat, 2010; Leinweber and Jokat, 2011]. The model by Gohl et al. (2011) constrains the maximum extent of the Mozambique Ridge to 120 Ma with the Antarctic-African spreading center underneath its eastern flank. The second major pulse is estimated to have occurred when the Antarctic-African-Atlantic triple junction passed over the Bouvet hotspot at ~100 Ma [Gohl et al., 2011]. Based on the available geophysical data and plate reconstructions the lifespan of the Southeast African LIP is estimated to be from 130-94 Ma with two major pulses at 123-121 Ma and 101-99 Ma (Table 2-3) [Parsiegla et al., 2008; Konig and Jokat, 2010; Leinweber and Jokat, 2011; Gohl et al., 2011].

2.4 TIMING OF THE SOUTH ATLANTIC APTIAN SALTS

The opening of the South Atlantic Ocean during the Early Cretaceous resulted in deposition of a 1-2 km thick evaporitic sequence within the central segment between Brazil and Africa (Angola-Congo-Gabon) [Burke and Sengor, 1988; Modica and Brush, 2004; Davison, 2007; Torsvik et al., 2009; Moulin et al., 2010; Chaboureau et al., 2012, 2013]. Initial age

estimates placed the South Atlantic salts within the Aptian where as more recent estimates identified initial deposition within the late Early Aptian and a second major phase of deposition in the Late Aptian [Burke and Sengor, 1988; Modica and Brush, 2004; Davison, 2007]. Revised tectonic and geodynamic models for the opening of the South Atlantic Ocean integrated with biostratigraphic and sedimentological records have provided new constraints on the timing of salt deposition [Toursvik et al., 2009; Moulin et al., 2010; Chaboureau et al., 2013]. The central segment of the South Atlantic was dominated by a large, rift controlled lacustrine system with episodic marine flooding during the Early Aptian (ostracode biozone AS10) [Modica and Brush, 2004; Chaboureau et al., 2013]. Just prior, near the Barremian-Aptian boundary within ostracode biozone AS9, the first small salt deposit with few anhydrites occurred within the Kwanza Basin on the African side, likely marking the first marine influence [Chaboureau et al., 2013]. With the exception of lacustrine deposits within the Santos and North Gabon Basins the remainder of the central segment of the South Atlantic experienced a major hiatus during the early Late Aptian [Chaboureau et al., 2013]. The first evaporitic sequence occurred in the northern Alagoas Basin along the Brazilian side during the intra biozone AP3 (local subzone) of the Middle Aptian [Chaboureau et al., 2013]. During the Late Aptian (intra biozone AP4, 116-114 Ma) approximately 90% of the central segment of the South Atlantic was covered by evaporites with gypsum/anhydrite and halite dominant within the southern basins and chloride evaporitic minerals (e.g. sylvite, carnaillite, and bischofite) dominant in the northern basins [Chaboureau et al., 2012, 2013]. This middle to late Late Aptian age for the evaporite deposition is consistent with the oldest marine sediments and faunas from the Sergipe Basin on the Brazilian side in the northern section of the central segment being of Late Aptian age [Koutsoukos, 1992 and references within]. Further the occurrence of deep water planktonic foraminifera did not occur

until the mid to late Albian within the Sergipe Basin [Koutsoukos, 1992]. Where as episodic marine flooding allowed for limited evaporite deposition during the Early Aptian within the central segment of the South Atlantic, the primary accumulation of the South Atlantic salts occurred during the Late Aptian.

2.5 TIMING OF EARLY CRETACEOUS POSITIVE CIEs AND OAEs

The first positive CIE or OAE within the Early Cretaceous is the Late Valanginian positive CIE known as the Weissert Event (Fig. 2-4) [Lini et al., 1992; Channell et al., 1993; Erba et al., 2004; Weissert & Erba, 2004; Duchamp-Alphonse et al., 2007; McArthur et al., 2007; Westermann et al., 2010; Kujau et al., 2012; Charbonnier et al., 2013; Martinez et al., 2013]. While initially proposed as the oldest evidence for greenhouse climate conditions during the Cretaceous by Lini et al. (1992), the mounting sedimentological, isotopic, and biotic evidence for cooler temperatures and the presence of high latitude ice during the Valanginian (Tables 2-1 and 2-2) indicate that positive CIEs may also occur during cold (glacial) episodes (See Section 2.2 above) [e.g., Grocke et al., 2005]. The Weissert Event is characterized by a ~2‰ positive CIE in marine carbonate that starts near the end of *Busnardoites campylotoxus* ammonite zone within the *Calcicalathina oblongata* calcareous nannofossil zone (NK3a) just below the Upper Valanginian substage boundary [Lini et al., 1992; Channell et al., 1993; Erba et al., 2004; Weissert & Erba, 2004; Duchamp-Alphonse et al., 2007; McArthur et al., 2007; Westermann et al., 2010; Kujau et al., 2012; Charbonnier et al., 2013; Martinez et al., 2013]. Despite the global nature of this positive CIE, development of thick black shales globally during this interval did not occur as organic matter enriched sediments have only been recovered from a few localities (Vocontian Basin, Southern Alps, Shatsky Rise) [Hennig et al., 1999; Bersezio et

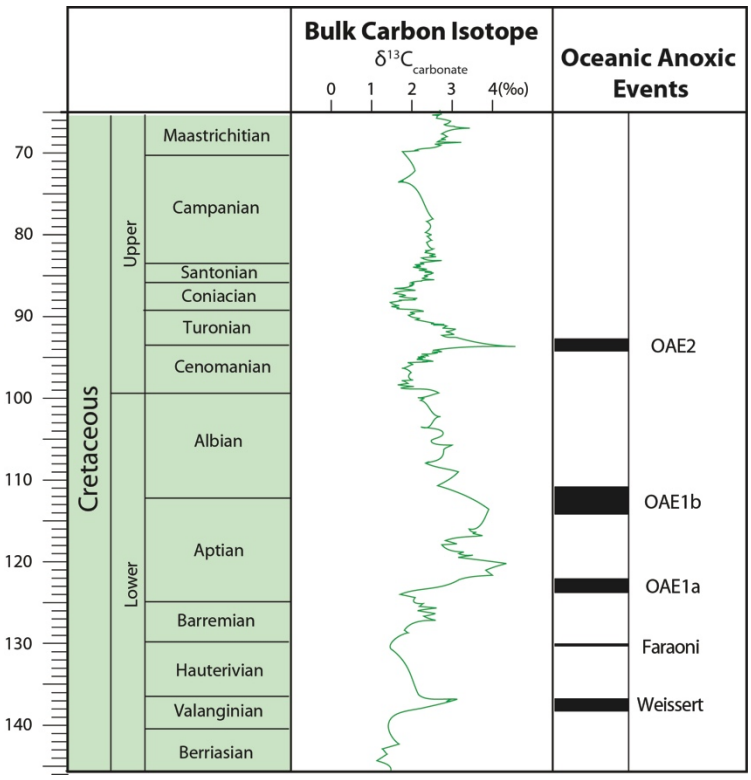

Figure 2-4 Cretaceous Carbon isotope record and OAEs

Composite carbonate carbon isotope record and OAEs for the Cretaceous modified from Takashima et al. (2006).

al., 2002; Brassell et al., 2004; Westermann et al., 2010; Kujau et al., 2012]. Limited organic carbon burial in the oceans is further supported by elevated Mn concentrations and the absence of any enrichment in redox sensitive trace elements during the CIE within several Tethyan sections, indicating deposition in an oxic environment [Westermann et al., 2010].

Recent astrochronologic analysis of Valanginian sections from France by Charbonnier et al. (2013) and Martinez et al. (2013) indicate that the duration of this stage may be 430-820 ka shorter than proposed by GTS2012 (5.51 ± 0.6 Ma). Using the carbon isotope stratigraphy from the Orpiere, France section, Charbonnier et al. (2013) define the Weissert Event from the start of the positive CIE to the end of the elevated values with a minimal duration of 2.08 Ma (Table 2-

4). Using corresponding tie points in the carbon isotope stratigraphy, cyclostratigraphic analysis of other Valanginian sections by Sprovieri et al. (2006) and Martinez et al., (2013) estimate slightly longer durations for the Weissert Event (2.3 and 2.14 Ma, respectively) (Table 2-4). Combining their recent cyclostratigraphic analysis of the Valanginian with the GTS2012 base of the Berriasian (145.0 ± 0.8 Ma), and uncertainty in the duration of the Berriasian, Martinez et al. (2013) estimated the absolute age for the onset of the Weissert Event to range from 136.8 to 140.2 Ma. A Hauterivian radioisotope age of 132.5 ± 1.3 Ma from the Neuquen Basin (Aguirre-Urreta et al., 2008) provided additional constraint for Martinez et al. (2013) to narrow the estimate for the onset of the Weissert Event to 136.8 ± 0.8 Ma (Table 2-4). The error for the onset of the Weissert Event is greater than the difference in estimates for the duration of the Valangian by Charbonnier et al. (2013) and Martinez et al. (2013) and therefore would cover any offset for the alternate cyclostratigraphic duration.

The next supposed OAE during the Early Cretaceous is the Late Hauterivian Faroni event (Fig. 2-4). Characterized by four thin organic-rich black shales intercalated with an ammonite-rich marker bed, the Faroni event occurs within the *Pseudothurmannia ohmi* ammonite zone above the last occurrence of calcareous nannofossil *Lithraphidites bollii* [Baudin & Riquier, 2014 and references within]. Expression of the Faroni event is currently limited to tropical and temperate paleolatitudes and displays considerable variability in total organic carbon (TOC) enrichment within this restricted region [Baudin & Riquier, 2014 and references within]. Despite TOC enrichments reaching 25% for some Faroni black shales within the Umbrian-Marche basin (Italy) there is no clear major positive shift in the $\delta^{13}C_{carb}$ signal that is characteristic and defining of other OAEs [Baudin & Riquier, 2014 and references within]. The small positive shift of 0.2-0.4‰ in $\delta^{13}C_{carb}$ observed in some localities displaying the Faroni event is about 10% of the

Table 2-4. Timing and duration of Early Cretaceous OAEs and positive CIEs

Name	Defining characteristic	Duration (Ma)	GTS2012 Onset Age (Ma)	Refs.
Weissert Event	Start of positive CIE to end of high values	2.08-2.3	136.8 ± 0.8	1, 2
Faroni Event	Continuous black chert and overlying 7 beds (A-G)	0.10-0.15	~131.5	3, 4
OAE 1a	Negative CIE preceding positive CIE; CIE longer than black shales	1.0-1.4 Selli; 2.6-3.0 CIE[a]	125.58 ± 0.45	5-8
OAE 1b	3 distinct black shale layers – Jacob, Kilian, Paquier	Jacob: 0.040	114.8 ± 0.5	6
		Kilian: 0.120	112.95 ± 0.45	6, 9
		Paquier: 0.046	111.23 ± 0.4	6, 10, 11

References: 1 – Charbonnier et al., 2013; 2 – Martinez et al., 2013; 3 – Martinez et al., 2012; 4 – Baudin and Riquier, 2014; 5 – Li et al., 2008; 6 – Huang et al., 2010; 7 – Malinverno et al., 2010; 8 – Ogg, 2012; 9 – Kennedy et al., 2014; 10 – Erbacher et al., 2001; 11 – Friedrich et al., 2005

magnitude of the excursion typically associated with other OAEs [Godet et al., 2006; Baudin & Riquier, 2014 and references within]. Recent cyclostratigraphic analysis of the Hauterivian-Barremian boundary at the Rio Argos, Spain section identified the marl-limestone couplets of the Faroni event to be aligned with the precessional orbital cycle [Martinez et al., 2012]. Alignment with the 23 ka precessional cycle results in an estimated duration of 100-150 ka for the Faroni event (Table 2-4) [Martinez et al., 2012]. The Faroni event starts at the *P. ohmi-P.catulloi* ammonite subzone boundary, which has an absolute age of ~131.5 Ma according to GTS2012 and the cyclostratigraphic analysis of Martinez et al. (2012) (Table 2-4).

One of the most prominent OAEs of the Cretaceous is OAE1a during the Early Aptian (Fig. 2-4) [Jenkyns, 1995; Menegatii et al., 1998; Erba et al., 1999; Leckie et al., 2002; Weissert and Erba, 2004; Jenkyns, 2010; Herrle et al. 2015]. This event is clearly characterized by both widespread deposition of meter thick black shales and a positive CIE in both carbonate and organic carbon that persists well after the termination of black shale deposition (Fig. 4-3) [Jenkyns, 1995; Menegatii et al., 1998; Erba et al., 1999; Leckie et al., 2002; Weissert and Erba, 2004; Jenkyns, 2010; Malinverno et al., 2010]. There is debate if the black shale interval, which is referred to as the Selli Level, defines the entirety of OAE1a or if the persistence of positive

$\delta^{13}C$ values is a more representative demarcation of the event [Arthur and Sageman, 1994; Menegatti et al., 1998; Erba et al., 1999; Li et al., 2008; Gomes et al., 2016]. The positive CIE in carbonate associated with OAE1a is preceded by a significant although brief negative excursion in carbonate $\delta^{13}C$ that coincides with the beginning of widespread black shale deposition [Jenkyns, 1995; Menegatti et al., 1998; Erba et al., 1999; Weissert and Erba, 2004; Li et al., 2008; Tejada et al., 2009; Herrle et al., 2015]. The base of OAE1a marked by the start of black shale deposition is estimated to occur 300-400 ka above the top of chron M0r (125.93 Ma) (Table 2.4) [Menegatti et al., 1998; Erba et al., 1999; Channell et al., 2000; Li et al., 2008; Huang et al., 2010; Malinverno et al., 2010; Ogg, 2012]. Orbital chronologies for this time period estimate the duration of the black shale deposition (Selli Level) to be 1.0-1.4 Ma while the elevated $\delta^{13}C$ values persist for another ~1.6 (C7) Ma before beginning to return to pre-event values [Menegatti et al., 1998; Li et al., 2008; Huang et al., 2010; Malinverno et al., 2010]. Where as the brief negative CIE immediately followed by the major positive CIE is characteristic and widely observed at different sites the expression of the persistent elevated $\delta^{13}C$ values (C7) and recovery (C8) is quite variable across different localities (Fig. 4-3) [Jenkyns, 1995; Menegatti et al., 1998; Erba et al., 1999; Dumitrescu and Brassel, 2006; Tejada et al., 2009; Herrle et al., 2015; Gomes et al., 2016]. The tectonic reconstructions of a singular OJMHP along with the proposed initiation of OAE1a early within the Cretaceous superchron (C34n) support the hypothesis of OJMHP triggering OAE1a as indicated by Os isotope records linking the two events [Taylor, 2006; Tejada et al., 2009; Bottini et al., 2012; Chandler et al., 2012; Hochmuth et al., 2015].

The Late Aptian-Early Albian contains several short-term, black shale horizons with at least three distinct, fairly widespread sub-events – Jacob, Kilian, and Paquier – that have been

grouped together as OAE 1b (Fig. 2-4) [Erbacher et al., 2001; Leckie et al., 2002; Friedrich et al., 2005; Wagner et al., 2007; Browning and Watkins, 2008; Trabucho Alexandre et al., 2011; Pettrizo et al., 2012, 2013; Kennedy et al., 2014; Herrle et al., 2015]. The black shales of OAE 1b correspond with negative excursions and lower $\delta^{13}C$ values in contrast with other OAEs and the expected isotopic impact of increased global organic carbon burial [Erbacher et al., 2001; Herrle et al., 2004; Trabucho Alexandre et al., 2011]. Chronostratigraphic and cyclostratigraphic analysis estimate the Paquier black shale to be ~46 ka in duration with an initiation age of 111.23 ± 0.4 Ma (Table 2-4) [Erbacher et al., 2001; Friedrich et al., 2005; Huang et al., 2010; Ogg and Hinnov, 2012]. The recently proposed GSSP site for the Aptian-Albian boundary from Col de Pre-Guittard, France has the Kilian black shale straddling the Aptian-Albian boundary [Kennedy et al., 2014]. Cyclostratigraphic analysis of the Aptian estimates the Kilian black shale to be ~120 ka in duration (Table 2-4) [Huang et al., 2010]. With the Kilian black shale straddling the Aptian-Albian boundary (113.0 ± 0.4 Ma, GTS2012) the onset age is set at 112.95 ± 0.45 Ma (Table 2-4). The Jacob black shale is estimated to be 40 ka in duration with an onset age ~1.8 Ma before the Aptian-Albian boundary (Table 2-4) [Huang et al., 2010].

2.6 REVISED AGE MODELS FOR CRETACEOUS SULFUR ISOTOPE CURVE

The Cretaceous seawater sulfate sulfur isotope curve from marine barite by Paytan et al. (2004) is a key record of the sulfur cycle during this time period (Fig. 2-5a). This record is comprised primarily from samples taken from DSDP Hole 305 at Shatsky Rise and ODP Hole 766A at Exmouth Plateau-Gascoyne Abyssal Plain (Figs. 2-1 and 2-5a). A handful of samples were also taken from six other DSDP/ODP drill cores (Hole 417D, 418B, 551, 577, 765C, and 1049C) (Figs. 2-1 and 2-5a) [Paytan et al., 2004]. The marine barites from Holes 305 and 766A

were also used to construct a strontium isotope curve during the Cretaceous [Mearon et al., 2003]. The age models for the ODP cores used in the Paytan et al. (2004) and Mearon et al., (2003) studies are based on biostratigraphy and strontium isotope stratigraphy from the 1995 Geologic Time Scale. With the updated value for the FCT standard used in calculating $^{40}Ar/^{39}Ar$ ages and astrochronological analysis of large portions of the Cretaceous, this portion of the GTS has had significant changes and improvements [Gradstein et al., 1995, 2004, 2012; Renne et al., 1998, 2010, 2011; Kuiper et al., 2008]. Key amongst those changes for the Early Cretaceous is the near 5 Ma difference in age assignment for the base of the Aptian (~121 Ma versus 126.3 Ma) [Gradstein et al., 1995, 2012]. As the timing of isotopic and geochemical records is critical to aligning them with major geologic events, the following section develops revised age models updated to The Geologic Time Scale 2012 (GTS2012) [Gradstein et al., 2012] for the cores used by Paytan et al., (2004) and Mearon et al., (2003).

Absolute age assignments and error estimates for most of the Early Cretaceous (Berriasian through Barremian) in the GTS2012 are constrained by a handful of radioisotope dates (Table 2-5) fitted to a spline that was enhanced and augmented by correlation with the M-sequence of marine magnetic anomalies and cycle stratigraphy [Ogg and Hinnov, 2012]. Most of the uncertainty in this section comes from carrying the error measured in the radioisotope dates through and adding the variance from the M-sequence line-fit model [Ogg, 2012; Ogg and Hinnov, 2012]. The M-sequence line-fit model originates from correlating durations of magnetic intervals derived from cyclostratigraphy in six selected sections spanning the Oxfordian to Barremian to a composite Hawaiian block model in order to determine spreading rates [Ogg, 2012 and references within].

The limited number of well constrained radioisotopic dates within the Early Cretaceous leads to the absolute age assignment for the base of the Cenomanian being a critical tie point for calculating Early Cretaceous ages. Two tuffs dated from Japan by Obradovich et al. (2002) constrain the top of lowermost subzone of the *Mantelliceras mantelli* ammonite zone to 99.8 ± 0.4 Ma [Ogg and Hinnov, 2012]. Cyclostratigraphy estimates a duration of 0.44 Ma for this subzone within the Vocontian Basin [Gale, 1995; Ogg and Hinnov, 2012]. However, the base of this subzone is located 6 m above the GSSP for the base of the Cenomanian in the Risou section [Ogg and Hinnov, 2012]. This leads to the base of the Cenomanian being assigned an age of 100.5 ± 0.4 Ma in the GTS2012. Although a strong radioisotope calibration point exists for the Aptian-Albian boundary within the Boreal realm, cyclostratigraphy from the Tethyan realm is extended from the base of the Cenomanian to the top of Chron M0r in the Early Aptian to determine the age for the base of the Aptian in the GTS2012 [Grippo et al., 2004; Selby et al., 2009; Huang et al., 2010; Ogg and Hinnov, 2012]. Cyclostratigraphic analysis of Italian

Table 2-5. Selected key radioisotope dates used in GTS2012 for the Early Cretaceous listed with original reference. See Appendix 2 of GTS2012 for more detail and full list of radioisotopic ages.

Geologic Stage	Age (Ma)	Biostratigraphic or magnetostratigraphic correlation	Method	Reference
Early Cenomanian	99.70 ± 0.38	*Mantelliceras mantelli* ammonite zone base of upper subzone	$^{40}Ar/^{39}Ar$	Obradovich et al., 2002
Early Cenomanian	99.89 ± 0.37	*Mantelliceras mantelli* ammonite zone top of lower subzone	$^{40}Ar/^{39}Ar$	Obradovich et al., 2002
Early Albian (Aptian-Albian boundary)	113.1 ± 0.3	65 cm above Boreal FO *Leymeriella (Proleymeriella) schrammeni anterior*	$^{206}Pb/^{238}U$ zircon WM	Selby et al., 2009
Early Aptian	124.07 ± 0.24	Calcareous nannofossil zone NC6 above LO *Conusphaera rothii*	$^{206}Pb/^{238}U$ zircon WM	Shimokawa, 2010
Early Aptian	125.4 ± 0.2	Top of reversed-polarity zone interpreted to be Chron M0r	$^{40}Ar/^{39}Ar$	Pringle and Duncan, 1995
Tithonian-Berriasian boundary	145.5 ± 0.8	Reversed-polarity sills intruding Early Berriasian calcareous nannofossil zone NK1	$^{40}Ar/^{39}Ar$	Mahoney et al., 2005

reference sections identified 62.5 long eccentricity cycles indicating a duration of 25.3 Ma from the base of the Cenomanian to the top of Chron M0r [Grippo et al., 2004; Huang et al., 2010; Ogg and Hinnov, 2012]. The duration of Chron M0r is estimated to be 0.5 Ma based on cyclostratigraphy [Malinverno et al., 2010]. This results in the base of the Aptian being assigned an age of 126.3 ± 0.4 Ma within the GTS2012 [Ogg and Hinnov, 2012]. The uncertainty in this age assignment originates from the error in the measurement of the Early Cenomanian radioisotopic dates by Obradovich et al. (2002). This 0.4 Ma combined with the accumulated statistical uncertainty from the M-sequence line fit is the uncertainty on absolute age assignments for most of the Early Cretaceous.

The Late Cretaceous, in contrast to the Early Cretaceous, has an abundance of radio-isotopically-dated horizons, primarily from the Western Interior Basin (WIB) of North America [Obradovich, 1993; Hicks et al., 1995, 1999; Coban et al., 2006; Meyers et al., 2012; Ogg and Hinnov, 2012]. Recalibration of these $^{40}Ar/^{39}Ar$ dates with the new FCT, new single crystal analyses and incorporated U-Pb dating of zircons has reduced the uncertainties and improved the age assignments for the stage boundaries within the Late Cretaceous from previous estimates [Meyers et al., 2012; Ogg and Hinnov, 2012]. The GTS2012 calculated a spline fit for these radio-isotopic dates and their assigned ammonite zones (WIB) that was augmented by cyclostratigraphic estimates for duration of biozones [Ogg and Hinnov, 2012]. The uncertainty in the age assignments for the Late Cretaceous stage boundaries is comprised primarily of the error from the bracketing age measurements.

In correlating GTS2012 age assigned global biostratigraphic first and last occurrences to biostratigraphic data from an ODP drill core there is a measure of uncertainty and error that originates from the sampling interval used in the biostratigraphic study. Without high resolution

sampling every centimeter it is not possible to know if the true first occurrence of an organism occurs in the sample observed or in the interval between the observation and the previous sample analyzed for biostratigraphy where it is absent. Therefore, the midpoint between the sample where the organism is observed and the previous or next sample analyzed where it is absent is the point where the GTS2012 age for first or last occurrence will be assigned. Half the distance between the samples where the organism is observed and where it is absent will be the uncertainty on this placement within the core.

2.6.1 ODP Leg 123 Hole 766A Exmouth Plateau-Gascoyne Abyssal Plain

ODP Hole 766A is a deep water drill hole located off the northwest coast of Australia in the Indian Ocean at the foot of the Exmouth Plateau facing the Gascoyne Abyssal Plain (Fig. 2-1) [Mutterlose, 1992]. Key biostratigraphic data used to determine sedimentation rates and constrain stage boundaries within the Early Cretaceous sections of Hole 766A are presented in Table 2-6 with their core depth and GTS2012 age assignments [Haig, 1992; Moran, 1992; Mutterlose, 1992]. Table 2-7 contains the key biostratigraphic data from Hole 766A used for determining ages during the Late Cretaceous [Moran, 1992].

The lowermost lithologic unit in Hole 766A (Subunit IIIB 304.2-466.7 mbsf) with its wedge shaped morphology, thickening eastward towards the Exmouth Plateau, is suspected to consist of redeposited material [SSP Leg 123, 1990b]. Therefore, the first reliable biostratigraphic datum used is the local last occurrence of calcareous nannofossil *Cruciellipsis cuvillieri* in sample 31R-3 29-31 cm, which is a key identifier for the Early-Late Hauterivian within GTS2012 [Mutterlose, 1992; Mutterlose et al., 1996; Anthonissen and Ogg, 2012; Ogg and Hinnov, 2012]. While the GTS2012 suggested that LO *C. cuvillieri* is a potential marker for the Lower-Upper Hauterivian boundary it has been noted to be extremely rare in its upper range

leading to some diachroneity and uncertainty in placement of its global LO [Bulot et al., 1992; Bergen, 1994; Mutterlose et al., 1996; Bown et al., 1998; Bown and Concheyro, 2004; Aquirre-Urreta et al., 2008; Ogg and Hinnov, 2012]. Bergen (1994) places the LO *C. cuvillieri* in bed 110 of the Vergons section in SE France, which occurs just within the *Pleisiospitidiscus ligatus* ammonite zone [Bulot et al., 1992; van de Schootbrugge et al., 2000]. In the Neuquen Basin of Argentina the LO *C. cuvillieri* occurs at the *S. ricacardii-C. schlagintweiti* ammonite zone boundary, which correlates with the upper *Subsaynella sayni* Tethyan ammonite zone [Bown and Concheyro, 2004; Aquirre-Urreta et al., 2008; Reboulet et al., 2014]. In the Boreal region the uncertainty of the LO *C. cuvillieri* crosses the BC9-BC10 calcareous nannofossil zone boundary, which correlates with the upper *Milanowskia speetonensis* Boreal ammonite zone [Bown et al., 1998]. Recent correlation of Tethyan and Boreal ammonite zones equates the upper *speetonensis* zone within the lower *ligatus* zone [Reboulet et al., 2014]. The GTS2012 assigns an interpolated numerical age of 133.09-132.68 Ma for the *S. sayni* ammonite zone and 132.68-132.37 Ma for the *P. ligatus* ammonite zone [Ogg and Hinnov, 2012]. The next sample analyzed for calcareous nannofossils within Hole 766A is located 2.90 m above the sample containing the LO *C. cuvillieri*. Therefore, this sample is assigned an age of 132.8 ± 0.75 Ma. The low abundance levels and sporadic distribution of *Conusphaera rothii* in Hole 766A prohibits it from being a reliable age indicator for this core. The local FO *Flabellites biforaminis* synonym *F. oblongus* and FO *Grantarhabdus coronadventis* in sample 27R-1 108-109 cm provide the next key biostratrigraphic data point [Mutterlose, 1992]. However, there is some uncertainty surrounding the age assignment of this sample and consequently the Barremian-Aptian boundary (BAB). *F. oblongus* is a Late Barremian identifier with its global FO at 129.41 Ma (Nannotax3) and GTS2012 marking its consistent presence at 127.31 Ma [Anthonissen and Ogg, 2012; Ogg and

Table 2-6. GTS2012 age assignments of select key biostratrigraphic data for Early Cretaceous from ODP Hole 766A. Data from Mutterlose (1992), Moran (1992), and Haig (1992). The age assignment location (listed below sample depth) is the midpoint between the sample containing FO or LO and next sample analyzed where the organism is absent unless noted otherwise.

Sample	mbsf	Biostratigraphic data	Age assignment	Comments
15R-CC	141.31	LO *Ellipsagelosphaera britannica* syn *Watznaueria britannica*		GTS2012 LO Early Cenomanian; 15R-CC only biostrat datum from core 15
16R-3 46-50 cm	146.38	(LO) *Planomalina buxtorfi*	101.18 ± 0.4	Late Albian foram marker w/in *P. appenninica* zone LO 101.18 Ma GTS2012; last sample analyzed
16R-5 60-64 cm	149.52	FO *Rotalipora appenninica* syn *Parathalmanninella appenninica*		Late Albian foram zone Late Albian to Albian-Cenomanian boundary zone/FO at 101.92 Ma
16R-CC	152.31	FO *Planomalina buxtorfi*		
17R-3 36-39 cm	155.875 (157.34 ± 1.465)	FO *Planomalina praebuxtorfi*	101.92 ± 0.4	GTS2012 Late Albian mark base of P. appenninica zone 101.92 Ma
17R-4 80-82 cm	157.81 (159.96 ± 2.15)	FO *Eiffellithus turriseiffelii*	103.13 ± 0.4	Late Albian start of CC9 GTS2012
21R CC	193.46	FO *Prediscosphaera columnata*		Aptian-Albian boundary GTS2012; Mutterlose, 1992 Early Albian
24R-1 140 cm	221.30	FO *Seribiscutum primitivum*		NC8a base Albian 112.95 Ma Nannotax3; Mutterlose, 1992 L. Aptian-E. Albian
24R CC	221.41	LO *Saracenaria spinosa*	Late Aptian	Characteristic Aptian taxon LO Late Aptian-Early Albian Holbourn & Kuhnt, 2001
25R CC	230.6	FO *Braarudosphaera hockwoldensis*	early Late Aptian	Nannotax3 Late Aptian 122.98 Ma
26R-1 10 cm	239.4 (239.42 - top of unconformity)	FO *Eprolithus floralis* FO *Rhagodiscus angustus* FO *Rucinolithus irregularis* synonym *Hayesites irregularis*	123.75 ± 0.5 definitely Aptian post OAE1a	Early Aptian post OAE1a (Selli); Mutterlose, 1992 Late Aptian-Early Albian; GTS2012 FO *E. floralis* 123.88 Ma
27R-1 108-109 cm	249.985	FO *Grantarhabdus coronadventis*	Early Aptian (126.0)	Nannotax3 FO Barr-Apt boundary; Mutterlose, 1992 Early Aptian
27R-1 108-109 cm	249.985 (251.035 ± 1.05)	FO *Flabellites biforaminis* synonym *F. oblongus*	127.3 ± 0.5	Late Barremian identifier GTS2012; Mutterlose, 1992 Early Aptian
31R-3 29-31 cm	290.8 (289.35 ± 1.45)	LO *Cruciellipsis cuvillieri*	132.8 ± 0.75	LO key identifier for Early–Late Hauterivian for GTS2012; Mutterlose, 1992 Hauterivian

FO – First occurrence; LO – Last occurrence

Table 2-7. GTS2012 age assignments of select key biostratrigraphic data for Late Cretaceous from ODP Hole 766A. Data from Moran (1992). The age assignment location (listed below sample depth) is the midpoint between the sample containing FO or LO and the next sample analyzed where the organism is absent unless noted otherwise.

Sample	mbsf	Biostratigraphic data	Age assignment	Comments
10R-CC	89.46 (88.69 ± 0.77)	LO *Reinhardtites levis*	70.14 ± 0.3	Early Maastrichtian top of CC24
12R-2 27-28 cm	106.075	LO *Eiffellithus eximius*		Late Campanian top of CC22
12R-CC	106.33 (110.31 ± 3.98)	FO *Quadrum trifidum* syn *Uniplanrius trifidum*	76.82 ± 0.4	Middle-Late Campanian base of CC22
13R-2 29-30 cm	115.695 (115.77 ± 0.07)	FO *Aspidolithus parcus* syn *Broinsonia parca parca*	80.9 ± 0.4	Early Campanian base CC18 GTS2012 before LO M. furcatus which is absent in this sample requiring maximum age to be slightly younger; midpoint with top of unconformity 13R-2 44 cm
13R-3 68-69 cm	117.585	LO *Lithastrinus septenarius* FO *Biscutum magnum*	85.6 ± 0.5	Early-Middle Santonian within CC16 GTS2012; base Santonian Nannotax3; FO and LO negate uncertainty in placement
14R-1 46-47 cm	124.065 (124.695 ± 0.63)	FO *Micula decussata* synonym *M. stauropora*	89.8 ± 0.4	M. stauropora base of UC10 & Coniacian GTS2012; abundance level few followed by next 12 samples at common abundance level
14R-2 22-23 cm	125.325	FO *Marthasterites furcatus* FO *Lithastrinus septenarius*		M. furcatus base CC13 Late Turonian just below Turonian-Coniacian boundary L. septenarius middle CC12 Middle-Late Turonian GTS2012
14R-3 23-24 cm	126.835	FO *Eiffellithus eximius*		Early-Middle Turonian base CC12 GTS2012
14R-CC	130.86 (133.665 ± 2.805)	FO *Quadrum gartneri*	93.5 ± 0.35	Early Turonian CC11 boundary post OAE2 GTS2012; midpoint with top of unconformity 15R-3 27 cm

Table 2-8. Early Cretaceous stage boundaries within ODP Hole 766A aligned with GTS2012

Stage boundary	mbsf	Age (Ma) GTS2012	Comments
Aptian-Albian	221.4 ± 0.1	113 ± 0.4	midpoint between 24R-1 140 and 24R-CC identified as Upper Aptian based on forams
Barremian-Aptian	239.42 (UC)		Lost within unconformity between lithologic unit II and III
	251.035 ± 1.0	126.3 ± 0.4	midpoint between 27R-1 108-109 cm and 27R-3 18-19 cm

Hinnov, 2012; Young et al., 2014]. The global FO *G. coronadventis* marks the BAB, which led Mutterlose (1992) to identify sample 27R-1 108-109 cm as Early Aptian [Young et al., 2014]. This would result in the potential placement of the BAB at the midpoint between samples 27R-1 108-109 cm and 27R-3 18-19 cm (Table 2-8).

In contrast, others suspect the BAB to be lost within the unconformity between the siliciclastic claystones and sandstones of lithologic unit III and the nannofossil chalks of lithologic unit II near the top of core 26 [Kaminski et al., 1992]. While seismic stratigraphy further supports the presence of the unconformity near the top of core 26 the placement of the BAB within it requires the singular rare occurrence of *G. coronadventis* in sample 27R-1 108-109 cm to be questioned and disregarded. The incorrect order of the FO of *G. coronadventis* coming before the Late Barremian FO *Rucinolithus irregularis* synonym *Hayesites irregularis* in Hole 766A supports the uncertainty surrounding the placement of the BAB and questioning the validity of this rare occurrence (Table 2-6). Unfortunately, there is no biostratigraphic data between sample 27R-1 108-109 cm and the unconformity at 26R-1 12 cm [Mutterlose, 1992; Haig, 1992]. If the BAB is lost in the unconformity between lithologic units II and III, this scenario allows the local FO *F. oblongus* in sample 27R-1 108-109 cm to be assigned to its GTS2012 "consistent presence" marker in the Late Barremian with an age of 127.3 ± 0.5 Ma [Anthonissen and Ogg, 2012]. The absence of any clear lithologic indication of OAE 1a within cores 27 or 26 further supports the BAB along with much of the Early Aptian being lost in the unconformity between lithologic units II and III (26R-1 12 cm). This uncertainty in placement of the BAB leads to two different constant sedimentation rates being calculated for the Hauterivian-Barremian/Early Aptian. Both sedimentation rates were used to determine ages for samples spanning cores 28 up to the unconformity in core 26 (Table 2-9).

The presence of a notable unconformity near the top of core 26 is further supported by the local FO *Eprolithus floralis* and FO *Rucinolithus irregularis* synonym *Hayesites irregularis* in sample 26R-1 10 cm. While the first occurrences of *H. irregularis* and *E. floralis* typically bracket OAE 1a, found together along with the FO *Rhagodoscis angustas* they necessitate a post OAE 1a age assignment [Anthonissen and Ogg, 2012; Ogg and Hinnov, 2012]. While the proximity to the unconformity raises some uncertainty if the local FO *E. floralis* in Hole 766A is coincident with its global FO, the first occurrence of Late Aptian calcareous nannofossil *Braarudosphaera hockwoldensis* in the core catcher of core 25 suggests that it is very close. Therefore, the top of the unconformity (26R-1 12 cm) is assigned an age of 123.75 ± 0.5 Ma. Determining sedimentation rates and ages for the Late Aptian requires defining the Aptian-Albian boundary as remaining key Aptian biostratigraphic marker species are absent within hole 766A.

Defining the Aptian-Albian boundary within ODP Hole 766A is a key aspect of the revised age model. The FO *Prediscosphaera columnata* marks the Aptian-Albian boundary (AAB) and the start of calcareous nannofossil zone CC8 (synonymous NC8a) in GTS2012 [Anthonissen and Ogg, 2012; Ogg and Hinnov, 2012]. The FO *Seribiscutum primitivum* occurs within NC8a and also marks the start of the Albian [Kennedy et al., 2000; Young et al., 2014]. In 766A the local FO of *P. columnata* occurs in sample 21R-CC (193.46 mbsf) at an abundance level of few where as the local FO of *S. primitivum* is nearly 25 m below in sample 24R-1 140 cm (221.3 mbsf). Mutterlose (1992) identifies samples 21R-CC and above as Early Albian and samples 22R-CC to 26R-1 10 cm as Late Aptian to Early Albian. The last occurrence of planktonic foraminifera *Saracenaria spinosa* in 24R-CC and its presence in core 25 contributed to Haig (1992) placing these samples within the Upper Aptian. The distribution of *S. spinosa*

further corroborates the presence of *S. primitivum* in 24R-1 140 cm being indicative of the Albian. Therefore, the AAB is estimated to occur between the FO *S. primitivum* in sample 24R-1 140 cm and sample 24R-CC (Table 2-8). Using this AAB and the FO *E. floralis* and FO *R. irregularis* in sample 26R-1 10 cm an average constant sedimentation rate was determined for the Late Aptian. This sedimentation rate was used to determine the age estimate for samples from the top 12 cm of core 26 to the estimated AAB in the middle of core 24 (Table 2-9).

Limited core recovery and biostratigraphic sampling within the Early to Middle Albian sections of Hole 766A (cores 21-23) hinder the development of the age model through this interval [Haig, 1992; Moran, 1992; Mutterlose, 1992]. Data for potential calcareous nannofossil marker species from the Early and Middle Albian such as *Axopodorhabdus albianus*, *Cribrospharella ehrenbergi*, and *Tranolithus phacelosus* synonym *T. orionatus* were sporadic and conflicting [Moran, 1992; Anthonissen and Ogg, 2012; Ogg and Hinnov, 2012]. The first consistent and reliable biostratigraphic data is the FO of *Eiffellithus turriseiffelii* in sample 17R-4 80-82 cm (157.81 mbsf) along with the foraminifera FO *Planomalina praebuxtorfi* in sample 17R-3 36-39 cm (155.875 mbsf) [Haig, 1992, Moran, 1992]. The global FO *P. praebuxtorfi* marks the start of the Late Albian foraminifera zone *Parathalmanninella appenninica* (formerly Rotalipora appenninica) while the FO. *E. turriseiffelii* marks the start of calcareous nannofossil zone CC9 [Petrizzo and Huber, 2006; Anthonissen and Ogg, 2012; Ogg and Hinnov, 2012]. Two sedimentation rates were calculated for most of the Albian using the estimated AAB and the FO *E. turriseiffelii* (103.13 ± 0.4 Ma) and FO *P. praebuxtorfi* (101.92 ± 0.4 Ma). Both sedimentation rates were used to determine ages for samples spanning cores 24 through 17R-3 (Table 2-9).

The presence of both *P. praeboxtorfi* and *P. buxtorfi* in cores 17 and 16 indicate a slightly expanded *P. appenninica* zone within Hole 766A. The global LO *P. buxtorfi* occurs more than half a million years before the Albian-Cenomanian boundary [Anthonissen and Ogg, 2012; Ogg and Hinnov, 2012]. The last sample analyzed for foraminifera by Haig (1992), 16R-3 46-50 cm, contains *P. buxtorfi* and is marked as its local LO with an age assignment of 101.18 ± 0.4 Ma. The sedimentation rate calculated for the FO *P. praebuxtorfi* to the LO *P. buxtorfi* is more than double the sedimentation rates for the Early to Late Albian section in Hole 766A. While this higher sedimentation rate is used to determine the age for samples in between the key biostratigraphic data points (Tables 2-6 and 2-9), it is uncertain if this elevated sedimentation rate is maintained through the remainder of the Albian and into the Cenomanian. Therefore, the average age determined from the elevated Late Albian sedimentation rate along with the Early to Late Albian sedimentation rate using the AAB and FO *P. praebuxtorfi* is the assigned age for samples from 16R-3 46-50 cm up to the unconformity at 15R-3 27.5 cm (Table 2-9). The extension of the combined sedimentation rates places the Albian-Cenomanian boundary within the lower portion of core 15, which is supported by the presence of *Ellipsagelosphaera britannica* synonym *Watznaueria britannica* in sample 15R-CC. The global LO *W. britannica* occurs in the Early Cenomanian very near the Albian-Cenomanian boundary [Anthonissen and Ogg, 2012; Ogg and Hinnov, 2012]. Where as sample 15R-CC is the local LO for *W. britannica* in Hole 766A, it is also the only sample from core 15 with biostratigraphic data before the unconformity at 15R-3 27.5 cm.

Determining stage assignments for the Late Cretaceous in Hole 766a is difficult with fairly short stages, key biostratigraphic data located near stage boundaries and several unconformities having been identified in this section [Moran, 1992]. After the Late Albian

Table 2-9. ODP Hole 766A original and GTS2012 ages along with S and Sr isotope data from Paytan et al., (2004) and Mearon et al., (2003), respectively.

Sample	Depth (mbsf)	Original Age (Ma)	GTS2012 age (Ma)	$\delta^{34}S_{barite}$ (‰)	$^{87/86}Sr$
10CC 3-5	89.46	73	70.38 ± 1.33	19.2	
11-2 106-108	97.27	75.33	72.79 ± 1.18	19.4	
13-1 18-20	114.09	78.4	79.64 ± 2.69	18.95	0.70756
13-2 106-108	116.47	83	84.94 ± 0.80	18.24	
13-3 74-76	117.65	83.9	85.64 ± 0.74	18.1	0.70745
14R-1 51-53	124.12	85.60	89.56 ± 1.34	18.34	0.707290
14R-2 138-142	126.5	91.0	90.54 ± 1.19	18.55	
14R-CC 5-7	130.86	93.5	92.34 ± 1.15	19.04	0.707370
15R-2 78-80	135.49	94.88	94.25 ± 1.45		0.707380
15R-2 96-98	135.67	95.0	94.33 ± 1.47	19.22	0.707380
15R-3 59-61	136.8	97.0	100.03 ± 0.72	18.51	0.707390
16R-4 121-123	148.62	100.0	101.33 ± 0.53	16.32	
17R-5 28-30	158.79	97.0	102.56 ± 0.61		0.70741
18R-1 34-39	162.465	104.0	103.17 ± 0.62	15.6	0.70745
18R-3 23-28	165.355	103.5	103.65 ± 0.57		0.70744
18R-3 109-113	166.21	104.4	103.79 ± 0.57		0.70743
18R-4 112-116	167.74	107.0	104.05 ± 0.60	15.65	0.707375
19R-1 31-36	172.035	108.0	104.77 ± 0.59	15.92	
19R-4 113-115	177.34	109.0	105.65 ± 0.57	16.05	
20R-1 47-50	181.885	111.0	106.41 ± 0.52		0.70735
20R-3 98-100	185.39	110.0	106.99 ± 0.56	15.92	
20R-CC	186.41	111.1	107.16 ± 0.56	16.09	0.70732
21R-1 22-26	191.24	111.9	107.97 ± 0.56	16.14	0.70730
21R-2 88-92	193.4	112.75	108.33 ± 0.51		0.70730
21R-CC 4-7	193.505	113.0	108.35 ± 0.51		0.70725
22R-1 27-33	200.90	112.0	109.58 ± 0.57	16.04	
24R-1 12-17	220.045	116.4	112.77 ± 0.64	15.42	0.70723
24R-1 64-68	220.56	114.5	112.86 ± 0.60		0.70725
24R-1 110-113	221.015	116.5	112.94 ± 0.64	15.52	
25R-1 41-46	230.035	114.7	118.15 ± 0.60		0.70727
25R-CC 12-15	230.635	114.6	118.51 ± 0.60		0.70727
26R-1 4-8	239.36	119.6	123.71 ± 0.68	15.54	0.70727
26R-3 40-45	242.725	119.1	125.50 ± 1.03		0.707389
26R-CC 3-9	243.72	119.9	125.65 ± 1.02		0.707406
27R-1 40-44	249.32	120	126.53 ± 0.94	17.23	0.70741
27R-2 97-100	251.385	120.7	126.85 ± 0.92	17.83	0.70745
28R-2 112-115	261.235	125	128.40 ± 0.82	19.7	

biostratigraphic data the next key datum is the FO *Quadrum gartneri* in sample 14R-CC (130.86 mbsf) that marks the Early Turonian (nannofossil zone CC11) and occurs post OAE 2 [Anthonissen and Ogg, 2012; Ogg and Hinnov, 2012]. While there is some uncertainty in the global placement of the FO *Q. gartneri*, the GTS2012 currently places it within the upper *P.*

flexuosum ammonite zone of the Western Interior Basin [Anthonissen and Ogg, 2012; Ogg and Hinnov, 2012]. A bentonite from the Western Interior Seaway within the upper *P. flexuosum* ammonite zone has recently been dated at 93.67 ± 0.31 Ma [Meyers et al., 2012]. Therefore, a post OAE 2 age assignment of 93.5 ± 0.35 Ma is given to sample 14R-CC (Table 2-9). Additional Turonian biostratigraphic markers in 766A include the FO *E. eximius* in sample 14R-3 23-24 cm (126.835 mbsf) and the FO *Marthasterites furcatus* and *Lithastrinus septenarius* in sample 14R-2 22-23 cm (125.325 mbsf) [Moran, 1992]. While the first occurrence of these organisms support a Turonian age assignment for this section there is diachroneity amongst all three hindering precise age assignment for calculating sedimentation rates [Burnett et al., 1998; Caron et al., 2006; Anthonissen and Ogg, 2012; Ogg and Hinnov, 2012]. The FO *Micula decussata* synonym *M. stauropora* in sample 14R-1 46-47 cm is a reliable marker as it coincides with the Turonian-Coniacian boundary in GTS2012 (Table 2-7) [Anthonissen and Ogg, 2012; Ogg and Hinnov, 2012]. The FO *Q. gartneri* and FO *Micula decussata* synonym *M. stauropora* are used to determine a sedimentation rate for the Turonian. This sedimentation rate is used to calculate ages for samples in core 14 and extended backwards for samples in core 15 above the unconformity at 15R-3 27.5 cm (Table 2-9).

The FO *Biscutum magnum* and the local LO *L. septenarius* in sample 13R-3 68-69 marks the Early-Middle Santonian [Anthonissen and Ogg, 2012; Ogg and Hinnov, 2012; Young et al., 2014]. However, the local FO *Lucianorhabdus cayeuxii*, which marks the Coniacian-Santonian boundary in GTS2012 does not occur until the following sample 13R-2 29-30 cm. There also appears to be an unconformity at 13R-2 44 cm, which is supported by the local FO *Aspidolithus parcus* synonym *Broinsonia parca parca* in sample 13R-2 29-30 and the local LO *M. furcatus* in sample 13R-3 68-69 cm [Moran, 1992]. In the GTS2012 both of these biostratigraphic events

occur in the late Early Campanian with the LO *M. furcatus* occurring later [Anthonissen and Ogg, 2012; Ogg and Hinnov, 2012]. The presence of a FO and LO in sample 13R-3 68-69 removes the uncertainty in the placement of these events negating the use of the midpoint between this sample and the previous or next sample. Therefore, sample 13R-3 68-69 is assigned an Early-Middle Santonian age of 85.6 ± 0.5 Ma. The midpoint between sample 13R-2 29-30 cm and the top of the unconformity at 13R-2 44 cm is assigned an Early Campanian age after the LO *M. furcatus* of 80.9 ± 0.4 Ma (Table 2-7). The FO *B. magnum* and FO *M. decussata* synonym *M. stauropora* are used to determine a sedimentation rate for the Coniacian-Santonion. This sedimentation rate is used to calculate ages for samples in core 13 below the unconformity (13R-2 44 cm) (Table 2-9).

The next Campanian marker species are the FO *Q. trifidum* synonym *Uniplanarius trifidium* in 12R-CC (106.33 mbsf) and the LO *E. eximius* in 12R-2 27-28 cm (106.075 mbsf) [Moran, 1992]. The diachronous nature of the LO *E. eximius* forces the FO *Q. trifidum* synonym *Uniplanarius trifidium* to be used in calculating Campanian sedimentation rates despite the significant uncertainty in the placement of the midpoint between the observed FO and the previous sample (Table 2-7) [Anthonissen and Ogg, 2012; Voigt et al., 2012]. An Early to Middle Campanian sedimentation rate was calculated using the FO *Q. trifidum* synonym *Uniplanarius trifidium* and the FO *A. parcus* synonym *B. parca parca* to determine the age of sample 13R-1 18-20 cm (Table 2-7). A final sedimentation rate was calculated for the Late Campanian-Early Maastrichtian using the FO *Q. trifidum* synonym *Uniplanarius trifidium* and the LO *Reinhardtites levis* in sample 10R-CC cm (89.46 mbsf) to determine the age for samples in cores 11 and 10 (Tables 2-7 and 2-9).

2.6.2 DSDP Leg 32 Hole 305 Shatsky Rise

DSDP Hole 305 is a deep water drill hole located in the northwest Pacific Ocean on the southern flank of the southern high of the Shatsky Rise oceanic plateau (Fig. 2-1). Calcareous nannofossil zone assignments and planktonic foraminifera biostratigraphic data from DSDP Hole 305 used to determine sedimentation rates for the Late Cretaceous are presented in Table 2-10 [Bukry, 1975; Caron, 1975]. Paleocene calcareous nannofossil zones are present throughout core 14 while the end Cretaceous planktonic foraminifera *Racemiguembelina fructicosa* has its LO near the top of core 15 (Table 2-10) [Bukry, 1975; Anthonissen and Ogg, 2012; Ogg and Hinnov, 2012]. Therefore, the Paleocene-Maastrichtian boundary is placed at the top of core 15 (Table 2-11). The last occurrence of planktonic foraminifera *Globotruncana linneiana* in sample 17R-1 30-32 cm is in line with the Late Maastrichtian calcareous nannofossil *Micula mura* zone extending into core 17R-3 (Tables 2-10 and 2-11) [Caron, 1975; Anthonissen and Ogg, 2012; Ogg and Hinnov, 2012]. The Campaninian-Maastrichtian calcareous nannofossil zone of

Table 2-10. GTS2012 correlation of select Late Cretaceous biostratigraphic data and zone assignments for DSDP Hole 305. Data from Caron, (1975) and Bukry, (1975).

Sample/interval	Biostratigraphic data/zone	Comments
14R-1 to 14R-3	*Discoaster mohleri* & *Heliolithus kleinpellii* zones	GTS2012 Paleocene Thanetian, NP6-NP7
14R-3 to 14R-4	*Fasciculithus tympaniformis* zone	GTS2012 Paleocene Selandian NP5
14R-5 to 14R-CC	*Cruciplacolithus tenuis* zone	GTS2012 Paleocene Danian NP2
15R-1 97-98 cm (130.475 mbsf)	LO *Racemiguembelina fructicosa*	GTS2012 marker species for end of Cretaceous
17R-1 30-32 cm (148.81 mbsf)	LO *Globotruncana linneiana*	GTS2012 Upper Maastrichtian 68.37 Ma
15R-1 to 17R-3	*Micula mura* zone	GTS2012 Late Maastrichtian CC25-CC26
19R-CC to 23R-3	*Tetralithus trifidus* zone synonym *Uniplanarius trifidius*	GTS2012 Campanian-Maastrichtian, LO U. trifidius E. Maastrichtian 71.31 Ma
21R-1 120-122 cm	LO *Globotruncana calcarata* syn *Radotruncana calcarata*	GTS2012 Late Campanian 75.71 Ma
23R-5 to 24R-5	*Broinsonia parca* zone	
29R-CC	LO *Globotruncana concavata* syn *Dicarinella concavata*	GTS2012 Campanian/Santonian boundary

Table 2-11. Late Cretaceous stage boundaries and tie points within DSDP Hole 305 aligned with GTS2012

Core Location	mbsf	Stage	Age assignment (Ma)
15 top	129.5 ± 0.9	Paleocene-Maastrichtian boundary	66.0 ± 0.2
16-17	147.65 ± 1.15	Late Maastrichtian	68.37 ± 0.2
19 bottom	175.3 ± 0.8	Early Maastrichtian	71.31 ± 0.25
28	257.625 ± 3.375	Campanian-Santonian boundary	83.6 ± 0.35

Tetralithus trifidus synonym *Uniplanarius trifidius* spans 19R-CC to 23R-3 in DSDP Hole 305 [Bukry, 1975]. Based on the Early Maastrichtian last occurrence of *U. trifidus* defining the end of this calcareous nannofossil zone the bottom of core 19 is assigned an age of 71.31 ± 0.25 Ma (Table 2-11) [Anthonissen and Ogg, 2012; Ogg and Hinnov, 2012]. These three tie points were used to determine three sedimentation rates for the Maastrichtian section of Hole 305. All three sedimentation rates were used to calculate ages for samples spanning cores 15 to 20. The average along with standard deviation was used as the new assigned age with error estimate for each of these samples (Table 2-12).

Clear biostratigraphic marker species or zones allowing assignment of absolute ages within the Campanian are not present in Hole 305 [Bukry, 1975; Caron, 1975; Anthonissen and Ogg, 2012; Ogg and Hinnov, 2012]. The Campanian-Santonian boundary in Hole 305 is marked by the LO *Globotruncana concavata* synonym *Dicarinella concavata* in core 29R-CC (Table 2-10 and 2-11) [Caron, 1975; Anthonissen and Ogg, 2012; Ogg and Hinnov, 2012]. The Early Maastrichtian tie point and the Campanian-Santonian boundary were used to determine a sedimentation rate and calculate ages for samples within cores 21 to 28 (Table 2-12).

Where as core recovery was good through the first 28 cores, it was extremely poor through the remainder of the hole [SSP Leg 32, 1975]. In the bottom 380 m of drilling (cores 29-68) there was only ~4% recovery as nearly 75% of the cores only had material recovered within the core catcher [SSP Leg 32, 1975]. The extremely poor core recovery along with the limited

Table 2-12. DSDP Hole 305 original and GTS2012 ages along with S and Sr isotope data from Paytan et al., (2004) and Mearon et al., (2003), respectively

Sample	Depth (mbsf)	Original Age (Ma)	GTS2012 Age (Ma)	$\delta^{34}S_{barite}$ (‰)	$^{87/86}Sr$
15R-2 57-60	131.585	65.17	66.39 ± 0.39	18.95	0.70786
15R-2 136-140	132.38	65.23	66.49 ± 0.39	18.94	
15R-5 35-42	135.885	65.53	66.90 ± 0.36		0.707821
16R-2 114-117	141.655	66.02	67.58 ± 0.34	18.76	0.70785
16R-4 41-50	143.955	66.21	67.85 ± 0.34		0.70781
17R-2 31-37	150.34	66.75	68.60 ± 0.34	18.80	
17R-4 44-51	153.475	67.04	68.97 ± 0.35		0.70780
18R-4 43-50	162.965	67.84	70.08 ± 0.40		0.707751
19R-2 112-115	169.635	68.65	70.87 ± 0.46	18.85	
20R-2 127-131	179.29	70.00	72.00 ± 0.56	18.82	0.707729
20R-4 48-55	181.515	70.25	72.26 ± 0.59		0.707721
21R-2 63-66	188.145	71.31	73.23 ± 0.72	19.09	0.707718
21R-4 50-58	191.04	71.78	73.66 ± 0.71		0.70768
21R-6 140-145	194.925	72.41	74.24 ± 0.70		0.70770
23R-1-60-70	205.65	74.19	75.84 ± 0.69	19.14	0.70767
23R-2 76-79	207.275	74.40	76.08 ± 0.69	19.33	
23R-4 50-58	210.04	75.81	76.50 ± 0.68		0.70766
23R-6 56-59	213.075	75.62	76.95 ± 0.68	19.30	
24R-4 47-53	219.0	76.95	77.83 ± 0.68		0.70764
24R-4 90-95	219.425	76.43	77.90 ± 0.68	19.14	
25R-2 108-110	226.09	78.75	78.89 ± 0.69	19.14	0.70766
25R-4 57-65	228.61	79.02	79.27 ± 0.69		0.70763
26R-2 45-50	234.975	80.32	80.22 ± 0.70	19.04	0.70764
26R-4 55-62	238.085	80.74	80.68 ± 0.70		0.7076
27R-2 67-75	244.21	81.94	81.60 ± 0.72		0.7076
27R-2 80-85	244.325	81.97	81.61 ± 0.72	18.87	0.70763
28R-2 73-77	253.75	83.63	83.02 ± 0.75	18.36	
28R-2 85-90	253.875	83.70	83.04 ± 0.75	18.40	0.70759
66R-1 125-130	617.775	129.17	132.8 ± 0.75	20.12	

and conflicting biostratigraphic data from cores 29-68 prevent the determination and assignment of reliable age models and absolute ages with any level of confidence for this portion of the core [SSP Leg 32, 1975; Bukry, 1975; Luterbacher, 1975]. Therefore, S and Sr isotope data from Paytan et al., (2004) and Mearon et al., (2003) for this portion of Hole 305 can be plotted against core depth but are excluded from an integrated absolute time plot. There is a singular exception to this as key Hauterivian calcareous nannofossils were found in the bottom three cores. The presence of *Cruciellipsis cuvillieri* in cores 66 to 68 along with *Tubodiscus verenae* present in core 67, but absent from core 66, enables the placement of core 66 in the Early-Late Hauterivian

[Bukry, 1975; Bulot, 1992; Bergen, 1994; Anthonissen and Ogg, 2012; Ogg and Hinnov, 2012]. Correlating these calcareous nannofossil last occurrences with the interpolated numerical ages for ammonite zones in GTS2012 allows sample 66R-1 125-130 cm to be assigned an age of 132.8 ± 0.75 Ma with reasonable confidence (Table 2-12) [Bulot, 1992; Bergen, 1994; van de Schootbrugge et al., 2001 Anthonissen and Ogg, 2012; Ogg and Hinnov, 2012].

2.6.3 ODP Leg 171B Hole 1049C Blake Nose

ODP Hole 1049C is the deepest hole within the Blake Plateau-Blake Nose transect, located in the subtropical western North Atlantic off the eastern coast of Florida (Fig. 2-1) [SSP Leg 171B, 1998; Huber et al., 2008]. There are two major unconformities present in Hole 1049C within the Cretaceous section of the core complicating the assignment of absolute ages in between these boundaries [SSP IR Ch. 3, 1998; Huber et al., 2008; Huber and Leckie, 2011]. The larger of the two unconformities represents a gap from the Campanian to the Albian and marks a distinct lithologic change (11X-2 120 cm) [SSP Leg171B, 1998; Huber et al., 2008; Huber and Leckie, 2011]. High-resolution analysis of planktonic foraminifera by Huber and Leckie (2011) identified the second unconformity at 12X-4 148 cm to contain the Aptian-Albian boundary. Below this unconformity is the Late Aptian foraminifera zone *Paraticinella eubejaouaensis* (= *P. rohri* zone; see Ando et al., 2013) where as the *Microhendbergella rischi* zone is the first Albian foraminifera zone following the hiatus (Table 2-13) [Huber and Leckie, 2011]. This indicates that the *M. miniglobularis* and *M. renilaevis* zones are missing along with the Kilian black shale of OAE 1b [Anthonissen and Ogg, 2012; Ogg and Hinnov, 2012; Petrizzo et al., 2012, 2013; Kennedy et al., 2014]. Recently, the FO *M. renilaevis* within the Kilian black shale of the Col de Pre-Guittard section in the Vocontian Basin has been proposed as a GSSP for the Aptian-Albian boundary [Kennedy et al., 2014]. This would then lead to the ~46 cm thick black shale at 12X-3

45-90 cm in ODP Hole 1049C being correlated with the Paquier/Urbino black shale of OAE 1b, as was suggested by Erbacher et al. (2001). Browning and Watkins (2008) placed the FO *Praediscophaera columnata* s.s. (circular) at the base of the black shale in Hole 1049C similar to its location of consistent presence just beneath the Niveau Paquier in Col de Pre-Guittard, reinforcing the correlation of this black shale (Table 2-13) [Kennedy et al., 2014]. The length of the Paquier black shale has been estimated at ~46 ka indicating a 1 cm/ka sedimentation rate during the event at Hole 1049C [Erbacher et al., 2001]. Cyclostratigraphic analysis through the Albian and Aptian indicates that the base of Paquier should be 26.5 long eccentricity cycles (405 ka) from the Albian-Cenomanian boundary [Huang et al., 2010; Ogg and Hinnov, 2012]. Using an absolute age of 100.5 Ma for the Albian-Cenomanian boundary this leads to the base of Paquier black shale having an age of 111.23 ± 0.4 Ma (Table 2-14).

Despite the strong absolute age assignment for the base of the Paquier from cyclostratigraphy and the estimated sedimentation rate within the black shale, it is uncertain if that same sedimentation rate was maintained before or after the event. If the ~1 cm/ka sedimentation rate was present before the Paquier black shale then the age at the top of the unconformity would be estimated at 111.438 Ma. This would then indicate the unconformity lasted ~2 Ma, which is double the estimated length by Huber and Leckie (2011). The local FO of calcareous nannofossil *Hayesites albiensis* just above the Aptian-Albian unconformity is more in

Table 2-13. Select Cretaceous biostratigraphic data for ODP Hole 1049C from Browning and Watkins (2008) and Huber and Leckie (2011).

Sample	mbsf	Bio/Litho stratigraphic data	Comments
11X-2 113-115 cm	132.33	FO *Radotruncana celcarata*	Campanian
11X-CC 30-31 cm	134.53	FO *Ticinella madecassiana*	Early-Middle Albian
12X-3 90 cm	143.20	FO *Praediscophaera columnata* s.s. (circular)	1.4 m below base of Niveau Paquier at Col de Pre-Guittard [Kennedy et al., 2014]
	145.25	FO *Hayesites albiensis*	GTS2012 Early Albian 112.65 Ma
12X-4 145-147 cm	145.26	FO *Microhedbergella rischi* FO *Microhedbergella renilaevis*	*M. rischi* Early Albian; FO *M. renilaevis* proposed marker Aptian-Albian boundary
12X-4 149-150 cm	145.29	LO *Paraticinella eubejaouaensis*	Late Aptian (= P. rohri; Ando et al., 2013)

Table 2-14. Albian tie points in ODP Hole 1049C aligned with GTS2012

Tie point feature	mbsf	GTS2012 (Ma)
Top Paquier OAE 1b black shale	142.75	111.184 ± 0.4
Base Paquier OAE 1b black shale	143.20	111.23 ± 0.4
12X-4 148 cm unconformity top	145.28	112.35 ± 0.5

line with the hiatus lasting ~ 1 Ma [Browning and Watkins, 2008; Anthonissen and Ogg, 2012; Ogg and Hinnov, 2012]. Therefore, the top of the unconformity is assigned an age of 112.35 ± 0.5 Ma (Table 2-14). There is no other confident tie point with an absolute age assignment between the two unconformities. According to GTS2012, the Paquier black shale should occur within the *Ticinella primula* foraminifera zone, whose first occurrence has been assigned an age of 111.84 Ma [Anthonissen and Ogg, 2012; Ogg and Hinnov, 2012]. In Hole 1049C *T. primula* is absent and the next biostratigraphic marker is the FO *T. madecassiana* in 11X-CC 30-31 cm [Huber and Leckie, 2011]. In the potential GSSP site Col de Pre-Guittard the Paquier black shale occurs within the *M. renilaevis* zone [Kennedy et al., 2014]. It is likely that the *M. rischi* zone in Hole 1049C is much more expanded than the standard length according to GTS2012, which has been observed in other deep sea drill cores (DSDP 511) [Huber and Leckie, 2011]. Albian sedimentation rate for ODP Hole 1049C was determined using the base of the Paquier black shale and the FO *H. albiensis* age estimate for the top of the Aptian-Albian unconformity. Because of limited available tie points with assignable absolute ages this sedimentation rate was used to calculate ages for samples below and above the Paquier black shale assuming the Paquier event has a length of 46 ka [Erbacher et al., 2001] (Tables 2-14 and 2-15).

Table 2-15. ODP Hole 1049C original and GTS2012 ages along with S isotope data from Paytan et al., (2004)

Sample	Depth (mbsf)	Original Age (Ma)	GTS2012 Age (Ma)	$\delta^{34}S_{barite}$ (‰)
12-1 42-44	139.73	111.50	109.56 ± 1.01	16.33
12-2 127-129	142.08	112.00	110.82 ± 0.45	16.29
12-3 100-102	143.31	112.70	111.29 ± 0.62	16.26

2.6.4 DSDP Legs 51-53 Holes 417D and 418B Bermuda Rise

DSDP Holes 417D and 418B are located in the western Atlantic Ocean near the southern extremity of the Bermuda Rise just north of the Vema Gap between the Abaco and Blake fracture zones (Fig. 2-1) [SSP Legs 51-53, 1980a,b]. Calcareous nannofossil and planktonic foraminifera data used to determine sedimentation rates and age assignments for Holes 417D and 418B are presented in Table 2-16. The sample analyzed by Paytan et al. (2004) from Hole 417D is located just a few meters above the first recovery of basement basalts in the core catcher of core 21 [SSP Legs 51-53, 1980a]. The sediments in Hole 417D core 21 are identified as Aptian given the presence of calcareous nannofossil *Assipetra infracretacea* throughout and the FO *Eprolithus floralis* in sample 21R-3 20-21 cm [Gartner, 1980]. The local last occurrence of planktonic foraminifera *Globigerinelloides maridalensis*, which occurs at the base of the Late Aptian *Paraticinella eubejaouaensis* zone (= *P. rohri* zone) in conjunction with the FO *E. floralis* are used to determine a sedimentation rate for the Aptian within Hole 417D (Table 2-16) [Miles and Orr, 1980; Verga and Premoli Silva, 2003; Anthonissen and Ogg, 2012; Ogg and

Table 2-16. GTS2012 age assignments of select key biostratrigraphic data for Mid Cretaceous from DSDP Holes 417D and 418B. Data from Miles and Orr (1980) and Gartner (1980). The age assignment location (listed below sample depth) is the midpoint between the sample containing FO or LO and the next sample analyzed where the organism is absent.

Sample	mbsf	Biostratigraphic data	Age assignment	Comments
417D 20-2 18-20 cm	326.69 (325.67 ± 1.02)	LO *Globigerinelloides maridalensis*	118.0 ± 0.45	LO occurs at base of Late Aptian *Paraticinella eubejaouaensis* zone (= P. rohri zone; Ando et al., 2013) Verga & Silva, 2003
417D 21-3 20-21 cm	337.705 (338.16 ± 0.455)	FO *Eprolithus floralis*	123.88 ± 0.45	Early Aptian post OAE 1a
418B 28-2 13-14	255.035 (255.375 ± 0.34)	FO *Eiffellithus turriseiffelii*	103.1 ± 0.4	Late Albian start of CC9 GTS2012
418B 33-1 39-40	301.395	FO *Watznaueria biporta*		FO Early Albian/AAB Nannotax3
418B 33-1 104-105	302.045	LO *Assipetra infracretacea*		LO Late Aptian/AAB Tremolada & Erba, 2002 + Nannotax3

Table 2-17. DSDP Holes 417D and 418B original and GTS2012 ages along with S isotope data from Paytan et al., (2004)

Sample	Depth (mbsf)	Original Age (Ma)	GTS2012 Age (Ma)	$\delta^{34}S_{barite}$ (‰)
417D 21-2 110-113	337.115	119.80	123.39 ± 0.79	16.40
418B 30-2 112-115	275.035	113.10	107.30 ± 0.50	15.35

Hinnov, 2012; Ando et al., 2013]. This sedimentation rate is used to calculate the age for sample 417D 21R-2 110-113 cm (Table 2-17).

In Hole 418B calcareous nannofossil A. *infracretacea* also identifies Aptian sediments within cores 34 and 33 [Gartner, 1980]. The LO *A. infracretacea* in sample 33R-1 104-105 cm followed by the first occurrence of Early Albian *Watznaueria biporta* in sample 33R-1 39-40 cm allows for the estimation of the Aptian-Albian boundary (AAB 113 ± 0.4 Ma) to be located at 301.72 ± 0.3 mbsf [Gartner, 1980; Tremolada and Erba, 2002; Ogg and Hinnov, 2012; Young et al., 2014]. This AAB and the Late Albian FO *Eiffellithus turriseiffelii* in core 28 are used to determine a sedimentation rate for the Albian within Hole 418B (Table 2-16) [Gartner, 1980; Anthonissen and Ogg, 2012; Ogg and Hinnov, 2012]. This sedimentation rate is used to calculate the age for sample 418B 30R-2 112-115 cm (Table 2-17).

2.6.5 DSDP Leg 80 Hole 551 Goban Spur

DSDP Hole 551 is located along the continental margin of Europe in the northeast Atlantic Ocean southwest of Ireland on the seaward edge of the Goban Spur (Fig. 2-1) [SSP Leg 80, 1985]. Approximately 86 cm of black shale recovered from Hole 551 starting at 5R-2 55 cm (134.55 mbsf) was bracketed by the local FO of calcareous nannofossil *Eiffellithus eximus* (5R-2 30 cm, 134.30 mbsf) and the local LO of calcareous nannofossils *Corollithion kennedyi* and *Axopodorhabdus albianus* (6R-1 27 cm, 138.77 mbsf) [SSP Leg 80, 1985; Bralower, 1988]. These key Late Cretaceous biostratigraphic markers and limited carbon isotopic analysis within

the organic-rich black shale have led to its correlation with the Cenomanian-Turonian OAE2 [de Graciansky and Poag, 1985; Cunningham and Kroopnick, 1985; Bralower, 1988; Anthonissen and Ogg, 2012; Ogg and Hinnov, 2012]. The full extent of the black shale in DSDP Hole 551 is estimated to fill the unrecovered portions of core 5 [SSP Leg 80, 1985; Bralower, 1988]. The limited biostratigraphic analysis within the black shale does not provide diagnostic data to determine sedimentation rates during its deposition nor calculate age assignments [Bralower, 1988]. In order to assign ages to two samples from Paytan et al. (2004) sampled within this black shale it is assumed that the full length of the black shale in core 5 of DSDP Hole 551 corresponds to the full length of the positive carbon isotope excursion from OAE2. Cyclostratigraphic analysis of OAE2 stratigraphic sections with corresponding carbon isotope data has produced an orbital time scale indicating that the event lasted ~600 ka [Sageman et al., 2006]. Combining this ~600 ka duration with the new Cenomanina-Turonin age of 93.90 ± 0.15 from Meyers et al. (2012) the timing of OAE2 should span from 94.40 ± 0.15 Ma to 93.80 ± 0.15 Ma. The two samples from Paytan et al. (2004) therefore must occur within this time span and their age assignments should not overlap, as they are clearly stratigraphically separate samples (Table 2-18).

Sedimentation rates within the Early Turonian nannofossil chalks from Hole 551 have been estimated at 2.7 m/my [SSP Leg 80, 1985]. This sedimentation rate is approximately an order of magnitude greater than a constant sedimentation calculated from the top of OAE2 at 5R-2 55 cm (134.55 mbsf) with an age of 93.80 ± 0.15 Ma and the local FO of calcareous nannofossil *Eiffellithus eximus* (5R-2 30 cm, 134.30 mbsf) with a GTS2012 assigned age of 92.99 ± 0.25 Ma [Meyers et al., 2012; Anthonissen and Ogg, 2012]. However, it has been shown that *E. eximus* may be diachronous [Burnett et al., 1998; Anthonissen and Ogg, 2012]. Therefore,

both the end of OAE2 and the local FO *E. eximus* are used with the 2.7 m/my estimated sedimentation rate to calculate an age assignment for Paytan et al. (2004) sample 5R-1 145-148 cm (133.975 mbsf) (Table 2-18).

Table 2-18. DSDP Hole 551 original and GTS2012 ages along with S isotope data from Paytan et al., (2004)

Sample	Depth (mbsf)	Original Age (Ma)	GTS2012 Age (Ma)	$\delta^{34}S_{barite}$ (‰)
5R-1 145-148	133.975	93.40	93.23 ± 0.24	19.10
5R-2 91-94	134.925	93.60	93.90 ± 0.1	18.84
5CC 1-4	135.225	93.80	94.20 ± 0.2	19.02

2.6.6 ODP Leg 123 Hole 765C Argo Abyssal Plain

ODP Hole 765C is a deep water drill hole located off the northwest coast of Australia in the Indian Ocean on the southern Argo Abyssal Plain just north of the Exmouth Plateau and west of the Scott Plateau [Mutterlose, 1992]. Calcareous nannofossil data used to determine the age assignment for the single sample from Hole 765C analyzed by Paytan et al. (2004) are presented in Table 2-19. The concurrent local FOs of *Eprolithos floralis* and *Rhagodiscus angustus* in sample 40R-4 30 cm (725.7 mbsf) clearly indicate an Aptian age near the Early-Late Aptian boundary [Mutterlose, 1992; Anthonissen and Ogg, 2012; Ogg and Hinnov, 2012]. The next useable biostratigraphic datum is the local FO *Prediscosphaera columnata* in sample 35R-1 105 cm [Mutterlose, 1992]. While the global first occurrence of *P. columnata* may mark the Albian-Aptian boundary in GTS2012, biostratigraphic data and updated age model analysis of nearby ODP Hole 766A indicate that this event in the paleo-Indian Ocean occurred much later in the Albian [Mutterlose, 1992; this study]. In both 765C and 766A, Mutterlose (1992) used the local FO *P. columnata* to mark the boundary between sections identified as Late-Early Albian and Early Albian-Late Aptian. Assuming the local FO *P. columnata* in Hole 766A and 765C are

Table 2-19. GTS2012 age assignments of select key biostratrigraphic data for Early Cretaceous from ODP Hole 765C. Data from Mutterlose (1992). The age assignment location (listed below sample depth) is the midpoint between the sample containing FO or LO and the next sample analyzed where the organism is absent.

Sample	mbsf	Biostratigraphic data	Age assignment	Comments
35R-1 105 cm	675.15 (675.61 ± 0.46)	FO *Prediscosphaera columnata*	108.47 ± 0.49	Albian; Mutterlose (1992) marker for Late-Early Albian
40R-4 30 cm	725.7 (726.19 ± 0.49)	FO *Eprolithus floralis* FO *Rhagodiscus angustus*	123.85 ± 0.45	Early-Late Aptian

contemporaneous the age model determined for Hole 766A would result in assigning an age of 108.47 ± 0.49 Ma to this event in Hole 765C. Distinct differences in the abundance level of *P. columnata* between the two cores and comparison of the sample spacing for biostratigraphic data along with core recovery surrounding the respective samples leads to questioning if the local FOs are exactly contemporaneous [SSP Leg 123, 1990a,b; Mutterlose, 1992]. These differences are thought to suggest that the FO in Hole 765C might be slightly older than that in Hole 766A. Assuming there is an age difference between the FO *P. columnata* in Hole 765C and Hole 766A, it would need to be at least ~1.25 Ma older in order to produce a significant (>0.5 Ma) difference in the age estimate for the sample of interest. Without correlation between Holes 766A and 765C, however, the age assignment for the FO *P. columnata* in Hole 765C based on GTS2012 would be at least 4 Ma older than that determined by the age model for Hole 766A. While diachroneity of key biostratigraphic events can occur across a single large basin/region it seems more reasonable to assume that the local FO *P. columnata* in Holes 766A and 765C are approximately contemporaneous instead of separated by more than 4 Ma. Using the age assignment for FO *P. columnata* determined by the model for Hole 766A and the FO *E. floralis* results in an age estimate of 117.64 ± 0.61 Ma for Hole 765C sample 38R-3 24-28 cm (Tables 2-19 and 2-20).

Table 2-20. ODP Hole 765C original and GTS2012 ages along with S isotope data from Paytan et al., (2004)

Sample	Depth (mbsf)	Original Age (Ma)	GTS2012 Age (Ma)	$\delta^{34}S_{barite}$ (‰)
38R-3 24-28 cm	705.76	115.97	117.64 ± 0.61	15.50

2.6.7 Updated GTS2012 ages

In comparing the GTS2012 revised age models for the Cretaceous seawater S isotope curve with the original ages assigned in Paytan et al. (2004), most of the major changes arise from the shifting of the Barremian-Aptian boundary older and the revised assignment of the Aptian-Albian boundary within the cores sampled (Fig. 2-5). In general, the major shifts and trends remain the same with the ~5‰ decrease starting near the Hauterivian- Barremian boundary, ending in the Early Aptian and the relatively low S isotope values persisting thru the Late Albian. The steep rise in $\delta^{34}S_{barite}$ values during the Late Albian-Early Cenomanian appears to be slightly steeper in the updated curve while the minor fluctuations through the Late Cretaceous hold to the same pattern.

2.7 SUMMARY

The growing evidence for glacial conditions and cooling trends during the Early Cretaceous indicates a much more dynamic climate state than the typical ice-free greenhouse that is often assumed for the entire Cretaceous. While the OAEs and positive CIEs of the Cretaceous were presumed to be expressions of the warm greenhouse conditions it appears that some may occur during glacial or cooling episodes. The cluster of Early- to Mid-Cretaceous LIPs in conjunction with the acceleration in the breakup of Pangea opening new ocean basins and gateways appears to have played a significant role in the transition from the cool greenhouse (icehouse) to warm greenhouse climate state that characterizes the Late Cretaceous. Revision of the high latitude, paleo-Indian Ocean ODP Hole 766A age model using GTS2012 first and lost

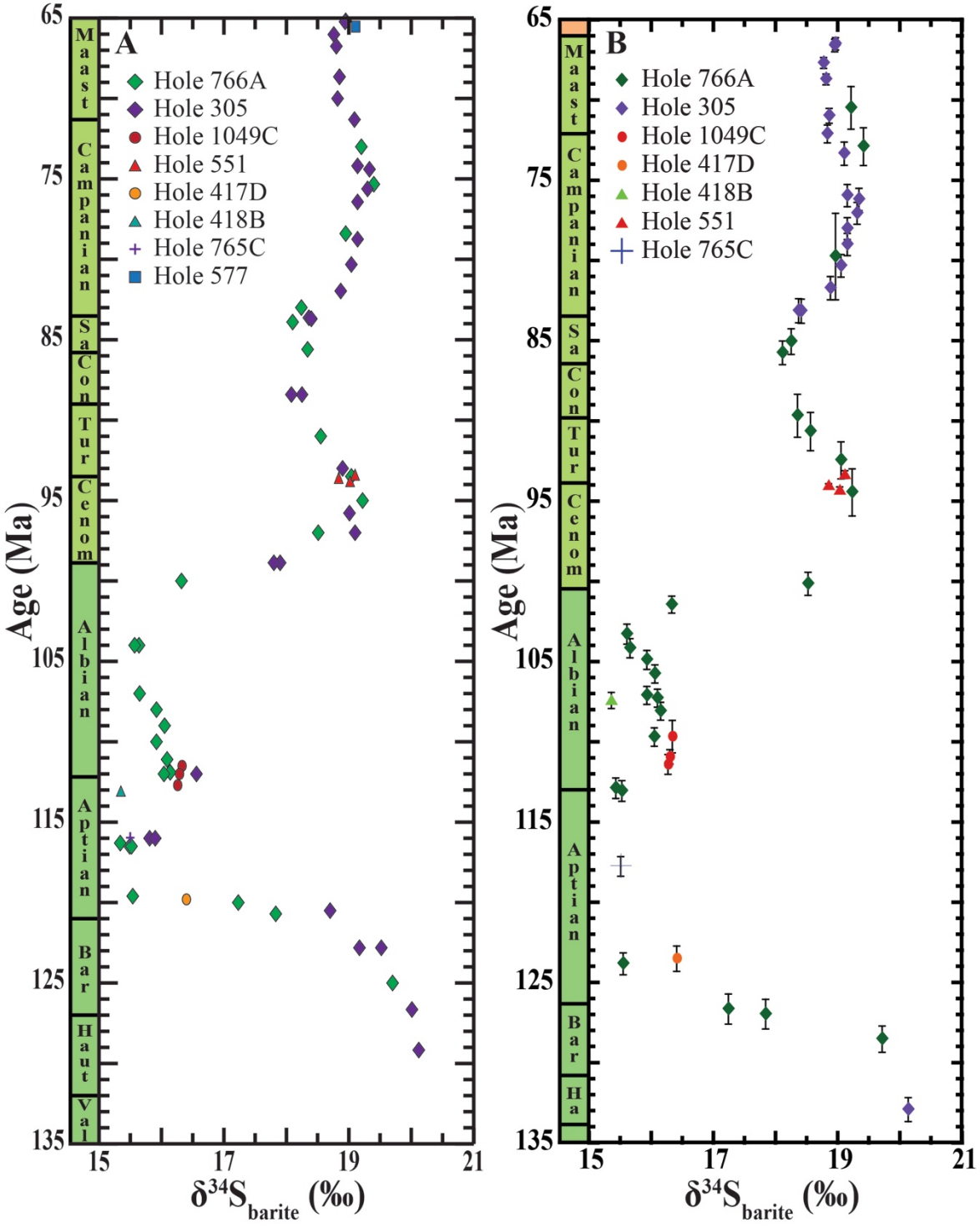

Figure 2-5 Cretaceous seawater S isotope curve age update

Cretaceous seawater S isotope curve with (**A**) original ages from Paytan et al. (2004) and Cretaceous stages from Gradstein et al., (1995) and (**B**) revised ages updated to be in line with GTS2012.

occurrence datum for calcareous nannofossils and planktonic foraminifera that are dominated by Tethyan species once again raises the issue of assumed isochroneity for these biological events [e.g., Caron et al., 2006]. During the Early Cretaceous with mounting evidence for a dynamic climate and cold, high latitude environments it is increasingly likely for there to have been ecological boundaries limiting and delaying the spread of tropical, warm water Tethyan organisms globally hindering correlation across distinct, separate ocean basins and climatic regimes [e.g. Caron et al., 2006].

CHAPTER 3

MODELING THE PHANEROZOIC SEAWATER RADIOGENIC STRONTIUM ISOTOPE RECORD: A CASE STUDY OF THE LATE JURASSIC-EARLY CRETACEOUS

3.1. Introduction

The radiogenic strontium isotope composition ($^{87}Sr/^{86}Sr$) of seawater represents a balance between Sr inputs from continental weathering (riverine ± submarine groundwater discharge) having relatively high $^{87}Sr/^{86}Sr$ ratios and the input of Sr derived from the hydrothermal alteration of oceanic crust having relatively low $^{87}Sr/^{86}Sr$ ratios [Brass, 1976; Kump, 1989; Palmer and Edmond, 1989; Berner and Rye, 1992; Francois and Walker, 1992; Richter and Turekian, 1993; Davis et al., 2003; Vance et al., 2009; Allegre et al., 2010; Krabbenhoft et al., 2010; Peucker-Ehrenbrink et al., 2010; Beck et al., 2013]. The long term evolution of seawater $^{87}Sr/^{86}Sr$ ratios recorded in marine carbonate rocks has been used to reconstruct changes in the balance between weathering and hydrothermal inputs to the ocean [Brass, 1976; Hodell et al., 1989, 1990; Kump, 1989; Berner and Rye, 1992; Francois and Walker, 1992; Richter and Turekian, 1993; Jones and Jenkyns, 2001; Coogan and Dasso, 2015]. Because the two input fluxes also affect several other elemental cycles (e.g., carbon, sulfur, and iron), quantifying secular changes in the Sr isotope composition of seawater also yields information critical for understanding the long-term evolution of climate and other Earth surface processes [e.g., Berner and Rye, 1992; Francois and Walker, 1992; Jones and Jenkyns, 2001; Wallmann, 2001, 2004].

Several time-dependent variables control the mass of seawater Sr and its isotope composition. Waltham and Grocke (2006) note that solving the equations (see Methods section

below) for the marine Sr cycle is "under-constrained rather than unconstrained." When modeling the Sr isotope composition of seawater, it is critical to identify how the controlling variables might have changed through time. Most model reconstructions of the Phanerozoic Sr isotope record use modern values for the Sr isotope ratio of the riverine, hydrothermal, and diagenetic fluxes, as well as the total mass of Sr in seawater [Jones and Jenkyns, 2001; Wallmann, 2001; Hansen and Wallmann, 2003; Young et al., 2009; Pogge van Strandmann et al., 2013]. While measurements of the modern system offer important constraints for interpreting the marine Sr isotope record, allowing the controlling variables to temporally vary should yield more accurate reconstructions.

This chapter presents an iterative method for estimating the Sr isotope composition of input fluxes in the geologic past using the composite seawater $^{87}Sr/^{86}Sr$ record of McArthur et al. (2012). New model equations that track each Sr isotope individually are employed in this method to avoid the common incorrect assumption that a minor isotope, namely ^{86}Sr, represents the entire mass of Sr in seawater or a given flux. To begin with, we review estimates for the fluxes and their isotope ratios that control the modern marine Sr cycle and describe how these variables can be better constrained when interpreting ancient conditions. Second, we focus on the Late Jurassic to Early Cretaceous (160.5-105.5 Ma) as a case study because the Sr isotope record exhibits a near constant, linear rise for 30 Ma (which provides a period of stable, consistent pre-conditions for a system that rarely achieves isotopic steady state) prior to experiencing a large downward perturbation, presumably due to the emplacement of multiple large igneous provinces (LIPs), increased continental arc volcanism, and elevated mid-ocean ridge (MOR) spreading rates (Fig. 3-1) [Larson, 1991; Jones and Jenkyns, 2001; Rowley, 2002; Hansen and Wallmann,

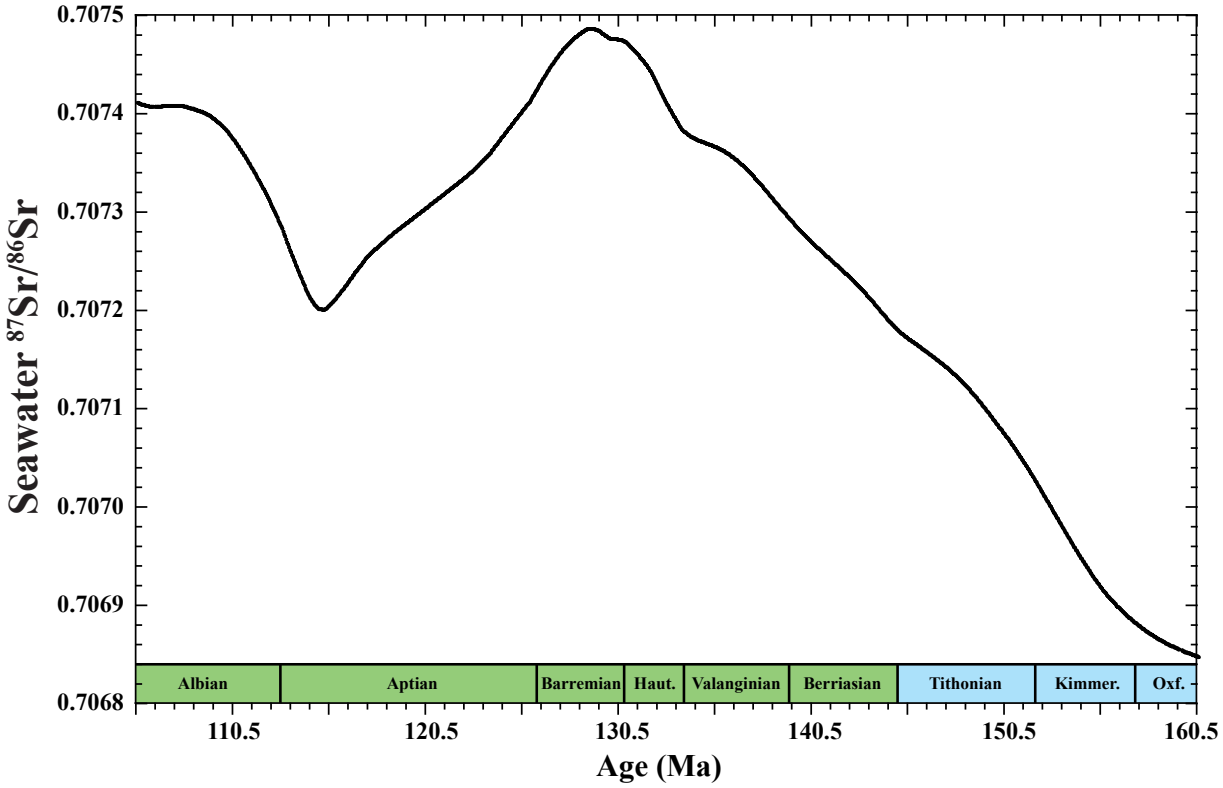

Figure 3-1 Late Jurassic-Early Cretaceous seawater $^{87}Sr/^{86}Sr$ curve

The Late Jurassic-Early Cretaceous seawater $^{87}Sr/^{86}Sr$ curve from McArthur et al. (2012) with GTS2012 stage boundaries.

2003; Bryan and Ernst, 2008; Seton et al., 2009, 2012; McArthur et al., 2012; Bryan and Ferrari, 2013; McKenzie et al., 2016; Wang et al., 2016].

3.2. Methods

Here, fully explicit equations are derived for modeling the Sr isotope composition of seawater, taking into consideration mass-dependent fractionation. Strontium has four stable isotopes: ^{84}Sr, ^{86}Sr, ^{87}Sr, and ^{88}Sr. In addition to mass-dependent fractionation effects, the

abundance of ^{87}Sr can vary due to radioactive decay of ^{87}Rb ($T_{1/2}$ = 4.9 x 10^{10} yr). Separate equations for each isotope are developed to avoid the assumption that one isotope represents the entire mass of Sr composing seawater or a given flux. This is particular relevant when tracking two minor isotopes, such as ^{87}Sr and ^{86}Sr, where the abundance ratios are much closer to one than <0.05. For some isotopic systems, such as C, O, and S, where the dominant isotope represents >95% of the total abundance and/or fractionations are not excessively large, this assumption makes little difference.

The isotope fractionation factor (α) for two substances X and Y (e.g., carbonate sediment and seawater) is given by the equation:

$$\alpha_{2/1}^{X-Y} = \frac{R_{2/1}^{X}}{R_{2/1}^{Y}}, \tag{3-1}$$

where 1 is the reference isotope, 2 refers to another isotope of the same element, and R is the isotope abundance ratio. In the case of the present study, ^{86}Sr is always the reference isotope, so for convenience, isotope abundance ratios are discussed as R_A, where A refers to either ^{84}Sr, ^{87}Sr, or ^{88}Sr. Fractionation factors for different abundance ratios (e.g., R_{88} and R_{87}) are related by the equation (Young et al., 2002):

$$\alpha_{2/1}^{X-Y} = \left(\alpha_{3/1}^{X-Y}\right)^{\beta}, \tag{3-2}$$

where the exponent, β, varies depending whether the mass-fractionation process follows an equilibrium or kinetic law. From Young et al. (2002), the equilibrium and kinetic laws follow the respective equations

$$\beta = \frac{\frac{1}{m_1} - \frac{1}{m_2}}{\frac{1}{m_1} - \frac{1}{m_3}} \tag{3-3}$$

$$\beta = \frac{\ln \frac{m_1}{m_2}}{\ln \frac{m_1}{m_3}}, \quad (3\text{-}4)$$

where *m* refers to exact atomic masses (e.g., ^{84}Sr = 83.913425 amu, ^{86}Sr = 85.909260, ^{87}Sr = 86.908877, ^{88}Sr = 87.905612).

To correct for instrumental mass-fractionation during analysis of radiogenic Sr isotope ratios (R_{87}), data are internally normalized to R_{88} of 8.375209. Correcting for instrumental mass-fractionation also eliminates any mass-fractionation that might occur in nature. Stable Sr isotope studies focus on fractionation of R_{88} ratios. Here, either standard-sample bracketing or double-spike isotope dilution techniques must be employed [Krabbenhoft et al., 2009, 2010; Moynier et al., 2010; Vollstaedt et al., 2014; Andrews et al., 2016]. It is also important to note that determination of fractionated R_{88} ratios requires knowledge of radiogenic R_{87} ratios [Krabbenhoft et al., 2009, 2010; Vollstaedt et al., 2014; Andrews et al., 2016]. Fractionated R_{88} ratios are reported in delta notation (per mil scale) according to the equation:

$$\delta^{88/86}\mathrm{Sr}_{smp} = \left[\frac{R^*_{88,smp}}{R_{88,std}} - 1 \right] \times 1000, \quad (3\text{-}5)$$

where *smp* refers to sample (or in the case of this study, a given flux or seawater), *std* refers to a designated standard reference material (typically NBS 987), and the * symbol designates that the abundance ratio is fractionated and is introduced to facilitate subsequent discussion. Delta notation has the advantage of making the small degree of isotopic variation easier to visualize. It also provides a convenient mechanism to account for instrumental drift, which is a factor for stable Sr isotope measurements [Andrews et al., 2016]. Once $\delta^{88/86}$Sr values are measured, delta values for the two remaining isotope ratios can be calculated using β:

$$\delta^{87/86}\mathrm{Sr} = \delta^{88/86} \times \beta^{87/86} \quad (3\text{-}6)$$

$$\delta^{84/86}\mathrm{Sr} = \delta^{88/86} \times \beta^{84/86} \quad (3\text{-}7)$$

Most stable Sr isotope studies assume that fractionation follows a kinetic law. Therefore, according to Equation 3-4, $\beta^{87/86} = 0.50359$ and $\beta^{84/86} = 1.0232$. While $\delta^{88}Sr$ and $\delta^{84}Sr$ values represent fractionations relative to the normalized/fixed cosmic abundance ratios for R_{88} and R_{84} (i.e. $R_{88,norm} = 8.375209$ and $R_{84,norm} = 0.05658$, respectively), $\delta^{87}Sr$ values, however, represent fractionation relative to the radiogenic R_{87} ratio of the sample itself instead of a fixed standard value.

Because the box model presented below tracks each Sr isotope individually, the delta values must be "inverted" to arrive at the fractionated abundance ratios for the sample:

$$R^*_{A,smp} = \left[\frac{\delta^{A/86}\mathrm{Sr}_{smp}}{1000} + 1 \right] \times R_{A,norm}, \quad (3\text{-}8)$$

where $R_{A,norm}$ follows from above. Table 3-1 provides the $\delta^{88/86}Sr$ value and R^*_A ratios for the IAPSO seawater standard, as measured by Andrews et al. (2016). These results agree well with previously published values for IAPSO [Krabbenhoft et al., 2009].

Table 3-1. $\delta^{88/86}Sr$ and R^*_A values for the modern seawater standard IAPSO as measured by Andrews et al. (2016).

	$\delta^{88/86}$Sr ($2\sigma_{SD}$) (‰)	R^*_{88} ($2\sigma_{SD}$)	R^*_{87} ($2\sigma_{SD}$)	R^*_{84} ($2\sigma_{SD}$)
IAPSO (n=54)	0.396 ± 0.02	8.378526 ± 0.000168	0.709321 ± 0.000017	0.0566069 ± 0.0000012

The time-dependent mass-balance for a given Sr isotope in seawater (sw) is given by the equation:

$$\frac{d^{A}N_{sw}}{dt} = \sum_{i} {}^{A}F_{i} - \sum_{j} {}^{A}F_{j}, \tag{3-9}$$

where N is the total number of moles of a given isotope in the oceans, F_i refers to input fluxes (mol/yr), F_j refers to output fluxes (mol/yr), and in this section A refers to either ^{84}Sr, ^{86}Sr, ^{87}Sr, or ^{88}Sr. For the case study presented below that focuses on the Late Jurassic-Early Cretaceous we assume an ice-free ocean volume of 1.35875 x 10^{21} L [Trenberth et al., 2007; Charette and Smith, 2010]. To determine the flux (or mass) of an individual isotope from a total flux (or total mass) requires a conversion factor that accounts for all stable isotopes of a given element or at least those that together compose >99% of the total abundance of the element. The values for the conversion factors are distinct for each flux or reservoir and will vary through time as R_A^* ratios change. Examples of the conversion factors are given for the input fluxes:

^{84}Sr: $$\frac{R^*_{84,i}}{1 + R^*_{87,i} + R^*_{88,i} + R^*_{84,i}} \tag{3-10}$$

^{86}Sr: $$\frac{1}{1 + R^*_{87,i} + R^*_{88,i} + R^*_{84,i}} \tag{3-11}$$

^{87}Sr: $$\frac{R^*_{87,i}}{1 + R^*_{87,i} + R^*_{88,i} + R^*_{84,i}} \tag{3-12}$$

^{88}Sr: $$\frac{R^*_{88,i}}{1 + R^*_{87,i} + R^*_{88,i} + R^*_{84,i}} \tag{3-13}$$

According to Equation 3-1, R_A^* ratios for output fluxes can be determined as $R^*_{A,j} = \alpha_A^{j-sw} \times R^*_{A,sw}$. Using total mass fluxes, the above conversion factors for the input fluxes, and the conversion factors modified to account for fractionation by the output fluxes, Equation 3-9 is expanded for each of the four Sr isotopes:

$$\frac{d}{dt}{}^{84}N_{sw} = \sum_i \frac{R^*_{84,i}}{1+R^*_{87,i}+R^*_{88,i}+R^*_{84,i}} \times F_i - \sum_j \frac{\alpha_{84}^{j-sw} R^*_{84,sw}}{1+\alpha_{87}^{j-sw} R^*_{87,sw}+\alpha_{88}^{j-sw} R^*_{88,sw}+\alpha_{84}^{j-sw} R^*_{84,sw}} \times F_j \quad (3\text{-}14)$$

$$\frac{d}{dt}{}^{86}N_{sw} = \sum_i \frac{1}{1+R^*_{87,i}+R^*_{88,i}+R^*_{84,i}} \times F_i - \sum_j \frac{1}{1+\alpha_{87}^{j-sw} R^*_{87,sw}+\alpha_{88}^{j-sw} R^*_{88,sw}+\alpha_{84}^{j-sw} R^*_{84,sw}} \times F_j \quad (3\text{-}15)$$

$$\frac{d}{dt}{}^{87}N_{sw} = \sum_i \frac{R^*_{87,i}}{1+R^*_{87,i}+R^*_{88,i}+R^*_{84,i}} \times F_i - \sum_j \frac{\alpha_{87}^{j-sw} R^*_{87,sw}}{1+\alpha_{87}^{j-sw} R^*_{87,sw}+\alpha_{88}^{j-sw} R^*_{88,sw}+\alpha_{84}^{j-sw} R^*_{84,sw}} \times F_j \quad (3\text{-}16)$$

$$\frac{d}{dt}{}^{88}N_{sw} = \sum_i \frac{R^*_{88,i}}{1+R^*_{87,i}+R^*_{88,i}+R^*_{84,i}} \times F_i - \sum_j \frac{\alpha_{88}^{j-sw} R^*_{88,sw}}{1+\alpha_{87}^{j-sw} R^*_{87,sw}+\alpha_{88}^{j-sw} R^*_{88,sw}+\alpha_{84}^{j-sw} R^*_{84,sw}} \times F_j \quad (3\text{-}17)$$

If ${}^{87}N_{sw}$ in Equation 3-16 is replaced with ${}^{87}N_{sw} = R^*_{87,sw} \times {}^{86}N_{sw}$ and the product rule is applied the following equation is obtained:

$$R^*_{87,sw} \times \frac{d}{dt}{}^{86}N_{sw} + {}^{86}N_{sw} \times \frac{dR^*_{87,sw}}{dt} = \sum_i \frac{R^*_{87,i}}{1+R^*_{87,i}+R^*_{88,i}+R^*_{84,i}} \times F_i - \sum_j \frac{\alpha_{87}^{j-sw} R^*_{87,sw}}{1+\alpha_{87}^{j-sw} R^*_{87,sw}+\alpha_{88}^{j-sw} R^*_{88,sw}+\alpha_{84}^{j-sw} R^*_{84,sw}} \times F_j \quad (3\text{-}18)$$

Substituting Equation 3-15 into Equation 3-18 and combining terms yields:

$$
\begin{aligned}
{}^{86}N_{sw} \times \frac{dR^*_{87,sw}}{dt} = & \sum_i \frac{R^*_{87,i} - R^*_{87,sw}}{1 + R^*_{87,i} + R^*_{88,i} + R^*_{84,i}} \times F_i \\
& - \sum_j \frac{R^*_{87,sw} \times \left(\alpha_{87}^{j-sw} - 1\right)}{1 + \alpha_{87}^{j-sw} R^*_{87,sw} + \alpha_{88}^{j-sw} R^*_{88,sw} + \alpha_{84}^{j-sw} R^*_{84,sw}} \times F_j
\end{aligned}
\tag{3-19}
$$

Similarly, if ${}^{88}N_{sw}$ in Equation 3-17 is replaced with ${}^{88}N_{sw} = R^*_{88,sw} \times {}^{86}N_{sw}$ and the product rule is applied results in Equation 3-20.

$$
\begin{aligned}
{}^{86}N_{sw} \times \frac{dR^*_{88,sw}}{dt} = & \sum_i \frac{R^*_{88,i} - R^*_{88,sw}}{1 + R^*_{87,i} + R^*_{88,i} + R^*_{84,i}} \times F_i \\
& - \sum_j \frac{R^*_{88,sw} \times \left(\alpha_{88}^{j-sw} - 1\right)}{1 + \alpha_{87}^{j-sw} R^*_{87,sw} + \alpha_{88}^{j-sw} R^*_{88,sw} + \alpha_{84}^{j-sw} R^*_{84,sw}} \times F_j
\end{aligned}
\tag{3-20}
$$

Equation 3-20 replaces the mass-balance equation using $\delta^{88/86}Sr$ notation commonly used to model the stable Sr isotope composition of seawater, as it correctly and explicitly accounts for the abundance of all Sr isotopes in seawater.

For modeling the traditional radiogenic Sr isotope composition of seawater, where mass-dependent fractionation is not a factor, R^*_A ratios are unnecessary, R_{87} is the only isotope ratio that varies, and all α values equal 1. Because R_{88} and R_{84} are fixed at 8.375209 and 0.056584, respectively, they can be combined into a constant:

$$Z = 1 + R_{84} + R_{88}, \tag{3-21}$$

where Z equals 9.431793. This leaves R_{87} as the only variable in the conversion factors:

$$^{84}\text{Sr:} \quad \frac{R_{84}}{R_{87,k}+Z} \tag{3-22}$$

$$^{86}\text{Sr:} \quad \frac{1}{R_{87,k}+Z} \tag{3-23}$$

$$^{87}\text{Sr:} \quad \frac{R_{87,k}}{R_{87,k}+Z} \tag{3-24}$$

$$^{88}\text{Sr:} \quad \frac{R_{88}}{R_{87,k}+Z}, \tag{3-25}$$

where *k* represents any input flux, output flux, or reservoir. Equations 3-14 to 3-17 and 3-19 therefore simplify to Equations 3-26 to 3-30, which are the ones used in the model described below. In these equations $R_{87,i}$ is the traditional radiogenic Sr isotope ratio of the hydrothermal (ht), riverine (r), submarine groundwater discharge (sgd), and diagenetic (d) fluxes (F_i), $R_{87,sw}$ is the traditional radiogenic Sr isotope ratio of seawater, F_{tb} is the total burial flux, and $^{T}N_{sw}$ is the total moles of Sr in seawater, which simply goes as the sum of all $^{A}N_{sw}$.

$$\frac{d}{dt}{}^{84}N_{sw} = \sum_i \frac{R_{84}}{R_{87,i}+Z} * F_i - F_{tb} * \frac{R_{84}}{R_{87,sw}+Z} \tag{3-26}$$

$$\frac{d}{dt}{}^{86}N_{sw} = \sum_i \frac{1}{R_{87,i}+Z} * F_i - F_{tb} * \frac{1}{R_{87,sw}+Z} \tag{3-27}$$

$$\frac{d}{dt}{}^{87}N_{sw} = \sum_i \frac{R_{87,i}}{R_{87,i}+Z} * F_i - F_{tb} * \frac{R_{87,sw}}{R_{87,sw}+Z} \tag{3-28}$$

$$\frac{d}{dt}{}^{88}N_{sw} = \sum_i \frac{R_{88}}{R_{87,i}+Z} * F_i - F_{tb} * \frac{R_{88}}{R_{87,sw}+Z} \tag{3-29}$$

$${}^{T}N_{sw}\frac{d}{dt}R_{87,sw} = \sum_i \frac{Z+R_{87,sw}}{Z+R_{87,i}}\left(R_{87,i}-R_{87,sw}\right)F_i \tag{3-30}$$

Equation 3-30 replaces the mass-balance equation more commonly used to model the radiogenic isotope composition of seawater, as it correctly and explicitly accounts for the abundance of all Sr isotopes in seawater. During discrete intervals of geologic time (e.g., the Neogene, Hodell, 1989) where the range of $^{87}Sr/^{86}Sr$ ratios is relatively small the impact of tracking each isotope

separately is quite small. However, when modeling longer intervals of time, such as the entire Phanerozoic ± Neoproterozoic (e.g., Kump, 1989), the range of $^{87}Sr/^{86}Sr$ ratios becomes large enough where notable differences can arise in the model results when isotopes are and are not tracked separately.

3.3. Modern Sr cycle fluxes and isotope ratios

3.3.1 Hydrothermal

The passage of seawater through basaltic oceanic crust at MORs yields extensive Sr isotope exchange between water and rock [Palmer and Edmond, 1989; Davis et al., 2003; Coogan, 2009]. Therefore, the $^{87}Sr/^{86}Sr$ ratio of hydrothermal fluids represents a mixture of Sr leached from basalt ($^{87}Sr/^{86}Sr$ ~0.7025) and seawater. The strong linear relationship between Sr and Cl concentrations in end-member hydrothermal solutions indicates that Sr behaves conservatively during hydrothermal circulation [Edmonds and Edmond, 1995; Davis et al., 2003]. This implies that despite significant isotope exchange during water-rock interactions, the Sr concentration of hydrothermal fluids should approximate seawater values.

Utilizing a simple three-component mixing model and assuming the modern ocean to be in steady-state with respect to Sr concentration and isotope composition, Palmer and Edmond (1989) estimated the modern hydrothermal Sr flux via difference. In their calculation, Palmer and Edmond (1989) used their estimates for the flux and isotope ratio of the riverine input (see below), the published diagenetic flux and Sr isotope ratio of Elderfield and Gieskes (1982), and an average hydrothermal end-member fluid Sr isotope ratio of 0.7035. These values produced a modern, steady-state, high-temperature hydrothermal Sr flux of 15×10^9 mol/yr, which is ~5-10 times greater than other estimates [Palmer and Edmond, 1989; Butterfield et al., 2001; Davis et

al., 2003]. The large discrepancy originates from the low riverine flux, which Palmer and Edmond (1989) noted was likely an underestimation, as well as their assumption that the Sr isotope composition of the modern ocean is in steady-state [Vance et al., 2009; Krabbenhoft et al., 2010].

More recently, Davis et al. (2003) attempted to better constrain the hydrothermal Sr input utilizing Sr isotope alteration profiles of oceanic crust and ophiolites. With a direct focus on isotope exchange between seawater and basalt, they recalculated a pure basaltic hydrothermal flux having an $^{87}Sr/^{86}Sr$ ratio of 0.7025 instead of a total hydrothermal flux, which is a mixture of seawater and basaltic components [i.e., Palmer and Edmond (1989) $^{87}Sr/^{86}Sr$ ratio of 0.7035]. Davis et al. (2003) estimated a cumulative hydrothermal basaltic flux of $3.1 \pm 0.8 \times 10^9$ mol/yr, which includes both high- and low-temperature hydrothermal fluxes and also accounts for the arc-related high-temperature hydrothermal fluxes [Davis et al., 2003].

3.3.2 Diagenetic

Relative to the hydrothermal and riverine inputs, the diagenetic flux of Sr into the oceans has received less attention because it is thought to represent a minor component of the Sr cycle [Elderfiedl and Gieskes, 1982; Palmer and Edmond, 1989; Richter and Liang, 1993]. Analyses of interstitial waters from 37 Deep Sea Drilling Program (DSDP) sites demonstrate that the concentration and isotope composition of Sr released during carbonate recrystallization controls the concentration and isotope composition of Sr in these waters [Elderfield and Gieskes, 1982]. While some research has suggested that Sr leached from mafic volcanic material dispersed within the sediments might contribute to the diagenetic flux [Elderfield and Gieskes, 1982; Jones et al., 2012a], model calculations assessing the rate of Sr exchange between carbonates and sedimentary porewaters indicates the contribution is minor [Richter and Liang, 1993]. Using a

compilation of interstitial waters from DSDP cores, Elderfield and Gieskes (1982) estimated the global Sr diagenetic flux and $^{87}Sr/^{86}Sr$ ratio to be 3.4 x 10^9 mol/yr and 0.7084, respectively. Model calculations for Sr exchange during diagenesis indicates ~15% loss of Sr from seafloor carbonates globally [Richter and Liang, 1993]. Assuming Sr burial and riverine fluxes are approximately equal, Richter and Liang (1993) estimated a diagenetic Sr flux of ~5 x 10^9 mol/yr with a Sr isotope composition similar to contemporary seawater (max difference 0.0007). Given that the isotopic composition of the diagenetic flux of Sr to the ocean is controlled by recrystallization of previously deposited marine carbonates, it should be noted that the value from Elderfield and Gieskes (1982) matches the seawater $^{87}Sr/^{86}Sr$ record at ~20 Ma [McArthur et al., 2012].

3.3.3 Riverine

Challenges exist to constrain the concentration and $^{87}Sr/^{86}Sr$ ratio of the modern global dissolved riverine input due to the complexity of lithology, bedrock age, climate, and weathering history within individual drainage basins [Palmer and Edmond, 1989; Vance et al., 2009; Allegre et al., 2010; Krabbenhoft et al., 2010; Peucker-Ehrenbrink et al., 2010; Luo et al., 2014; Voss et al., 2014; Pearce et al., 2015]. Riverine Sr concentrations can vary over three orders of magnitude from <0.1 μmol/L to >100 μmol/L [Palmer and Edmond, 1989; Krabbenhoft et al., 2010; Voss et al., 2014; Pearce et al., 2015]. Within a single river, Sr concentrations can vary seasonally from less than a factor of two up to an order of magnitude [Bagard et al., 2011; Luo et al., 2014; Voss et al., 2014; Chapman et al., 2015]. The $^{87}Sr/^{86}Sr$ ratio of the global riverine input largely reflects three-component mixing between young mafic rocks (basalt), old felsic rocks (granites), and marine carbonates. In the current icehouse climatic state, riverine Sr concentrations and isotopic ratios may also be impacted by substrate age and variable chemical

weathering rates following the retreat of major continental ice sheets and alpine glaciers [Taylor and Blum, 1995; Blum, 1997; Blum and Erel, 1997; Brantley et al., 1998; Millot et al., 2002; White and Brantley, 2003; Vance et al., 2009; von Blanckenburg et al., 2015; Mokadem et al., 2015]. A detailed study of the Fraser River Basin, Canada demonstrates the variability and complexity of Sr concentrations and $^{87}Sr/^{86}Sr$ ratios within a single large river system [Voss et al., 2014]. Within the multiple tributaries and sub-basins, as well as various points along the main stem, Sr concentrations and $^{87}Sr/^{86}Sr$ ratios range from 0.126-2.757 μmol/L and 0.70410-0.75150, respectively [Voss et al., 2014]. Time series analysis at the mouth of the Fraser River shows a more limited, but still significant range, of values for both parameters, which clearly correlate with seasonal changes [Voss et al., 2014]. Voss et al. (2014) ultimately calculated a discharge weighted Sr concentration and $^{87}Sr/^{86}Sr$ ratio for the Fraser River of 0.85 ± 0.04 μmol/L and 0.7120 ± 0.0003, respectively. Other time series and spatial analyses conducted for drainage basins in China, Myanmar, and Siberia have also documented distinct seasonal and spatial variability in Sr concentrations and isotope ratios [Bagard et al., 2011; Wei et al., 2013; Luo et al., 2014; Chapman et al., 2015]. These studies highlight the limitations and uncertainty imposed by using compilations of spot measurements to estimate the concentration and isotope ratio of the global riverine input. Along these lines, Palmer and Edmond (1989) noted that most of the river water samples in their compilation were biased towards high to moderate discharge, implying possible underestimation of the annual Sr flux.

The compilation of riverine Sr concentrations and $^{87}Sr/^{86}Sr$ ratios by Palmer and Edmond (1989) comprises eight of the ten largest rivers by discharge, which collectively constitute over 47% of the total global runoff. However, the authors acknowledged lack of data for several rivers, especially those east of the Ural Mountains. The weighted mean of the data produced a

global riverine Sr flux of 3.33 x 10^{10} mol/yr (average concentration of 0.89 μmol/L) with an $^{87}Sr/^{86}Sr$ ratio of 0.7119. Using more recent data, Davis et al. (2003) calculated similar values of 3.4 x 10^{10} mol/yr (average concentration of 0.902 μmol/L) and 0.7116, respectively. In contrast, the compilation of riverine $^{87}Sr/^{86}Sr$ ratios by Allegre et al. (2010) containing more than 30 of the world's principal rivers produced a discharge weighted average $^{87}Sr/^{86}Sr$ ratio of 0.7136. Using a total riverine water flux of 3.74 x 10^{19} g/yr and a mean Sr concentration of 44 ± 15 ppb (0.5 μmol/L), Allegre et al. (2010) calculated a global riverine Sr flux of 1.88 x 10^{10} mol/yr. With such a low continental riverine flux estimate relative to previous estimates, Allegre et al. (2010) argued for the presence of an additional 4.24 x 10^{18} g/yr water flux from mafic volcanic islands with a near-mantle $^{87}Sr/^{86}Sr$ ratio of 0.7035 to address the imbalance. The Sr concentration of this surface water flux from mafic volcanic islands is poorly constrained and could range from 35-200 ppb [Allegre et al., 2010]. Combining the minimum (i.e., most conservative) concentration estimate for surface waters from mafic volcanic islands with the continental riverine flux increases the total river flux to 2.05 x 10^{10} mol/yr, while reducing the $^{87}Sr/^{86}Sr$ ratio to 0.7128 [Allegre et al., 2010].

Peucker-Ehrenbrink et al. (2010) developed a model to determine the global riverine Sr flux and $^{87}Sr/^{86}Sr$ ratio based on bedrock age and lithology. This model also uses a riverine chemistry database containing 193 rivers representing 50.3% of the exorheic land surface and 48.3% of the global exorheic water discharge. The rivers were grouped into 19 large-scale drainage regions comprising non-glaciated land surfaces. Within each drainage region, weighted Sr concentrations, isotope ratios, and water discharges were determined before extrapolating to the ice-free area of the entire drainage region [Peucker-Ehrenbrink et al., 2010]. The model produced a global Sr flux of 4.7 x 10^{10} mol/yr (average concentration of 1.22 μmol/L) and an

$^{87}Sr/^{86}Sr$ ratio of 0.7111 [Peucker-Ehrenbrink et al., 2010]. This estimate is the least radiogenic $^{87}Sr/^{86}Sr$ ratio for the global riverine flux available within the literature, which Peucker-Ehrenbrink et al. (2010) attributed to difference in bedrock age calculated according to the Sr and water fluxes – 339 vs. 394 Ma. This difference in bedrock age indicates a greater contribution from younger sedimentary and volcanic rocks with lower $^{87}Sr/^{86}Sr$ ratios. It is possible that the impact of younger sedimentary and volcanic rocks on the global riverine $^{87}Sr/^{86}Sr$ ratio could be greater than currently estimated given the lack of data for smaller coastal rivers, island arcs, and oceanic islands [Allegre et al., 2010; Peucker-Ehrenbrink et al., 2010].

Beyond the dissolved load, rivers also deliver a significant suspended particulate and bedload to the oceans that can significantly impact global elemental cycles [Meybeck et al., 2003; Syvitski et al., 2003; Gislason et al., 2006; Jones et al., 2012a, b; Jeandel and Oelkers, 2015]. Over 60% of the suspended sediment flux is thought to originate from small mountainous rivers draining geologically young terrains with wet climates [Milliman and Farnsworth, 2011]. The majority of such river systems are located within continental volcanic arcs, as well as volcanic and tectonically active islands. Global estimates of the suspended particulate and bedload material delivered to the oceans annually is an order of magnitude greater than the total dissolved load (16.6-30 Gt/yr vs. ~1 Gt/yr) [Meybeck et al., 2003; Syvitski et al., 2003; Milliman and Farnsowrth, 2011; Jeandel and Oelkers, 2015]. Therefore, dissolution of even minor amounts of this sediment flux upon entering seawater could notably contribute to mass and isotope balances of several global elemental cycles [Gislason et al., 2006; Jones et al., 2012a, b; Jeandel and Oelkers, 2015]. Recent experimental work has highlighted the reactivity of the basaltic component of the sediment flux with regards to Sr, where similar to MOR hydrothermal systems, reaction with seawater causes significant isotopic exchange with only minor changes in

concentration [Jones et al., 2012a, b]. Using separate experimentally determined mean Sr release rates for continental and volcanic material, as well as assuming 45% of the riverine particulate flux is volcanically derived, Jones et al. (2012b) conservatively estimated the Sr particulate release flux to be 5.2 x 10^9 mol/yr. With ~70% of this flux originating from volcanic sediment the $^{87}Sr/^{86}Sr$ ratio of this input is likely less radiogenic than seawater.

3.3.4 Submarine Groundwater Discharge

Similar to the riverine input flux, estimates for the Sr concentration and isotope ratio of submarine groundwater discharge (SGD) are highly variable, as the input determined for any given system is influenced by bedrock age, lithology, history of water-rock interaction within the drainage basin-aquifer system, and exchange during subterranean mixing between fresh and saline groundwaters [Basu et al., 2001; Dowling et al., 2003; Allegre et al., 2010; Beck et al., 2013]. Groundwater Sr concentrations can vary over two to three orders of magnitude (0.1-100 μmol/L) with higher concentrations (>20 μmol/L) typically controlled by mixing with seawater [Basu et al., 2001; Dowling et al., 2003; Beck et al., 2013]. In many locations, the riverine and groundwater $^{87}Sr/^{86}Sr$ ratios are broadly similar; however, the distribution and/or type of rocks composing subterranean aquifer systems can differ from those exposed at the surface [Basu et al., 2001; Dowling et al., 2003; Beck et al., 2013]. While drainage basins comprising old granitic and metamorphic rocks, such as the Ganges-Brahmaputra basin, can yield large SGD fluxes, most SGD originates from relatively young coastal carbonate platforms (e.g., Yucatan and Florida Peninsulas) and volcanic islands [Basu et al., 2001; Allegre et al., 2010; Beck et al., 2013]. Thus, estimates for the SGD $^{87}Sr/^{86}Sr$ ratio are relatively low (0.7089) [Basu et al., 2001; Beck et al., 2013], which implies that the $^{87}Sr/^{86}Sr$ ratio of the total weathering flux (riverine + SGD) is slightly lower than that for the riverine input. SGD fluxes are highly uncertain. Current

estimates range from 7.1-16.5 x 10^9 mol/yr [Basu et al., 2001; Beck et al., 2013].

3.3.5 Burial Flux and Residence Time

Strontium is removed from the oceans through carbonate and sulfate precipitation and via alteration of the oceanic crust during hydrothermal circulation (epidote ± clays). Direct estimates of Sr burial fluxes are poorly constrained because Sr is a minor-to-trace component within marine carbonates, sulfates, and epidote, requiring assumptions about variable concentrations within each host mineral. The conservative behavior of Sr during hydrothermal circulation within the oceanic crust requires that the total mass of Sr leached from the oceanic crust be balanced by the formation of alteration minerals within the crust containing seawater Sr. Some models address this constraint by having a hydrothermal input flux with a basaltic Sr isotope ratio and a hydrothermal burial flux of equal magnitude with a seawater Sr isotope ratio [e.g., Kump, 1989]. In the model equations presented above, it is embedded in the total burial flux. Because carbonate deposition greatly exceeds deposition of anhydrite, barite, and epidote (both individually and combined), the Sr burial flux is primarily tied to the carbonate burial flux, except during massive basin-scale evaporite (calcium sulfate) deposition [Krabbenhoft et al., 2010; Vollstaedt et al., 2014]. Carbonate and sulfate minerals are presumed to record the seawater $^{87}Sr/^{86}Sr$ ratio. Ignoring minor output terms does not affect model calculations, especially given that carbonate burial flux estimates widely vary [Krabbenhoft et al, 2010 and references within; Vollstaedt et al., 2014].

Aragonite incorporates more Sr than calcite because strontianite ($SrCO_3$) is isostructural with aragonite. Substitution of Sr into $CaCO_3$ is sensitive to temperature and other thermodynamic variables, as well as the Sr/Ca ratio of seawater, which varies spatially within the modern ocean and throughout geologic time [de Villiers et al, 1994; de Villiers, 1999; Gothmann

et al., 2015]. Using carbonate burial estimates for different carbonate secreting organisms (i.e., corals, cooccoliths, planktonic foraminifera) and the mean molar Sr/Ca ratio for each group, Krabbenhoft et al. (2010) estimated a modern, total carbonate Sr burial flux of 174 x 10^9 mol/yr, which is approximately three times higher than estimates for the total input flux of Sr. In contrast, mass-balance model calculations using Phanerozoic radiogenic and stable Sr isotope ratios ($^{87}Sr/^{86}Sr$ and $^{88}Sr/^{86}Sr$) suggest carbonate Sr burial fluxes range from 0-47 x 10^9 mol/yr, with a mean value of 16 x 10^9 mol/yr, which is approximately half to a third of the riverine flux [Palmer and Edmond, 1989; Peucker-Ehrenbrink et al., 2010; Vollstaedt et al., 2014]. Given the degree of uncertainty surrounding Sr burial flux estimates, as well as the lack of impact on seawater $^{87}Sr/^{86}Sr$ ratios, the Sr burial flux is often ignored or substituted with assumptions about a constant residence time [Hodell et al., 1989, 1990; Jones and Jenkyns, 2001; Wallmann, 2001; Hansen and Wallmann, 2003; Walthman and Grocke, 2006; Young et al., 2009; Pogge van Strandmann et al., 2013]. The modern residence time for seawater Sr – calculated by dividing the mass of Sr in seawater by the total input flux – is estimated at ~2 Ma [Hodell et al., 1989, 1990; Palmer and Edmond, 1989; Basu et al., 2001; Peucker-Ehrenbrink et al., 2010; Beck et al., 2013]. Assuming a constant residence time, which presumes total input and output fluxes are in steady-state, limits concentration changes during major perturbations and artificially returns concentrations to initial values following the end of perturbations.

3.4. Estimating Sr cycle fluxes and isotope ratios for the Late Jurassic-Early Cretaceous

The global riverine (dissolved and particulate) and SGD $^{87}Sr/^{86}Sr$ ratios likely varied throughout the Phanerozoic given variations in the type and age of bedrock exposed to weathering [Wallmann, 2004; Peucker-Ehrenbrink et al., 2010; Beck et al., 2013; Voss et al.,

2014], as well as the time dependent nature of weathering reactions [Taylor and Blum, 1995; Blum, 1997; Blum and Erel, 1997; Brantley et al., 1998; White and Brantley, 2003]. Therefore, assuming that ancient Sr inputs have the same isotopic composition as modern inputs introduces uncertainty into model calculations. Because the complete distribution and age of marine carbonates, felsic rocks, and mafic rocks available for weathering on the continents at any time during the deep geologic past are unknown, the isotopic composition of the total weathering flux is a poorly constrained parameter (Equations 3-26 to 3-30). In contrast, Sr isotope analyses of microfossils and bulk carbonate from ODP cores over the past 25 years have greatly improved the density of Phanerozoic $^{87}Sr/^{86}Sr$ data and allowed construction of a high-resolution, composite seawater $^{87}Sr/^{86}Sr$ curve [McArthur et al., 2012 and references within]. Here, we suggest that the LOWESS FIT 5 of McArthur et al. (2012) (with time steps of 50 ka) provides a key constraint to Equation 3-30 that has been underutilized, namely the rate of change of seawater $^{87}Sr/^{86}Sr$ ratios ($\frac{d}{dt}R_{87,sw}$). The method for modeling the marine Sr cycle presented below is an iterative process that begins with calculating an $^{87}Sr/^{86}Sr$ ratio for a combined riverine (dissolved and particulate) and SGD flux ($F_{tw} = F_r + F_{sgd}$, tw = total weathering) that produces a reasonable match with the McArthur et al. (2012) $^{87}Sr/^{86}Sr$ record given prescribed values for the other parameters.

In the first step of this iterative process we prescribe a set of $\frac{d}{dt}R_{87,sw}$ values determined from the LOWESS FIT 5 of McArthur et al. (2012) in order to calculate $^{87}Sr/^{86}Sr$ ratios for F_{tw}

$$R_{87,tw} = \frac{\left(\frac{{}^{T}N_{sw} * \frac{d}{dt}R_{87,sw} - B\left(R_{87,ht} - R_{87,sw}\right)F_{ht} - B\left(R_{87,d} - R_{87,sw}\right)F_d}{F_{tw}}\right) + R_{87,sw} * \left(Z + R_{87,sw}\right)}{Z + R_{87,sw} - \left(\frac{{}^{T}N_{sw} * \frac{d}{dt}R_{87,sw} - B\left(R_{87,ht} - R_{87,sw}\right)F_{ht} - B\left(R_{87,d} - R_{87,sw}\right)F_d}{F_{tw}}\right)} \quad (3\text{-}31)$$

$$\text{where} \quad B = \frac{Z + R_{87,sw}}{Z + R_{87,i}} \quad (3\text{-}32)$$

The resultant $R_{87,tw}$ is then used to solve Equations 3-26 to 3-29 (modified for $F_{tw} = F_r + F_{sgd}$) to calculate $R_{87,sw}$ values that best match the McArthur et al. (2012) curve and enable calculation of $R_{87,tw}$ at the next time step. Selecting the resolution at which to time-step $\frac{d}{dt}R_{87,sw}$ depends on the magnitude and frequency of the variations being modeled, along with the need to match each inflection within the composite curve. For this case study, with a time interval of interest spanning 55 Ma, constant $\frac{d}{dt}R_{87,sw}$ were determined for intervals of varying length ranging from 0.1-2.4 Ma (Table 3-2).

The resulting range of $R_{87,tw}$ values from Equation 3-31 are checked against the range of $R_{87,sw}$ for the time interval of interest to qualitatively evaluate the potential strength of the hydrothermal and total weathering levers. In addition, the range of $R_{87,tw}$ values is compared to older portions of the $^{87}Sr/^{86}Sr$ seawater record to assess the potential availability of marine carbonates exposed on the continents for weathering that would reasonably contribute to a three-component mixture producing values within this range. Following these two assessments, Equations 3-26 to 3-29 (modified for $F_{tw} = F_r + F_{sgd}$) are used to determine the frequency at which prescribed constant $R_{87,tw}$ values should be modified to best match target seawater $^{87}Sr/^{86}Sr$ ratios (e.g., inflection points and plateaus) and the range of $\frac{d}{dt}R_{87,sw}$ determined from the LOWESS FIT 5 of McArthur et al. (2012). Table 3-3 presents the fluxes, isotope ratios, oceanic concentrations, and perturbation factors used for the Late Jurassic-Early Cretaceous

Table 3-2. Rate of change of $R_{87,sw}$ for the Late Jurassic to Early Cretaceous calculated from McArthur et al. (2012) LOWESS FIT 5 used in the modeling to calculate $R_{87,tw}$

Age (Ma)	Model Time (Ma)	Rate of Change of Seawater $^{87}Sr/^{86}Sr$ (per Ma)
160.5	0	8.65E-06
158.5	2.00	1.495E-05
156.5	4.00	2.525E-05
154.5	6.00	3.310E-05
152.5	8.00	3.055E-05
150.5	10.00	2.465E-05
148.5	12.00	1.723E-05
146.5	14.00	1.594E-05
144.5	16.00	2.192E-05
142.5	18.00	1.812E-05
140.5	20.00	2.170E-05
138.5	22.00	2.098E-05
136.5	24.00	9.86E-06
134.5	26.00	2.686E-05
132.5	28.00	2.405E-05
130.5	30.00	2.40E-06
130	30.5	1.292E-05
129.35	31.15	6.7E-07
128.75	31.75	-1.580E-05
127.75	32.75	-2.660E-05
126.75	33.75	-3.270E-05
125.75	34.75	-2.510E-05
124.75	35.75	-2.560E-05
123.75	36.75	-1.970E-05
122.75	37.75	-1.565E-05
120.75	39.75	-1.515E-05
118.75	41.75	-1.730E-05
117.75	42.75	-2.310E-05
116.75	43.75	-2.620E-05
115.75	44.75	-1.964E-05
115.2	45.3	0.000E+00
115.1	45.4	3.000E-05
113.9	46.6	4.933E-05
112.7	47.8	3.867E-05
111.5	49	3.008E-05
110.3	50.2	1.767E-05
109.1	51.4	6.67E-06
107.9	52.6	1.54E-6

Table 3-3. Fluxes, isotopic values, oceanic concentration, and perturbation factors used for Late Jurassic-Early Cretaceous Sr cycle model runs where $R_{87,tw}$ is calculated. Model times at which perturbations occur are noted. Model time 0 = 160.5 Ma. sw – seawater; tw – total weathering (riverine + submarine groundwater discharge); d – diagenetic; ht – hydrothermal

	Model A	Model B	Model C	Model D	Model E	Model F	Model A modern	Model B modern
[Sr] (µmol/L)	450	450	450	450	450	450	90	90
$R_{87,sw}$ initial	0.706849	0.706849	0.706849	0.706849	0.706849	0.706849	0.706849	0.706849
F_{tw} (mol/yr)	67.2e9	49.35e9	67.2e9	49.35e9	47e9	34e9	67.2e9	49.35e9
F_d (mol/yr)	3.4e9	3.4e9	3.4e9	3.4e9	3.4e9	3.4e9	3.4e9	3.4e9
$R_{87,d}$ initial[1]	0.70714	0.70714	0.70714	0.70714	0.70714	0.70714	0.70714	0.70714
F_{ht} (mol/yr)	18.6e9	18.6e9	18.6e9	18.6e9	18.6e9	18.6e9	3.72e9	3.72e9
$R_{87,ht}$	0.7030	0.7030	0.7030	0.7030	0.7030	0.7030	0.7030	0.7030
Perturbations								
Hydrothermal Flux								
LIP Initial Phase (30-31.75 Ma)	1.196X	1.196X	1.25X	1.25X	1.137X	1.137X	1.21X	1.20X
LIP Main Phase (31.75-35.75 Ma)	2.029X	1.986X	2.55X	2.485X	1.887X	1.857X	2.285X	2.13X
Post LIP (35.75 Ma)	1.4X	1.4X	1.6X	1.6X	1.35X	1.35X	1.4X	1.4X
Post Evaporite (46.75 Ma)	1.2X	1.2X	1.3X	1.3X	1.15X	1.15X	1.2X	1.2X
Total Weathering Flux								
LIP Initial Phase (30-31.75 Ma)	1.045X	1.045X	1.09X	1.092X	1.00X	1.00X	1.04X	1.04X
LIP Main Phase (31.75-35.75 Ma)	1.41X	1.41X	1.80X	1.792X	1.3375X	1.3375X	1.24X	1.25X
Post LIP (35.75 Ma)	1.1X	1.1X	1.2X	1.2X	1.1X	1.1X	1.1X	1.1X
Late Aptian-Early Albian rise (45.4 Ma)	1.21X	1.21X	1.32X	1.32X	1.21X	1.21X	1.21X	1.21X

[1]See Table 3-4 for full list of $^{87}Sr/^{86}Sr$ values for the diagenetic flux adjusting every 2.5 Ma.

marine Sr cycle model calculations presented below.

3.4.1 Hydrothermal

The $^{87}Sr/^{86}Sr$ ratio of the hydrothermal flux depends whether a purely basaltic hydrothermal flux or a total hydrothermal flux is assumed [Palmer and Edmond, 1989; Davis et al., 2003]. Unaltered MOR basalt from the Cretaceous indicates a basaltic hydrothermal $^{87}Sr/^{86}Sr$ ratio of 0.7030, which is slightly greater than the modern value of 0.7025 [Coogan, 2009]. As noted previously, Sr behaves conservatively during hydrothermal circulation despite experiencing significant isotopic exchange, therefore the basaltic hydrothermal flux should scale

linearly with seawater Sr concentrations [Davis et al., 2003]. There is growing evidence that major, minor, and trace element concentrations in seawater significantly varied throughout the Phanerozoic [Lowenstein et al., 2003; Coogan, 2009; Vollstaedt et al., 2014; Gothmann et al., 2015]. Mass-balance calculations focusing on the abundance and isotopic composition of Sr in altered sheet dike complexes from Cretaceous oceanic crust indicate that seawater Sr concentrations were ~450 μmol/L [Coogan, 2009]. In contrast, the modern seawater Sr concentration is 90 μmol/L [Pilson, 1998]. Elevated Sr concentrations in the Cretaceous ocean are consistent with elevated Ca concentrations, as well as a peak in seawater Sr/Ca ratios during this time [Lowenstein et al., 2003; Gothmann et al., 2015]. In addition, the Cretaceous experienced increased MOR spreading rates and hydrothermal fluxes (relative to the present) due to continued break up of Pangea [Larson, 1991; Rowley, 2002; Seton et al., 2009, 2012]. An appropriate estimate for the Sr hydrothermal flux during the Late Jurassic-Early Cretaceous must account for both the higher MOR spreading rates and elevated seawater Sr concentrations. Therefore, the basaltic hydrothermal flux of Davis et al. (2003) is first increased by 20% before multiplying by a factor of five to produce an estimated flux of 18.6×10^9 mol/yr (Models A-F, Table 3-3). To test the validity of the elevated Sr concentrations in the Cretaceous ocean and linear scaling of the hydrothermal flux, models employing a modern Sr concentration (90 μmol/L) and hydrothermal fluxes, elevated only to account for the increased MOR spreading rates, are run for comparison (Models A modern & B modern, Table 3-3).

3.4.2 Diagenetic

Considering that the diagenetic flux is a minor component of the Sr cycle and noting that the two estimates for the modern are about the same, the flux from Elderfield and Gieskes (1982) is used for all Late Jurassic-Early Cretaceous models (Table 3-3). However, the isotope

composition of the diagenetic flux, which is controlled by recrystallization of carbonate sediments present on the seafloor, has likely varied through time given temporal changes in the isotope composition of seawater [Elderfield and Gieskes, 1982; Richter and Liang, 1993; McArthur et al., 2012; Coogan and Dosso, 2015]. Here, we use the LOWESS FIT 5 of McArthur et al. (2012), which provides seawater/carbonate $^{87}Sr/^{86}Sr$ ratios with a time step of 50 ka for most of the Phanerozoic, to provide a more accurate and time variable isotope composition for the diagenetic flux. Following the observation that the modern diagenetic $^{87}Sr/^{86}Sr$ ratio corresponds with the Phanerozoic seawater record at 20 Ma, we assume that the isotope composition of the diagenetic input matches the seawater curve at ~20 Ma prior to the time period being modeled. In addition, we allow the value to change every 2.5 Ma. Therefore, we take the average over a 2.5 Ma interval (n=51) centered at 20 Ma prior to model age. Table 3-4 provides the values used for the Sr isotopic composition of the diagenetic flux in all models. These diagenetic $^{87}Sr/^{86}Sr$ ratios range from both greater than and less than the corresponding contemporaneous modeled seawater Sr isotope composition, with differences <0.0005.

3.4.3 Burial

As noted previously, most models of the marine Sr cycle assume that the burial flux goes as the mass of seawater Sr divided by the modern residence time of ~2 Ma. However, the relatively high Sr concentrations suspected for the Cretaceous (e.g., Coogan, 2009; Gothman et al., 2015) inherently imply a longer residence time. Therefore, we allow residence time to vary and assume Sr concentrations remain constant except during major perturbations, such as the emplacement of large igneous provinces (LIPs) and deposition of massive evaporites, when significant concentration changes are expected.

Table 3-4. Diagenetic input $^{87}Sr/^{86}Sr$ values used in all models. Using the McArthur et al. (2012) LOWESS FIT 5 the values are determined by taking the average spread over 2.5 Ma (n=51) centered at 20 Ma prior to model age.

Age (Ma)	Model Age (Ma)	Model Time (Ma)	Diagenetic input $^{87}Sr/^{86}Sr$
180.5	160.5	0	0.70714
178	158	2.5	0.70722
175.5	155.5	5	0.70728
173	153	7.5	0.70729
170.5	150.5	10	0.70726
168	148	12.5	0.70706
165.5	145.5	15	0.70692
163	143	17.5	0.70685
160.5	140.5	20	0.70685
158	138	22.5	0.70687
155.5	135.5	25	0.70692
153	133	27.5	0.70700
150.5	130.5	30	0.70707
148	128	32.5	0.70713
145.5	125.5	35	0.70717
143	123	37.5	0.70722
140.5	120.5	40	0.70727
138	118	42.5	0.70732
135.5	115.5	45	0.70737
133	113	47.5	0.70741
130.5	110.5	50	0.70747
128	108	52.5	0.70747

3.4.4 Riverine and SGD (Total Weathering)

In the initial model runs, where $R_{87,tw}$ is the calculated unknown, the models are paired (e.g., models A and B) to have a low and high F_{tw} (Table 3-3). In models E and F, F_{tw} represents the high and low dissolved riverine flux estimates, respectively, available in the literature with no contribution from SGD or particulate release from the sediment flux [Palmer and Edmond, 1989; Davis et al., 2003; Peucker-Ehrenbrink et al., 2010]. In all other models, F_{tw} is a summation covering the range of estimates for the dissolved riverine, SGD, and particulate release fluxes. The low F_{tw} estimate (49.35 x 10^9 mol/yr) is based on values from Palmer and Edmond (1989), Beck et al. (2013), and Jones et al. (2012b), while the high F_{tw} estimate (67.2 x 10^9 mol/yr) is based on values from Peucker-Ehrenbrink et al. (2010), Basu et al. (2001), and Jones et al.

(2012b). Both of these estimates also include a 5% increase over the sum of the modern estimates to account for the climatic and continental ice differences between the cool greenhouse of the Late Jurassic-Early Cretaceous and the current bipolar icehouse conditions [Frakes et al., 1992; Boucot et al., 2013]. For 30 Ma prior to the Early Cretaceous (Barremain), the marine $^{87}Sr/^{86}Sr$ record shows a near constant, linear increase that is assumed to represent stable, consistent preconditions (instead of steady state). In model runs where $R_{87,tw}$ is being calculated, F_{tw} is assumed to be constant during the 30 Ma increase in $^{87}Sr/^{86}Sr$ ratios. In the paired model runs where $R_{87,tw}$ values are prescribed, F_{tw} begins at intermediate values (57 x 10^9 mol/yr or 37 x 10^9 mol/yr) and gradually increases by 1 x 10^9 mol/yr every 2.5 Ma over the 30 Ma time interval (Table 3-5).

3.4.5 Perturbations

Major geologic events during the Early Cretaceous that could broadly impact the marine Sr cycle include emplacement of multiple LIPs, increased continental arc volcanism, elevated MOR spreading rates, and deposition of the anhydrite-rich Late Aptian South Atlantic Salts [Larson, 1991; Jones and Jenkyns, 2001; Rowley, 2002; Hansen and Wallmann, 2003; Davison, 2007; Bryan and Ernst, 2008; Seton et al., 2009, 2012; Chandler et al., 2012; McArthur et al., 2012; Bryan and Ferrari, 2013; Chaboureau et al., 2013; Hochmuth et al., 2015; McKenzie et al., 2016; Wang et al., 2016]. Marine $^{87}Sr/^{86}Sr$ ratios increase for 30 Ma and plateau during the Barremian (Fig. 3-1) [McArthur et al., 2012]. This plateau is thought to be the result of the initial phase of emplacement of the Ontong Java-Manihiki-Hikurangi Plateau (OJMHP), the largest of the Early Cretaceous LIPs [Jones and Jenkyns, 2001; Bryan and Ernst, 2008; Chandler et al., 2012; Bryan and Ferrari, 2013; Hochmuth et al., 2015]. The initial decrease in $^{87}Sr/^{86}Sr$ ratios during the Barremian-Aptian likely corresponds to the main phase of OJMHP emplacement, while the

Table 3-5. Fluxes, R_{87}, oceanic concentration, and perturbation factors used for Late Jurassic-Early Cretaceous Sr cycle model runs where $R_{87,tw}$ is prescribed. See Figure 3-5 for single prescribed $R_{87,tw}$ values and Table 3-6 for list of prescribed $R_{87,tw}$ values used to test frequency variation with Model AB. See Table 3-7 for list of prescribed $R_{87,tw}$ values that vary every 1-2.5 Ma. Model times at which perturbations perturbations occur are noted. Model time and abbreviations same as Table 3-3.

	Model AB	**Model CD**	**Model EF**	**Model AB modern**
[Sr] (µmol/L)	450	450	450	90
$R_{87,sw}$ initial	0.706849	0.706849	0.706849	0.706849
F_{tw} (mol/yr)[1]	57e9 → 68e9	57e9 → 68e9	37e9 → 48e9	57e9 → 68e9
$R_{87,tw}$	Prescribed	Prescribed	Prescribed	Prescribed
F_d (mol/yr)	3.4e9	3.4e9	3.4e9	3.4e9
$R_{87,d}$ initial[2]	0.70714	0.70714	0.70714	0.70714
F_{ht} (mol/yr)	18.6e9	18.6e9	18.6e9	3.72e9
$R_{87,ht}$	0.7030	0.7030	0.7030	0.7030
Perturbation Factors				
Hydrothermal Flux				
LIP Initial Phase (30-31.75 Ma)	1.196X	1.25X	1.137X	1.21X
LIP Main Phase (31.75-35.75 Ma)	2.029X	2.55X	1.887X	2.285X
Post LIP (35.75 Ma)	1.4X	1.6X	1.35X	1.4X
Post Evaporite (46.75 Ma)	1.2X	1.3X	1.15X	1.2X
Total Weathering Flux				
LIP Initial Phase (30-31.75 Ma)	1.045X	1.09X	1.00X	1.04X
LIP Main Phase (31.75-35.75 Ma)	1.41X	1.80X	1.3375X	1.24X
Post LIP (35.75 Ma)	1.1X	1.2X	1.1X	1.1X
Late Aptian-Early Albian rise (45.4 Ma)	1.21X	1.32X	1.21X	1.21X

[1]During consistent preconditions (0-30 Ma) F_{tw} increases 1e9 mol/yr every 2.5 Ma
[2]See Table 3-4 for full list of $^{87}Sr/^{86}Sr$ values for the diagenetic flux adjusting every 2.5 Ma

continued decrease may represent a new, quasi steady-state (mass balance but isotope imbalance) with elevated hydrothermal and total weathering fluxes related to the subsequent emplacement of the Kerguelen Plateau, increased continental arc volcanism, and higher MOR spreading rates (Tables 3-3 and 3-5) [Larson, 1991; Rowley, 2002; Bryan and Ernst, 2008; Seton et al., 2009, 2012; Bryan and Ferrari, 2013; McKenzie et al., 2016; Wang et al., 2016]. While the deposition

of the Late Aptian South Atlantic Salts would not directly impact seawater $^{87}Sr/^{86}Sr$ ratios, Sr concentrations would have decreased significantly, which in turn would have lowered the hydrothermal flux. While no specific major geologic event appears to correspond with the Late Aptian-Early Albian rise in seawater $^{87}Sr/^{86}Sr$ ratios, in general, increases in the marine Sr isotope record are presumed to reflect increased riverine inputs and/or decreased hydrothermal inputs [Palmer and Edmond, 1989; Jones and Jenkyns, 2001; Hansen and Wallmann, 2003; McArthur et al., 2012].

According to Equation 3-31, major unbalanced perturbations to the marine Sr cycle, such as the emplacement of OJMHP, could yield unreasonably large step changes to $R_{87,tw}$ (Fig. 3-2A). Therefore, $R_{87,tw}$ values are assumed to change at a constant, linear rate (2.0e-5/Ma) during the perturbation instead of being calculated, as they are during the other portions of the model runs. The constant linear rate of change in $R_{87,tw}$ is estimated based on the overall rate of change in $R_{87,tw}$ determined for the 30 Ma precondition interval. Using a prescribed constant, linear rate of change for $R_{87,tw}$ during the OJMHP perturbation while calculating $R_{87,tw}$ during other parts of the model, allows hydrothermal and total weathering fluxes to be adjusted until target seawater $^{87}Sr/^{86}Sr$ ratios are met at the end of the initial and main phases of OJMHP (Fig. 3-2). Once appropriate perturbation fluxes are identified, the linearized rate of change for $R_{87,tw}$ during the OJMHP perturbation is removed and $R_{87,tw}$ values are calculated over the entire model.

Figure 3-2 Aligning magnitude of perturbation factor

Modeled total weathering (**A**) and seawater (**B**) $^{87}Sr/^{86}Sr$ ratios demonstrating the use of a prescribed linearized $R_{87,tw}$ value to constrain fluxes and minimize step changes in $R_{87,tw}$ during the emplacement of the OJMHP. The non-linear $R_{87,tw}$ curve (A, black) shows the large theoretical step change in $R_{87,tw}$ for initial unconstrained perturbation fluxes necessary to match the McArthur et al. (2012) curve (B, black). The linear $R_{87,tw}$ and seawater curves (light blue) demonstrate the large step change in $R_{87,tw}$ following the end of the perturbation and the extreme mismatch in modeled $R_{87,sw}$ values and the McArthur et al. (2012) curve upon first linearization of the initial unconstrained perturbation fluxes. Modification to the perturbation fluxes (linear adjusted curves – purple/magenta) eventually results in minimizing the step change in $R_{87,tw}$ following the end of the perturbation while also meeting target seawater $^{87}Sr/^{86}Sr$ ratios at the end of the initial and main phases of the OJMHP perturbation.

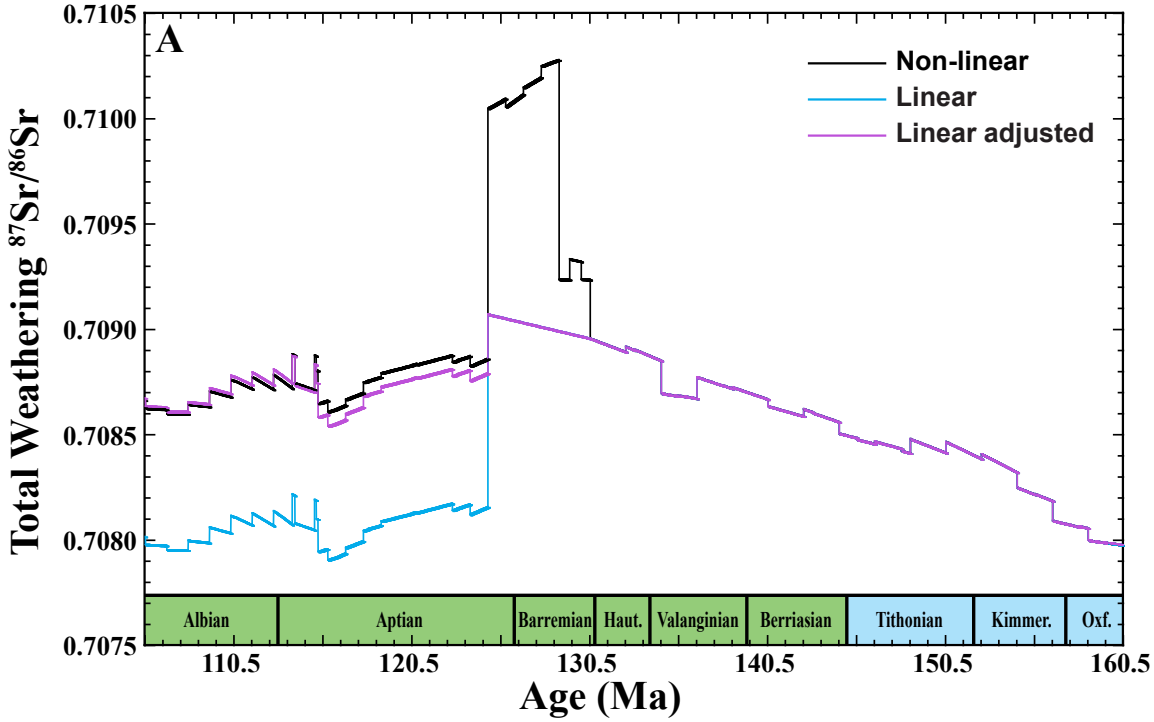
A
Non-linear
Linear
Linear adjusted
Total Weathering $^{87}Sr/^{86}Sr$
0.7105
0.7100
0.7095
0.7090
0.7085
0.7080
0.7075
Albian
Aptian
Barremian
Haut.
Valanginian
Berriasian
Tithonian
Kimmer.
Oxf.
110.5
120.5
130.5
140.5
150.5
160.5
Age (Ma)

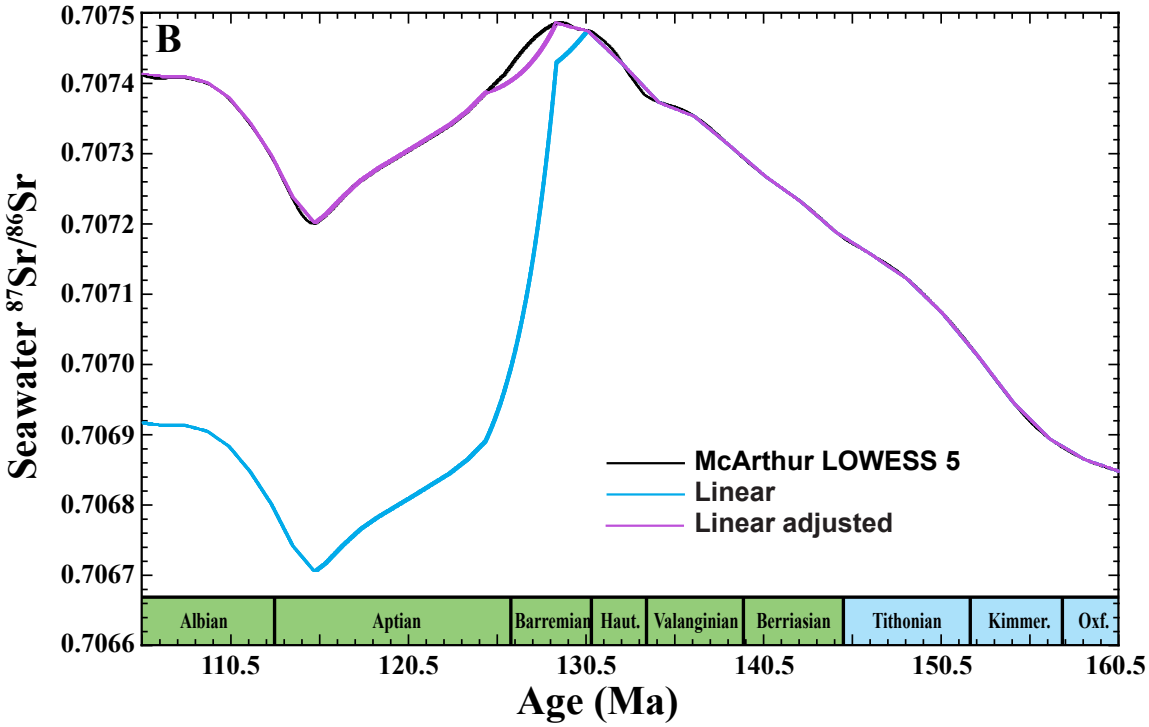
B
McArthur LOWESS 5
Linear
Linear adjusted
Seawater $^{87}Sr/^{86}Sr$
0.7075
0.7074
0.7073
0.7072
0.7071
0.7070
0.7069
0.7068
0.7067
0.7066
Albian
Aptian
Barremian
Haut.
Valanginian
Berriasian
Tithonian
Kimmer.
Oxf.
110.5
120.5
130.5
140.5
150.5
160.5
Age (Ma)

3.5. Model Implementation, Results, and Discussion

3.5.1 Checking calculated R_{tw} and Sr concentrations

Figure 3-3 presents the calculated $R_{87,tw}$ values for all eight models listed in Table 3-3. The difference between the calculated $R_{87,tw}$ values and the range of Late Jurassic-Early Cretaceous seawater $^{87}Sr/^{86}Sr$ ratios for a 450 µmol/L Sr ocean is similar to that between estimates for $R_{87,r}$ and seawater today (~0.002) [Peucker-Ehrenbrink et al., 2010]. In contrast, the difference between calculated $R_{87,tw}$ values and the range of Late Jurassic-Early Cretaceous seawater $^{87}Sr/^{86}Sr$ ratios for a 90 µmol/L Sr ocean is small (approximately one eighth to one quarter of today's difference). With only two primary levers controlling changes in seawater $^{87}Sr/^{86}Sr$ ratios, such small differences between the Sr isotope ratio of one lever and seawater will significantly weaken the impact of the other lever. The model output supports the presumed linear scaling of the hydrothermal Sr flux with seawater Sr concentrations based on conservative behavior during circulation within the oceanic crust. The linear scaling of the hydrothermal Sr flux with seawater Sr concentrations highlights the need for reasonable estimates of marine Sr concentrations throughout the Phanerozoic to properly model the marine Sr cycle in the geologic past. These results also validate prior estimates for a ~450 µmol/L Sr ocean during the Cretaceous, which are consistent with elevated Ca concentrations at this time [Lowenstein et al., 2003; Coogan, 2009; Vollstaedt et al., 2014].

In Figure 3-4, the total range of calculated $R_{87,tw}$ values for a 450 µmol/L (Models A-F) and a 90 µmol/L (Models A modern and B modern) Sr ocean are highlighted in light blue and yellow, respectively, against the known Phanerozoic and Neoproterozoic seawater $^{87}Sr/^{86}Sr$ record (McArthur et al., 2012). In the three-component mixing model controlling $R_{87,tw}$ values, a small contribution from granite weathering can have a significant impact. Because granite

Figure 3-3 Calculated total weathering Sr isotope ratio

Calculated $R_{87,tw}$ values during the Late Jurassic-Early Cretaceous for a 450 µmol/L Sr ocean (Models A-F) and a 90 µmol/L Sr ocean (Models A modern + B modern). Range of seawater $^{87}Sr/^{86}Sr$ ratios for Late Jurassic-Early Cretaceous from McArthur et al. (2012) highlighted in gray box. Modern riverine $^{87}Sr/^{86}Sr$ ratio (dashed green line) shown for comparison is taken from Peucker-Ehrenbrink et al. (2010).

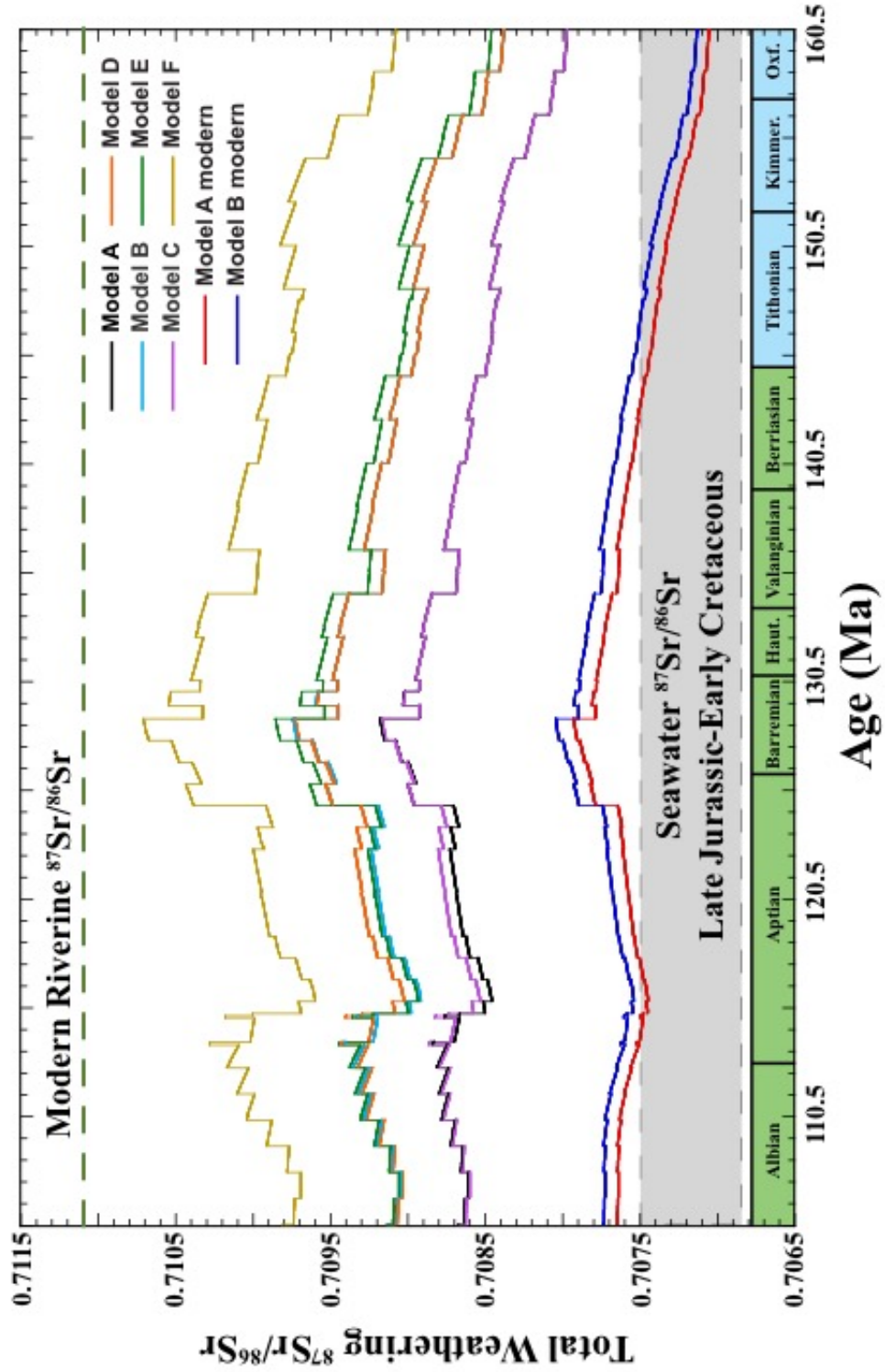
Modern Riverine $^{87}Sr/^{86}Sr$
Model A
Model B
Model C
Model D
Model E
Model F
Model A modern
Model B modern
Seawater $^{87}Sr/^{86}Sr$
Late Jurassic-Early Cretaceous
Total Weathering $^{87}Sr/^{86}Sr$
Age (Ma)
0.7115
0.7105
0.7095
0.7085
0.7075
0.7065
110.5
120.5
130.5
140.5
150.5
160.5
Albian
Aptian
Barremian
Haut.
Valanginian
Berriasian
Tithonian
Kimmer.
Oxf.

weathering increases $R_{87,tw}$, the majority of marine carbonates available for weathering should therefore have $^{87}Sr/^{86}Sr$ ratios less than or similar to the calculated $R_{87,tw}$ value. However, a large contribution of non-radiogenic Sr from basalt weathering can greatly extend the upper range of $^{87}Sr/^{86}Sr$ ratios available from carbonate weathering. For a 90 µmol/L Sr ocean experiencing minimal contributions from basalt weathering, few carbonate rocks older than 160.5 Ma are suitable (below yellow rectangle in Fig. 3-4). In contrast, a 450 µmol/L Sr ocean that similarly experiences minimal contributions from basalt weathering allows for a much larger and reasonable range of older marine carbonates available for weathering (below blue rectangle in

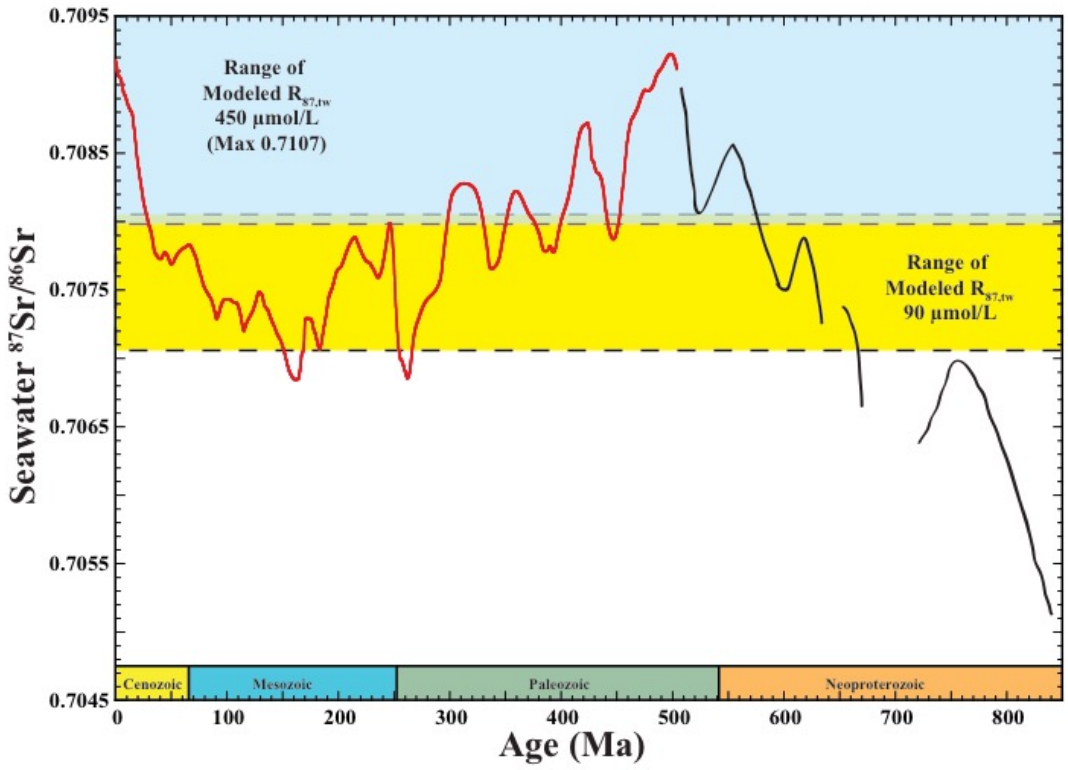

Figure 3-4 Phanerozoic and Neoproterozoic seawater Sr isotope record

The Phanerozoic and Neoproterozoic seawater $^{87}Sr/^{86}Sr$ record from McArthur et al. (2012) with the total range of calculated $R_{87,tw}$ values highlighted for a 450 µmol/L (light blue) and 90 µmol/L (yellow) Sr ocean during the Late Jurassic-Early Cretaceous.

Fig. 3-4). This further supports the existence of a ~450 µmol/L Sr ocean during the Cretaceous and the linear scaling of the hydrothermal Sr flux with marine Sr concentrations. In addition, the linear scaling of the hydrothermal Sr flux with seawater Sr concentration strongly supports the lower modern hydrothermal flux estimate of Davis et al. (2003) because a 5-fold increase in the Palmer and Edmond (1989) hydrothermal flux produces unrealistic flux values.

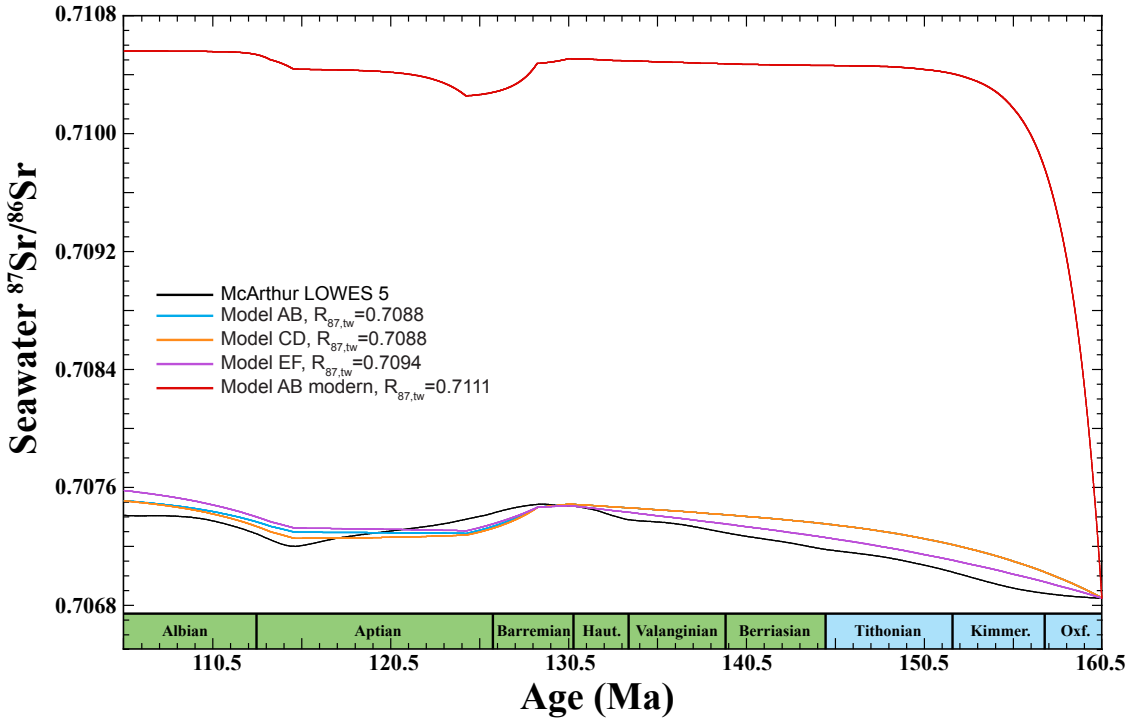

Figure 3-5 Single prescribed $R_{87,tw}$ value

Modeled $R_{87,sw}$ ratios from models AB, CD, EF, and AB modern with a single, prescribed constant $R_{87,tw}$ value and the McArthur et al. (2012) curve shown for comparison. $R_{87,tw}$ value for models AB and CD is 0.7088. $R_{87,tw}$ value for model EF is 0.7094. $R_{87,tw}$ value for model AB modern is the global riverine estimate of 0.7111 from Peucker-Ehrnebrink et al. (2010).

3.5.2 Prescribing constant $R_{87,tw}$ values

Prescribing a single constant $R_{87,tw}$ value for models with long time frames (e.g., 55 Ma), even when appropriately estimated for the time interval of interest, produces $R_{87,sw}$ values and a curve structure that poorly match the McArthur et al. (2012) record (Fig. 3-5). This result is expected as the iterative model presented here assumes that the global, integrated $R_{87,tw}$ value varies considerably over geologic timescales. Prescribing $R_{87,tw}$ values that change every 10 Ma moderately improves the match to the near-linear Late Jurassic-Early Cretaceous rise in seawater $^{87}Sr/^{86}Sr$ ratios, including the plateau during the initial phase of OJMHP in the Barremian (blue line Fig. 3-6A and Table 3-6). However, during the main phase of OJMHP, the modeled $R_{87,sw}$ decreases at a steeper rate than the McArthur curve before drastically diverging from the

Table 3-6. Prescribed $R_{87,tw}$ values used to test frequency variation with Model AB presented in Figure 3-6a.

Age (Ma)	Model Time (Ma)	Prescribed $R_{87,tw}$ 10 Ma	Age (Ma)	Model Time (Ma)	Prescribed $R_{87,tw}$ 5 Ma	Age (Ma)	Model Time (Ma)	Prescribed $R_{87,tw}$ 2.5 Ma
160.5	0	0.70843	160.5	0	0.70831	160.5	0	0.7082
150.5	10	0.70867	155.5	5	0.70852	158	2.5	0.70830
140.5	20	0.70883	150.5	10	0.70861	155.5	5	0.70847
130.5	30	0.70895	145.5	15	0.70868	153	7.5	0.70858
120.5	40	0.70868	140.5	20	0.70875	150.5	10	0.70859
110.5	50	0.70865	135.5	25	0.70887	148	12.5	0.70861
			130.5	30	0.70895	145.5	15	0.70863
			125.5	35	0.70871	143	17.5	0.70868
			120.5	40	0.70857	140.5	20	0.70874
			115.5	45	0.70872	138	22.5	0.70875
			110.5	50	0.70865	135.5	25	0.70884
						133	27.5	0.7089
						130.5	30	0.70896
						128	32.5	0.70909
						125.5	35	0.70887
						123	37.5	0.70870
						120.5	40	0.70861
						118	42.5	0.70851
						115.5	45	0.70864
						113	47.5	0.70877
						110.5	50	0.70867
						108	52.5	0.70862

Figure 3-6 Multiple prescribed $R_{87,tw}$ values

A) Modeled seawater $^{87}Sr/^{86}Sr$ ratios from model AB with prescribed constant $R_{87,tw}$ values varying every 10 Ma, 5 Ma, 2.5 Ma, and a mixture of 2.5 and 1 Ma. McArthur et al. (2012) curve included for comparison. See Table 3-6 for lists of prescribed $R_{87,tw}$ values. **B**) Modeled seawater $^{87}Sr/^{86}Sr$ ratios from models AB, CD and EF with prescribed constant $R_{87,tw}$ values varying a mixture of every 2.5 or 1 Ma. McArthur et al. (2012) curve included for comparison. See Table 3-7 for list of prescribed $R_{87,tw}$ values for the mixed 2.5 and 1 Ma model runs for all three models.

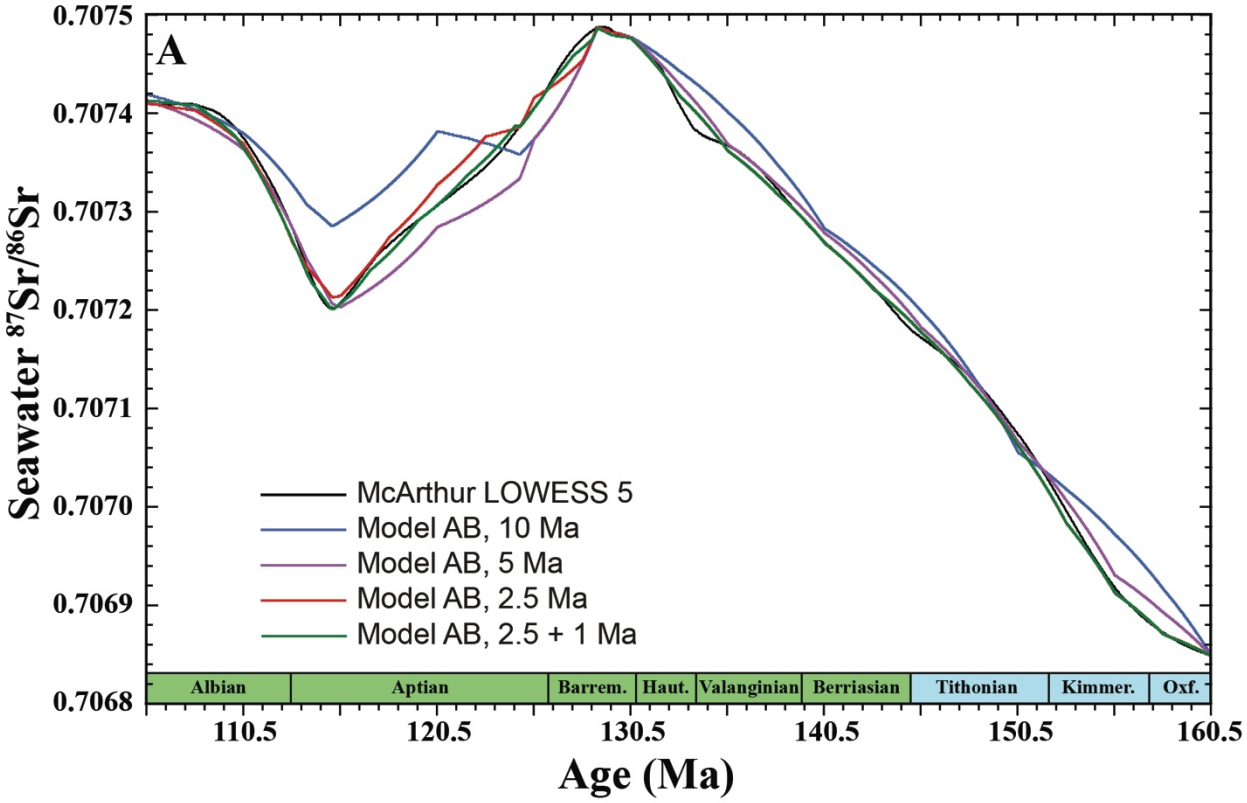
A
Seawater $^{87}Sr/^{86}Sr$
0.7075
0.7074
0.7073
0.7072
0.7071
0.7070
0.7069
0.7068
McArthur LOWESS 5
Model AB, 10 Ma
Model AB, 5 Ma
Model AB, 2.5 Ma
Model AB, 2.5 + 1 Ma
Albian
Aptian
Barrem.
Haut.
Valanginian
Berriasian
Tithonian
Kimmer.
Oxf.
110.5
120.5
130.5
140.5
150.5
160.5
Age (Ma)

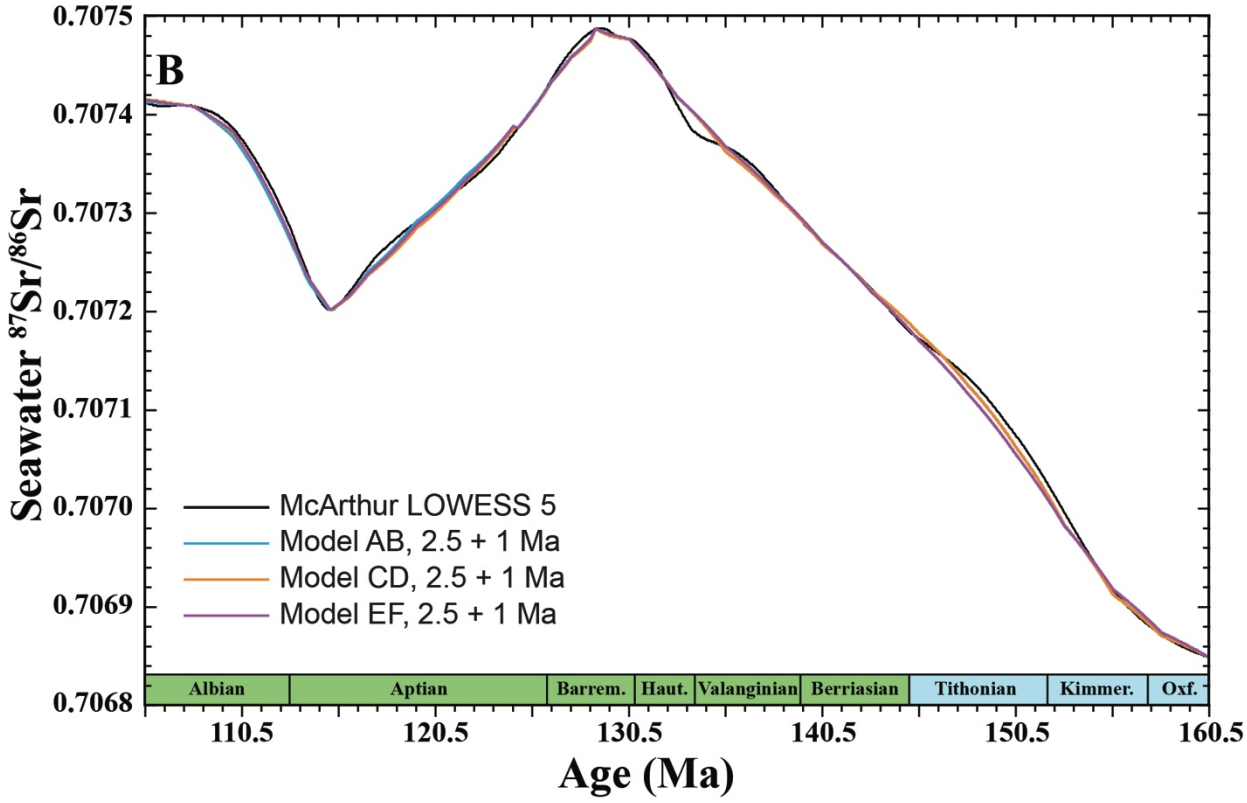
B
Seawater $^{87}Sr/^{86}Sr$
0.7075
0.7074
0.7073
0.7072
0.7071
0.7070
0.7069
0.7068
McArthur LOWESS 5
Model AB, 2.5 + 1 Ma
Model CD, 2.5 + 1 Ma
Model EF, 2.5 + 1 Ma
Albian
Aptian
Barrem.
Haut.
Valanginian
Berriasian
Tithonian
Kimmer.
Oxf.
110.5
120.5
130.5
140.5
150.5
160.5
Age (Ma)

continued Barremian-Aptian decrease following the end of the main phase of the OJMHP eruption (blue line Fig. 3-6A). Adjusting $R_{87,tw}$ values every 5 Ma improves the match (purple line Fig. 3-6A and Table 3-6). Adjusting $R_{87,tw}$ values every 2.5 Ma further improves agreement between measured and model $R_{87,sw}$ (red line Fig. 3-6A and Table 3-6). However, notable differences still remain in the $\frac{d}{dt}R_{87,sw}$ during the main phase of OJMHP, as well as $R_{87,sw}$ values determined for the Late Aptian minimum and Early-Middle Albian plateau. The best overall fit with $\frac{d}{dt}R_{87,sw}$ and target seawater $^{87}Sr/^{86}Sr$ ratios occurs when $R_{87,tw}$ is allowed to vary every 2.5 to 1 Ma (Fig. 3-6 and Table 3-7). The more frequent variation in $R_{87,tw}$ values is needed during the major perturbations and transitions (inflection points) within the seawater $^{87}Sr/^{86}Sr$ record (Tables 3-5 and 3-7). This frequency of change is reasonable considering the range of estimates for average denudation rates implying that erosion can remove 10-1000 meters of rock within 1 Ma [Portenga and Bierman, 2011; Herman et al., 2013]. In addition, cyclic variation in orbital parameters can influence climate change on timescales ≤1Ma, such as the distribution of precipitation (wet versus dry regions), that could impact the global integrated $R_{87,tw}$ value [i.e., Elkibbi and Rial, 2001; Graziano and Raspini, 2015; Charbonnier et al., 2016].

Although the model presented here presumes the global integrated $R_{87,tw}$ value can vary on geologically short time scales (~10^6 yr), these changes are not expected to be large. While the new exposure of a Precambrian granite or large amounts of basalt, for example, could greatly shift river water $^{87}Sr/^{86}Sr$ ratios in a single drainage basin, the impact on global $R_{87,tw}$ values would be muted by opposing changes in other drainage basins, the integration of all rivers, and additional contributions from SGD. Therefore, when prescribing $R_{87,tw}$ values, a goal should be to minimize the magnitude of step changes. The improved match between measured and

Table 3-7. Prescribed total weathering $^{87}Sr/^{86}Sr$ ratios for models AB, CD and EF for initial (Fig. 3-6b) and reassessed (final) fluxes at the mixed 2.5 and 1 Ma intervals.

Age (Ma)	Model Time (Ma)	Prescribed $R_{87,tw}$ Model AB		Prescribed $R_{87,tw}$ Model CD		Prescribed $R_{87,tw}$ Model EF	
		Initial	Final	Initial	Final	Initial	Final
160.5	0	0.70820	0.70820	0.70820	0.70820	0.70895	0.70895
158	2.5	0.70830	0.70830	0.70830	0.70830	0.70906	0.70906
155.5	5	0.70847	0.70847	0.70847	0.70847	0.70921	0.70921
153	7.5	0.70858	0.70858	0.70858	0.70858	0.70931	0.70931
150.5	10	0.70859	0.70859	0.70859	0.70859	0.70930	0.70930
148	12.5	0.70860	0.70860	0.70860	0.70860	0.70930	0.70930
145.5	15	0.70863	0.70863	0.70863	0.70863	0.70932	0.70932
143	17.5	0.70868	0.70868	0.70868	0.70868	0.70935	0.70935
140.5	20	0.70874	0.70874	0.70874	0.70874	0.70939	0.70939
138	22.5	0.70875	0.70875	0.70875	0.70875	0.70938	0.70938
135.5	25	0.70884	0.70884	0.70884	0.70884	0.70943	0.70943
133	27.5	0.70890	0.70890	0.70890	0.70890	0.70951	0.70951
130.5	30	0.70893	0.70893	0.70893	0.70893	0.70954	0.70954
129.5	31	0.70899	0.70899	0.70899	0.70899	0.70959	0.70959
128.5	32	0.70913	0.70908	0.70912	0.70908	0.70975	0.70968
127.5	33	0.70905	0.70900	0.70905	0.70902	0.70966	0.70960
126.5	34	0.70898	0.70893	0.70898	0.70895	0.70957	0.70950
125.5	35	0.70896	0.70892	0.70897	0.70893	0.70957	0.70950
124.5	36	0.70871	0.70890	0.70877	0.70891	0.70918	0.70948
122	38.5	0.70866	0.70886	0.70872	0.70886	0.70915	0.70944
119.5	41	0.70857	0.70879	0.70865	0.70879	0.70905	0.70936
117	43.5	0.70848	0.70871	0.70857	0.70874	0.70896	0.70927
116	44.5	0.70853	0.70876	0.70862	0.70877	0.70903	0.70934
115	45.5	0.70864	0.70880	0.70869	0.70882	0.70918	0.70939
114	46.5	0.70872	0.70887	0.70872	0.70885	0.70926	0.70946
113	47.5	0.70874	0.70888	0.70874	0.70887	0.70928	0.70948
112	48.5	0.70876	0.70890	0.70875	0.70889	0.70927	0.70948
111	49.5	0.70875	0.70891	0.70874	0.70889	0.70926	0.70946
110	50.5	0.70869	0.70889	0.70867	0.70888	0.70913	0.70943
108	52.5	0.70862	0.70883	0.70862	0.70883	0.70906	0.70936
Weighted average		0.70867	0.70873	0.70868	0.70873	0.70927	0.70936
Standard deviation		0.000210	0.000202	0.000203	0.000202	0.000208	0.000151
Maximum difference		0.00093	0.00088	0.00092	0.00088	0.00080	0.00073
Maximum step magnitude		0.00025	0.00017	0.00020	0.00017	0.00039	0.00015
Step magnitude average ± SD (10^{-5})		6.9 ± 5.3	5.3 ± 3.8	6.1 ± 4.7	4.9 ± 3.7	7.5 ± 7.7	5.2 ± 3.8

modeled data obtained by increasing the frequency at which $R_{87,tw}$ changes (Fig. 3-6A) supports this conclusion. When $R_{87,tw}$ values change every 5 Ma, the magnitude of change is ≥0.0001 50% of the time compared to only 21% of the time when the $R_{87,tw}$ varies every 2.5 to 1 Ma (model AB).

The persistence of large changes in $R_{87,tw}$ values for the "best fit" scenario (Table 3-7) is interpreted as a need to reassess the flux values. Excluding the precondition interval, there are three large changes in $R_{87,tw}$ that occur near the beginning and end of the main phase of OJMHP, as well as during the Late Aptian-Early Albian rise in seawater $^{87}Sr/^{86}Sr$ ratios (Table 3-7 – model times 32, 36 and 45.5 Ma, respectively). Decreasing the hydrothermal perturbation factor by 5% and adjusting the post-OJMHP hydrothermal flux to 1.6X in model AB, 1.75X in model CD, and 1.55X in model EF significantly reduces the changes in $R_{87,tw}$ and greatly improves the match between modeled and measured $\frac{d}{dt}R_{87,sw}$ (Tables 3-3, 3-5, and 3-8). The magnitude of the decrease in the hydrothermal flux during the deposition of the Late Aptian South Atlantic Salts is maintained in all models. In models AB and EF, the increase in the total weathering flux during the Late Aptian is adjusted to 1.25X, while a decrease to 1.20X at model time 50.5 Ma is included to help minimize changes in $R_{87,tw}$ during the Albian plateau in seawater $^{87}Sr/^{86}Sr$ ratios (Tables 3-3, 3-5, and 3-8). While model CD did not require an adjustment to the total weathering flux during the Late Aptian, similar to models AB and EF, a decrease in the total weathering flux to 1.25X at model time 50.5 Ma is included. These adjustments in the fluxes significantly reduce the maximum step size, along with the average and standard deviation of the step size (Table 3-7 and Fig. 3-7).

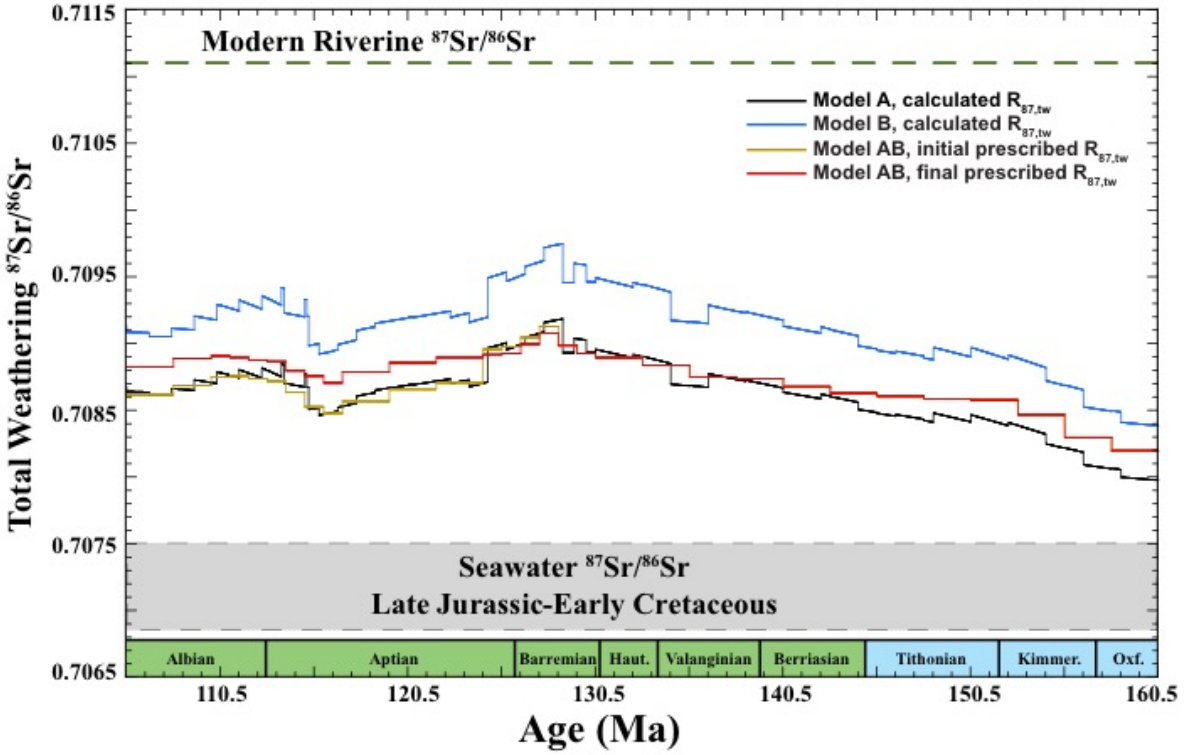

Figure 3-7 Initial versus final prescribed $R_{87,tw}$ values

Calculated $R_{87,tw}$ values for models A and B, same as in Figure 3-4, along with initial and final prescribed $R_{87,tw}$ for model AB (Table 3-7). Range of seawater $^{87}Sr/^{86}Sr$ ratios for Late Jurassic-Early Cretaceous from McArthur et al. (2012) highlighted in gray box. Modern riverine $^{87}Sr/^{86}Sr$ value (dashed green line) for comparison is taken from Peucker-Ehrenbrink et al. (2010).

Table 3-8. Fluxes, isotopic ratios, oceanic concentration, and final adjusted perturbation factors for Late Jurassic-Early Cretaceous Sr cycle model runs where $R_{87,tw}$ is prescribed with values that vary every 1-2.5 Ma (Table 3-7). Model times at which perturbations occur are noted. Model time and abbreviations same as Table 3-3.

	Model AB	**Model CD**	**Model EF**
[Sr] (µmol/L)	450	450	450
$R_{87,sw}$ initial	0.706849	0.706849	0.706849
F_{tw} (mol/yr)[1]	57e9 → 68e9	57e9 → 68e9	37e9 → 48e9
$R_{87,tw}$	Prescribed	Prescribed	Prescribed
F_d (mol/yr)	3.4e9	3.4e9	3.4e9
$R_{87,d}$ initial[2]	0.70714	0.70714	0.70714
F_{ht} (mol/yr)	18.6e9	18.6e9	18.6e9
$R_{87,ht}$	0.7030	0.7030	0.7030
Perturbation Factors			
Hydrothermal Flux			
LIP Initial Phase (30-31.75 Ma)	1.196X	1.25X	1.137X
LIP Main Phase (31.75-35.75 Ma)	1.976X	2.50X	1.837X
Post LIP (35.75 Ma)	1.6X	1.75X	1.55X
Post Evaporite (46.75 Ma)	1.4X	1.45X	1.35X
Total Weathering Flux			
LIP Initial Phase (30-31.75 Ma)	1.045X	1.09X	1.00X
LIP Main Phase (31.75-35.75 Ma)	1.41X	1.80X	1.3375X
Post LIP (35.75 Ma)	1.1X	1.2X	1.1X
Late Aptian-Early Albian rise (45.4 Ma)	1.25X	1.32X	1.25X
Albian Plateau (50.5 Ma)	1.20X	1.25X	1.20X

[1]During consistent preconditions (0-30 Ma) F_{tw} increases 1e9 mol/yr every 2.5 Ma
[2]See Table 3-4 for full list of $^{87}Sr/^{86}Sr$ values for the diagenetic flux adjusting every 2.5 Ma

3.6. Conclusions

This study presents a new, iterative method for modeling the marine Sr cycle in the geologic past. The model capitalizes on the LOWESS FIT 5 of McArthur et al. (2012), which provides constraints and improves estimates for the Sr isotope composition of the input fluxes. The results from a case study focusing on the Late Jurassic-Early Cretaceous time period, show

the importance of estimating the variability in seawater Sr concentrations in the geologic past. Results further indicate that the Sr isotope composition of the total weathering input ($R_{87,tw}$) has varied throughout Earth history on short and long geologic timescales. Model results indicate that $R_{87,tw}$ values should be adjusted every 5 Ma, if not more frequently, at least when examining the Early Cretaceous Sr cycle. The minimum frequency at which $R_{87,tw}$ values should be changed can vary throughout the Phanerozoic depending on the rate of change of the seawater Sr isotope record ($\frac{d}{dt}R_{87,sw}$) and the residence time of Sr during the specific time interval being examined. By attempting to match measured $\frac{d}{dt}R_{87,sw}$ and minimize the step size for prescribed $R_{87,tw}$ values, the iterative model also improves flux estimates. The model output supports estimates for a ~450 µmol/L Sr ocean during the Cretaceous and demonstrates that increases in both hydrothermal and total weathering fluxes during the emplacement of OJMHP are needed to produce the Barremian-Aptian decrease in seawater $^{87}Sr/^{86}Sr$ ratios. Moreover, variations in seawater $^{87}Sr/^{86}Sr$ ratios resulting from perturbations to the weathering system are not limited to changes in the flux but could result from shifts in $R_{87,tw}$ while F_{tw} remains nearly constant. The improved constraints and more representative model of the Sr cycle within the geologic past presented here should enhance coupled modeling of linked key biogeochemical cycles (e.g., Sr with C, S, Fe) allowing for better paleoclimatic and paleoceanographic reconstructions.

CHAPTER 4

COUPLED STRONTIUM-SULFUR CYCLE MODELING AND THE EARLY CRETACEOUS SULFUR ISOTOPE RECORD

4.1 INTRODUCTION

The Early Cretaceous rock record exhibits a ~5‰ negative excursion in the sulfur isotope composition of marine sulfate ($\delta^{34}S_{sulfate}$) that persisted for ~20 Ma (Fig. 2-4) [Paytan et al., 2004]. The mechanism/s responsible for this perturbation are still being debated [Paytan et al., 2004; Wortmann and Chernyavsky, 2007; Wortmann and Paytan, 2012; Gomes et al., 2016; Mills et al., 2013]. There are two major geologic events – the eruption of the Ontong Java Plateau and the deposition of the Aptian South Atlantic Salts – that are thought to be responsible for the perturbation: while enhanced volcanism would increase the input of isotopically light sulfur to the ocean, the deposition of the Aptian South Atlantic Salts would significantly lower sulfate concentrations leading to a decrease in the burial flux of light sulfur as pyrite [Paytan et al., 2004; Wortmann and Chernyavsky, 2007; Wortmann and Paytan, 2012; Gomes et al., 2016; Mills et al., 2013]. The falling limb of the $\delta^{34}S_{sulfate}$ excursion also coincides with the first of several positive carbon isotope excursions associated with widespread deposition of ^{13}C-depleted organic matter – termed oceanic anoxic events (OAEs) – that occur repeatedly throughout the Cretaceous [Leckie et al., 2002; Jenkyns, 2010; Gomes et al., 2016]. A clear understanding of the temporal relationship of the major geologic events during the Early Cretaceous is critical to elucidate the mechanisms that drove this perturbation and maintained the alternate conditions for so long. In Chapter 2 of this thesis I update the temporal framework for the existing Cretaceous

marine barite S isotope ($\delta^{34}S_{barite}$) record in accordance with The Geological Time Scale 2012 (GTS2012 – Gradstein et al., 2012) and review the timing of relevant major geologic and climatic events of the Early Cretaceous. In this chapter a brief summary of the relevant geologic events is provided. This study also expands the Early Cretaceous $\delta^{34}S_{barite}$ record and adds an open, deep ocean pyrite S isotope record.

The S isotope composition of marine sulfate is controlled by the mass and isotope composition of sulfate entering and leaving the ocean. Sulfate is delivered to the ocean via weathering (sulfide oxidation and sulfate mineral dissolution), hydrothermal, and subaerial volcanic inputs. Sulfate is removed from seawater through sulfate deposition (primarily calcium sulfate) and pyrite burial. Importantly, the marine geochemical cycles of S and Sr are linked via common weathering and hydrothermal input fluxes. Therefore, we utilize a coupled Sr-S box model to better constrain the mechanism/s responsible for the Early Cretaceous S isotope excursion [Mills et al., 2013]. There are three guiding principles in using this tool that allow for the identification of parameters to be changed during modeling exercises:

I) If $^{87}Sr/^{86}Sr$ and $\delta^{34}S_{barite}$ shift sympathetically, then the common input terms dominate the perturbation;

II) If $\delta^{34}S_{barite}$ changes but $^{87}Sr/^{86}Sr$ ratios do not, then S output terms likely dominate the perturbation;

III) If $^{87}Sr/^{86}Sr$ changes but $\delta^{34}S_{barite}$ does not, then S output terms balance the perturbation to input terms

The coupling of the Sr-S cycles and the above guidelines are most applicable and useful when the residence times of Sr and S are similar. Fluid inclusion data, Sr/Ca ratios of corals, and geochemical modeling indicate that the Cretaceous ocean was characterized by elevated Sr and

relatively low sulfate concentrations compared to the modern ocean [Lowenstein et al., 2003; Coogan, 2009; Gothmann et al. 2015; Gomes et al., 2016; Chapter 3 this thesis]. Therefore, the residence times of Sr and S were likely to have been more aligned during the Cretaceous than they are currently [Garrels and Lerman, 1981, 1984; Hodell et al., 1989, 1990; Arthur, 2000].

4.2 Geologic Background

4.2.1 Early Cretaceous volcanism

The Early Cretaceous was a time period of significant geological change. These changes include the continued break-up of Pangea (Fig. 4-1) (Seton et al., 2009, 2012), increased continental arc volcanism (McKenzie et al., 2016; Tucker et al., 2016; Wang et al., 2016), elevated mid ocean ridge (MOR) spreading rates (Larson, 1991; Rowley, 2002), deposition of basin-scale evaporites (Chaboureau et al., 2012, 2013), the emplacement of several large igneous provinces (LIPs) (Bryan and Ernst, 2008; Bryan and Ferrari, 2013), and a climatic shift from a cool greenhouse to a warm greenhouse [Frakes et al., 1992; Alley and Frakes, 2003; Boucot et al., 2013]. The emplacement of the Ontong Java-Manihiki-Hikurangi Plateau (OJMHP) – the single most voluminous LIP known – highlights a cluster of LIPs that span the Early- to Mid-Cretaceous (Table 2-3) [Taylor, 2006; Chandler et al., 2012; Bryan and Ferrari, 2013; Hochmuth et al., 2015]. In accordance with the revised LIP definition of Bryan and Ernst (2008), recent tectonic reconstructions of a singular OJMHP mark the termination of its construction with rift initiation near the start of the Cretaceous magnetic superchron (C34n) in the Early Aptian [Taylor, 2006; Chandler et al., 2012; Hochmuth et al., 2015]. This Early Aptian termination of OJMHP construction maintains its temporal connection with OAE 1a, which many authors have suggested was triggered by the emplacement of OJMHP [Leckie et al., 2002; Tejada et al., 2009;

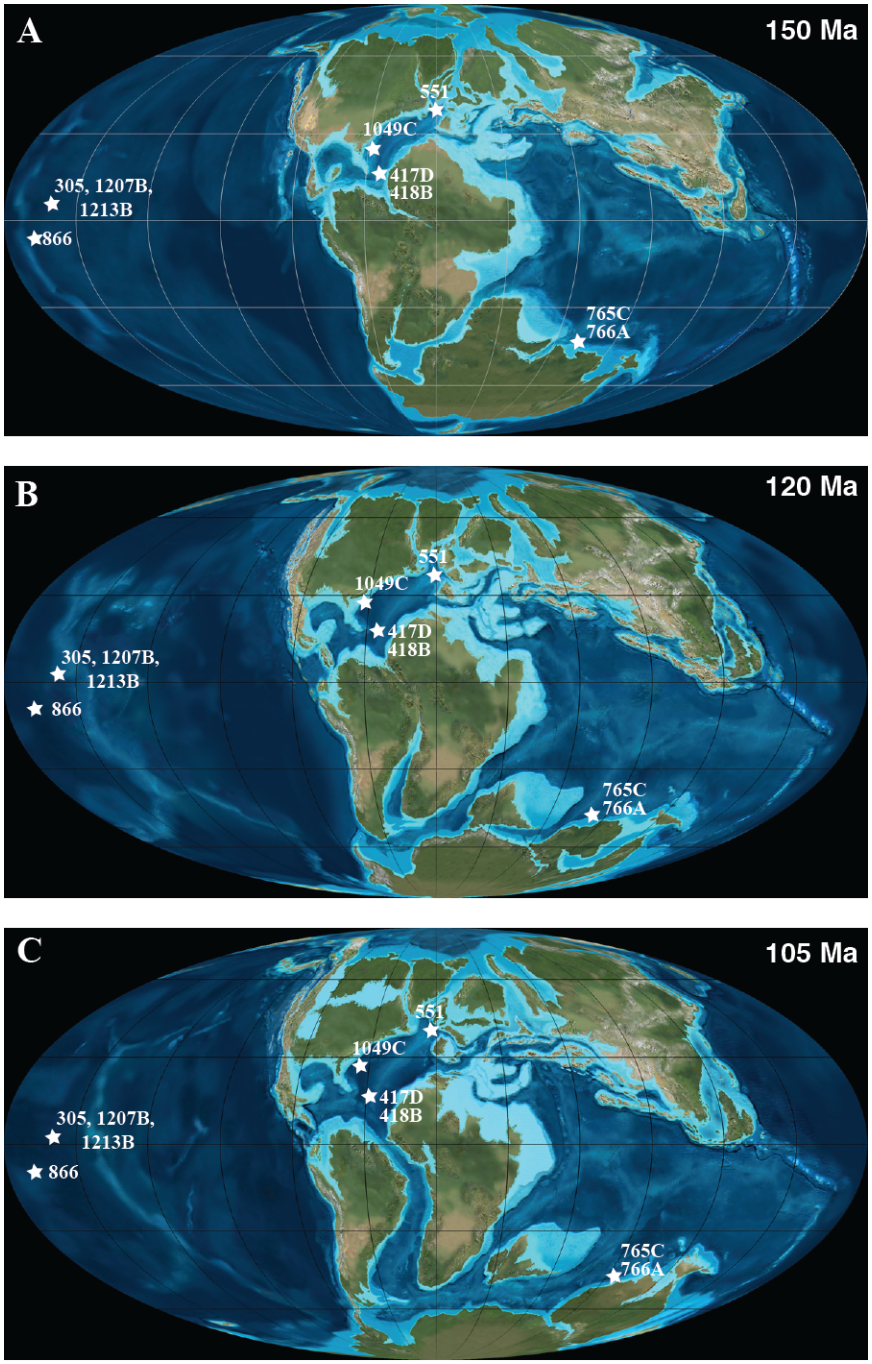

Figure 4-1 Late Jurassic-Early Cretaceous paleogeographic maps and sample locations

Paleogeographic maps by Ron Blakely (cpgeosystems.com) for the **A**) Late Jurassic (150 Ma), **B**) Early Cretaceous (120 Ma), and **C**) Mid-Cretaceous. ODP and DSDP cores sampled in this study and by Paytan et al. (2004) are displayed.

Jenkyns, 2010; Bottini et al., 2012; Gomes et al., 2016]. The start of the Barremian-Aptian decline in marine $^{87}Sr/^{86}Sr$ during the Late Barremian Boreal ammonite zone *Paracrioceras elagans* (lower part Tethyan *Ancyloceras vandenheckei*) supports a Late Barremian or earlier initiation for OJMHP (Table 2-3) [MacArthur et al., 2004, 2007, 2012; Ogg and Hinnov, 2012].

Preceding the emplacement of OJMHP, the Early- to Mid-Cretaceous cluster of LIPs began with two separate, temporally overlapping continental LIPs, the Parana-Etendeka LIP located in South America and western Africa and the Comie-Bunbury LIP located in western Australia and Tibet (Table 2-3) [Frey et al., 1996; Coffin et al., 2002; Gibson et al., 2006; Zhu et al., 2009; Thiede and Vasconcelos, 2010; Janasi et al., 2011; Pinto et al., 2011]. During the later half of emplacement of OJMHP, the first major pulse of the oceanic-continental High Arctic LIP began (Table 2-3) [Buchan and Ernst, 2006; Villeneuve and Williamson, 2006; Nejbert et al., 2011; Shipilov and Karyakin, 2011; Corfu et al., 2013; Dossing et al., 2013; Saltus and Oakey, 2015]. The continued breakup of Gondwana involved one more LIP during the the Early- to Mid-Cretaceous, the Kerguelen Plateau and Rajmahal-Bengal-Sylhet Traps located in the Indian Ocean and eastern India (Table 2-3) [Coffin et al., 2002; Duncan, 2002; Kent et al., 2002; Ray et al., 2005].

4.2.2 Early Cretaceous evaporite deposition

The opening of the South Atlantic Ocean during the Early Cretaceous resulted in a 1-2 km thick gypsum/anhydrite-rich evaporitic sequence deposited within the central segment between Brazil and Africa [Burke and Sengor, 1988; Modica and Brush, 2004; Davison, 2007; Torsvik et al., 2009; Moulin et al., 2010; Chaboureau et al., 2012, 2013]. Initial age estimates broadly placed the South Atlantic salts within the Aptian [Burke and Sengor, 1988; Modica and Brush, 2004; Davison, 2007]. However, revised tectonic and geodynamic models for the opening

of the South Atlantic Ocean, integrated with biostratigraphic and sedimentological records, have constrained the primary accumulation of the South Atlantic salts to the Late Aptian (intra biozone AP4, 116-114 Ma). [Toursvik et al., 2009; Moulin et al., 2010; Chaboureau et al., 2013]. During the Early Aptian the rift controlled lacustrine system of the central segment of the South Atlantic experienced episodic marine flooding that allowed for limited evaporite deposition [Modica and Brush, 2004; Chaboureau et al., 2013].

4.3 SAMPLE LOCATIONS AND AGE MODELS

Samples analyzed in this study were taken from ODP holes spread across the northeast Indian Ocean (ODP Hole 766A) and western Pacific Ocean (ODP Holes 866A, 1207B and 1213B) (Fig. 4-1). Absolute age assignments and error estimates for the GTS2012 Early Cretaceous and placement with uncertainty of FOs and LOs are discussed in Chapter 2 Section 6 (Table 2-5). Ages for marine barite and pyrite samples are presented with their isotope data in Appendix II.

4.3.1 ODP Leg 198 Hole 1213B Shatsky Rise

ODP Hole 1213B is the deepest and southernmost drill hole in a depth transect across the southern high (Tamu Massif) of the Shatsky Rise oceanic plateau located in the northwest Pacific Ocean [Bown, 2005]. Planktonic foraminifers are very rare and poorly preserved in the Early Cretaceous sections of ODP Hole 1213B [SSP Leg 198 IR Ch9, 2002]. Therefore, development of an age model for the Early Cretaceous section of ODP Hole 1213B relies on calcareous nannofossils and lithostratrigraphy. Key biostratigraphic data from Bown (2005) used to determine sedimentation rates and age estimates for the Early Cretaceous section of ODP Hole 1213B are presented in Table 4-1. The top of core 26 provides the first key Early Berriasian

marker species with the local FOs of *Assipetra infracretacea* and *Diadorhombus rectus* (Table 4-1). Considering the high abundance level and consistent presence of *A. infracretacea* along with proximity of the sample containing the FO *D. rectus* it is reasonable to presume that local FO of *A. infracretacea* in ODP Hole 1213B is younger than the global FO noted in the GTS2012 [Anthonissen and Ogg, 2012]. Therefore, sample 26R-1 15 cm (429.25 mbsf) containing the local FO *D. rectus* is assigned an age of 143.14 ± 0.8 Ma in line with its GTS2012 global FO (Table 4-1) [Anthonissen and Ogg, 2012]. The Late Berriasian appearance of *Haqius circumradiatus* in sample 22R-1 58-60 cm (391.68) supports the presence of a slightly expanded Berriasian section in ODP Hole 1213B (Table 4-1) [Bown, 2005; Nannotax3]. While FO *Rucinolithus wisei* may be a reliable marker species for the Late Berriasian in the Tethys, Bown (2005) suggests that the presence of this Tethyan taxa in the Early Cretaceous paleo-Pacific Ocean is not a reliable age constraint for this area. Therefore, the next reliable tie point is taken to be the Early Valanginian FO *Rhagodiscus dekaenelii* in sample 15R-1 34 cm (324.14 mbsf) (Table 4-1) [Bown, 2005]. Using the FO *D. rectus* and *R. dekaenelii* to determine a sedimentation rate and age estimates for Early Cretaceous samples in ODP Hole 1213B results in a Late Valanginain age assignment just below the unconformity at 9R-1 40 cm(266.8 mbsf). The local LO of *Cruciellipsis cuvillieri* and *R. dekaenelii* in sample 9R-1 47 cm (266.87 mbsf) imply an Early Hauterivian age for the base of the unconformity instead of Late Valanginian [Bown, 2005; Anthonissen and Ogg, 2012; Nannotax3]. Therefore, a second sedimentation rate was determined for the Early Cretaceous section of Hole 1213B using FO *D. rectus* and LO *R. dekaenelii* with an age assignment of 133.3 ± 0.65 Ma (Table 4-1). Both sedimentation rates were used to calculate ages for samples below the unconformity at 9R-1 40 cm in Hole 1213B. The average along with standard deviation (n=2) was used as the new

Table 4-1. GTS2012 age assignments of select key biostratrigraphic data for Early Cretaceous from ODP Hole 1213B. Data from Bown (2005). The age assignment location (listed below sample depth) is the midpoint between the sample containing FO or LO and the next sample analyzed where the organism is absent.

Sample	mbsf	Biostratigraphic data	Age Assignment	Comments
8R-1 3 cm	256.83	FO *Eprolithus floralis*		Post OAE 1a Early Aptian
9R-1 17-18 cm	266.57 (266.685 ± 0.115)	FO *Hayesites irregularis* FO *Flabellites oblongus*	126.4 ± 0.5	Midpoint from sample to top of unconformity
9R-1 47 cm	266.87	LO *Cruciellipsis cuvillieri*		Early Hauterivian
9R-1 47 cm	266.87 (266.835 ± 0.035)	LO *Rhagodiscus dekaenelii*	133.3 ± 0.65	Early Hauterivian Nannotax3 133.09 Ma
14R-1 148	315.58	FO *Eiffellithus windii*		Early Valanginian GTS2012 137.55 Ma
15R-1 34 cm	324.14 (328.83 ± 4.69)	FO *Rhagodiscus dekaenelii*	137.65 ± 0.75	abundance level few + consistent presence; GTS2012 Early Valanginian 137.68 Ma
22R-1 58-60 cm	391.68	FO *Haqius circumradiatus*		Nannotax3 Late Berriasian 141.93 Ma
26R-1 15 cm	429.25 (429.26 ± 0.01)	FO *Diadorhombus rectus*	143.14 ± 0.8	Abundance level rare; Early Berriasian GTS2012 143.14 Ma
26R1 17-18 cm	429.275	FO *Assipetra infracretacea*		Abundance level common + consistent presence; Early Berriasian GTS2012 143.86 Ma

assigned age with error estimate for each of these samples.

Most of the Hauterivian and Barremian are thought to be missing in the unconformity at 9R-1 40 cm in Hole 1213B, which is confirmed by the presence of organic carbon rich layers along with gamma ray and uranium logs identifying OAE 1a in core 8 [SSP Leg 198 Ch 9, 2002; Bown, 2005; Marsaglia, 2005]. This is further supported by the local FO of the Late Barremian taxa *Hayasites irregularis* and *Flabellites oblongus* in sample 9R-1 17-18 cm (266.57 mbsf) [Bown, 2005]. The samples from within the organic-rich interval in core 8 were barren of calcareous nannofossils [Bown, 2005]. The next key biostratigraphic datum is the post OAE 1a FO of *Eprolithus floralis* in sample 8R-1 3 cm (256.83) [Bown, 2005]. Sedimentation rates before, during and after the black shale deposition associated with OAE 1a are likely to be significantly different preventing the use of FOs *H. irregularis* and *E. floralis* to determine a

constant sedimentation rate for this interval. Downhole measurements of gamma radiation, density, and porosity indicate the start of the OAE 1a black shale to be at 259.9 ± 0.1 mbsf in Hole 1213B [SSP Leg 198 Ch 9, 2002]. The FO *H. irregularis* and the start of OAE 1a (125.4 ± 0.4 Ma) are used to calculate a Late Barremian-Early Aptian sedimentation rate and ages for samples in the top of core 9 above the unconformity.

4.3.2 ODP Leg 198 Hole 1207B Shatsky Rise

ODP Hole 1207B is located near the center of the sediment cap on the northern high (Shirshov Massif) of the Shatsky Rise oceanic plateau located in the northwest Pacific Ocean [Bown, 2005]. Limited planktonic foraminifera data along with calcareous nannofossil biostratigraphy and chemolithostratigraphy (Table 4-2) are used determine sedimentation rates and age estimates for the Early Cretaceous section of ODP Hole 1207B [SSP Leg 198 IR Ch3, 2002; Bown, 2005; Dumitrescu and Brassel, 2006]. The oldest material recovered and analyzed for calcareous nannofossils in ODP Hole 1207B (49R-2 24 cm) contains *Assipetra terebrodentarius* synonym *Rucinolithus terebrodentarius*, which has a global FO in the Late Hauterivian (131.94 Ma) [Bown, 2005; Anthonissen and Ogg, 2012]. The oldest material analyzed for planktonic foraminifera (47R-3 79-81 cm) contained *Hedbergella similis* and *Hedbergella sigali* indicating an Early Barremian age [SSP Leg 198 IR Ch3, 2002; Anthonissen and Ogg, 2012; Ogg and Hinnov, 2012]. However, Bown (2005) focused on the absence of *Lithraphidites bollii* and *Calcicalathina oblongata* whose global LO occur within the Late Hauterivian and Early Barremian, respectively, when assigning cores 49-45 of Hole 1207B to the Barremian calcareous nannofossil zone NC5d-NC5e [Anthonissen and Ogg, 2012]. Both the presence and absence of organisms within these deepest samples from Hole 1207B are taken in consideration for the revised age model. This results in assigning sample 49R-2 24 cm an age

that lies in between the FO *A. terebrodentarius* synonym *R. terebrodentarius* and the LO *C. oblongata* (Table 4-2) [Anthonissen and Ogg, 2012]. The limited core recovery in Hole 1207B results in the local FO of *H. irregularis* occurring much closer to the start of the Early Aptian positive carbon isotope excursion (CIE) associated with OAE 1a than would be expected (Table 4-2) [Bown, 2005; Dumitrescu and Brassel, 2006]. Therefore, the start of the positive CIE at 44R-1 101.5 cm along with the FO *A. terebrodentarius* synonym *R. terebrodentarius* and the absence of *C. oblongata* are used to determine a sedimentation rate for the Late Hauterivian/Early Barremian to Early Aptian section of Hole 1207B (Table 4-2). This sedimentation rate results in sample 47R-3 79-81 cm containing the local FO *Hedbergella similis* and *Hedbergella sigali* having an age estimate of 129.05 ± 0.86 Ma. While this calculated age is considerably younger than the 130.37 Ma assigned the FO *H. similis* in GTS2012 it is still older

Table 4-2. GTS2012 age assignments of select key Early Cretaceous biostratigraphic and chemolithostratigraphic data from ODP Hole 1207B. Data from SSP Leg 198 (2002a), Bown (2005) and Dumitrescu and Brassel (2006).

Sample	mbsf	Biostratigraphic Chemolithostratigraphic data	Age Assignment	Comments
40R-CC 15-17 cm	526.66	*Globigerinelloides barri*, *G. blowi*, *G. aptiense* indicate *G. algerianus* zone	120.55 ± 1.62	GTS2012 *G. algerianus* zone 122.17-118.93 Ma
43R-2 12 cm	557.02	FO *Eprolithus floralis*		Abundance level few GTS2012 123.88 Ma
44R-1 60 cm	565.60	End of organic carbon rich black shale (Selli Level)	124.24 ± 0.45	Early part of C7 of CIE; Selli Level duration 1.11 ± 0.11 Ma from Malinverno et al., 2010
44R-1 101.5 cm	566.015	Start of CIE (C4) associated with OAE 1a	125.4 ± 0.4	
44R-2 40 cm	566.90	FO *Hayesites irregularis*		GTS2012 just below BAB
47R-3 79-81 cm	594.60	FO *Hedbergella similis*		Oldest sample analyzed for planktonic foraminifera; FO *H. similis* 130.37 Ma GTS2012
49R-2 24 cm	614.94	FO *Assipetra terebrodentarius* syn *Rucinolithus terebrodentarius* Absent *Lithraphidites bollii* Absent *Calcicalathina oblongata*	131.0 ± 0.9	Oldest material recovered and analyzed for calcareous nannofossils; FO *R. terebrodentarius* 131.94 Ma GTS2012; LO *C. oblongata* 130.08 Ma GTS2012

than the next foraminifera marker event listed in GTS2012 (FO *Globigerinelloides blowi* 128.73 Ma) [Anthonissen and Ogg, 2012]. Considering the limited core recovery in Hole 1207B, the sampling interval for biostratigraphic data, and the absence of *L. bollii* and *C. oblongata* throughout the lower samples it is felt that the calculated age estimate for sample 47R-3 79-81 is reasonable. Therefore, the constant sedimentation rate determined using the start of the positive CIE associated with OAE 1a and the intermediate age assignment for sample 49R-2 24 cm is used the calculate age estimates throughout this interval.

Correlation of the Shatsky Rise C isotope stratigraphy with Tethyan records places the end of the Shatsky Rise record in the early part of C7 of the CIE indicating that the recovered organic carbon rich black shale interval in Hole 1207B is representative of the full Selli Level and part of C7 [Menegatti et al., 1998; Dumitrescu and Brassel, 2006]. Using the floating astrochronology determined by Malinverno et al. (2010) for the OAE 1a interval the top of the recovered black shale in Hole 1207B (44R-1 60 cm) is assigned an age of 124.24 ± 0.45 Ma (Table 4-2). The limited recovery within Hole 1207B placed the local FO of *Eprolithus floralis* ~8.5 m above the end of the OAE 1a black shale raising concern about its direct correlation with the global FO at 123.88 Ma as it would produce a sedimentation rate more than double previous estimates [SSP Leg 198 Ch3, 2002; Bown, 2005; Dumitrescu and Brassel, 2006; Anthonissen and Ogg, 2012]. The next reliable biostratigraphic tie point comes from the presence of planktonic foraminifera *Globigerinelloides barri*, *G. blowi*, and *G. aptiense* in the core catcher of core 40 indicating the *G. algerianus* foraminifera zone (Table 4-2) [SSP Leg 198 Ch3, 2002; Anthonissen and Ogg, 2012]. The end of the OAE 1a black shale and the foraminifera zone *G. algerianus* are used to determine a sedimentation rate for the post-OAE 1a Early to Late Aptian

interval of Hole 1207B. This sedimentation rate is used to calculate ages for samples in core 44 above the OAE 1a black shale through core 40.

4.3.3 ODP Leg 123 Hole 766A Exmouth Plateau-Gascoyne Abyssal Plain

Samples selected from ODP Hole 766A for this study fall within the constraints of the age model developed previously in Chapter 2 section 6.1 for updating the temporal framework of the Paytan et al. (2004) seawater sulfate isotope record. Again ages for samples from ODP Hole 766A from this study are presented with their isotope data in Appendix II.

4.3.4 ODP Leg 143 Hole 866A Resolution Guyot

ODP Hole 866A is a shallow water drill hole located on the northern rim of Resolution Guyot in the western Mid-Pacific Mountains [Arnoud et al., 1995]. Determining a revised age profile for Resolution Guyot ODP Hole 866A in line with GTS2012 requires the use of magnetostratigraphy (Fig. 4-2), benthic foraminifera, stable carbon isotope stratigraphy (Fig. 4-3), strontium isotope stratigraphy (Fig. 4-4), lithostratigraphy, and sequence stratigraphy [Arnaud et al., 1995; Arnaud-Vanneau and Sliter, 1995; Jenkyns et al., 1995; Tarduno et al., 1995; Menegatti et al., 1998; Malinverno et al., 2010; McArthur et al., 2012; Ogg, 2012; Ogg and Hinnov, 2012; Mills et al., 2016]. The key data points used for this revised age profile are listed in Table 4-3 with their new age assignments. The transition from the volcanic basement of Resolution Guyot to the start of carbonate sedimentation occurs in the top section of core 171 at 1619.3 mbsf. Initial facies evolution and sequence stratigraphy by Arnaud et al. (1995) identified the first 220 m of sediment as a single lithologic unit consisting of oolitic and oncolytic limestones with significant dolomitization. This section ends in core 148 at 1400.35 mbsf with a change from limestone to mudstone that contains algal mats and stromatolites. This change has been identified as a major sequence boundary that is thought to correspond to an

emersion level [Arnaud et al., 1995]. Arnaud-Vanneau and Sliter (1995) have assigned a Hauterivian age to this section based on benthic foraminifera. The consistent presence of *Vercorsella wintereri* and *Valvulineria* sp. from the top of core 171 to core 148 along with *Decussolocullina mirceai* in cores 171-167 is taken to indicate an Early Hauterivian age for this entire section [Arnaud-Vanneau and Sliter, 1995]. The assignment of an Early Hauterivian age for this entire section is further supported by correlation of the massive sequence boundary in core 148 to the megacycle regression of Ha5 [Ogg and Hinnov, 2012; Arnaud et al., 1995 Figure 5]. This places the entire section – 220 m of carbonate – precipitating within ≤2 Ma from ~134-132 Ma. Such a large amount of carbonate deposition during the short time frame of the Early Hauterivian is consistent with other massive carbonate sections in the Tethys region at this time (Swiss Alps Alvier region 500 m of carbonate in ≤1 Ma and Vocontian Basin 2 km of limestone-marl in 5 Ma) [van de Schootbrugge et al., 2000].

On the GTS2012 the Ha5 megacycle regression occurs within M7r of the magnetostratographic M-series. Tarduno et al. (1995) identified 10 polarity zones (5 pairs of normal and reversed) based on 78 characteristic magnetization measurements in the lower 600 meters of sediment (Fig. 4-2). Tarduno et al. (1995) identifies a change from reversed to normal polarity (J-/J+) at 1396 mbsf, just a few meters above the sequence boundary in the lower part of core 148 and the end of lithologic unit VIII (see Figure 4 of Arnaud et al., 1995). Arnaud et al. (1995) characterize the lithologic units following this massive sequence boundary as representative of shallow subtidal and supratidal environments. Within this section (cores 148-103; ~1400-975 mbsf) Arnaud et al. (1995) identified algal-microbial mats, paleosoils, desiccation cracks, subaerial exposure and sabkha parasequences more than once. Considering these features, the magnitude of the Ha5 megacycle regression and identification of the sequence

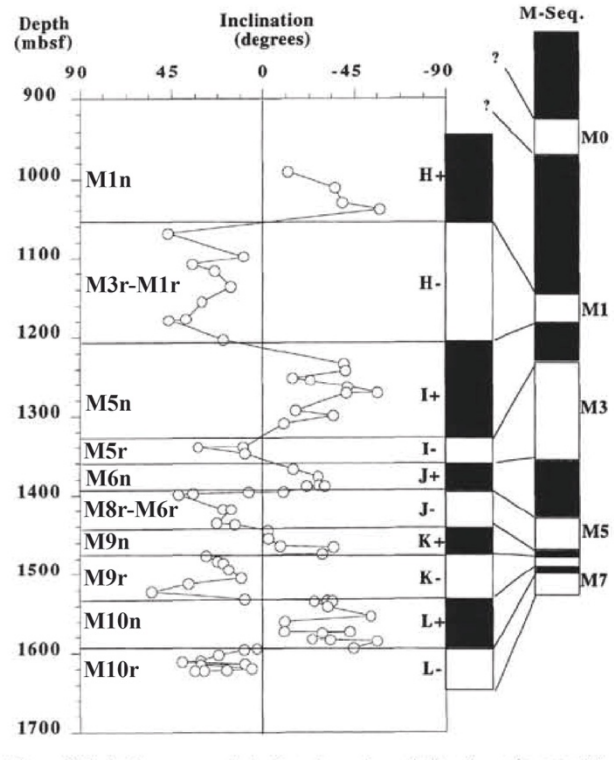

Figure 4-2 Magnetostratigraphy ODP Hole 866A

Magnetostratigraphic data from Tarduno et al. (1995) for ODP Hole 866A with initial M-series correlation (right side) and revised alignment with GTS2012 (left side).

boundary as an emersion level in Hole 866A it appears reasonable to assume that there was erosion of sediment and, or a gap in sedimentation producing a minor unconformity. Needing to place this initial ~220 m of carbonate within the Early Hauterivian below M7r it becomes reasonable to correlate the L-/L+ polarity transition at 1594.5 mbsf as the M10r-M10n transition of GTS2012, which is identified as the Hauterivian-Valanginian boundary with an age of 133.88 ± 0.6 Ma (Fig. 4-2 and Table 4-3) [Tarduno et al., 1995; Ogg, 2012]. This leads to K-/K+ corresponding to M9r and M9n, with the end of K+ (M9n) at 1441.4 mbsf representing an age of 133.05 ± 0.6 Ma (Fig. 4-2 and Table 4-3) [Tarduno et al., 1995; Ogg, 2012]. Sedimentation rates

Table 4-3. GTS2012 age assignments of select key magnetostratigraphic, chemostratigraphic, and lithologic data for Early Cretaceous samples from ODP Hole 866A

mbsf	data	Age Assignment	notes
130 ± 15	Benthic foraminifera stratigraphy	104.0 ± 0.5	Arnaud-Vanneau&Sliter, 1995 estimate with uncertainty Late Albian in core 15R-CC
343.23	$^{87/86}$Sr = 0.707395 (normalized 0.707383)	109.4 ± 0.7	Albian-Cenomanian Plateau 0.707420±15 start 108.70 Ma; 866A before data plateaus
434.43	$^{87/86}$Sr = 0.707229 (normalized 0.707217)	114.15 ± 0.55	Late Aptian min 0.707203 115.25-114.90 Ma GTS2012; 866A min on L. Aptian/E. Albian rise
599.3	$\delta^{13}C$ = 2.36‰ Mills et al. (2013)	122.0 ± 0.5	End of C8 end of positive CIE associated with OAE1a; Menegatti et al., 1998 C8 ends within planktonic foraminifera G. algerianus
	Planktonic foraminifera zone boundary G. ferreolensis/G. algerianus	122.17 ± 0.4	GTS2012
676.55	Lithologic boundary unit V to unit IV, SB17, and change from open marine to restricted Arnoud et al., 1995	Top 123.15 ± 0.425 Base 124.65 ± 0.425	suspected unconformity; suspect end of C5 missing C6 and most of C7 (1.5 of 1.94 Ma Malinverno et al., 2010)
819 ± 2		125.4 ± 0.4	Start of positive CIE (C4 of Menegatti et al., 1998) associated with OAE1a/start of Selli Level equivalent
821.6	$\delta^{13}C$ = -0.59‰ Mills et al. (2013)		C3 of Menegatti et al., 1998; peak negative excursion prior to start OAE1a
1054.2	H-/H+ magenetostratigraphic reversal Tarduno et al., 1995	128.32 ± 0.5	Assigned M3r-M1r/M1n Late Barremian
1218.7	I+/H- magenetostratigraphic reversal Tarduno et al., 1995	130.6 ± 0.5	Assigned M5n/M3r-M1r Early Barremian
1240 ± 2.5		130.8 ± 0.5	Hauterivian-Barremian boundary
1400.35	SB5 Arnaud et al., 1995 equivalent to Ha5 R/T megacycles GTS2012		Ha5 occurs within M7r
1441.4	K+/J- magnetostratigraphic reversal Tarduno et al., 1995	133.05 ± 0.6	Assigned M9n-M8r boundary
1475.3	K-/K+ magnetostratigraphic reversal Tarduno et al., 1995	133.30 ± 0.6	Assigned M9r-M9n boundary
1532.6	L+/K- magnetostratigraphic reversal Tarduno et al., 1995	133.58 ± 0.6	Assigned M10n-M9r boundary
1594.5	L-/L+ magnetostratigraphic reversal Tarduno et al., 1995	133.88 ± 0.6	Assigned M10r-M10n Valanginian-Hauterivian boundary

within this Early Hauterivian section are extremely high. The calculated individual sedimentation rates for M10n and M9r in Hole 866A are nearly equal leading to a singular sedimentation rate spanning both magnetic intervals being used to calculate ages for this section of Hole 866A. This sedimentation rate is also used to determine ages for older samples extending backwards from

the base of M10n to the volcanic basement. While there appears to be a significant reduction in the sedimentation rate during the M9n magnetic interval in Hole 866A compared to the section below, it is uncertain if the lower sedimentation rate is continued upward until the unconformity or if higher sedimentation rates returned. With the Ha5 megacycle regression occurring within M7r the J- polarity zone of Tarduno et al. (1995) is thought to correspond to M8r-M6r with M8n, M7 and parts of both M8r and M6r missing (Fig. 4-2) [Ogg and Hinnov, 2012]. Therefore, the unconformity at 1400.35 mbsf must be older than the top of M8r (132.80 Ma) to maintain the continuous magnetic reversal state with M6r. Extending the lower sedimentation rate for the M9n interval up to the unconformity does not meet this constraint. Returning to the higher sedimentation rate of the M10n-M9r interval along with using the intermediate sedimentation rate for the M10n-M9n interval to determine ages for samples from the base of M8r up to the unconformity does meet the age constraint (>132.80 Ma). Therefore, both sedimentation rates were used to calculate ages for samples in the interval between the base of M8r and the unconformity.

Following the alignment of the J- polarity zone corresponding to M8r-M6r and assuming there were no other major gaps in sedimentation, this would result in the large polarity zone of H- (1218.7-1054.2 mbsf) corresponding to M3r, which lasts 1.49 Ma and spans Early to Late Barremian in the GTS2012 (Fig. 4-2) [Tarduno et al., 1995; Ogg, 2012]. Unfortunately, the magnetostratigraphic record from Hole 866A ends at ~1000 mbsf during a normal polarity event. The next reliable major tie point comes from $\delta^{13}C$ stratigraphy identifying the start of the positive carbon isotope excursion (CIE) associated with OAE1a (Fig. 4-3 and Table 4-3) [Menegatti et al., 1998]. The truncation of the magnetostratigraphic record well before the $\delta^{13}C$ stratigraphy tie point in combination with the lithology and sedimentilogical interpretations of

Arnaud et al. (1995) leaves some uncertainty in the precise correlation of the H+ polarity zone. The identification of subaerial exposures along with paleosoils, desiccation cracks, and sabkha parasequences throughout this section (~1400-950 mbsf) results in a high probability for the presence of minor unconformities [Arnaud et al, 1995]. While there is reasonable confidence in correlating the I+/H- polarity transition to M5n/M3r it is possible that the H- polarity zone represents M3r through to M1r with M3n completely missing instead of just M3r. Therefore, the H+ polarity zone could represent M3n, M1n, or M3n and M1n with M1r missing. Again the truncation of the magnetostratigraphic record precludes a definitive assignment. The lithostratigraphy and facies analysis suggesting a highly restricted environment with numerous subaerial exposures through this section (1200-1000 mbsf) support the preferred assignment of the H- polarity zone representing M3r-M1r with M3n missing.

Following this revised magnetostratigraphic correlation for Hole 866A the M5n/M3r-M1r (I+/H-) boundary at 1218.7 mbsf was assigned an age of 130.6 ± 0.5 Ma and the M3r-M1r/M1n (H-/H+) boundary at 1054.2 mbsf was assigned an age of 128.32 ± 0.5 Ma (Fig. 4-2 and Table 4-3). The placement of M3r in Hole 866A allowed for an estimation of the Hauterivian-Barremian boundary at 1240 ± 2.5 mbsf (130.8 ± 0.5 Ma GTS2012). As noted above the next major reliable tie point comes from the $\delta^{13}C$ stratigraphy identifying the positive CIE associated with OAE1a. Using the $\delta^{13}C$ stratigraphy of Mills et al., (2013) the peak of the negative CIE that precedes the positive CIE associated with OAE1a (labeled C3 by Menegatti et al. (1998)) occurs at 821.6 mbsf (Fig. 4-3 and Table 4-3). The Jenkyns (1995) $\delta^{13}C$ stratigraphy, however, has the peak of the negative CIE preceding the positive CIE associated with OAE1a occurring at 841.7 mbsf. While this difference is notable it does not alter the age profile noticeably or the interpretations presented in Mills et al. (2013) and this study. Therefore, to be consistent with the

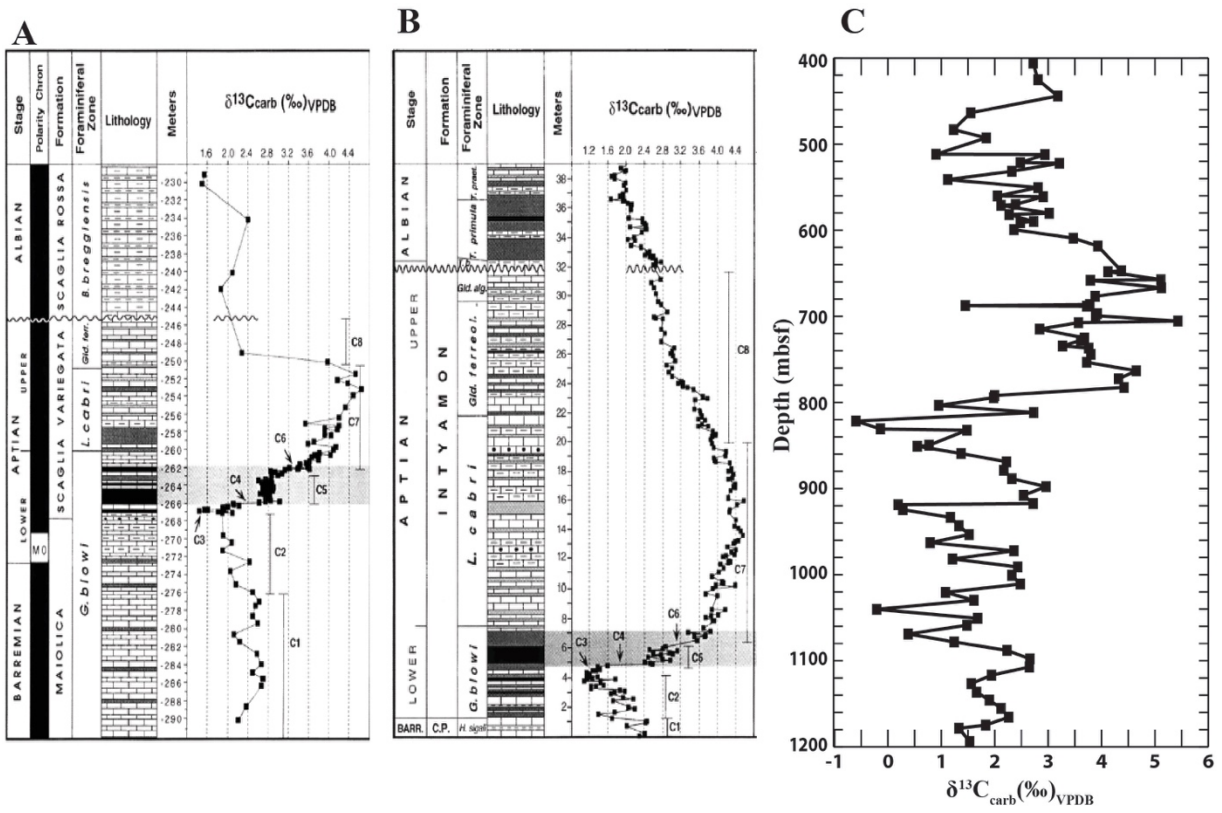

Figure 4-3 $\delta^{13}C$ stratigraphy correlation for OAE1a at ODP Hole 866A

Lithologic logs and $\delta^{13}C_{carb}$ for the Cismon core (A) and Rotter Sattel section (B) from Menegatti et al. (1998). Highlighted portion indicates the Selli Level black shales. C) $\delta^{13}C_{carb}$ versus depth for ODP Hole 866A from Mills et al. (2013).

corresponding S isotope data the $\delta^{13}C$ stratigraphy of Mills et al. (2013) is used instead of that from Jenkyns (1995). Correlation of the $\delta^{13}C$ stratigraphy from Mills et al. (2013) with that of Menegatti et al. (1998) results in assigning the start of the positive CIE associated with OAE1a (labeled C4) in Hole 866A to a depth of 819 ± 2 mbsf with an age of 125.4 ± 0.4 Ma (Fig. 4-3 and Table 4-3). As mentioned above the lithologic units during the Barremian are thought to represent shallow subtidal and supratidal environments containing algal-microbial mats,

paleosoils, desiccation cracks, subaerial exposure and sabkha parasequences [Arnaud et al., 1995]. While such sedimentalogical evidence suggests that sedimentation was not likely to be constant the limited tie points within this section leave no option but to assume constant sedimentation in order to assign ages. Therefore, four different constant sedimentation rates are calculated for the Barremian section of Hole 866A. The combination of age assigned tie points for calculating Barremian sedimentation rates are (S1) the base to the top of M3r-M1r, (S2) the top of M3r-M1r to the start of the Early Aptian positive CIE, (S3) the base of M3r-M1r to the start of the Early Aptian positive CIE, and (S4) the estimated Hauterivian-Barremian boundary to the start of the Early Aptian positive CIE. The average and standard deviation of the ages determined using S1, S3, and S4 (n=3) is the assigned age with 1 sigma error for CAS $\delta^{34}S$, carbonate $\delta^{13}C$ (Mills et al., 2013), and Sr isotope (Jenkyns et al., 1995) samples between 1218.7-1054.2 mbsf. Similarly, the average and standard deviation of the ages determined using S2, S3, and S4 (n=3) is the assigned age with 1 sigma error for CAS $\delta^{34}S$, carbonate $\delta^{13}C$ (Mills et al., 2016), and Sr isotope (Jenkyns et al., 1995) samples between 1054.2-819 mbsf.

Within the section of Hole 866A containing the Early Aptian positive CIE there is a distinct lithologic change from oolitic grainstone to cyclic packstone/wackstone that has been identified as a potential sequence boundary (676.55 mbsf, core 73R-1 75 cm) [Unit V-IV and SB17 of Arnaud et al., 1995 see Figure 4]. Considering that Arnaud et al. (1995) identify this boundary as a possible change from open marine conditions to shallow subtidal restricted marine conditions it is proposed to represent a minor unconformity. Comparing the $\delta^{13}C$ stratigraphy of Mills et al., (2013) to that of Menegatti et al., (1998) it is believed that the unconformity at 676.55 mbsf occurs at the end of the C5 stage (Fig. 4-3). Orbital tuning of the Early Aptian positive CIE by Malinverno et al., (2010) estimates the duration of the C4 and C5 stages to be

749 ± 80 ka. Therefore, the base of the unconformity at 676.55 mbsf is assigned an age of 124.65 ± 0.425 Ma (Table 4-3). An additional 25 ka is added to the uncertainty from the radioisotope dating to account for the uncertainty from the cyclostratigraphy, correlation of the $\delta^{13}C$ stratigraphy and placement of the unconformity. A constant sedimentation rate calculated from the age assignments for the base of the unconformity at 676.55 mbsf and the start of the Early Aptian positive CIE is used to determine ages for samples from this interval (819-676.55 mbsf).

Continuing the correlation of the $\delta^{13}C$ stratigraphy from Mills et al., (2013) with that of Menegatti et al. (1998) the unconformity at 676.55 mbsf is believed to have removed stage C6 stage and most of stage C7 of the Early Aptian positive CIE (Fig. 4-3). According to the astrochronology time scale for the Early Aptian CIE by Malinverno et al. (2010) stage C7 is the longest at 1.59 ± 0.07 Ma. It is estimated that approximately three fourths of stage C7 is missing. Therefore, the top of the unconformity at 676.55 mbsf is assigned an age of 123.15 ± 0.425 Ma (Table 4-3). The end of the Early Aptian positive CIE associated with OAE1a in Hole 866A is believed to occur at 599.3 mbsf on the $\delta^{13}C$ stratigraphy from Mills et al. (2013) (Fig. 4-3). Compared to the Roter Sattel Early Aptian section the C8 stage of the positive CIE is quite compressed in Hole 866A [Menegatti et al., 1998]. According to Menegatti et al. (1998) the positive CIE associated with OAE1a ends within the planktonic foraminifera zone *Globigerinelloides algerianus*. The boundary between planktonic foraminifera zones *G. ferreolensis* and *G. algerianus* occurs at 122.17 ± 0.4 Ma according to GTS2012. Therefore, the end of the positive CIE in Hole 866A at 599.3 mbsf is assigned an age of 122.0 ± 0.5 Ma (Table 4-3). A constant sedimentation rate calculated from the age assignments for the end of the Early

Aptian positive CIE associated with OAE1a and the top of the unconformity at 676.55 mbsf is used to determine ages for samples from this interval (676.55-599.3 mbsf).

Core recovery in the upper 550 m of Hole 866A was extremely poor, rarely getting above 10% recovery [Initial Reports, Leg 143 Chapter 7]. Hence, the limited benthic foraminifera data for this section of the core are not very diagnostic [Arnaud-Vanneau and Sliter, 1995]. Considering that the shape of the Sr isotope stratigraphy from Hole 866A plotted against depth matches very well with the global Sr isotope curve and the values from Hole 866A are reasonably within error of the global Sr isotope record the LOWESS Fit 5 for the global Sr isotope record from GTS2012 was used to provide age constraints for the Late Aptian and Middle Albian (Fig. 4-4) [Jenkyns et al., 1995; McArthur et al., 2012]. The global Sr isotope record has a minimum during the Late Aptian with a $^{87/86}$Sr value of 0.707203 [McArthur et al., 2012]. Using the LOWESS Fit 5 the age span of this minimum is estimated to be 115.25-114.90 Ma. In Hole 866A the $^{87/86}$Sr minimum value of 0.707229 occurs at 434.43 mbsf. Taking into account the surrounding samples and their $^{87/86}$Sr values it is postulated that the sample at 434.43 mbsf would be located above the global minimum along the Late Aptian-Albian rising arm of the Sr isotope record. Therefore, this sample is assigned an age of 114.15 ± 0.55 Ma (Table 4-3). Using age assignments for the Late Aptian Sr isotope minimum in Hole 866A and the end of the positive CIE associated with OAE1a a constant sedimentation rate for the Late Aptian is calculated. This sedimentation rate is used to determine age estimates for samples between 599.3-434.43 mbsf.

The Late Aptian-Albian rise in the global Sr isotope record reaches a plateau in the Middle Albian that continues through most of the Cenomanian [McArthur et al., 2012]. This plateau with a $^{87/86}$Sr value of 0.707420 ± 0.000015 is estimated to begin at 108.70 Ma according

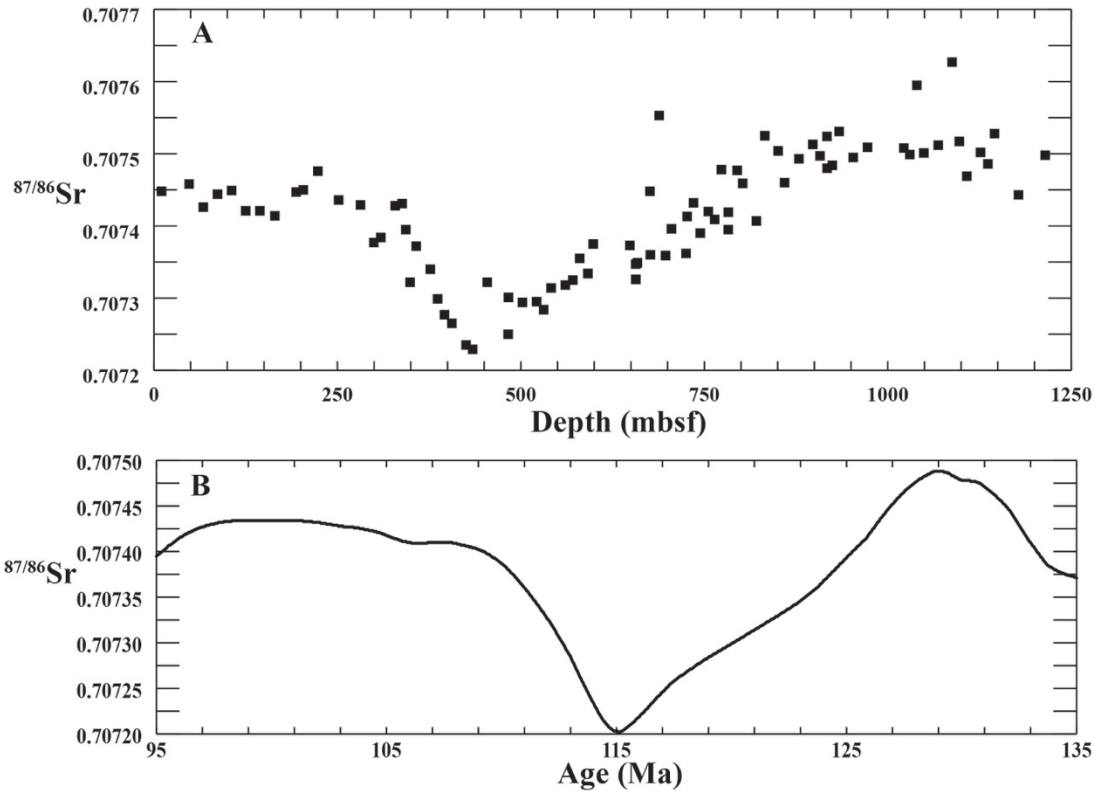

Figure 4-4 Sr isotope stratigraphy correlation ODP Hole 866A

Sr isotope stratigraphy for (**A**) ODP Hole 866A from Jenkyns et al. (1995) and (**B**) the GTS2012 LOWESS FIT 5 from McArthur (2012).

to the LOWESS Fit 5 [McArthur et al., 2012]. In Hole 866A the $^{87/86}$Sr value of 0.707395 at 343.23 mbsf is thought to be representative of approaching the start of the Albian-Cenomanian to the LOWESS Fit 5 [McArthur et al., 2012]. In Hole 866A the $^{87/86}$Sr value of 0.707395 at 343.23 mbsf is thought to be representative of approaching the start of the Albian-Cenomanian Sr isotope plateau. Therefore, this sample is assigned an age of 109.4 ± 0.7 Ma (Table 4-3). The age assignments near the beginning and end of the Late Aptian-Albian rise in the global Sr

isotope record are used to calculate a constant sedimentation rate and ages across this section (434.43-343.23 mbsf).

Based on the limited benthic foraminifera data Arnaud-Vanneau and Sliter (1995) loosely identify the Late Albian within the core catcher sample from core 15 (125-134.7 mbsf) through the remainder of the hole. With considerable uncertainty a Late Albian tie point is defined at 130 ± 15 mbsf with an age of 104.0 ± 0.5 Ma in order to provide additional constraint for the dating of the remainder of the drill hole. The Middle Albian Sr isotope tie point and this Late Albian tie point are used to calculate a constant sedimentation rate that is used to determine age assignments for the remaining ~340 m of Hole 866A. Continuation of the sedimentation rate for the Late Aptian-Middle Albian through the remainder of the core would result in it extending into the Early Coniacian. The limited sampling and benthic foraminifera in the top of the core suggest that it might have reached or crossed the Albian-Cenomanian boundary [Arnaud-Vanneau and Sliter, 1995]. Therefore, extension of 866A well into the Late Cretaceous is considered unreasonable and age calculations from the extension of the sedimentation rate used for the Late-Aptian-Albain are not considered.

4.4 Methods

4.4.1 Barite Extraction

Marine barite was extracted from ODP sediment samples using a gravimetric heavy liquid (lithium heteropolytungstates – LST) procedure developed by Turchyn (2005). Powdered samples (20-30 g) were initially decarbonated with 4 N acetic acid. The remaining insoluble residue was dried and recrushed. Approximately 4 mL of loosely packed powdered insoluble residue was suspended in a LST solution in a 15 mL polypropylene centrifuge tube to separate

the barite from clays. The cleaned heavy residue was reacted with warmed (60°C) sodium hypochlorite for 5 days to oxidize remaining organic matter. Heated (80°C) sodium hydroxide (1N) was then used for 8 hours to remove any opal and base-soluble organics. Any remaining acid soluble minerals in the heavy residue were dissolved with 6 N HCl. Finally transition metal oxyhydroxides were removed from the barite using 0.02 M hydroxylamine hydrochloride in a 10% acetic acid solution. SEM analysis of the remaining heavy residue identified both marine and diagenetic barite in most samples examined along with some heavy metal oxides and silicates (Fig. 4-5). Marine barite was separated from diagenetic barite based on the size difference using 8 μm hole filter papers and recollected with 0.45 μm filter paper. The samples were disaggregated using an ultrasonic bath prior to the fine filtration step separating marine and diagentic barite.

4.4.2 Pyrite S Extraction

Pyrite sulfur was extracted by the chromium reduction method (Canfield et al., 1986) from powdered insoluble residue produced during the acidification step of the barite extraction procedure. Samples were reacted in an O_2-purged vessel for 2 hours in a boiling 6N HCl solution with 1M $CrCl_3$. H_2S released by the reaction was driven by an N_2 carrier gas into a trap vessel with a 10% NH_4OH solution with 3% $AgNO_3$ and trapped as Ag_2S for S isotope analysis.

4.4.3 S Isotopic Analyses

S isotopes were measured in the Stable Isotope Laboratory at Northwestern University on a ThermoElectron Delta V continuous-flow isotope ratio mass spectrometer via combustion of $BaSO_4$ or Ag_2S with V_2O_5 to SO_2 gas. Isotopic compositions are reported as permil deviations from the Vienna Canyon Diablo Troilite (V-CDT) using standard delta notation ($\delta^{34}S = [\{(^{34}S/^{32}S)_{sample}/(^{34}S/^{32}S)_{V\text{-}CDT}\}-1] \times 1000$). S isotope data are reproducible within 0.2‰ based

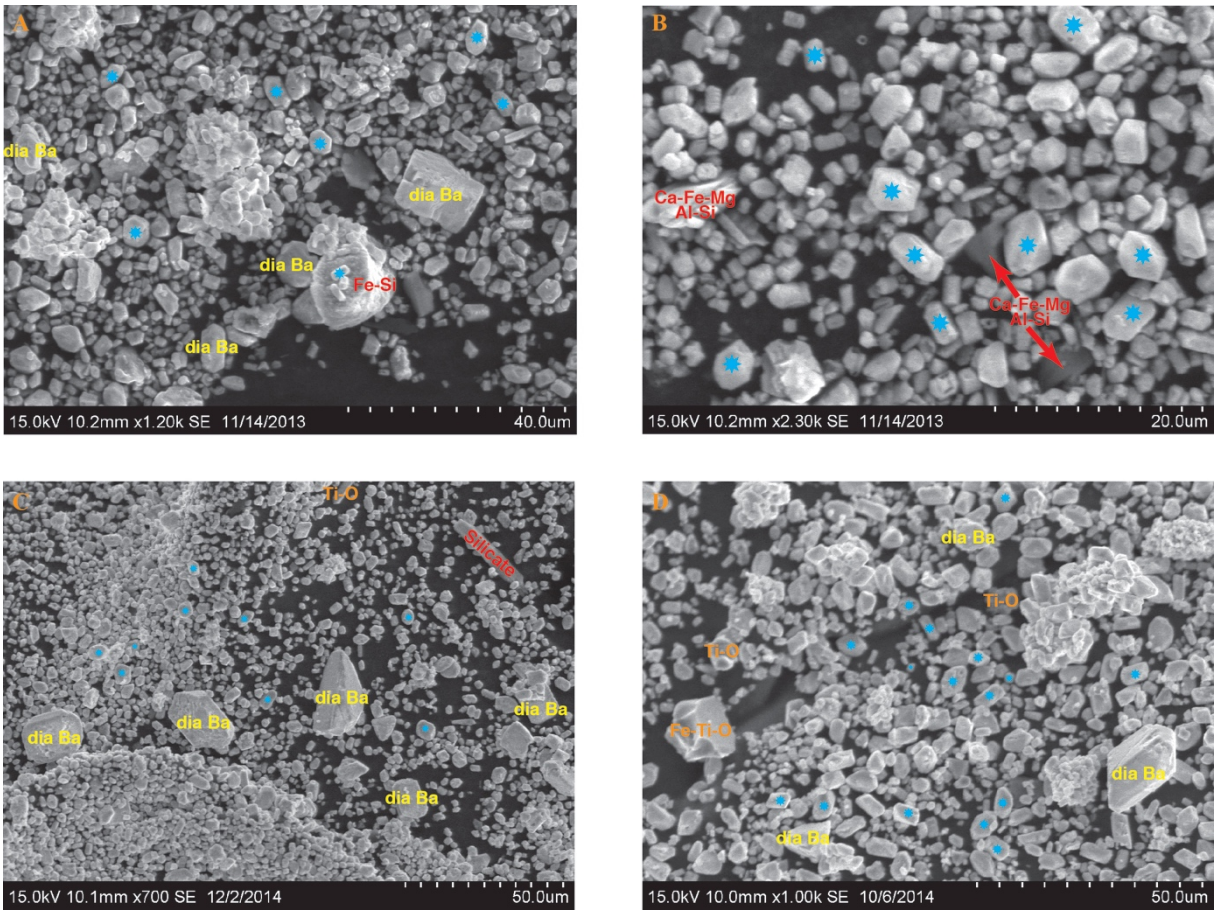

Figure 4-5 SEM images of LST heavy residue extracts

Select representative SEM images of LST heavy residue extracts before fine filtration showing mixtures of marine and diagenetic barite along with some heavy metal oxides and silicates. Chemical and mineralogical identification based on EDS and size. In all images the light blue stars indicate marine barite grains confirmed by EDS spectra. Images **A** and **B** from sample ODP Hole 1207B 43R-1 68-70 cm. Image **C** from sample ODP Hole 1213B 9R-1 29-32 cm. Image **D** from sample ODP Hole 1213B 21R-1 26-28 cm. dia Ba – diagenetic barite

on repeated analyses of samples and international standards (IAEA-S1, IAEA-S2, IAEA-S3, IAEA-SO5, and NBS 127).

4.5 Results

The new $\delta^{34}S_{barite}$ data extend the Paytan et al. (2004) curve back in time about 8 Ma into the Early Cretaceous initially maintaining the elevated $\delta^{34}S$ values (Fig. 4-6). However, the enriched seawater $\delta^{34}S$ values may be preceded by more moderate values in the Berriasian (single sample 18.12 ± 0.07, n=3). The major decrease in $\delta^{34}S_{barite}$ during the Barremian-Aptian is maintained with the new data although the timing, structure, and spatial heterogeneity of this shift is more uncertain (Fig. 4-6). Near the Albian-Cenomanian boundary, following nearly 20 Ma of low $\delta^{34}S_{barite}$ values (15-16‰), the new data show a rapid ~1‰ negative shift before reaffirming the previously observed steep and equally rapid positive shift in $\delta^{34}S_{barite}$ (Fig. 4-6) [Paytan et al., 2004]. This new minor negative shift increases the magnitude of the positive change in $\delta^{34}S_{barite}$ surrounding the Albian-Cenomanian boundary to be nearly equal to that observed in the Barremian-Aptian, but occurring much more rapidly (Fig. 4-6).

While the expansion of the Early Cretaceous $\delta^{34}S_{Ba}$ record presented here raises questions about the timing, structure, and spatial heterogeneity of the Barremian-Aptian negative excursion it also opens the possibility for questions regarding the quality and purity of the extraction procedures, especially between labs (Fig. 4-6) [Paytan et al., 1993; Turchyn, 2005]. Samples in this study were filtered through 8 μm filter paper to separate the larger diagenetic barite from the marine barite while only SEM analysis and XRD data were used in other studies to determine the quality of the barite extract before isotopic analysis (Fig. 4-5) [Paytan et al., 1993, 1998, 2002, 2004; Turchyn and Schrag 2004, 2006; Turchyn et al., 2009]. Ideally this filtering should

adequately separate the different types of barite based on the size difference, however, the possibility of diagenetic barite fracturing off small pieces must still be acknowledged [Paytan et al., 2002]. There is also the possibility of contamination from pyrite, either fine grained or small fragments, that wasn't removed during the extraction procedure, fine filtration or spotted during SEM analysis. In addition, when examining geologically rapid excursions the amount of time integrated within a single sample and the potential variability within $\delta^{34}S_{Ba}$ over that period must also be considered.

The S isotope composition of the pyrite ($\delta^{34}S_{py}$) from these deep, open ocean drill cores is ^{34}S-depleted with nearly all the samples having values ≤-30‰ (-42.0 ± 5.6 ‰, n=169) (Fig. 4-7). These depleted $\delta^{34}S_{py}$ values result in most of the barite-pyrite paired samples (15 of 17) producing $\Delta^{34}S_{py\text{-}Ba}$ values ≤-60‰ (Fig. 4-8). Overall there appears to be a slight shift in $\delta^{34}S_{py}$ to more ^{34}S-enriched values during the Barremian to Aptian. However, in ODP Hole 1207B, $\delta^{34}S_{py}$ values start ^{34}S-enriched at the Barremian-Hauterivian boundary and then shift lower before returning to heavier values. In ODP Hole 766A there is an ~10‰ decrease in $\Delta^{34}S_{py\text{-}Ba}$ during the Barremian to Aptian (Fig. 4-8).

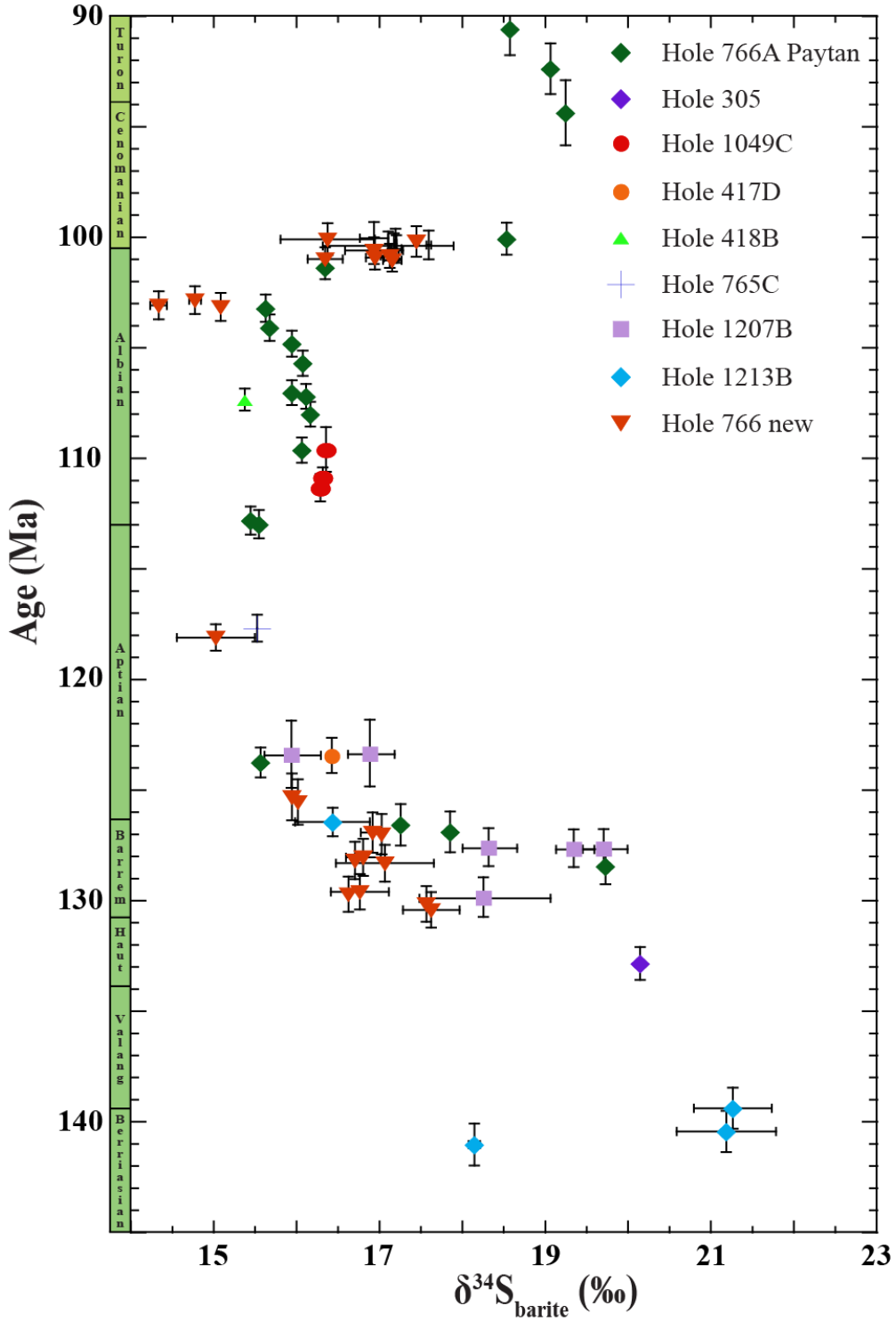

Figure 4-6 Early Cretaceous barite S isotope record

Early Cretaceous $\delta^{34}S_{Ba}$ from this study and Paytan et al. (2004) with GTS2012 age assignments. Data tables are provided in Appendix II.

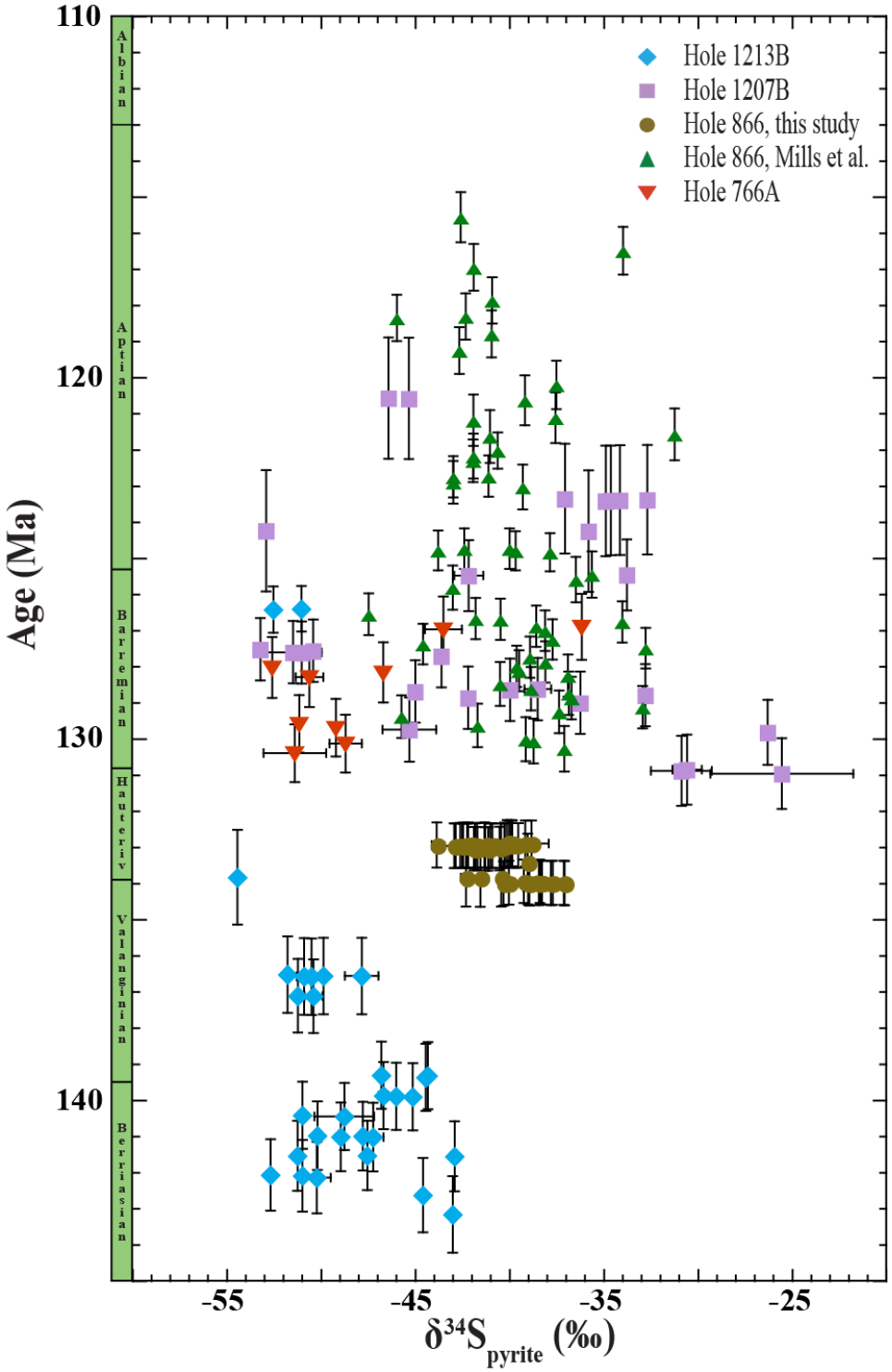

Figure 4-7 Early Cretaceous pyrite S isotope record

Early Cretaceous $\delta^{34}S_{py}$ from this study and Mills et al. (2013) with GTS2012 age assignments. Data tables are provided in Appendix II.

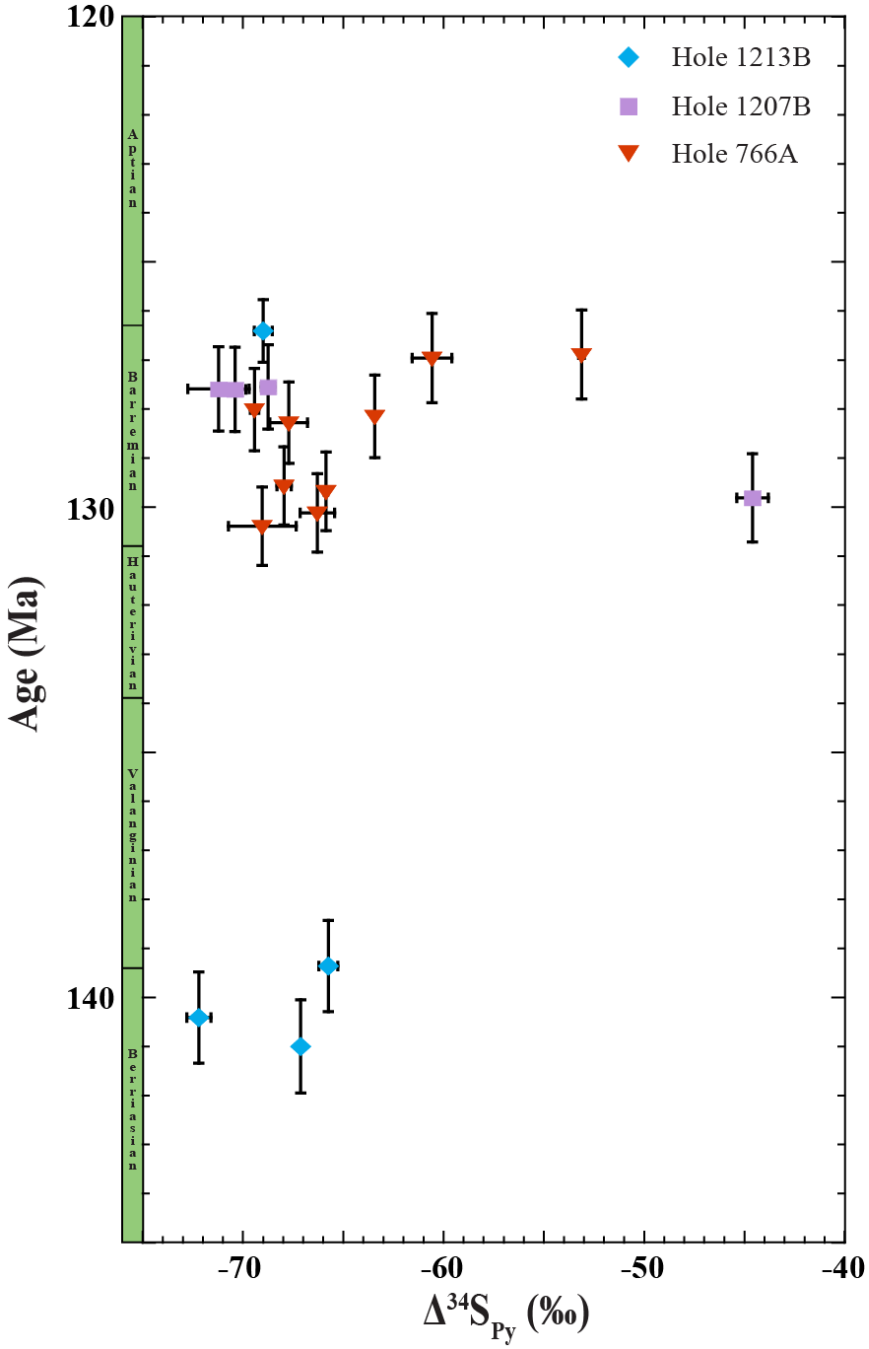

Figure 4-8. Early Cretaceous $\Delta^{34}S_{py}$

Early Cretaceous $\Delta^{34}S_{py}$ from samples yielding both minerals with GTS2012 age assignments. Data tables are provided in Appendix II.

4.6 Coupled Sr-S modeling of the Early Cretaceous

4.6.1 Linking the two cycles – hydrothermal and total weathering fluxes

As derived in detail in Chapter 3, when mass-dependent fractionation is ignored, the Sr isotope composition of seawater is described by the following isotope mass balance equations:

$$\frac{d}{dt}{}^{84}N_{sw} = \sum_i \frac{R_{84}}{R_{87,i}+Z} \times F_i - F_{tb} \times \frac{R_{84}}{R_{87,sw}+Z} \tag{4-1}$$

$$\frac{d}{dt}{}^{86}N_{sw} = \sum_i \frac{1}{R_{87,i}+Z} \times F_i - F_{tb} \times \frac{1}{R_{87,sw}+Z} \tag{4-2}$$

$$\frac{d}{dt}{}^{87}N_{sw} = \sum_i \frac{R_{87,i}}{R_{87,i}+Z} \times F_i - F_{tb} \times \frac{R_{87,sw}}{R_{87,sw}+Z} \tag{4-3}$$

$$\frac{d}{dt}{}^{88}N_{sw} = \sum_i \frac{R_{88}}{R_{87,i}+Z} \times F_i - F_{tb} \times \frac{R_{88}}{R_{87,sw}+Z}, \tag{4-4}$$

$$\text{where } Z = 1 + R_{84} + R_{88}, \tag{4-5}$$

is a constant reflecting fixed isotope abundance ratios for $^{88}Sr/^{86}Sr$ (R_{88} = 8.375209) and $^{84}Sr/^{86}Sr$ (R_{84} = 0.056584), ${}^{A}N_{sw}$ is the mass of isotopes ^{87}Sr, ^{86}Sr, ^{88}Sr, and ^{84}Sr in the oceans, $R_{87,sw}$ is the radiogenic Sr isotope ratio of seawater, and $R_{87,i}$ represents the radiogenic isotope ratio of the hydrothermal (ht), total weathering (tw = riverine + submarine groundwater discharge), and diagenetic (d) fluxes (F_i), and F_{tb} is the total burial flux. When linked with the Sr cycle the S isotope composition of seawater is described by the following isotope mass-balance equations:

$$\begin{aligned}\frac{d}{dt}{}^{32}N_{sw} = {} & hF_{ht}^{\mathrm{Sr}} \times \frac{1000}{r_0 \times (\delta_{ht}+1000)+1000} + wF_{tw}^{\mathrm{Sr}} \times \frac{1000}{r_0 \times (\delta_{tw}+1000)+1000} + F_{vg}^{\mathrm{S}} \times \frac{1000}{r_0 \times (\delta_{vg}+1000)+1000} \\ & - F_{SO_4}^{\mathrm{S}} \times \frac{1000}{r_0 \times (\delta_{sw}+1000)+1000} - F_{py}^{\mathrm{S}} \times \frac{1000}{r_0 \times (\delta_{sw}+\Delta_{py}+1000)+1000}\end{aligned} \tag{4-6}$$

$$\frac{d}{dt}{}^{34}N_{sw} = hF_{ht}^{\mathrm{Sr}} \times \frac{r_0\times(\delta_{ht}+1000)}{r_0\times(\delta_{ht}+1000)+1000} + wF_{tw}^{\mathrm{Sr}} \times \frac{r_0\times(\delta_{tw}+1000)}{r_0\times(\delta_{tw}+1000)+1000} + F_{vg}^{\mathrm{S}} \times \frac{r_0\times(\delta_{vg}+1000)}{r_0\times(\delta_{vg}+1000)+1000}$$
$$- F_{SO_4}^{\mathrm{S}} \times \frac{r_0\times(\delta_{sw}+1000)}{r_0\times(\delta_{sw}+1000)+1000} - F_{py}^{\mathrm{S}} \times \frac{r_0\times(\delta_{sw}+\Delta_{py}+1000)}{r_0\times(\delta_{sw}+\Delta_{py}+1000)+1000}, \quad (4\text{-}7)$$

where ${}^{A}N_{sw}$ is the mass of ^{32}S and ^{34}S in the oceans, δ_{sw} is the δ^{34}S of seawater, δ_i is the δ^{34}S of the hydrothermal (ht), total weathering (tw = riverine + submarine groundwater discharge), and volcanic gas (vg) input fluxes (F_i), sulfate mineral deposition (SO_4) and pyrite burial (py) are the output fluxes (F_i), Δ_{py} ($\Delta^{34}\mathrm{S_{py}} = \delta^{34}\mathrm{S_{SO4}} - \delta^{34}\mathrm{S_{py}}$ expressed as a negative number) is the global integrated fractionation from microbial sulfate reduction (MSR) associated with total pyrite burial, r_0 is the $\frac{^{34}S}{^{32}S}$ ratio of the international standard, and h and w are scalars linking the hydrothermal and total weathering fluxes, respectively. In equations 4-6 and 4-7 we assume that all S is comprised by the two isotopes ^{32}S and ^{34}S, which constitute more than 99% of all S and disregard the presence of the two other minor isotopes, ^{33}S and ^{36}S.

With this coupling the F_{ht} and F_{tw} of the S cycle are constrained by the Sr cycle and assumed constant scalars. Therefore, the Sr cycle is modeled independently prior to coupling with the S cycle in order to determine a reasonable range for F_{ht}^{Sr} and F_{tw}^{Sr}. A detailed discussion and revised method of modeling the Sr isotope record during the Phanerozoic is presented in Chapter 3. For ease, extended results for three different scenarios for the Early Cretaceous Sr cycle from Chapter 3 are shown in Figure 4-9 and the model parameters are listed in Tables 4-4 to 4-6. To summarize, the iterative method developed in Chapter 3 utilizes the LOWESS FIT 5 of McArthur et al. (2012) to provide additional constraints while focusing on matching $\frac{d}{dt}R_{sw}$, minimizing the step size within the set of prescribed $R_{87,tw}$ values along with matching target seawater ^{87}Sr/^{86}Sr values. The proposed variable $R_{87,tw}$ changes every 1-2.5 Ma (Fig. 4-9C and

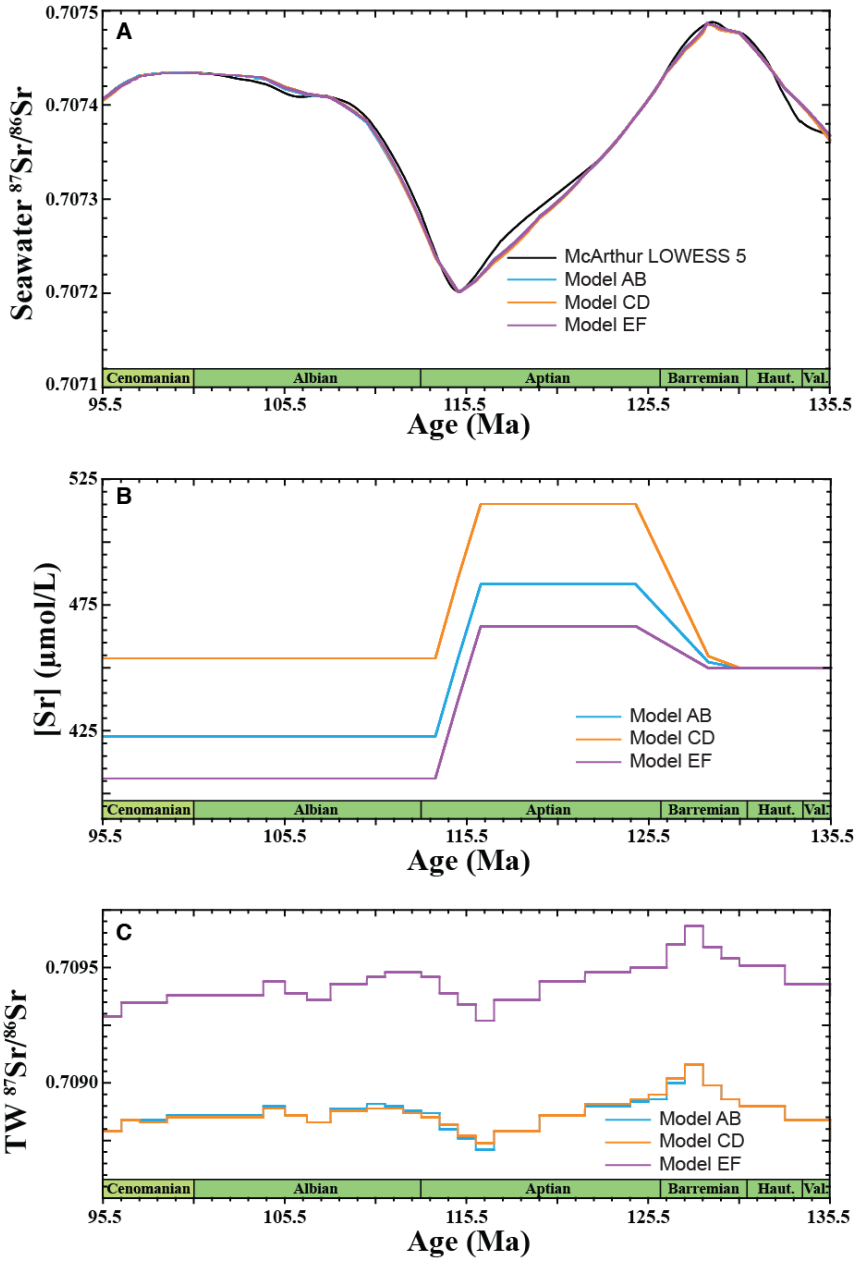

Figure 4-9 Summarized Sr cycle model results

Modeled $R_{87,sw}$ (**A**) and seawater Sr concentration for models AB, CD, and EF with prescribed $R_{87,tw}$ values varying a mixture of every 1-2.5 Ma. McArthur et al. (2012) curve included for comparison. See Table 4-4 for list of parameters and perturbation factors. **C**) Prescribed $R_{87,tw}$ values for models AB, CD, and EF. See Table 4-6 for list of prescribed $R_{87,tw}$ values.

Table 4-4. Parameters and perturbation factors used for Early Cretaceous Sr cycle models. Model times at which perturbations occur are noted. Model time 0 = 135.5 Ma. sw – seawater; tw – total weathering; d – diagenetic; ht – hydrothermal

	Sr Model AB	**Sr Model CD**	**Sr Model EF**
[Sr] (µmol/L)	450	450	450
$R_{87,sw}$ initial	0.706849	0.706849	0.706849
F_{tw} (mol/yr)[1]	67e9	67e9	47e9
$R_{87,tw}$	variable[3]	variable[3]	variable[3]
F_d (mol/yr)	3.4e9	3.4e9	3.4e9
$R_{87,d}$ initial[2]	0.70692	0.70692	0.70692
F_{ht} (mol/yr)	18.6e9	18.6e9	18.6e9
$R_{87,ht}$	0.7030	0.7030	0.7030
Perturbation Factors			
Hydrothermal Flux			
LIP Initial Phase (5-6.75 Ma)	1.196X	1.25X	1.137X
LIP Main Phase (6.75-10.75 Ma)	1.976X	2.50X	1.837X
Post LIP (10.75 Ma)	1.60X	1.75X	1.55X
Post Evaporite (21.75 Ma)	1.40X	1.45X	1.35X
LIP #2 (38 Ma)	1.4645X	1.533X	1.404X
Total Weathering Flux			
LIP Initial Phase (5-6.75 Ma)	1.045X	1.09X	1.00X
LIP Main Phase (6.75-10.75 Ma)	1.41X	1.80X	1.3375X
Post LIP (10.75 Ma)	1.10X	1.20X	1.10X
Late Aptian-Early Albian rise (20.4 Ma)	1.25X	1.32X	1.25X
Late Albian-Early Cenomanian plateau (25.5 Ma)	1.20X	1.25X	1.20X

[1]In Chapter 3 the F_{tw} gradually increases 1e9 mol/yr every 2.5 Ma over the 30 Ma preconditions interval (160.5-130.5 Ma). Pre-LIP F_{tw} value is 68e9 mol/yr for models AB and CD and 48e9 mol/yr for model EF. Perturbation weathering factors multiply by the pre-LIP F_{tw} value.
[2]See Table 4-5 for full list of $^{87}Sr/^{86}Sr$ ratios for the diagenetic flux adjusting every 2.5 Ma.
[3]See Table 4-6 for prescribed variable $^{87}Sr/^{86}Sr$ ratios for the total weathering flux.

and Table 4-6), which is in line with average denudation rates removing 10-1000 meters of material every 1 Ma within a watershed [Portenga and Bierman, 2011; Herman et al., 2013]. In light of recent reconstructions of a singular OJMHP and the revised LIP definition (see Chapter 2 Section 3), the Barremian-Aptian plateau and initial decrease in seawater $^{87}Sr/^{86}Sr$ is attributed to the LIP stage of OJMHP, while the continued decrease is associated with higher MOR spreading rates including the rifting of OJMHP, increased continental arc volcanism, and the emplacement of the Kerguelen Plateau (Fig. 4-9A and Tables 2-3 and 4-4) [Larson, 1991; Rowley, 2002; Taylor, 2006; Bryan and Ernst, 2008; Seton et al., 2009, 2012; Chandler et al., 2012; Bryan and

Table 4-5. Diagenetic input $^{87}Sr/^{86}Sr$ ratios used in all models. Using McArthur et al. (2012) LOWESS FIT 5 the values are determined by taking the average spread over 2.5 Ma (n = 51) centered at 20 Ma prior to model age.

Age (Ma)	Model Age (Ma)	Model Time (Ma)	Diagenetic input $^{87}Sr/^{86}Sr$
155.5	135.5	0	0.70692
153	133	2.5	0.70700
150.5	130.5	5	0.70707
148	128	7.5	0.70713
145.5	125.5	10	0.70717
143	123	12.5	0.70722
140.5	120.5	15	0.70727
138	118	17.5	0.70732
135.5	115.5	20	0.70737
133	113	22.5	0.70741
130.5	110.5	25	0.70747
128	108	27.5	0.70747
125.5	105.5	30	0.70741
123	103	32.5	0.70735
120.5	100.5	35	0.70731
118	98	37.5	0.70727

Ferrari, 2013; Hochmuth et al., 2015; McKenzie et al., 2016; Tucker et al., 2016; Wang et al., 2016].

Determination of the scalar linking the hydrothermal fluxes of Sr and S must take into consideration the differences in behavior of Sr and S during hydrothermal circulation within the oceanic crust. Despite significant isotope exchange between the evolving fluid and the basaltic crust, Sr behaves conservatively during hydrothermal circulation [Edmonds and Edmond, 1995; Davis et al., 2003; Coogan, 2009]. Therefore, the hydrothermal Sr flux should scale linearly with seawater Sr concentration, which has varied considerably throughout the Phanerozoic [Coogan, 2009; Vollstaedt et al., 2014; Gothmann et al., 2015; Chapter 3 this thesis]. In contrast, S does not behave conservatively as the amount of leached basaltic sulfide does not come close to replacing the ≳90% of seawater sulfate removed from solution primarily as anhydrite [Shanks, 2001; Alt et al., 2003; Ono et al., 2007]. Despite venting hydrothermal fluids being a mixture of seawater and basaltic components for both Sr and S, flux estimates for just the basaltic

Table 4-6. Prescribed $R_{87,tw}$ values for Sr models AB, CD, and EF during coupling.

Age (Ma)	Model Time (Ma)	Prescribed $R_{87,tw}$ Model AB	Prescribed $R_{87,tw}$ Model CD	Prescribed $R_{87,tw}$ Model EF
135.5	0	0.70884	0.70884	0.70943
133	2.5	0.70890	0.70890	0.70951
130.5	5	0.70893	0.70893	0.70954
129.5	6	0.70899	0.70899	0.70959
128.5	7	0.70908	0.70908	0.70968
127.5	8	0.70900	0.70902	0.70960
126.5	9	0.70893	0.70895	0.70950
125.5	10	0.70892	0.70893	0.70950
124.5	11	0.70890	0.70891	0.70948
122	13.5	0.70886	0.70886	0.70944
119.5	16	0.70879	0.70879	0.70936
117	18.5	0.70871	0.70874	0.70927
116	19.5	0.70876	0.70877	0.70934
115	20.5	0.70880	0.70882	0.70939
114	21.5	0.70887	0.70885	0.70946
113	22.5	0.70888	0.70887	0.70948
112	23.5	0.70890	0.70889	0.70948
111	24.5	0.70891	0.70889	0.70946
110	25.5	0.70889	0.70888	0.70943
108	27.5	0.70883	0.70883	0.70936
106.7	28.8	0.70886	0.70886	0.70939
105.5	30	0.70890	0.70889	0.70944
104.3	31.2	0.70886	0.70885	0.70938
101.9	33.6	0.70886	0.70885	0.70938
99	36.5	0.70884	0.70883	0.70935
97.5	38	NA	0.70884	NA
96.5	39	0.70879	0.70879	0.70929
Weighted average		0.70887	0.70887	0.70944
Standard deviation		0.000076	0.000074	0.000094

component have only been made for Sr [Davis et al., 2003]. Therefore, the cumulative hydrothermal basaltic Sr flux of $3.1 \pm 0.8 \times 10^9$ mol/yr from Davis et al. (2003) must first be adjusted to a total hydrothermal fluid flux before determining the modern Sr-S hydrothermal scalar value. The mean end-member hydrothermal fluid is estimated to contain 82% basaltic strontium, which results in an adjusted total Sr hydrothermal flux of $3.78 \pm 0.98 \times 10^9$ mol/yr [Davis et al., 2003]. Most estimates for the modern hydrothermal S flux range from 0.2-0.5 x 10^{12} mol/yr [Elderfield and Shultz, 1996; Arthur, 2000; Canfield, 2004]. This produces a modern Sr-S hydrothermal flux scalar of 42.1-178.6. However, the Cretaceous seawater Sr

concentrations are thought to have reached 450 μmol/L compared to the 90 μmol/L in the modern ocean, which would necessitate the hydrothermal flux scalar being reduced by a factor of 5 to 8.4-35.7 [Coogan, 2009; Chapter 3 this thesis].

Calculation of the scalar linking the total weathering fluxes of Sr and S relies on dissolved riverine flux estimates because of the difficulty in measuring and limited estimates for global fluxes of submarine groundwater discharge (SGD) and particulate load dissolution [Basu et al., 2001; Beck et al., 2013; Jones et al., 2012a, b; Jeandel and Oelkers, 2015]. Estimates for the global Sr dissolved riverine flux range widely from 2.05-4.7 x 10^{10} mol/yr [Palmer and Edmond, 1989; Davis et al., 2003; Allegre et al., 2010; Peucker-Ehrenbrink et al., 2010]. The preferred estimate is that of Peucker-Ehrenbrink et al. (2010) – 4.7 x 10^{10} mol/yr – which used the bedrock age and lithology of 19 large-scale drainage regions along with water discharge values and an extensive database of riverine chemistry to determine the global riverine Sr flux and $^{87}Sr/^{86}Sr$ value. Estimates for the global S riverine flux generally range from 0.89-2.5 x 10^{12} mol/yr [Holser et al., 1988; Berner and Berner, 1996; Arthur, 2000; Hansen and Wallman, 2003; Halevy et al., 2012]. Using the preferred Sr riverine flux estimate of Peucker-Ehrenbrink et al. (2010) results in a scalar ranging from 18.9-53.2. Considering the uncertainty in SGD and particulate load dissolution flux estimates along with the differences in chemical behavior for Sr and S during water-rock interactions, the Sr-S scalar determined for the dissolved riverine flux may not be applicable to these components of the total weathering flux. Therefore, the range of the total weathering scalar values to be tested is extended 10% lower.

4.6.2 $\delta^{34}S$ of hydrothermal and total weathering fluxes

While the Sr model and assumed constant scalars will constrain the S F_{ht} and F_{tw}, the $\delta^{34}S$ of these fluxes remain free variables that need to be determined. As indicated above, the $\delta^{34}S$ of

hydrothermal fluids is a mixture of thermochemically reduced seawater sulfate and leached basaltic sulfide [Shanks, 2001; Canfield, 2004; Ono et al., 2007]. This results in the $\delta^{34}S$ of the H_2S in the hydrothermal fluid being slightly greater than the mantle value of 0‰ [Shanks, 2001; Canfield, 2004; Ono et al., 2007]. Eruptions and cracking events along the mid-ocean ridges continually resupply the system with fresh basalt that periodically lowers the $\delta^{34}S$ value of the vent fluid towards the mantle value [Shanks, 2001 and references within]. The modern global estimate for the $\delta^{34}S$ of hydrothermal fluids is 3.5‰ [Arthur, 2000; Shanks, 2001; refs]. However, it is possible for it to be lower in the geologic past when seawater $\delta^{34}S$ values were lower than present, or when global spreading rates resupplied hydrothermal systems with fresh basalt at a higher frequency than today.

The $\delta^{34}S$ of riverine water is determined by the proportion of weathered evaporite (gypsum or anhydrite) to pyrite within the drainage basin. Pyrite constitutes a minor component of sedimentary (biogenic), igneous, and metamorphic rocks with an enormous range in $\delta^{34}S$ values (-60-60‰) [Alt et al., 1993, 2012, 2013; de Hoog et al., 2001; Canfield and Farquhar, 2009; Farquhar et al., 2010; Huston et al., 2010; Alt and Shanks, 2011; this study]. In general, the pyrite available for weathering is presumed to be dominated by sedimentary, biogenic pyrite with ^{34}S-depleted $\delta^{34}S$ values [i.e. Arthur, 2000; Canfield, 2004]. Significant evaporite deposition is episodic throughout Earth's history and these deposits can differ greatly in the extent and amount of sulfate rich layers [Hay et al., 2006; Warren, 2010; Halevy et al., 2012; Wortmann and Paytan, 2012]. For most of the Phanerozoic and Proterozoic, the $\delta^{34}S$ of evaporite deposits generally ranges from 15-25‰ with some Cambrian and Proterozoic values recording heavier values (30-40‰) [Claypool et al., 1980; Holser et al., 1988, 1989; Strauss, 1997, 1999; Kah et al., 2001, 2004; Strauss et al., 2001; Kampshulte and Strauss, 2004; Canfield

and Farquhar, 2009; Farquhar et al., 2010]. Using the pyrite-S to Ca ratio of sedimentary rocks and the presumption that gypsum (or anhydrite) weathers twice as fast as pyrite, Berner and Berner (1996) estimate that most modern natural riverine sulfate results from weathering of evaporites and pyrite in a 2:1 ratio. This estimate is in stark contrast to Holser et al. (1988) who estimated the weathered pyrite flux to be 2.5X the weathered evaporite flux. The 2:1 weathered evaporite:pyrite ratio of Berner and Berner (1996) results in a positive $\delta^{34}S$ value for riverine sulfate typically around 6-7‰, which has been widely used in global S cycle box models [Arthur, 2000; Hansen and Wallmann, 2003; Paytan et al., 2004; Adams et al., 2010]. If Holser et al. (1988) is correct, however, a 35‰ difference in the S isotope composition of weathered evaporite and weathered pyrite would result in a global riverine sulfate $\delta^{34}S$ value around -5.0‰ to -6.0‰. Several studies using S or S and O isotopes of riverine sulfate have clearly demonstrated the importance and dominance of oxidative sulfide weathering in several river basins in contrast to the Berner and Berner (1996) estimates [Cameron et al, 1995; Karim and Veizer, 2000; Spence and Telmer, 2005; Calmels et al., 2007; Cortecci et al., 2007; Li et al., 2011; Das et al., 2012; Yuan and Mayer, 2012]. Improved constraints on evaporite burial during the Phanerozoic have led to the suggestion that riverine $\delta^{34}S_{sulfate}$ values were negative for most of the Phanerozoic [Halevy et al., 2012]. In addition, the present exposure of multiple major Neogene evaporite deposits has led some to hypothesize that the modern riverine sulfate flux and $\delta^{34}S$ are both anomalously high [Halevy et al., 2012]. With the increasing evidence for the importance of oxidative sulfide weathering and the episodic nature of major evaporite deposition, it is more likely that the evaporite:pyrite weathering ratio is $\lesssim 1$ for most of the Phanerozoic with a global riverine $\delta^{34}S_{sulfate}$ values near zero or negative (Table 4-7) [e.g. Holser et al., 1988; Halevy et al., 2012].

Table 4-7. Possible combinations of $\delta^{34}S$ for weathered evaporite (we) and pyrite (wp) along with evaporite:pyrite (E:P) weathering ratios to produce the $\delta^{34}S_{tw}$ of the 10 S models tested. See Tables 4-8 and 4-9. The $\delta^{34}S_{we}$ = 22‰ and $\delta^{34}S_{wp}$ = -18‰ (bold ratios) is the initial combination used in the models.

	S 1+3	**S 2**	**S 4**	**S 5**	**S 6**	**S 7**	**S 8**	**S 9+10**
δ_{tw}	-4.50	-8.57	-7.85	-6.20	-3.00	3.00	5.62	1.00
E:P (28,-17)	0.3846	0.2305	0.2552	0.3157	0.4516	0.80	1.0108	0.6667
E:P (25,-18)	0.4576	0.2809	0.3089	0.3782	0.5357	0.9546	1.2873	0.7917
E:P (22,-18)	**0.5094**	**0.3084**	**0.34**	**0.4184**	**0.60**	**1.1053**	**1.442**	**0.9048**
E:P (23,-17)	0.4545	0.267	0.2965	0.3698	0.5384	1.00	1.3015	0.8182
E:P (24,-16)	0.4035	0.2281	0.2558	0.3245	0.4814	0.9048	1.1763	0.7392
E:P (27,-13)	0.2698	0.1245	0.1477	0.2048	0.3333	0.6667	0.871	0.5385
E:P (24,-14)	0.3333	0.1667	0.193	0.2582	0.4074	0.8096	1.0675	0.6522
E:P (21,-16)	0.4509	0.2512	0.2824	0.3602	0.5416	1.0556	1.4058	0.85
E:P (22,-13)	0.3207	0.1449	0.1725	0.2411	0.40	0.8422	1.1368	0.6667
E:P (20,-15)	0.4285	0.225	0.2567	0.3358	0.5217	1.0589	1.434	0.8422
E:P (24,-11)	0.228	0.0746	0.0989	0.1589	0.2962	0.6667	0.9043	0.5218
E:P (18,-12)	0.3333	0.129	0.1605	0.2396	0.4285	1.00	1.4233	0.7648
E:P (17,-13)	0.3953	0.1732	0.2072	0.2931	0.50	1.1429	1.6362	0.875
E:P (20,-10)	0.2244	0.05	0.0772	0.145	0.3043	0.7648	1.0863	0.579

4.6.3 Volcanic gas S flux and isotope composition

The remaining S input flux is subaerial volcanic gas emissions which encompasses the continuous degassing of arc volcanoes, continental rifts, ocean island volcanoes and major sporadic explosive eruptions [Bluth et al., 1993; Andres and Kasgnoc, 1998; Graf et al., 1998; Halmer et al., 2002]. Estimates of the modern total S (SO_2, H_2S, organic sulfur compounds) subaerial volcanic gas flux range from 0.28-0.33 x 10^{12} mol/yr; subduction zone arc volcanism is the dominant contributor (70-80%) [Andres and Kasgnoc, 1998; Halmer et al., 2002]. The $\delta^{34}S$

of subduction zone arc volcanic gases is a mixture of mantle S and slab related S (pore water and minerals) generally resulting in a slight enrichment of $\delta^{34}S$ values over the mantle value (~0‰) [Ueda & Sakai 1984; Woodhead et al 1987; Torssander, 1989; Alt et al 1993, 2012, 2013; Herzig et al 1998; de Hoog et al 2001]. The global annual subaerial volcanic gas S flux is generally assigned a $\delta^{34}S$ value of 2-3‰ [Arthur, 2000; Hansen and Wallmann, 2003; Halevy et al., 2012].

4.6.4 S output fluxes and fractionation factors

The F_{SO4} is taken to either primarily or solely consist of evaporitic gypsum and anhydrite but may also include barite (diagenetic, hydrothermal, and biogenetic) and hydrothermal anhydrite deep within the oceanic crust [Maynard and Okita, 1981; Kump and Garrels, 1986; Holser et al., 1988, 1989; Paytan and Kastner, 1996; Arthur, 2000; Greinert et al., 2002; Alt et al., 2003; Hansen and Wallmann, 2003; Canfield, 2004; Huston and Logan, 2004; Hein et al., 2007; Johnson et al., 2009; Halevy et al., 2012; Zhou et al., 2015]. Global Ba fluxes are poorly constrained and there is debate regarding the retention of crustal hydrothermal anhydrite over geologically relevant time scales [Holser et al., 1988, 1989; Paytan and Kastner, 1996; Arthur, 2000; Alt et al., 2003; Hansen and Wallmann, 2003; Hay et al., 2006; Halevy et al., 2012]. Therefore, sulfate burial flux estimates for the geologic past are based on Phanerozoic average evaporite deposition rates [Holser et al., 1988, 1989; Paytan and Kastner, 1996; Arthur, 2000; Alt et al., 2003; Hansen and Wallmann, 2003; Hay et al., 2006; Halevy et al., 2012]. Considering the episodic nature of massive evaporite deposition and modern observations of minimal to no evaporite deposition, estimates of modern sulfate evaporite burial range from 0-0.3 x 10^{12} moles/yr [Holser et al., 1988; Arthur, 2000; Hansen and Wallmann, 2003; Hay et al., 2006; Warren, 2010; Halevy et al., 2012]. This is in contrast to most models of the global S cycle where the initial steady-state evaporite burial flux is slightly more than half of the total output

flux (0.83-1.1 x 10^{12} mol/yr) [Kurtz et al., 2003; Paytan et al., 2004; Wortmann and Chernyavsky, 2007; Canfield and Farquhar, 2009; Adams et al., 2010; Wortmann and Paytan, 2012]. Recent quantitative analysis of macrostratigraphic data for the North American Continent that was scaled globally and corrected for decay of evaporite deposits resulted in an average Phanerozoic sulfate evaporite burial flux of 0.33-0.45 x 10^{12} moles/yr, which is ~10-30% of steady state riverine flux estimates [Halevy et al., 2012]. While there is considerable uncertainty in F_{SO4} estimates, the S isotope fractionation imparted during the precipitation of sulfate minerals is generally zero except during evaporitic sequences where the precipitate can be ~1‰ heavier or lighter than the solution depending on the active saturation field [Raab and Spiro, 1991; Paytan et al., 2002; Alt et al., 2003; Johnson et al., 2009]. Therefore, in nearly all models of the S cycle, fractionation associated with the evaporite (sulfate) burial flux is zero [e.g., Arthur, 2000; Canfield, 2004; Paytan et al., 2004; Wortmann and Chernyavsky, 2007; Adams et al., 2010].

Estimates of the F_{py} are highly variable ranging from 0.22-1.8 x 10^{12} mol/yr, which represent pyrite burial fractions ($f_{py} = \frac{F_{py}}{F_{SO4}+F_{py}}$) ranging from 0.2-0.9 [Holser et al., 1988; Arthur, 2000; Hansen and Wallmann, 2003; Kurtz et al., 2003; Paytan et al., 2004; Wortmann and Chernyavsky, 2007; Halevy et al., 2012]. Recently revised global rates of marine sulfate reduction rate indicate that 11.3 x 10^{12} mol of sulfate are reduced annually in the modern ocean [Bowles et al., 2014]. It is generally presumed that around 10% and no more than 25% of the microbially reduced sulfate is buried as pyrite while the remaining H_2S is reoxidized to sulfate [Jorgensen, 1982; Canfield, 1991; Lin and Morse, 1991; Turchyn and Schrag, 2004, 2006]. Therefore, at the minimum steady-state pyrite burial fluxes should be around 1.02-1.24 x 10^{12} mol/yr, instead of ≤0.9 x 10^{12} mol/yr which is used in most previous models [Hansen and Wallmann, 2003; Kurtz et al., 2003; Paytan et al., 2004; Wortmann and Chernyavsky, 2007;

Adams et al., 2010; Wortmann and Paytan, 2012; Gomes et al., 2016]. Considering that 11.3 x 10^{12} mol of sulfate consumed annually by MSR would represent <0.0001% of a 1 mmol/L ocean and only ~10% of that is buried as pyrite it seems unlikely that sulfate concentrations would affect pyrite burial fluxes until sulfate levels are extremely low [Chernyavsky and Wortmann, 2007; Wortmann and Chernyavsky, 2007; Bowles et al., 2014]. Instead pyrite burial fluxes are more likely to be determined by dissolved oxygen levels – thereby impacting hydrogen sulfide oxidation rates – and the availability of reactive iron to form pyrite. The Cretaceous oceans were likely much warmer relative to today and therefore contained less dissolved oxygen. Therefore, we suggest it is unlikely that F_{py} <0.9 x 10^{12} mol/yr (<8% of 11.3 Tm/yr) during this time [Hansen and Wallmann, 2003; Wortmann and Chernyavsky, 2007; Adams et al., 2010; Halevy et al., 2012; Paytan and Wortmann, 2012; Bowles et al., 2014; Gomes et al., 2016]. Most models of the Phanerozoic S isotope record explain $\delta^{34}S_{sulfate}$ variability by leveragin f_{py} between ~0.2 and ~0.6 [with an initial steady state value of 0.4 ± 0.05; Garrels and Lerman, 1981, 1984; Hansen and Wallmann, 2003; Kurtz et al., 2003; Canfield, 2004; Kampschulte and Strauss, 2004; Paytan et al., 2004; Wortmann and Chernyavsky, 2007; Adams et al., 2010; Gomes et al., 2016]. In contrast, the recent quantitative estimate of Phanerozoic sulfate burial rates by Halevy et al. (2012) implies that f_{py} may be consistently higher (0.7-0.9) than presumed in most other models. These modeled higher f_{py} values are in line with the greater estimates for the steady state F_{py} (1.02-1.24 x 10^{12} mol/yr) especially if the total input/output flux is ≤2 x 10^{12} mol/yr.

Recent work indicates that sulfurization of organic matter with sulfide generated during MSR, may represent an additional sink of reduced sulfur, thereby impacting $\delta^{34}S_{sw}$ evolution [Mazumdar et al., 2012; Raven et al., 2015, 2016a,b]. While the sulfurization process may impart a fractionation in addition to that resulting from MSR and have an isotopic composition different

from coexisting pyrite, the burial of sulfurized organic matter can be broadly viewed as burial of isotopically light, reduced sulfur similar to pyrite [Mazumdar et al., 2012; Raven et al., 2015, 2016a,b]. Given our limited understanding of the sulfurization process and estimates for its global impact, this potential burial flux is not included in the model but viewed as support for the higher F_{py} values.

The fractionation imparted during MSR varies widely depending on the organism, availability and type of organic matter, metabolic pathway, metabolic rate, and sulfate concentration [Detmers et al., 2001; Habicht et al., 2002; Brunner and Bernasconi, 2005; Bradley et al., 2011, 2016; Sim et al., 2011a,b; Leavitt et al., 2013; Wing and Halevy, 2014]. In general, microbes are not as selective when there is an abundance of highly labile organic matter and metabolic rates are high producing smaller fractionations, which is characteristic of continental shelf environments with high primary productivity [Sim et al., 2011a, b; Leavitt et al., 2013; Wing and Halevy, 2014]. When metabolic rates are low and the availability of organic matter is limited, individual microbial fractionations can reach up to -70‰, typical of deep open marine environments (Fig. 4-8) [Sim et al., 2011a, b; Leavitt et al., 2013; Wing and Halevy, 2014]. The relationship between sulfate concentration and fractionation has been shown to be quite complex and species specific, but is broadly viewed to be positive in most cases with very limited fractionation (-20 to 0‰) occurring at sulfate concentrations <200 μM [Habicht et al., 2002; Adams et al., 2010; Gomes and Hurtgen, 2013; Bradley et al., 2016]. The fractionation factor in the isotope mass balance equations (Equations 4-6 and 4-7) represents a global integrated average of the fractionation imparted by MSR. This global integrated fractionation factor represents an enormous range of environmental and physiological conditions within the oceans from the continental shelves to basaltic crust at spreading centers. Most Phanerozoic S cycle

models use an integrated fractionation factor of -30 to -35‰ [Garrels and Lerman, 1984; Arthur, 2000; Hansen and Wallmann, 2003; Kurtz et al., 2003; Paytan et al., 2004; Wortmann and Chernyavsky, 2007; Adams et al., 2010; Gomes et al., 2016]. The arithmetic difference from global compilations of $\delta^{34}S$ sulfate and contemporaneous pyrite indicate a distinct difference in the range of $\Delta^{34}S_{py}$ values for most of the Paleozoic (~-30‰) and the Jurassic to present (-40 to -45‰) [Wu et al., 2010]. The Jurassic to present $\Delta^{34}S_{py}$ values also demonstrate a strong negative relationship with shallow shelf area [Leavitt et al., 2013].

4.7. Model Implementation, Results, and Discussion

The focus of this study is on identifying the most reasonable and likely range of flux and isotope values for the initial conditions and magnitude of perturbations. Therefore, ten different sulfur models are coupled to three different Sr models testing a range of scalar values, initial conditions and perturbations (Figs. 4-9 to 4-14 and Tables 4-4, 4-8 and 4-9).

According to the guiding principles for coupled Sr-S modeling outlined above, the concurrent negative shift in the Sr and S isotope records during the Barremian to Early Aptian should reflect changes to the common input fluxes (Figs. 4-6 and 4-9a). Therefore, initial model testing focuses on whether the hydrothermal and total weathering perturbation factors determined in Chapter 3 for Sr model AB are sufficient to reproduce the Early Cretaceous S isotope record (Table 4-4 and Fig. 4-10). In line with the recently revised definition for LIPs and tectonic reconstructions of OJMHP, the F_{ht} and F_{tw} perturbations occur in two steps with a minor initial phase lasting 1.75 Ma and a main phase lasting 4 Ma (Table 4-4 and Fig. 4-10c) [Taylor, 2006; Bryan and Ernst, 2008; Chandler et al., 2012; Hochmuth et al., 2015]. Following the end

Table 4-8. Scalar values linking the Sr and S cycle box models and select S cycle model parameters. See Table 4-4 for Sr cycle model parameters and Table 4-9 for full list of S cycle initial condition parameters. The LIP S Gas Total HT Factor represents that total molar S gas input versus the total excess hydrothermal input over the lifetime of the LIP perturbation. WT – weathering; HT – hydrothermal; tw – total weathering

	WT scalar	HT scalar	$\delta^{34}S_{tw}$	Total Input (mol/yr)	f_{py}	$\Delta^{34}S_{py}$	LIP Main Phase S Gas Flux (mol/yr) LIP S Gas Total HT Factor
Sr Model AB							
S Model 1	23	14	-4.50	2.1814E12	0.55	-42.75	0.32e12; 1.31X HT
S Model 2	21	13	-8.57	2.0288E12	0.6565	-40	0.35E12; 1.55X HT
S Model 3	20	14	-4.50	1.9804E12	0.62	-37.61	0.37E12; 1.51X HT
S Model 4	19	13.5	-7.85	1.9041E12	0.5667	-45	0.37E12; 1.57X HT
S Model 5	17.5	14	-6.20	1.8129E12	0.70	-34.6	0.40E12; 1.65X HT
S Model 6	17	12.5	-3.00	1.7515E12	0.58	-38.22	0.425E12; 1.96X HT
S Model 7	23	13	3.00	2.1628E12	0.58	-31.42	0.60E12; 2.66X HT
S Model 8	21	12	5.62	2.0102E12	0.45	-36.44	0.55E12; 2.64X HT
S Model 9	17	12.5	1.00	1.7515E12	0.65	-30.11	0.67E12; 3.05X HT
S Model 10	17	12.5	1.00	1.7515E12	0.4568	-42.83	0.62E12; 2.85X HT
Sr Model CD							
S Model 1	23	14	-4.50	2.1814E12	0.55	-42.75	None
S Model 2	21	13	-8.57	2.0288E12	0.6565	-40	None
S Model 3	20	14	-4.50	1.9804E12	0.62	-37.61	None
S Model 4	19	13.5	-7.85	1.9041E12	0.5667	-45	None
S Model 5	17.5	14	-6.20	1.8129E12	0.70	-34.6	None
S Model 6	17	12.5	-3.00	1.7515E12	0.58	-38.22	None
S Model 7	23	13	3.00	2.1628E12	0.58	-31.42	0.20E12; 0.51X HT
S Model 8	21	12	5.62	2.0102E12	0.45	-36.44	0.31E12; 0.98X HT
S Model 9	17	12.5	1.00	1.7515E12	0.65	-30.11	0.36E12; 1.07X HT
S Model 10	17	12.5	1.00	1.7515E12	0.4568	-42.83	0.30E12; 0.89X HT
Sr Model EF							
S Model 1	32.8	14.5	-4.50	2.1913E12	0.55	-42.72	0.68E12; 3.15X HT
S Model 2	30	13	-8.57	2.0318E12	0.6565	-40	0.67E12; 3.50X HT
S Model 3	28.5	14.5	-4.50	1.9892E12	0.62	-37.57	0.78E12; 3.59X HT
S Model 4	27.1	13.5	-7.85	1.9048E12	0.5667	-45	0.82E12; 3.88X HT
S Model 5	25	14.5	-6.20	1.8247E12	0.70	-34.57	0.69E12; 3.19X HT
S Model 6	24.2	12.5	-3.00	1.7499E12	0.58	-38.22	0.80E12; 4.23X HT
S Model 7	32.8	13.5	3.00	2.1727E12	0.58	-31.42	0.78E12; 3.83X HT
S Model 8	30	12.5	5.62	2.0225E12	0.45	-36.45	0.80E12; 4.23X HT
S Model 9	24.2	12.5	1.00	1.7499E12	0.65	-30.12	0.90E12; 4.71X HT
S Model 10	24.2	12.5	1.00	1.7499E12	0.4568	-42.83	0.90E12; 4.71X HT

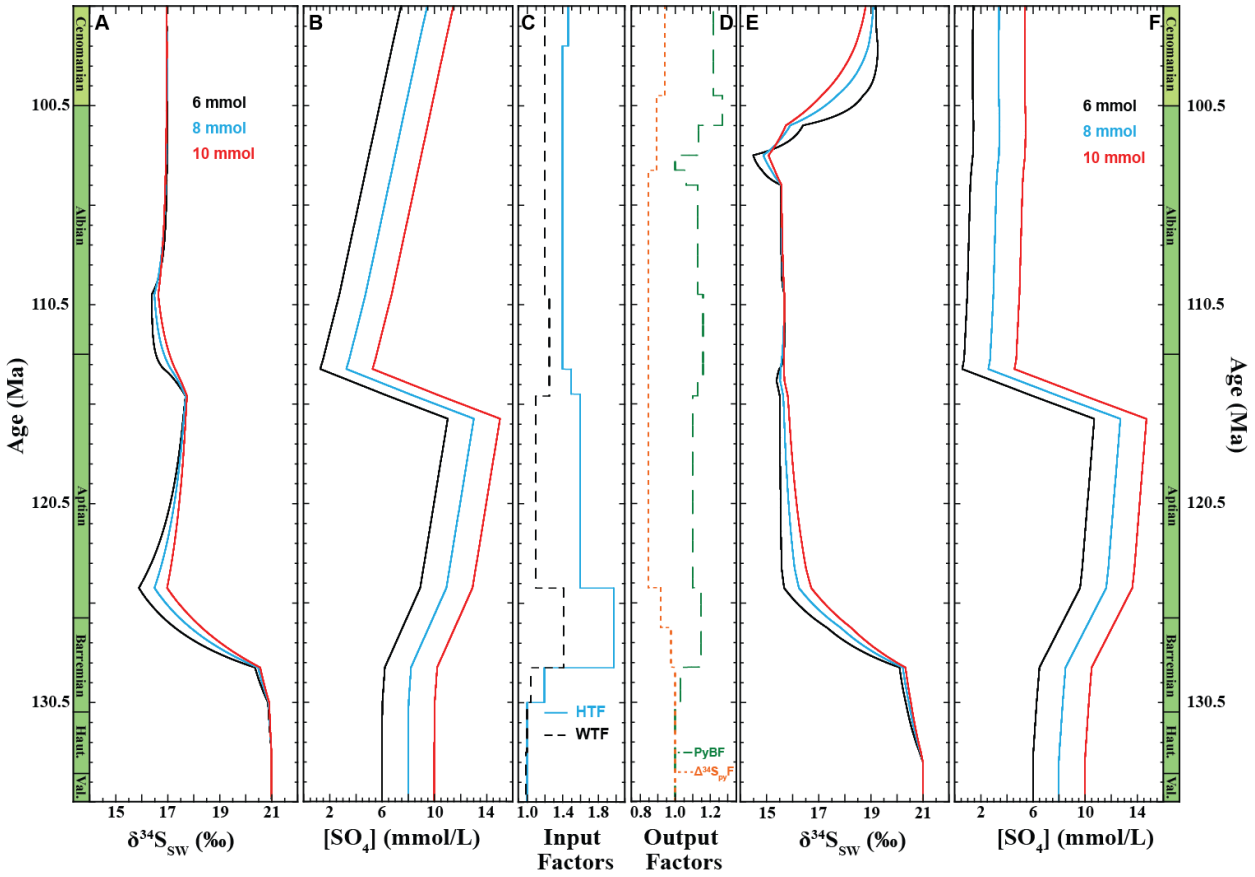

Figure 4-10 S cycle model results hydrothermal and total weathering versus full perturbation

Modeled $\delta^{34}S_{sw}$ (**A**) and sulfate concentration (**B**) for Sulfur model 1 coupled to Sr model AB at 3 different initial sulfate concentrations (6, 8, and 10 mmol/L) with perturbations to just the hydrothermal and total weathering fluxes (Tables 4-4 and 4-8). (**C**) Perturbation factors for the hydrothermal (HTF) and total weathering (WTF) fluxes. Modeled $\delta^{34}S_{sw}$ (**E**) and sulfate concentration (**F**) for Sulfur model 1 coupled to Sr model AB at 3 different initial sulfate concentrations with perturbations to additional S input and output parameters along with perturbations to the hydrothermal and total weathering fluxes. See main text for description. (**D**) Perturbation factors for the pyrite burial flux (PyBF) and pyrite fractionation factor ($\Delta^{34}S_{py}F$).

of the main phase of OJMHP, the F_{ht} and F_{tw} decrease to levels greater than the initial conditions in order to maintain the continued decrease in seawater $^{87}Sr/^{86}Sr$ ratio (Table 4-4 and Fig. 4-10c). These elevated input fluxes are in line with the rifting of OJMHP, elevated MOR spreading rates, increased continental arc volcanism, and emplacement of the Kerguelen Plateau and associated traps (Table 2-3) [Larson, 1991; Rowley, 2002; Seton et al., 2009, 2012; Bryan and Ferrari, 2013; McKenzie et al., 2016; Tucker et al., 2016; Wang et al., 2016]. The Late Aptian-Early Albian rise in seawater $^{87}Sr/^{86}Sr$, which is attributed to an increase in F_{tw} (prescribed in two equal steps) begins during the deposition of the Late Aptian South Atlantic Salts (Table 4-4 and Figs. 4-9 and 4-10) [Chaboureau et al., 2012, 2013; McArthur et al., 2012; Chapter 3 this thesis]. Because a range of initial total output and f_{py} values are to be tested, the perturbation burial flux for the Late Aptian South Atlantic Salts is set at 5.75×10^{12} mol S/yr for 2.5 Ma (Sr/SO_4 molar ratio 0.005625) across all models [Wortmann and Chernyavsky, 2007; Chaboureau et al., 2012, 2013; Wortmann and Paytan, 2012; Chapter 3 this thesis]. The drop in seawater strontium concentration produced by the deposition of the South Atlantic Salts also contributes to a decrease in the F_{ht}, which assists with the Late Aptian-Early Albian rise in seawater $^{87}Sr/^{86}Sr$ (Table 4-4 and Fig. 4-10c). The plateau in seawater $^{87}Sr/^{86}Sr$ ratio that begins in the Late Albian is accommodated by a minor decrease in F_{tw} (Table 4-4 and Figs. 4-9 and 4-10).

The changes in F_{ht} and F_{tw} along with the deposition of the South Atlantic Salts do not reproduce the Early Cretaceous S isotope record (Figs. 4-6 and 4-10a). The modeled $\delta^{34}S_{sw}$ Barremian-Aptian negative shift is less than observed and is followed immediately by a gradual recovery instead of plateauing (Figs. 4-6 and 4-10a). Surrounding the Late Aptian rise in seawater $^{87}Sr/^{86}Sr$ ratio and deposition of the South Atlantic Salts, the modeled $\delta^{34}S_{sw}$ displays a minor decrease followed by minimal recovery before a prolonged plateau (Fig. 4-10a). This is in

Table 4-9. S cycle model initial condition values. $[SO_4]_{tw}$ calculated assuming a 40E15 L/yr total continental water flux [Trenberth et al., 2007]. E:P is the weathered evaporite to weathered pyrite ratio that is typically assumed to be 2:1 [Berner and Berner, 1996]. The initial isotopic composition of the average weathered evaporite (22‰) and weathered pyrite (-18‰) are listed. % SRR represents the pyrite burial flux fraction of the revised global sulfate reduction rate (SRR) of 11.3 Tmol/yr by Bowles et al. (2014). RT_6 is the residence time at the start of the model run for a 6 mmol/L ocean. Units are – F_i – Tmol/yr; $[SO_4]_{tw}$ - µmol/L; δ_i – ‰; Δ_i – ‰; RT_6 –Ma. tw – total weathering; ht – hydrothermal; vg – volcanic gas; py – pyrite burial; SO4 – sulfate burial.

	S1	**S2**	**S3**	**S4**	**S5**	**S6**	**S7**	**S8**	**S9**	**S10**
Sr Models AB and CD										
$\mathbf{F_{tw}}$	1.541	1.407	1.34	1.273	1.1725	1.139	1.541	1.407	1.139	1.139
$\mathbf{[SO_4]_{tw}}$	38.53	35.18	33.50	31.83	29.31	28.48	38.53	35.18	28.48	28.48
$\mathbf{\delta_{tw}}$	-4.50	-8.57	-4.50	-7.85	-6.20	-3.00	3.00	5.62	1.00	1.00
E:P (22,-18)	0.5094	0.3084	0.5094	0.34	0.4184	0.60	1.1053	1.442	0.9048	0.9048
$\mathbf{F_{ht}}$	0.2604	0.2418	0.2604	0.2511	0.2604	0.2325	0.2418	0.2232	0.2325	0.2325
$\mathbf{\delta_{ht}}$	2.5	2.5	2.5	2.5	2.5	2.5	2.5	2.5	2.5	2.5
$\mathbf{F_{vg}}$	0.38	0.38	0.38	0.38	0.38	0.38	0.38	0.38	0.38	0.38
$\mathbf{\delta_{vg}}$	2	2	2	2	2	2	2	2	2	2
$\mathbf{F_{in}}$	2.1814	2.0288	1.9804	1.9041	1.8129	1.7515	2.1628	2.0102	1.7515	1.7515
$\mathbf{\delta_{in}}$	-2.53	-5.27	-2.33	-4.52	-3.23	-1.19	2.77	4.59	1.42	1.42
$\mathbf{f_{py}}$	0.55	0.6565	0.62	0.5667	0.70	0.58	0.58	0.45	0.65	0.4568
$\mathbf{F_{py}}$	1.1998	1.3319	1.2278	1.0791	1.2690	1.0159	1.2544	0.9046	1.1385	0.8001
% SRR	10.62	11.79	10.87	9.55	11.23	8.99	11.10	8.01	10.075	7.08
$\mathbf{\Delta^{34}S_{py}}$	-42.75	-40	-37.63	-45	-34.6	-38.22	-31.42	-36.44	-30.11	-42.83
$\mathbf{F_{SO4}}$	0.9816	0.6969	0.7526	0.8250	0.5439	0.7356	0.9084	1.1056	0.6130	0.9514
$\mathbf{RT_6}$	3.74	4.02	4.12	4.28	4.50	4.65	3.77	4.06	4.65	4.65
Sr Model EF										
$\mathbf{F_{tw}}$	1.5416	1.410	1.3395	1.2737	1.175	1.1374	1.5416	1.410	1.1374	1.1374
$\mathbf{[SO4]_{tw}}$	38.54	35.25	33.49	31.84	29.38	28.44	38.54	35.25	28.44	28.44
$\mathbf{\delta_{tw}}$	-4.50	-8.57	-4.50	-7.85	-6.20	-3.00	3.00	5.62	1.00	1.00
E:P (22,-18)	0.5094	0.3084	0.5094	0.34	0.4184	0.60	1.1053	1.442	0.9048	0.9048
$\mathbf{F_{ht}}$	0.2697	0.2418	0.2697	0.2511	0.2697	0.2325	0.2511	0.2325	0.2325	0.2325
$\mathbf{\delta_{ht}}$	2.5	2.5	2.5	2.5	2.5	2.5	2.5	2.5	2.5	2.5
$\mathbf{F_{vg}}$	0.38	0.38	0.38	0.38	0.38	0.38	0.38	0.38	0.38	0.38
$\mathbf{\delta_{vg}}$	2	2	2	2	2	2	2	2	2	2
$\mathbf{F_{in}}$	2.1913	2.0318	1.9892	1.9048	1.8247	1.7499	2.1727	2.0225	1.7499	1.7499
$\mathbf{\delta_{in}}$	-2.51	-5.28	-2.31	-4.52	-3.21	-1.18	2.77	4.58	1.42	1.42
$\mathbf{f_{py}}$	0.55	0.6565	0.62	0.5667	0.70	0.58	0.58	0.45	0.65	0.4568
$\mathbf{F_{py}}$	1.2052	1.3339	1.2333	1.07945	1.2773	1.0149	1.2602	0.9101	1.1374	0.7994
% SRR	10.67	11.80	10.91	9.55	11.30	8.98	11.15	8.05	10.07	7.07
$\mathbf{\Delta^{34}S_{py}}$	-42.72	-40	-37.57	-45	-34.57	-38.22	-31.42	-36.45	-30.12	-42.83
$\mathbf{F_{SO4}}$	0.9861	0.6979	0.7559	0.82535	0.5474	0.7350	0.9125	1.1124	0.6125	0.9505
$\mathbf{RT_6}$	3.72	4.01	4.10	4.28	4.47	4.66	3.75	4.03	4.66	4.66

contrast to the slightly arced trajectory of $\delta^{34}S_{sw}$ values while still maintaining low values before the rapid excursions near the Albian-Cenomanian boundary (Fig. 4-6). Modeled sulfate concentrations increase and decrease as expected with the perturbations described above, however, the lack of additional changes to the output fluxes in the S cycle prevents the maintenance of very low sulfate concentrations that are suspected to be present throughout the Late Cretaceous (Fig. 4-10b) [Lowenstein et al., 2003; Wortmann and Chernyavsky, 2007; Adams et al., 2010; Wortmann and Paytan, 2012]. In addition, the gradual ~1‰ decrease in $\delta^{34}S_{sw}$ prior to the major negative shift is not present in the model (Figs. 4-6 and 4-10a).

To begin with, the gradual decrease in $\delta^{34}S_{sw}$ prior to the major negative shift is attributed to an increase in F_{vg} (30% for 3 Ma) related to the emplacement of the continental LIPs Parana-Etendeka and Comie-Bunbury (Table 2-3). Considering the volatility difference between S and Sr, an additional S gas flux from OJMHP ($\delta^{34}S$= 0‰) is added to enable the modeled $\delta^{34}S_{sw}$ to match the ~5‰ negative shift (Table 4-8). Consequently, the increased F_{tw} and F_{ht} would also enhance delivery of nutrients and reactive iron throughout the ocean impacting primary productivity, microbial sulfate reduction, and pyrite burial as evidenced by the concurrence of OAE1a [Jenkyns, 1995; Menegatii et al., 1998; Erba et al., 1999; Leckie et al., 2002; Weissert and Erba, 2004; Dumitrescu and Brassell, 2006; Bennett et al., 2008; Bottini et al., 2009; Tejada et al., 2009; Toner et al., 2009; Sander and Koschinsky, 2011; Wu et al., 2011; Herrle et al. 2015; Gomes et al., 2016]. Therefore, an increase in pyrite burial is expected despite its opposing effect on $\delta^{34}S_{sw}$ (Fig. 4-10d). The impact of the increased pyrite burial on $\delta^{34}S_{sw}$ is balanced by the additional gas flux from OJMHP and a decrease in $\Delta^{34}S_{py}$ that is likely related to physiological changes resulting from the increased delivery of labile organic matter to the seafloor (Table 4-8 and Fig. 4-10d-e) [Jenkyns, 1995; Menegatii et al., 1998; Erba et al., 1999; Leckie et al., 2002;

Weissert and Erba, 2004; Dumitrescu and Brassell, 2006; Sim et al., 2011a, b; Leavitt et al., 2013; Wing and Halevy, 2014; Gomes et al., 2016]. A minimum in the arithmetic difference from global compilations of $\delta^{34}S$ sulfate and contemporaneous pyrite during the Early Cretaceous supports this change in the fractionation factor [Wu et al., 2010].

The divergence from the concurrent negative shift in Sr and S isotope records following the emplacement of OJMHP requires a change in S output terms to balance the elevated input fluxes necessitated by the coupling with the Sr cycle (Figs. 4-6, 4-9a, and 4-10c). To minimize the mass imbalance and isotopic change, F_{py} is lowered from its peak perturbation during the emplacement of OJMHP and F_{SO4} is increased slightly (Fig. 4-10c-d). An additional decrease in $\Delta^{34}S_{py}$ is needed in order to maintain the low $\delta^{34}S_{sw}$ values (~15.5‰) for nearly 20 Ma (Fig. 4-10). However, to limit the reduction in $\Delta^{34}S_{py}$ it is also necessary to lower $\delta^{34}S_{tw}$ (Figs. 4-10 and 4-12). Maintenance of the low $\delta^{34}S_{sw}$ during the Late Aptian-Early Albian rise in the seawater $^{87}Sr/^{86}Sr$ ratios that begins during the deposition of the South Atlantic Salts is accommodated by minor increases in F_{py} and $\delta^{34}S_{tw}$ (Figs. 4-9a, 4-10 and 4-12). Similarly, the decrease in F_{tw} associated with the Albian plateau in the seawater $^{87}Sr/^{86}Sr$ ratio is balanced by decreases in F_{py} and $\delta^{34}S_{tw}$ (Figs. 4-9a, 4-10 and 4-12). The changes in multiple S cycle parameters along with the termination of the LIP stage of OJMHP as $\delta^{34}S_{sw}$ plateaus indicates that the ~20 Ma maintenance of low $\delta^{34}S_{sw}$ values represents a new alternate state and not persistence of a perturbation (Figs. 4-10 and 4-12) [Wortmann and Chernyavsky, 2007; Wortmann and Paytan, 2012]. The coupling of the Sr and S cycles highlights this notion of an alternate state in the need for minor increases in F_{py} and $\delta^{34}S_{tw}$ to accommodate changes related to the Late Aptian-Early Albian rise in the seawater $^{87}Sr/^{86}Sr$ ratio (Table 4-4 and Figs. 4-9a, 4-10, and 4-12).

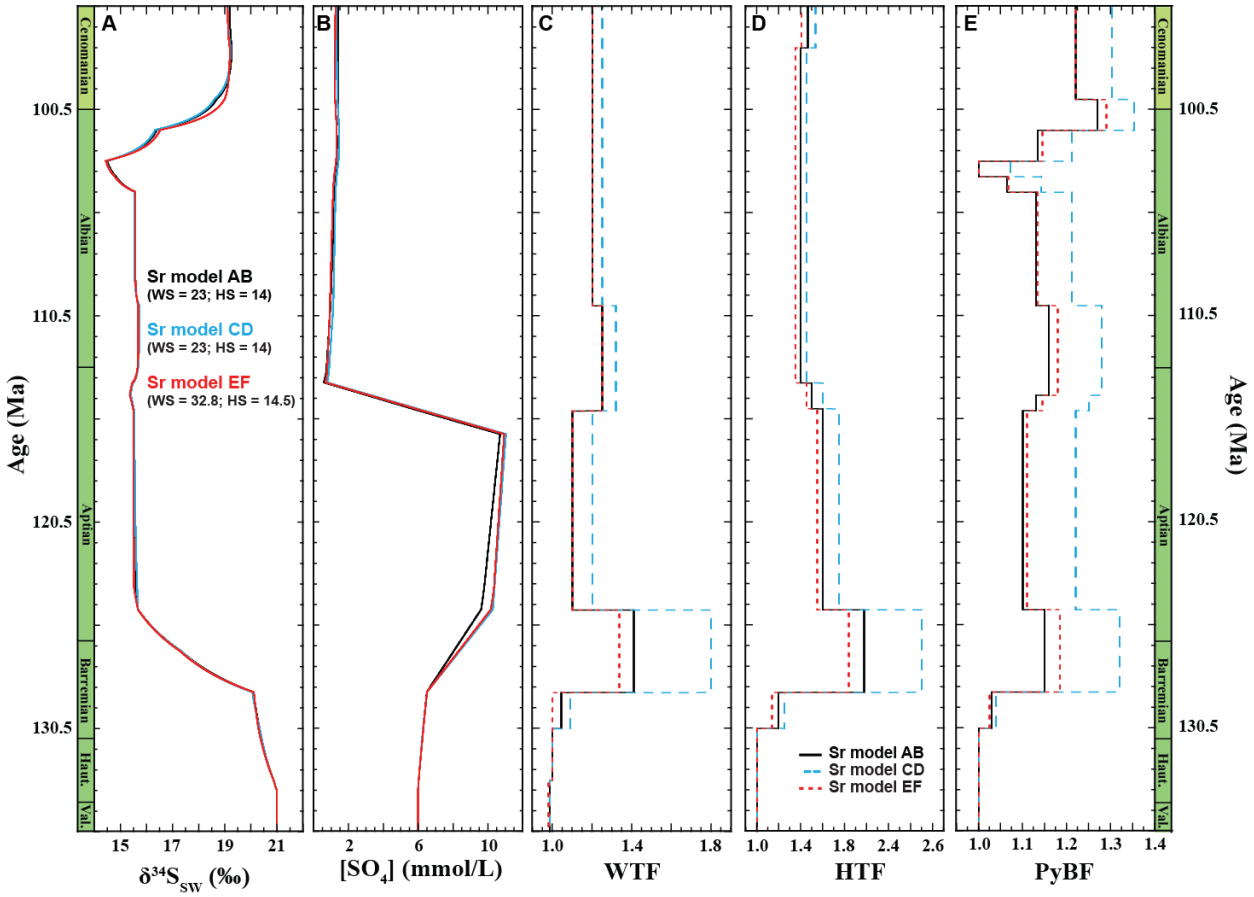

Figure 4-11 S cycle model results with variable Sr models

Modeled $\delta^{34}S_{sw}$ (**A**) and sulfate concentration (**B**) for Sulfur model 1 coupled to Sr models AB, CD, and EF at an initial sulfate concentration of 6 mmol/L (Tables 4-4 and 4-8). (**C-E**) Perturbation factors for total weathering (WTF), hydrothermal (HTF), and pyrite burial (PyBF) fluxes highlighting the major differences between the three coupled models. See Figures 4-12 and 4-14 for changes in $\Delta^{34}S_{py}$, $\delta^{34}S_{tw}$, and f_{py}.

In order to constrain the increase in sulfate concentrations following deposition of the Late Aptian South Atlantic Salts to appropriately low levels, it is necessary for F_{SO4} to eventually return to values greater than prior to the event (Fig. 4-10). The importance of this constraint is

clearly demonstrated in trying to match the rapid, successive negative and positive excursions in $\delta^{34}S_{sw}$ at the Albian-Cenomanian boundary with the different initial sulfate concentrations examined (Fig. 4-10). With the coupled modeling, the concurrence of these rapid, successive excursions in $\delta^{34}S_{sw}$ with a plateau in seawater $^{87}Sr/^{86}Sr$ ratios necessitates changes in S cycle output parameters to drive the perturbation (Figs. 4-6 and 4-9a). Major sea level changes exposing and flooding continental shelves and epicontinental seas (e.g., Western Interior Seaway) surrounding the Albian-Cenomanian boundary can produce rapid, significant fluctuations in F_{py} as these regions are primary deposition centers for pyrite [Kauffman, 1977; Holser et al., 1989; Lin and Morse, 1991; Kauffman and Caldwell, 1993; Immenhauser and Scott, 1999; Ogg and Hinnov, 2012; Bowles et al., 2014; Haq, 2014]. However, such rapid, large magnitude changes in $\delta^{34}S_{sw}$ as observed at the Albian-Cenomanian boundary require sulfate concentrations ≤1.5 mmol/L and residence times <1 Ma if they are to be driven by reasonable fluctuations in F_{py} (Figs. 4-6, 4-10, and 4-12). Slight increases in $\Delta^{34}S_{py}$ are also included in the model during the Albian-Cenomanian excursions in $\delta^{34}S_{sw}$ to modulate and maintain reasonable perturbation factors for F_{py} (Fig. 4-12). The increase in $\Delta^{34}S_{py}$ could result from changes in the distribution of pyrite burial throughout the ocean, an increase in sulfate concentrations, and/or physiological changes [Adams et al., 2010; Sim et al., 2011a, b; Leavitt et al., 2013; Bowles et al., 2014; Wing and Halevy, 2014; Bradley et al., 2016].

Sulfur model 1 is coupled with Sr models CD and EF to test the magnitude of the perturbation from the emplacement of OJMHP and the range of Sr riverine fluxes, respectively (Tables 4-4 and 4-8, Figs. 4-11, 4-12, and 4-14). Sulfate concentration sensitivity tests clearly indicate that an initial 6 mmol/L SO_4 ocean provides the best scenario for readily matching the observed $\delta^{34}S_{sw}$ record and reaching sufficiently low concentrations during the Mid- to Late-

Cretaceous (Fig. 4-10) [Gomes et al., 2016]. Therefore, an initial 6 mmol/L SO_4 ocean is used for the sulfur model 1 couplings with Sr models CD and EF along with all further models. To ensure a similar total input flux the scalars coupling S model 1 to Sr model EF are different from those for Sr models AB and CD. With a focus on identifying the most reasonable and likely range of values for the initial conditions and magnitude of perturbations the amount of change to the free parameters in S model 1 are adjusted so that coupling with Sr models CD and EF produce a match to the S isotope record (Fig. 4-11). This is helpful in demonstrating that the size of the perturbations to F_{ht} and F_{tw} in Sr model CD are sufficient to produce the ~5‰ negative shift in $\delta^{34}S_{sw}$ without requiring an excess S gas flux from OJMHP (Tables 4-4 and 4-8, and Fig. 4-11). In contrast, the size of the excess S gas flux from OJMHP required for Sr model EF is unreasonably large and is therefore dismissed as a possible solution (Table 4-8). This also implies that the global Sr riverine flux estimated by Palmer and Edmond (1989) is too low even when a significant submarine groundwater discharge flux is included (Table 4-4).

Ten different S models are coupled with the Sr models to test a range of different initial conditions. These S models are separated into two groups: models 1-6 have negative $\delta^{34}S_{tw}$ values whereas models 7-10 have positive $\delta^{34}S_{tw}$ values (Table 4-8 and 4-9 and Figs. 4-12 to 4-14). When coupled with Sr model AB, all S models require an excess S gas flux from OJMHP, while only the four S models with an initial positive $\delta^{34}S_{tw}$ require an excess S gas flux when coupled with Sr model CD (Table 4-8). As with S model 1, when coupled with Sr model EF the other nine S models also require an excessively large S gas flux from OJMHP that allows them to be dismissed as possible solutions (Table 4-8 and Fig. 4-14). With reduction in $\Delta^{34}S_{py}$ being constrained to ~-28‰ during the Mesozoic, models that have a low initial $\Delta^{34}S_{py}$ (#7 and #9) will require larger shifts in $\delta^{34}S_{tw}$ following the emplacement of OJMHP in order to maintain the low

Figure 4-12 Variable S cycle models with negative $\delta^{34}S_{tw}$ for Sr models AB and CD

Modeled $\delta^{34}S_{sw}$, sulfate concentration, pyrite burial factor (PyBF), $\Delta^{34}S_{py}$, $\delta^{34}S_{tw}$, and f_{py} for S models 1-6 coupled with Sr models AB (top panel) and CD (bottom panel) all with an initial sulfate concentration of 6 mmol/L (Tables 4-4, 4-8 and 4-9).

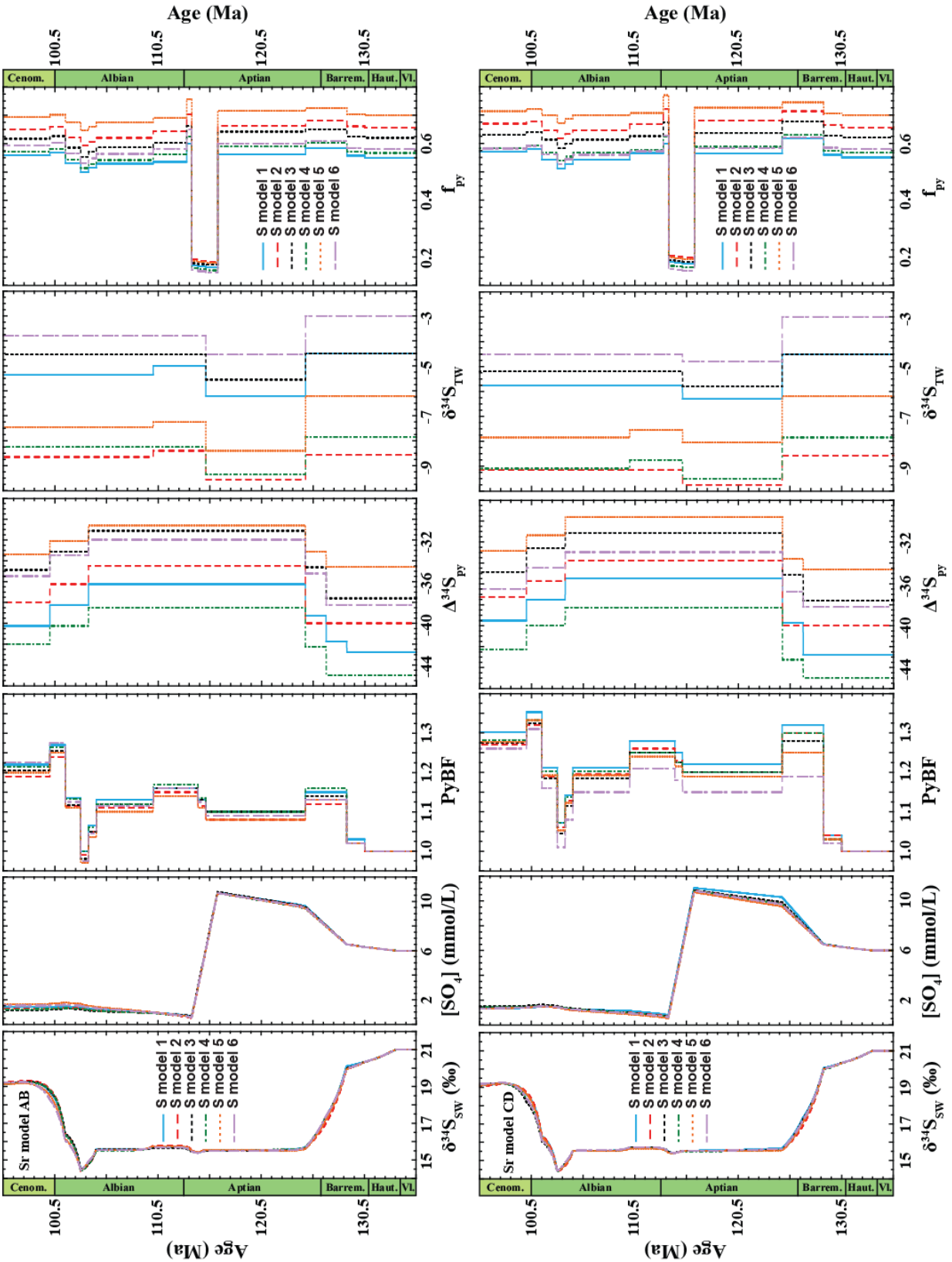
Age (Ma)
100.5
110.5
120.5
130.5
Cenom.
Albian
Aptian
Barrem.
Haut.
Vl.
S model 1
S model 2
S model 3
S model 4
S model 5
S model 6
f_{py}
$\delta^{34}S_{TW}$
$\Delta^{34}S_{py}$
PyBF
$[SO_4]$ (mmol/L)
$\delta^{34}S_{SW}$ (‰)
Sr model AB
Sr model CD

Figure 4-13 Variable S cycle models with positive $\delta^{34}S_{tw}$ for Sr models AB and CD

Modeled $\delta^{34}S_{sw}$, sulfate concentration, pyrite burial factor (PyBF), $\Delta^{34}S_{py}$, $\delta^{34}S_{tw}$, and f_{py} for S models 7-10 coupled with Sr models AB (top panel) and CD (bottom panel) all with an initial sulfate concentration of 6 mmol/L (Tables 4-4, 4-8 and 4-9).

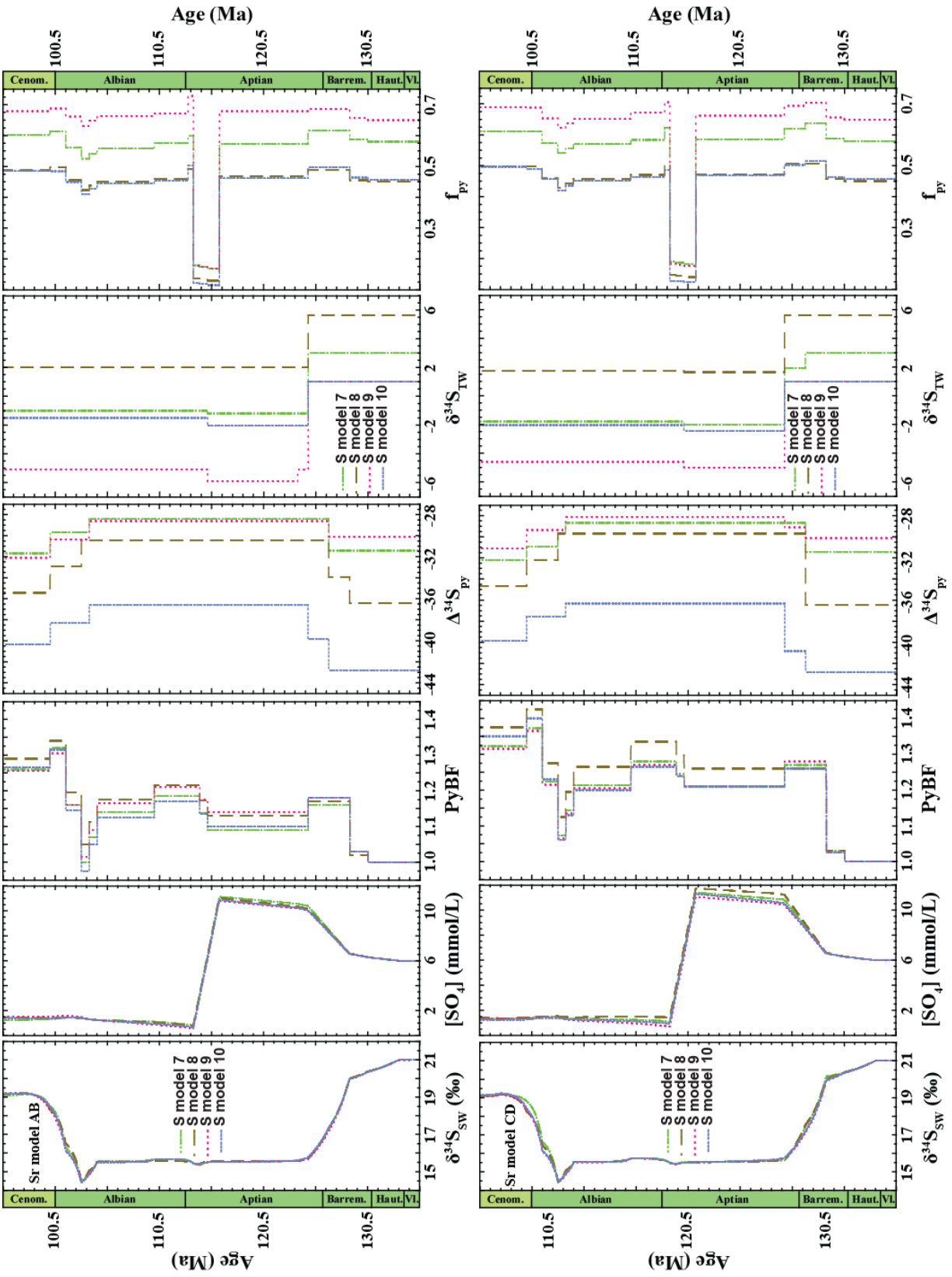
Age (Ma)
100.5
110.5
120.5
130.5
Cenom.
Albian
Aptian
Barrem.
Haut.
Vl.
f_{py}
$\delta^{34}S_{TW}$
S model 7
S model 8
S model 9
S model 10
$\Delta^{34}S_{py}$
PyBF
$[SO_4]$ (mmol/L)
$\delta^{34}S_{SW}$ (‰)
Sr model AB
Sr model CD
Age (Ma)

$\delta^{34}S_{sw}$ (Figs. 4-12 and 4-13) [Wu et al., 2010] The magnitude of $\delta^{34}S_{tw}$ change needed to maintain low $\delta^{34}S_{sw}$ following the ~5‰ negative shift amongst the four S models with an initial positive $\delta^{34}S_{tw}$ is comparatively much larger than that for models with an initial negative $\delta^{34}S_{tw}$ (0.98-2.2‰ vs. 3.05-6.91‰) (Figs. 4-12 and 4-13). The fact that three of the four S models with positive $\delta^{34}S_{tw}$ need to shift to negative values to produce a reasonable match to the S isotope record further supports the notion that $\delta^{34}S_{tw}$ has been negative or near 0‰ for most of the Phanerozoic [Holser et al., 1989; Halevy et al., 2012]. These large changes in $\delta^{34}S_{tw}$, along with the greater excess S gas flux required for the eight coupled models with an initial positive $\delta^{34}S_{tw}$ (Sr models AB and CD with S models 7-10), lead to their dismissal as possible solutions (Table 4-8 and Fig. 4-13). In addition, the low f_{py} values (<0.5) in S models 8 and 10 result in F_{py} values that are unreasonably low for a warm Cretaceous ocean with less dissolved oxygen than currently, further supporting their dismissal (Table 4-9). With OJMHP being the largest known LIP, it is plausible for the perturbation factors to reach a maximum, however, they still must remain realistic. A near doubling of F_{tw}, which is rather excessive and unlikely, coupled with the absence of a S gas flux from a massive oceanic plateau leads to S models 1-6 when coupled with Sr model CD providing an upper limit for the magnitude of the perturbations resulting from the emplacement of OJMHP (Tables 4-4 and 4-8 and Figs. 4-11 and 4-12).

The model results presented here indicate S cycle model parameter values for the Mesozoic that are distinctly different from those that have been used previously (Tables 4-8 to 4-10 and Fig. 4-12) [Arthur, 2000; Hansen and Wallmann, 2003; Kurtz et al., 2003; Canfield, 2004; Kampschulte and Strauss, 2004; Paytan et al., 2004; Wortmann and Chernyavsky, 2007; Adams et al., 2010; Wortmann and Paytan, 2012; Gomes et al., 2016]. Similar to Halevy et al., (2012), although not as extreme, the model results here suggest higher initial f_{py} values and

Figure 4-14 Variable S cycle models for Sr model EF

Modeled $\delta^{34}S_{sw}$, sulfate concentration, pyrite burial factor (PyBF), $\Delta^{34}S_{py}$, $\delta^{34}S_{tw}$, and f_{py} for S models 1-6 (top panel) and 7-10 (bottom panel) coupled with Sr model EF all with an initial sulfate concentration of 6 mmol/L (Tables 4-4, 4-8 and 4-9).

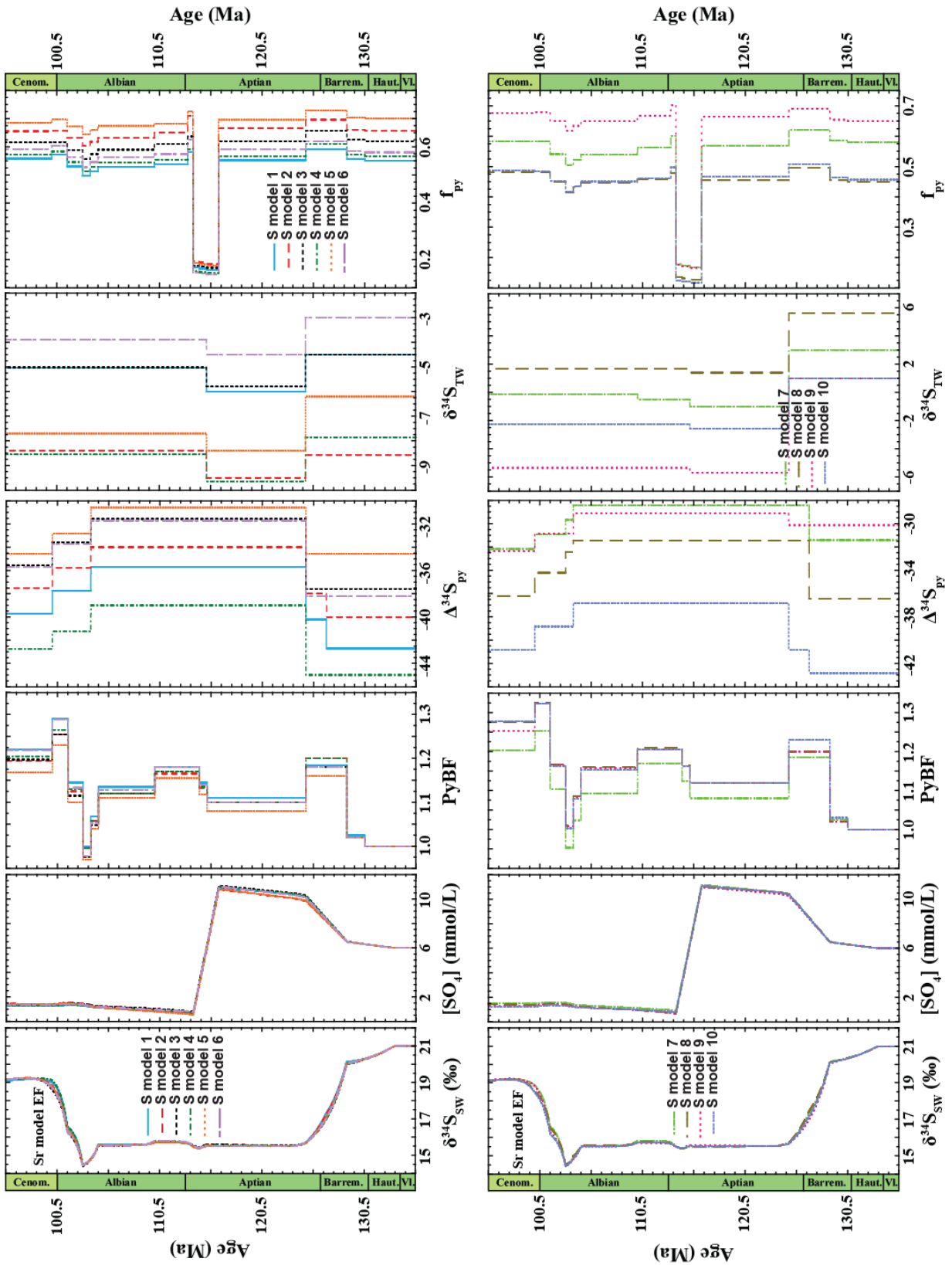
Age (Ma)
100.5
110.5
120.5
130.5
Cenom.
Albian
Aptian
Barrem.
Haut.
Val.
S model 1
S model 2
S model 3
S model 4
S model 5
S model 6
S model 7
S model 8
S model 9
S model 10
Sr model EF
f_{py}
$\delta^{34}S_{TW}$
$\Delta^{34}S_{py}$
PyBF
$[SO_4]$ (mmol/L)
$\delta^{34}S_{SW}$ (‰)

Table 4-10. Comparison of key S cycle parameter initial condition values for the Mesozoic proposed by this study and those used in previous models. E:P is the weathered evaporite to weathered pyrite ratio. % SRR represents the pyrite burial flux fraction of the revised modern global sulfate reduction rate (SRR) of 11.3 Tmol/yr by Bowles et al. (2014). tw – total weathering

	$\delta^{34}S_{tw}$ (‰)	E:P	f_{py}	% SRR	$\Delta^{34}S_{py}$ (‰)
Previous	~6	2	~0.45	≤8	30-35
This Study	-6 to 0	0.25-1	0.55-0.65	9-11	35-45

$\delta^{34}S_{tw}$ should be slightly negative or near zero instead of ~6‰ (Tables 4-7 to 4-10 and Fig. 4-12). Because the possibility of additional sulfate sinks – barite and deep crustal hydrothermal anhydrite – are considered instead of just evaporite deposition, this study suggests an initial f_{py} range of 0.55-0.65 compared to 0.7-0.9 as proposed by Halevy et al. (2012). These higher f_{py} values result in F_{py} values that are in line with ~10% burial of the recent estimates for modern global MSR rates and reduce the magnitude of the F_{py} perturbation factor needed to match rapid excursions in $\delta^{34}S_{sw}$ [Jorgensen, 1982; Canfield, 1991; Lin and Morse, 1991; Turchyn and Schrag, 2004, 2006; Adams et al., 2010; Bowles et al., 2014; Gomes et al., 2016]. The higher f_{py} values and the negative $\delta^{34}S_{tw}$ used in these models also require a slightly larger $\Delta^{34}S_{py}$ (-35‰ to -45‰) than typically used by others (-35 to -30‰) [Arthur, 2000; Kurtz et al., 2003; Paytan et al., 2004; Wortmann and Chernyavsky, 2007; Adams et al 2010; Wortmann and Paytan, 2012; Gomes et al., 2016]. These higher $\Delta^{34}S_{py}$ values, however, are in line with the arithmetic difference from global compilations of $\delta^{34}S$ sulfate and contemporaneous pyrite for the Mesozoic-Cenozoic [Wu et al., 2010]. With fractionations of -60‰ to -70‰ characterizing the open, deep ocean (Fig. 4-8), along with 30-40% of the total MSR occurring in such regions than it is possible to produce global $\Delta^{34}S_{py}$ values of -35‰ to -45‰ with fractionations as low as -15‰ to -25‰ dominating shallow marine environments [Bowles et al., 2014].

Results from the models presented here, similar to Gomes et al. (2016), clearly demonstrate that the emplacement of OJMHP is the initial source mechanism causing changes in the S cycle that drives the geologically rapid ~5‰ negative shift of the Early Cretaceous. The revised timing of the South Atlantic Salts to the Late Aptian removes any question of its potential influence on producing this major isotopic shift [Wortmann and Chernyavsky, 2007; Chaboureau et al., 2012, 2013; Wortmann and Paytan, 2012; Gomes et al., 2016]. While the deposition of the Late Aptian South Atlantic Salts is key for producing the low sulfate concentrations necessary for the rapid, successive excursions in $\delta^{34}S_{sw}$ near the Albian-Cenomanian boundary it does not directly or indirectly cause a change in the $\delta^{34}S_{sw}$. In contrast to Wortmann and Chernyavsky (2007), the coupled Sr-S modeling requires a minor increase in F_{py} during the evaporite deposition to compensate the increased F_{tw} responsible for the Late Aptian-Albian rise in the seawater $^{87}Sr/^{86}Sr$ ratio despite decreasing sulfate concentrations (Figs. 4-9a, 4-11 and 4-12). As was the case with the Sr cycle (see Chapter 3), the impact of OJMHP on the S cycle is not singular in just increasing the F_{ht} and S gas flux, but also impacting F_{tw}, F_{py} and $\Delta^{34}S_{py}$ either directly or through a cascade of effects (Figs. 4-11 to 4-13). Similar to Sr, changes in $\delta^{34}S_{tw}$ are the result of erosion of the land surface changing the proportion of pyrite and evaporite (sulfate minerals) exposed to weathering along with the increased weathering of geologically recent evaporite deposition with lower $\delta^{34}S$ values [Halevy et al., 2012; Chapter 3 this thesis]. This complex interplay of changes to multiple S cycle parameters is necessary to reasonably produce the major Barremian-Aptian and Albian-Cenomanian $\delta^{34}S_{sw}$ excursions along with maintaining low $\delta^{34}S_{sw}$ values for nearly 20 Ma and establishing low sulfate concentrations necessary for the Mid- to Late-Cretaceous (Figs. 4-11 and 4-12).

4.8. Conclusions

While building upon the Early Cretaceous S isotope record for both barite and pyrite, this study expands the development of coupled Sr-S cycle modeling clearly demonstrating the value of the additional constraint from coupling linked biogeochemical cycles. The linkage of the S and Sr cycles through their primary input fluxes – F_{ht} and F_{tw} – allows for differentiating which parameters dominate concurrent (input) and divergent (output) perturbations to their isotopic records. Constraining the linked parameters with constant scalars readily enables examination of a range of initial condition values. This leads to the dismissal of models with positive $\delta^{34}S_{tw}$ and the lower Sr F_{tw} derived from Palmer and Edmond (1989) as being unable to reasonably reproduce both isotopic records during the Early Cretaceous. The requirement to match both isotopic records with the constrained linked parameters also reveals differences in the chemical behavior of S and Sr as evidenced by the need for an additional S gas flux from OJMHP along with the increased F_{ht}. Model results also suggest a distinctly different range of $\delta^{34}S_{tw}$ values, weathered evaporite-pyrite ratios, f_{py}, and $\Delta^{34}S_{py}$ during the Mesozoic compared to those used in previous S cycle models. In addition, the larger $\Delta^{34}S_{py}$ values proposed here are supported by the large fractionations (≤-60‰) observed from the deep, open ocean drill cores presented in this study. With changes to the F_{ht} and F_{tw} constrained by the Sr isotope record and a constant scalar, the coupling of the S and Sr cycles allows for the impact of variations to other variables within the S cycle to be demonstrated. As the model results indicate, the geologically rapid Early Cretaceous ~5‰ negative shift in $\delta^{34}S_{sw}$ and the long term maintenance of low $\delta^{34}S_{sw}$ values is the result of a complex interplay of changes to multiple S cycle parameters – not simply F_{ht} and F_{tw}. The coupled modeling and changes to multiple S cycle parameters during the ~20 Ma isotopically light sulfate ocean clearly distinguishes this period as a distinct alternate state and

not the persistence of the ~5‰ negative excursion. In addition, the model results further support the necessity of low sulfate concentrations (≲1.5 mmol/L) during the Mid- to Late-Cretaceous to allow for large, rapid shifts in $\delta^{34}S_{sw}$. This study also demonstrates the usefulness of coupling the Sr cycle (assuming no mass dependent fractionation) to biogeochemical cycles that share F_{ht} and F_{tw} as their dominant input fluxes. The coupling with the Sr cycle provides the capacity to differentiate which parameters dominate a perturbation (see guiding principles) and enables focus on the impact of variations in parameters other than F_{ht} and F_{tw} within the coupled biogeochemical cycle.

CHAPTER 5

CONCLUSION

In this dissertation I explored the dynamics of the marine S and Sr cycles under a shifting climate state with major tectonic and oceanographic reorganization during the Early Cretaceous. With its strong connections to the carbon, oxygen, iron, and phosphorus cycles, the S cycle is a key component in determining ocean redox conditions and influencing climate conditions. While not as tightly coupled through biological processes, the marine Sr cycle, which primarily records a balance between weathering and hydrothermal inputs provides an excellent constraint to the sulfur and other biogeochemical cycles linked via common input fluxes.

The timing of the major geologic and climatic transformations during the Early Cretaceous are key to properly understanding and aligning geochemical and sedimentological records from this time period. In Chapter 2, I review the evidence for a cool greenhouse during the Early Cretaceous from a tillite and glacial dropstones in southern Australia to glendonites and oxygen isotope records from both hemispheres. In light of the recent Geologic Time Scale 2012 and refinements in standards for radiometric timing I also review the timing of Early Cretaceous LIPs, OAEs, and deposition of the South Atlantic Salts in addition to updating the necessary age models for the composite marine barite S isotope record by Paytan et al. (2004).

In order to properly couple the Sr and S cycle box models and fully utilize the additional constraint this coupling can provide it was necessary to revise how to model $R_{87,sw}$ in the geologic past. While uniformitarianism underlies many aspects of the Earth sciences, modeling geochemical cycles throughout Earth history requires critically assessing the reliability and constancy of projecting modern fluxes and their isotope ratios into deep geologic time. In Chapter 3, I present an iterative technique utilizing the composite radiogenic strontium isotope

record of McArthur et al. (2012) as a constraint and tool in determining estimates for the Sr isotope ratio of the input fluxes. This method goes beyond trying to match the general structure of composite record, but focuses on matching $\frac{d}{dt}R_{SW}$, minimizing the step size within the set of prescribed $R_{87,tw}$ values along with matching target seawater $^{87}Sr/^{86}Sr$ values. In contrast to previous Sr cycle models I clearly demonstrate that a single prescribed $R_{87,tw}$ value, even when appropriately estimated for the time period of interest, does not produce a reasonable match to the record. Instead, the model results support using a variable $R_{87,tw}$ that changes every 1-2.5 Ma. Such high frequency variation for $R_{87,tw}$ is in line with average denudation rates altering the landscape within watersheds and astronomically driving changes in the climate. This proposed frequency at which $R_{87,tw}$ varies is specific to the Late Jurassic-Early Cretaceous time period examined in this study and can differ throughout the Phanerozoic depending on the rate of change of the seawater Sr isotope record ($\frac{d}{dt}R_{87,sw}$) and the residence time of Sr.

With growing evidence for significant variation in seawater concentrations throughout the Phanerozoic, claims for a 450 µmol/L Sr concentration during the Cretaceous in contrast to the modern 90 µmol/L concentrations were tested and validated with the new Sr cycle model. Such wide ranging variability in seawater Sr concentrations in the geologic past becomes a critical variable since Sr behaves conservatively during hydrothermal circulation through the oceanic crust resulting in the hydrothermal flux scaling linearly with seawater Sr concentration. Therefore, holding the modern residence time constant throughout the geologic past is no longer a reasonable assumption and calls for improved estimates of Sr burial fluxes.

Recent observations on the flux magnitude and potential global impact of both submarine groundwater discharge and dissolution of the riverine particulate load upon entering the ocean

for Sr has led to their combination with the dissolved riverine flux into a total weathering flux for this model. With the majority of submarine groundwater discharge coming from coastal carbonate platforms and volcanic islands along with mafic particles dominating the particulate riverine load, this contributes to lower (more radiogenic) $^{87}Sr/^{86}Sr$ ratios for the global total weathering flux.

Utilizing recent tectonic reconstructions of OJMHP and the recently revised definition for LIPs along with a focus on matching $\frac{d}{dt}R_{SW}$ the model results demonstrated that the Barremian-Aptian decrease in seawater $^{87}Sr/^{86}Sr$ ratios required variable increases in both the hydrothermal and total weathering fluxes plus changes in the $R_{87,tw}$. The tectonic reconstructions of OJMHP and the revised definition for LIPs also indicate that OJMHP is not solely responsible for the Barremian-Aptian decrease in seawater $^{87}Sr/^{86}Sr$ ratios. The maintenance of elevated hydrothermal and weathering fluxes following the end of the LIP stage of OJMHP necessary to continue the decrease in seawater $^{87}Sr/^{86}Sr$ ratios is thought to be related to the emplacement of the Kerguelen Plateau, elevated MOR spreading rates and increased continental arc volcanism. In addition, the weathering of more mafic material from the increased continental arc volcanism and prior Early Cretaceous LIPs would contribute to lowering the $R_{87,tw}$, further assisting the continued decrease in seawater $^{87}Sr/^{86}Sr$ ratios.

Expansion of the Early Cretaceous marine barite S isotope record presented here raises questions regarding the timing, structure, and spatial heterogeneity of the Barremian-Aptian ~5‰ negative shift and identifies a rapid ~1‰ negative shift immediately preceding the large, rapid positive shift surrounding the Albian-Cenomanian boundary. The highly ^{34}S-depleted pyrite isotope record from deep, open ocean drill cores presented here supports culture

experiments and theoretical calculations indicating large fractionations (60-70‰) by microbial sulfate reducers under limiting and slow physiological conditions.

In coupling the Sr and S cycle models I examined ten different initial conditions for the S cycle linked to three different scenarios for the Sr cycle along with a range of constant scalars linking the hydrothermal and total weathering fluxes. The linkage of the S and Sr cycles through these dominant input fluxes allows for differentiating which parameters dominate concurrent (input) and divergent (output) perturbations to their isotopic records. Considering that any model can be adjusted to match the data, the purpose of examining 30 different model scenarios was to identify the most reasonable and likely range of values for the initial conditions and magnitude of perturbations to the various parameters. With changes to the hydrothermal and total weathering fluxes constrained by the Sr isotope record and a constant scalar, the coupling of the S and Sr cycles allows for examining the impact that variation in other variables has on the S cycle. In addition, this linkage and constraint to match both isotopic records demonstrated differences in the chemical behavior of S and Sr as evidenced by the need for an additional S gas flux from OJMHP along with the increased F_{ht}. Testing a range of different model scenarios clearly demonstrated that models with the lower Sr F_{tw} derived from Palmer and Edmond (1989) or a positive $\delta^{34}S_{tw}$ did not reasonably reproduce both isotopic records leading to their dismissal as possible solutions (18 of 30 model scenarios). The model results also suggest a distinctly different range of values for $\delta^{34}S_{tw}$, weathered evaporite-pyrite ratios, f_{py}, and $\Delta^{34}S_{py}$ during the Mesozoic compared to those used in previous S cycle models.

While OJMHP was the principle driver for the geologically rapid Early Cretaceous ~5‰ negative shift in $\delta^{34}S_{sw}$, the model results presented here demonstrate that this excursion and the maintenance of low $\delta^{34}S_{sw}$ for ~20 Ma resulted from a complex interplay of changes to multiple

S cycle parameters, not just F_{ht} and F_{tw}. In conjunction with rifting of OJMHP marking the end of LIP phase construction starting in the Early Aptian, the coupled modeling clearly distinguishes the Aptian-Albian isotopically light sulfate ocean as a distinct alternate state and not persistence of the Barremian-Aptian negative excursion. In addition, the excursions in $\delta^{34}S_{barite}$ surrounding the Albian-Cenomanian boundary are thought to represent a separate and distinct perturbation instead of recovery from termination of the Barremian-Aptian perturbation. Model results indicate that the successive, geologically rapid excursions at the Albian-Cenomanian boundary can be the result of changes in the pyrite burial flux associated with fluctuations in sea level if sulfate concentrations are sufficiently low ($\lesssim$1.5 mmol/L). Such low sulfate concentrations resulting from the deposition of the Late Aptian South Atlantic Salts are thought to persist and be characteristic of the Late Cretaceous.

Marine biogeochemical cycles are complex and highly interwoven with one another. This study has clearly demonstrated the usefulness of coupling the Sr cycle (assuming no mass dependent fractionation) to the S cycle. The improved constraints and more representative method of modeling the Sr cycle during the Phanerozoic presented here should lead to more enhanced coupled modeling of biogeochemical cycles that share F_{ht} and F_{tw} as their dominant input fluxes, thus enabling paleoclimatic and paleoceanographic reconstructions.

References

Adams, D. D., Hurtgen, M. T., & Sageman, B. B. (2010). Volcanic triggering of a biogeochemical cascade during Oceanic Anoxic Event 2. *Nature Geoscience, 3*, 201-204.

Aguirre-Urreta, M. B., Pazos, P. J., Lazo, D. G., Mark Fanning, C., & Litvak, V. D. (2008). First U–Pb SHRIMP age of the Hauterivian stage, Neuquén Basin, Argentina. *Journal of South American Earth Sciences, 26*(1), 91-99.

Allegre, C. J., Louvat, P., Gaillardet, J., Meynadier, L., Rad, S., & Capmas, F. (2010). The fundamental role of island arc weathering in the oceanic Sr isotope budget. *Earth and Planetary Science Letters, 292*, 51-56.

Alley, N. F., & Frakes, L. A. (2003). First known Cretaceous glaciation: Livingston Tillite Member of the Cadna-owie Formation, South Australia. *Australian Journal of Earth Sciences, 50*, 139-144.

Alt, J. C., Davidson, G. J., Teagle, D. A. H., & Karson, J. A. (2003). Isotopic composition of gypsum in the Macquarie Island ophiolite: Implications for the sulfur cycle and the subsurface biosphere in oceanic crust. *Geology, 31*(6), 549.

Alt, J. C., Garrido, C. J., Shanks, W. C., Turchyn, A., Padrón-Navarta, J. A., López Sánchez-Vizcaíno, V., Gomez Pugnaire, M. T., & Marchesi, C. (2012). Recycling of water, carbon, and sulfur during subduction of serpentinites: A stable isotope study of Cerro del Almirez, Spain. *Earth and Planetary Science Letters, 327-328*, 50-60.

Alt, J. C., Schwarzenbach, E. M., Früh-Green, G. L., Shanks, W. C., Bernasconi, S. M., Garrido, C. J., Crispini, L., Gaggero, L., Padron-Navarta, J. A., & Marchesi, C. (2013). The role of serpentinites in cycling of carbon and sulfur: Seafloor serpentinization and subduction metamorphism. *Lithos, 178*, 40-54.

Alt, J. C., & Shanks, W. C. (2011). Microbial sulfate reduction and the sulfur budget for a complete section of altered oceanic basalts, IODP Hole 1256D (eastern Pacific). *Earth and Planetary Science Letters, 310*, 73-83.

Alt, J. C., Shanks, W. C., & Jackson, M. C. (1993). Cycling of sulfur in subduction zones: The geochemistry of sulfur in the Mariana Island Arc and back-arc trough. *Earth and Planetary Science Letters, 119*, 477-494.

Altis, S. (1999). Origin and tectonic evolution of the Caroline Ridge and the Sorol Trough, western tropical Pacific, from admittance and a tectonic modeling analysis. *Tectonophysics, 313*, 271-292.

Ando, A., Huber, B. T., & Premoli Silva, I. (2013). *Paraticinella rohri* (Bolli, 1959) as the valid name for the latest Aptian zonal marker species of planktonic foraminifera traditionally called *bejaouaensis* or *eubejaouaensis*. *Cretaceous Research, 45*, 275-287.

Andres, R. J., & Kasgnoc, A. D. (1998). A time-averaged inventory of subaerial volcanic sulfur emissions. *Journal of Geophysical Research, 103*, 25,251-225,261.

Andrews, M. G., Jacobson, A. D., Lehn, G. O., Horton, T. W., & Craw, D. (2016). Radiogenic and stable Sr isotope ratios ($^{87}Sr/^{86}Sr$, $\delta^{88/86}Sr$) as tracers of riverine cation sources and biogeochemical cycling in the Milford Sound region of Fiordland, New Zealand. *Geochimica et Cosmochimica Acta, 173*, 284-303.

Anthonissen, D. E., & Ogg, J. G. (2012). Cenozoic and Cretaceous biochronology of planktonic foraminifera and calcareous nannofossils. In F. M. Gradstein, J. G. Ogg, M. Schmitz, & G. M. Ogg (Eds.), *The Geologic TIme Scale 2012* (Vol. 2, pp. 1083-1127). New York: Elsevier.

Arnaud, H. M., Flood, P. G., & Strasser, A. (1995). Resolution Guyot (Hole 866A, Mid-Pacific Mountains): Facies evolution and sequence stratigraphy. In E. L. Winterer, W. W. Sager, J. V. Firth, & J. M. Sinton (Eds.), *Proceedings of the Ocean Drilling Program, Scientific Results* (Vol. 143, pp. 133--159). College Station, Texas: Ocean Drilling Program.

Arnaud-Vanneau, A., & Sliter, W. V. (1995). Early Cretaceous shallow-water benthic foraminifers and fecal pellets from Leg 143 compared with coeval faunas from the Pacific Basin, Central America and the Tethys. In E. L. Winterer, W. W. Sager, J. V. Firth, & J. M. Sinton (Eds.), *Proceedings of the Ocean Drilling Program, Scientific Results* (Vol. 143, pp. 537-564). College Station, Texas: Ocean Drilling Program.

Arthur, M. A. (2000). Volcanic contributions to the carbon and sulfur geochemical cycles and global change. In H. Sigurdsson, B. F. Houghton, S. R. McNutt, H. Rymer, & J. Stix (Eds.), *Encyclopedia of Volcanoes* (pp. 1045-1056). New York: Academic Press.

Arthur, M. A., Dean, W. E., & Pratt, L. M. (1988). Geochemical and climatic effects of increased marine organic carbon burial at the Cenomanian/Turonian boundary. *Nature, 335*, 714-717.

Bagard, M.-L., Chabaux, F., Pokrovsky, O. S., Viers, J., Prokushkin, A. S., Stille, P., Rihs, S. Schmitt, A.-D., & Dupre, B. (2011). Seasonal variability of element fluxes in two Central Siberian rivers draining high latitude permafrost dominated areas. *Geochimica et Cosmochimica Acta, 75*, 3335-3357.

Basu, A. R., Jacobsen, S. B., Poreda, R. J., Dowling, C. B., & Aggarwal, P. K. (2001). Large groundwater strontium flux to the oceans from the Bengal Basin and the marine strontium isotope record. *Science, 293*, 1470-1473.

Baudin, F., & Riquier, L. (2014). The Late Hauterivian Faraoni 'Oceanic Anoxic Event': an update. *Bulletin de la Societe Geologique de France, 185*, 359-377.

Beck, A. J., Charette, M. A., Cochran, J. K., Gonneea, M. E., & Peucker-Ehrenbrink, B. (2013). Dissolved strontium in the subterranean estuary - Implications for the marine strontium isotope budget. *Geochimica et Cosmochimica Acta, 117*, 33-52.

Bennett, S. A., Achterberg, E. P., Connelly, D. P., Statham, P. J., Fones, G. R., & German, C. R. (2008). The distribution and stabilisation of dissolved Fe in deep-sea hydrothermal plumes. *Earth and Planetary Science Letters, 270*(3-4), 157-167.

Bergen, J. A. (1994). Berriasian to Early Aptian calcareous nannofossils from the Vocontian Trough (SE France) and Deep Sea Drilling Site 534: New nannofossil taxa and a summary of low-latitude biostratigraphic events. *Journal of Nannoplankton Research, 16*, 59-69.

Berner, E. K., & Berner, R. A. (1996). *Global Environment: Water, Air, and Geochemical Cycles*. Upper Saddle River, New Jersey: Prentice Hall.

Berner, R. A., & Rye, D. M. (1992). Calculation of the Phanerozoic strontium isotope record of the oceans from a carbon cycle model. *American Journal of Science, 292*, 136-148.

Bersezio, R., Erba, E., Gorza, M., & Riva, A. (2002). Berriasian-Aptian black shales of the Maiolica formation (Lombardian Basin, Southern Alps, Northern Italy): local to global events. *Palaeogeography, Palaeoclimatology, Palaeoecology, 180*, 253-275.

Blakey, R. (2011). Colorado Plateau Geosystems, Inc. Retrieved from http://cpgeosystems.com/index.html

Blum, J. D. (1997). The Effect of Late Cenozoic Glaciation and Tectonic Uplift on Silicate Weathering rates and the Marine $^{87}Sr/^{86}Sr$ Record. In W. F. Ruddiman (Ed.), *Tectonic Uplift and Climate Change* (pp. 259-288). New York: Plenum Press.

Blum, J. D., & Erel, Y. (1997). Rb-Sr isotope systematics of granitic soil chronosequence: The importance of biotite weathering. *Geochimica et Cosmochimica Acta, 61*, 3193-3204.

Bluth, G. J. S., Schnetzler, C. C., Krueger, A. J., & Walter, L. S. (1993). The contribution of explosive volcanism to global atmospheric sulfur dioxide concentrations. *Nature, 366*, 327-329.

Bots, P., Benning, L. G., Rickaby, R. E. M., & Shaw, S. (2011). The role of SO_4 in the switch from calcite to aragonite seas. *Geology, 39*, 331-334.

Bottini, C., Cohen, A. S., Erba, E., Jenkyns, H. C., & Coe, A. L. (2012). Osmium-isotope evidence for volcanism, weathering, and ocean mixing during the early Aptian OAE 1a. *Geology, 40*(7), 583-586.

Boucot, A. J., Xu, C., & Scotese, C. R. (2013). *Phanerozoic Paleoclimate: An Atlas of Lithologic Indicators of Climate*. Tulsa, Oklahoma: SEPM.

Bowles, M. W., Mogollon, J. M., Kasten, S., Zabel, M., & Hinrichs, K.-U. (2014). Global rates of marine sulfate reduction and implication for sub-sea-floor metabolic activities. *Science, 344*, 889-891.

Bown, P. R. (2005). Early to Mid-Cretaceous calcareous nannoplankton from the Northwest Pacific Ocean, Leg 198, Shatsky Rise. In T. J. Bralower, I. Premoli Silva, & M. J. Malone (Eds.), *Proceedings of the Ocean Drilling Program, Scientific Results* (Vol. 198, pp. 1-82). College Station, TX: Ocean Drilling Program.

Bown, P. R., & Concheyro, A. (2004). Lower Cretaceous calcareous nannoplankton from the Neuquén Basin, Argentina. *Marine Micropaleontology, 52*(1-4), 51-84.

Bown, P. R., Rutledge, D. C., Crux, J. A., & Gallagher, L. T. (1998). Lower Cretaceous. In P. R. Bown (Ed.), *Calcareous Nannofossil Biostratigraphy*. London: Chapman & Hall.

Bradley, A. S., Leavitt, W. D., & Johnston, D. T. (2011). Revisiting the dissimilatory sulfate reduction pathway. *Geobiology, 9*(5), 446-457.

Bradley, A. S., Leavitt, W. D., Schmidt, M., Knoll, A. H., Girguis, P. R., & Johnston, D. T. (2016). Patterns of sulfur isotope fractionation during microbial sulfate reduction. *Geobiology, 14*(1), 91-101.

Bralower, T. J. (1988). Calcareous nannofossil biostratigraphy and assemblages of the Cenomanina-Turonian boundary interval: Implications for the origin and timing of oceanic anoxia. *Paleoceanography, 3*, 275-316.

Bralower, T. J. (1992). Stable isotopic, assemblage, and paleoenvironmental investigations of juvenile-ocean sediments recovered on Leg 122, Wombat Plateau, northwest Australia. In U. von Rad, B. U. Haq, & e. al. (Eds.), *Proceedings of the Ocean Drilling Program, Scientific Results* (Vol. 122, pp. 569-585). College Station, TX: Ocean Drilling Program.

Brantley, S. L., Chesley, J. T., & Stillings, L. L. (1998). Isotopic ratios and release rats of strontium measured from weathering feldspars. *Geochimica et Cosmochimica Acta, 62*, 1493-1500.

Brass, G. W. (1976). The variation of the marine $^{87}Sr/^{86}Sr$ ratio during Phanerozoic time: interpretation using a flux model. *Geochimica et Cosmochimica Acta, 40*, 721-730.

Brassell, S. C., Dumitrescu, M., & SSP, L. (2004). Recognition of alkenones in a lower Aptian porcellanite from the west-central Pacific. *Organic Geochemistry, 35*(2), 181-188.

Browning, E. L., & Watkins, D. K. (2008). Elevated primary productivity of calcareous nannoplankton associated with ocean anoxic event 1b during the Aptian/Albian transition (Early Cretaceous). *Paleoceanography, 23*(2), doi:10.1029/2007pa001413

Brunner, B., & Bernasconi, S. M. (2005). A revised isotope fractionation model for dissimilatory sulfate reduction in sulfate reducing bacteria. *Geochimica et Cosmochimica Acta, 69*(20), 4759-4771.

Bryan, S. (2007). Silicic large igneous provinces. *Episodes, 30*, 20-31.

Bryan, S. E., & Ernst, R. E. (2008). Revised definition of large igneous provinces (LIPs). *Earth Science Reviews, 86*, 175-202.

Bryan, S. E., & Ferrari, L. (2013). Large igneous provinces and silicic large igenous provinces: Progress in our understanding over the last 25 years. *GSA Bulletin, 125*, 1053-1078.

Bryan, S. E., Riley, T. R., Jerram, D. A., Stephans, C. J., & Leat, P. T. (2002). Silicic volcanism: An undervalued component of large igneous provinces and volcanic rifted margins. In M. A. Menzies, S. L. Klemperer, C. J. Ebinger, & J. Baker (Eds.), *Volcanic Rifted Margins* (Vol. 362, pp. 99-120). Boulder, CO: Geological Society of America.

Buchan, K. L., & Ernst, R. E. (2006). Giant dyke swarms and the reconstruction of the Canadian Arctic islands, Greenland, Svalbard and Franz Josef Land. In E. Hanski, S. Mertanen, T. Ramo, & J. Vuillo (Eds.), *Dike Swarsm: Time Markers of Crustal Evolution* (pp. 27-48). Rotterdam, Netherlands: Taylor and Francis/Balkema.

Bukry, D. (1975). Coccolith and silicoflagellate stratigraphy, Northwestern Pacific Ocean, Deep Sea Drilling Project Leg 32. In R. L. Larson, R. Moberly, & e. al. (Eds.), *Initial Reports of the Deep Sea Drilling Project* (Vol. 32, pp. 677-701). Washington, DC: US Government Printing Office.

Bulot, L. G., Thieuloy, J.-P., Blanc, E., & Klein, J. (1992). The stratigraphic frame of the Late Valanginian and Hauterivian of South-East France: Definition of the ammonite biochronozones and recognition of new biohorizons. *Geologie Alpine, 68*, 13-56.

Burke, K., & Sengor, A. M. C. (1988). Ten metre global sea-level change associated with South Atlantic Aptian Salt deposition. *Marine Geology, 83*, 309-312.

Burnett, J. A., Gallagher, L. T., & Hampton, M. J. (1998). Upper Cretaceous. In P. R. Bown (Ed.), *Calcareous Nannofossil Biostratigraphy* (pp. 132-199). London: Chapman & Hall.

Butterfield, D. A., Nelson, B. K., Wheat, G., Mottl, M. J., & Roe, K. K. (2001). Evidence for basaltic Sr in midocean ridge-flank hydrothermal systems and implications for the global oceanic Sr isotope balance. *Geochimica et Cosmochimica Acta, 66*, 4141-4153.

Calmels, D., Gaillardet, J., Brenot, A., & France-Lanord, C. (2007). Sustained sulfide oxidation by physical erosion processes in the Mackenzie River basin: Climatic perspectives. *Geology, 35*(11), 1003.

Cameron, E. M., Hall, G. E. M., Veizer, J., & Krouse, H. R. (1995). Isotopic and elemental hydrogeochemistry of a major river system: Fraser River, British Columbia, Canada. *Chemical Geology, 122*, 149-169.

Canfield, D. E. (2004). The evolution of the Earth surface sulfur reservoir. *American Journal of Science, 304*, 839-861.

Canfield, D. E., & Farquhar, J. (2009). Animal evolution, bioturbation, and the sulfate concentration of the oceans. *Proc Natl Acad Sci U S A, 106*(20), 8123-8127.

Canfield, D. E., Raiswell, R., Westrich, J. T., Reaves, C. M., & Berner, R. A. (1986). The use of chromium reduction in the analysis of reduced inorganic sulfur in sediments and shales. *Chemical Geology, 54*, 149-155.

Caron, M. (1975). Late Cretaceous planktonic foraminifera from the Northwestern Pacific" Leg 32 of the Deep Sea Drilling Project. In R. L. Larson, R. Moberly, & e. al. (Eds.), *Initial Reports of the Deep Sea Drilling Project* (Vol. 32, pp. 719-724). Washington, DC: US Government Printing Office.

Caron, M., Dall'Agnolo, S., Accarie, H., Barrera, E., Kauffman, E. G., Amédro, F., & Robaszynski, F. (2006). High-resolution stratigraphy of the Cenomanian–Turonian boundary interval at Pueblo (USA) and wadi Bahloul (Tunisia): stable isotope and bio-events correlation. *Geobios, 39*(2), 171-200.

Castillo, P. R. (2004). Geochemistry of Cretaceous volcaniclastic sediments in the Nauru and East Mariana basins provides insights into the mantle sources of giant oceanic plateaus. In J. G. Fitton, J. J. Mahoney, P. J. Wallace, & A. D. Saunders (Eds.), *Origin and Evolution of the Ontong Java Plateau* (Vol. 229, pp. 353-368). London: The Geological Society.

Castillo, P. R., Carlson, R. W., & Batiza, R. (1991). Origin of Nauru Basin igneous complex: Sr, Nd and Pb isotope and REE constraints. *Earth and Planetary Science Letters, 103*, 200-213.

Castillo, P. R., Pringle, M. S., & Carlson, R. W. (1994). East Mariana Basin tholeiites: Cretaceous intraplate basalts or rift basalts related to Ontong Java plume? *Earth and Planetary Science Letters, 123*, 139-154.

Chaboureau, A.-C., Donnadieu, Y., Sepulchre, P., Robin, C., Guillocheau, F., & Rohais, S. (2012). The Aptian evaporites of the South Atlantic: a climatic paradox? *Climate of the Past Discussions, 8*, 121-144.

Chaboureau, A.-C., Guillocheau, F., Robin, C., Rohais, S., Moulin, M., & Aslanian, D. (2013). Paleogeographic evolution of the central segment of the South Atlantic during Early Cretaceous times: Paleotopographic and geodynamic implications. *Tectonophysics, 604*, 191-223.

Chambers, L. M., Pringle, M. S., & Fitton, J. G. (2004). Phrearomagmatic eruptions on the Ontong Java Plateau: an Aptian $^{40}Ar/^{39}Ar$ age for volcaniclastic rocks at ODP Site 1184. In J. G. Fitton, J. J. Mahoney, P. J. Wallace, & A. Saunders (Eds.), *Origin and Evolution of the Ontong Java Plateau* (Vol. 229, pp. 325--332). London: The Geological Society.

Chandler, M. T., Wessel, P., Taylor, B., Seton, M., Kim, S.-S., & Hyeong, K. (2012). Reconstructing Ontong Java Nui: Implications for Pacific absolute plate motion, hotspot drift and true polar wander. *Earth and Planetary Science Letters, 331-332*, 140-151.

Channell, J. E. T., Erba, E., & Lini, A. (1993). Magnetostratigraphic calibration of the Late Valanginian carbon isotope event in pelagic limestones from Northern Italy and Switzerland. *Earth and Planetary Science Letters, 118*, 145-166.

Channell, J. E. T., Erba, E., Muttoni, G., & Tremolada, F. (2000). Early Cretaceous magnetic stratigraphy in the APTICORE drill core and adjacent outcrop at Cismon (Southern Alps, Italy), and correlation to the proposed Barremian-Aptian boundary stratotype. *Geological Society of America Bulletin, 112*(9), 1430-1443.

Chapman, H., Bickle, M., Thaw, S. H., & Thiam, H. N. (2015). Chemical fluxes from time series sampling of the Irrawaddy and Salween Rivers, Myanmar. *Chemical Geology, 401*, 15-27.

Charbonnier, G., Boulila, S., Gardin, S., Duchamp-Alphonse, S., Adatte, T., Spangenberg, J. E., Follmi, K. B., Colin, C., & Galbrun, B. (2013). Astronomical calibration of the Valanginian "Weissert" episode: The Orpierre marl-limestone succession (Vocontian Basin, southeastern France). *Cretaceous Research, 45*, 25-42.

Charbonnier, G., Duchamp-Alphonse, S., Adatte, T., Follmi, K. B., Spangenberg, J. E., Gardin, S., Galbrun, B., & Colin, C. (2016). Eccentricity paced monsoon-like system along the northwestern Tethyan margin during the Valanginian (Early Cretaceous): New insights from detrital and nutrient fluxes into the Vocontian Basin (SE France). *Palaeogeography, Palaeoclimatology, Palaeoecology, 443*, 145-155.

Chavagnac, V., German, C. R., & Taylor, R. N. (2008). Global environmental effects of large volcanic eruptions on ocean chemistry: Evidence from "hydrothermal" sediments (ODP Leg 185, Site 1149B). *Journal of Geophysical Research, 113*.

Chernyavsky, B. M., & Wortmann, U. G. (2007). REMAP: A reaction transport model for isotope ratio calculations in porous media. *Geochemistry, Geophysics, Geosystems, 8*(2), Q02009. doi:10.1029/2006gc001442

Claypool, G. E., Holser, W. T., Kaplan, I. R., Saki, H., & Zak, I. (1980). THe age curves of sulfur and oxygen isotopes in marine sulfate and their mutual interpretation. *Chemical Geology, 28*, 199-260.

Coban, W. A., Walaszczyk, I., Obradovich, J. D., & McKinney, K. C. (2006). *A USGS Zonal Table for the Upper Cretaceous Middle Cenomanian-Maastrichtian of the Western Interior of the United States Based on Ammonites, Inoceramids, and Radiometric Ages* (OFR 2006-1250). USGS.

Coffin, M. F., Pringle, M. S., Duncan, R. A., Gladczenko, T. P., Storey, M., Muller, R. D., & Gahagan, L. A. (2002). Kerguelen hotspot magma output since 130 Ma. *Journal of Petrology, 43*, 1121-1139.

Colman, A. S., & Holland, H. D. (2000). The global diagenetic flux of phosphorus from marine sediments to the oceans: Redox sensitivity and the control of atmospheric oxygen levels. In C. R. Glenn, L. Prevot-Lucas, & J. Lucas (Eds.), *Marine AuthigenesisL From Global to Microbial* (Vol. 66, pp. 53-75). Tulsa, OK: SEPM.

Colman, A. S., Mackenzie, F. T., Holland, H. D., van Cappellen, P., & Ingall, E. D. (1997). Redox stabilization of the atmosphere and oceans and marine productivity. *Science, 275*, 406-408.

Constantine, A., Chinsamy, A., Vickers-Rich, P., & Rich, T. H. (1998). Periglacial environments and polar dinosaurs. *South African Journal of Science, 94*(3).

Coogan, L. A. (2009). Altered oceanic crust as an inorganic record of paleoseawater Sr concentration. *Geochemistry Geophysics Geosystems, 10*(4), Q04001. doi:10.1029/2008GC002341

Coogan, L. A., & Dosso, S. E. (2015). Alteration of ocean crust provides a strong temperature dependent feedback on the geological carbon cycle and is a primary driver of the Sr-isotopic composition of seawater. *Earth and Planetary Science Letters, 415*, 38-46.

Corfu, F., Polteau, S., Planke, S., Faleide, J. I., Svensen, H., Zayoncheck, A., & Stolbov, N. (2013). U–Pb geochronology of Cretaceous magmatism on Svalbard and Franz Josef Land, Barents Sea Large Igneous Province. *Geological Magazine, 150*(06), 1127-1135.

Cortecci, G., Dinelli, E., & Boschetti, T. (2007). The River Arno catchment, northern Tuscany: chemistry of waters and sediments from the River Elsa and River Era sub-basins, and sulphur and oxygen isotopes of aqueous sulphate. *Hydrological Processes, 21*(1), 1-20.

Cunningham, R., & Kroopnick, P. M. (1985). Inorganic and isotopic geochemistry of sediments from Sites 549 to 551, Northeastern North Atlantic. In P. C. de Graciansky & C. W. Poag (Eds.), *Initial Reports of the Deep Sea Drilling Project* (Vol. 80, pp. 1073-1079). Washington: US Government Printing Office.

Das, A., Chung, C.-H., & You, C.-F. (2012). Disproportionately high rates of sulfide oxidation from mountainous river basins of Taiwan orogeny: Sulfur isotope evidence. *Geophysical Research Letters, 39*(12), L12404. doi:10.1029/2012gl051549

Davis, A. C., Bickle, M. J., & Teagle, D. A. H. (2003). Imbalance in the oceanic strontium budget. *Earth and Planetary Science Letters, 211*, 173-187.

Davison, I. (2007). Geology and tectonics of the South Atlantic Brazilian salt basins. In A. C. Ries, R. W. H. Butler, & R. H. Graham (Eds.), *Deformation of the Continental Crust: The Legacy of Mike Coward* (Vol. 272, pp. 345-359). London: Geological Soceity of London.

de Graciansky, P. C., & Poag, C. W. (1985). Geologic history of Goban Spur, Northwest Europe continental margin. In P. C. de Graciansky & C. W. Poag (Eds.), *Initial Reports of the Deep Sea Drilling Project* (Vol. 80, pp. 1187-1216). Washington: US Government Printing Office.

de Hoog, J. C. M., Taylor, B. E., & van Bergen, M. J. (2001). Sulfur isotope systematics of basaltic lavas from Indonesia: implications for the sulfur cycle in subduction zones. *Earth and Planetary Science Letters, 189*, 237-252.

De Lurio, J. L., & Frakes, L. A. (1999). Glendonites as a paleoenvironmental tool: Implications for early Cretaceous high latitude climates in Australia. *Geochimica et Cosmochimica Acta, 63*, 1039-1048.

de Villiers, S. (1999). Seawater strontium and Sr/Ca variability in the Atlantic and Pacific oceans. *Earth and Planetary Science Letters, 171*, 623-634.

de Villiers, S., Shen, G. T., & Nelson, B. K. (1994). The Sr/Ca-temperature relationship in coralline aragonite: Influence of variability in $(Sr/Ca)_{seawater}$ and skeletal growth parameters. *Geochimica et Cosmochimica Acta, 58*, 197-208.

Dera, G., Brigaud, B., Monna, F., Laffont, R., Puceat, E., Deconinck, J.-F., Pellenard, P., Joachimski, M., & Durlet, C. (2011). Climatic ups and downs in a disturbed Jurassic world. *Geology, 39*, 215-218.

Detmers, J., Bruchert, V., Habicht, K. S., & Kuever, J. (2001). Diversity of sulfur isotope fractionations by sulfate-reducing prokaryotes. *Appl Environ Microbiol, 67*(2), 888-894.

Døssing, A., Jackson, H. R., Matzka, J., Einarsson, I., Rasmussen, T. M., Olesen, A. V., & Brozena, J. M. (2013). On the origin of the Amerasia Basin and the High Arctic Large Igneous Province—Results of new aeromagnetic data. *Earth and Planetary Science Letters, 363*, 219-230.

Dowling, C. B., Poreda, R. J., & Basu, A. R. (2003). The groundwater geochemistry of the Bengal Basin: Weathering, chemsorption, and trace metal flux to the oceans. *Geochimica et Cosmochimica Acta, 67*, 2117-2136.

Drachev, S., & Saunders, A. (2006). *The Early Cretaceous Arctic LIP: Its geodynamic setting and implications for Canada Basin opening*. Paper presented at the Proceedings of the Fourth International Conference on Arctic Margins, Dartmouth, Nova Scotia, Canada.

Du, X., Chen, X., Wang, C., Wei, Y., Li, Y., & Jansa, L. (2015). Geochemistry and detrital zircon U-Pb dating of Lower Cretaceous volcaniclastics in the Babazhadong section, Northern Tethyan Himalaya: Implications for the breakup of Eastern Gondwana. *Cretaceous Research, 52*, 127-137.

Duchamp-Alphonse, S., Gardin, S., Fiet, N., Bartolini, A., Blamart, D., & Pagel, M. (2007). Fertilization of the northwestern Tethys (Vocontian basin, SE France) during the Valanginian carbon isotope perturbation: Evidence from calcareous nannofossils and trace element data. *Palaeogeography, Palaeoclimatology, Palaeoecology, 243*(1-2), 132-151.

Dumitrescu, M., & Brassell, S. C. (2006). Compositional and isotopic characteristics of organic matter for the early Aptian Oceanic Anoxic Event at Shatsky Rise, ODP Leg 198. *Palaeogeography, Palaeoclimatology, Palaeoecology, 235*(1-3), 168-191.

Duncan, R. A. (2002). A time frame for construction of the Kerguelen Plateau and Broken Ridge. *Journal of Petrology, 43*, 1109-1119.

Edmonds, H. N., & Edmond, J. M. (1995). A three component mixing model for ridge-crest hydrothermal fluids. *Earth and Planetary Science Letters, 134*, 53-67.

Elderfield, H., & Gieskes, J. M. (1982). Sr isotopes in interstitial waters of marine sediments from Deep Sea Drilling Project cores. *Nature, 300*, 493-497.

Elderfield, H., & Shultz, A. (1996). Mid-ocean ridge hydrothermal fluxes and the chemical composition of the ocean. *Annual Reviews of Earth and Planetary Sciences, 24*, 191-224.

Elkibbi, M., & Rial, J. A. (2001). An outsider's review of the astronomical theory of the climate: Is the eccentricity-driven insolation the main driver of the ice ages? *Earth-Science Reviews, 56*, 161-177.

Embry, A. F., & Osadetz, K. G. (1988). Stratigraphy and tectonic significance of Cretaceous volcanism in the Queen Elizabeth Islands, Canadian Arctic Archipelago. *Canadian Journal of Earth Sciences, 25*, 1209-1219.

Erba, E., Bartolini, A., & Larson, R. L. (2004). Valanginian Weissert oceanic anoxic event. *Geology, 32*(2), 149.

Erba, E., Channell, J. E. T., Claps, M., Jones, C., Larson, R., Opdyke, D., Premoli Silva, I., Riva, A., Salvini, G., & Torricelli, S. (1999). Integrated stratigraphy of the Cismon APTICORE (Southern Alps, Italy): A "reference section" for the Barremian-Aptian interval at low latitudes. *Journal of Foraminiferal Research, 29*, 371-399.

Erbacher, J., Huber, B. T., Norris, R. D., & Makrey, M. (2001). Increased thermohaline stratification as a possible cause for an ocean anoxic event in the Cretaceous period. *Natrue, 409*, 325-327.

Estrada, S., & Henjes-Kunst, F. (2004). Volcanism in the Canadian High Arctic related to the opening of the Arctic Ocean. *Zeitschrift der Deutschen Geologischen Gesellschaft, 154*, 579-603.

Farquhar, J., Wu, N., Canfield, D. E., & Oduro, H. (2010). Connections between sulfur cycle evolution, sulfur isotopes, sediments, and base metal sulfide deposits. *Economic Geology, 105*, 509-533.

Fitton, J. G., Mahoney, J. J., Wallace, P. J., & Saunders, A. D. (2005). The Ontong Java Plateau. *LIP of the Month.* Retrieved from http://www.largeigneousprovinces.org/05apr

Frakes, L. A., Alley, N. F., & Deynoux, M. (1995). Early Cretaceous ice rafting and climate zonation in Australia. *International Geology Review, 37*(7), 567-583.

Frakes, L. A., & Francis, J. E. (1988). A guide to Phanerozoic cold polar climates from high-latitude ice-rafting in the Cretaceous. *Nature, 333*, 547-549.

Frakes, L. A., Francis, J. E., & Syktus, J. I. (1992). *Climate Modes of the Phanerozoic: the history of the Earth's climate over the past 600 million years*. Cambridge: Cambridge University.

Francois, L. M., & Walker, J. C. G. (1992). Modeling the Phanerozoic carbon cycle and climate: Constraints from the $^{87}Sr/^{86}Sr$ isotopic ratio of seawater. *American Journal of Science, 292*, 81-135.

Frey, F. A., McNaughton, N. J., Nelson, D. R., deLaeter, J. R., & Duncan, R. A. (1996). Petrogenesis of the Bunbury Basalt, Western Australia: interaction between the Kerguelen plume and Gondwana lithosphere? *Earth and Planetary Science Letters, 144*, 163-183.

Friedrich, O., Nishi, H., Pross, J., Schmiedl, G., & Hemleben, C. (2005). Millennial- to Centennial-Scale Interruptions of the Oceanic Anoxic Event 1b (Early Albian, mid-Cretaceous) Inferred from Benthic Foraminiferal Repopulation Events. *Palaios, 20*(1), 64-77.

Gaina, C., Werner, S. C., Saltus, R., Maus, S., & Group, T. C.-G. (2011). Circum-Arctic mapping project: new magnetic and gravity anomaly maps of the Arctic. In A. M. Spencer, A. F. Embry, D. L. Gautier, A. V. Stoupakova, & K. Sorensen (Eds.), *Arctic Petroleum Geology* (Vol. 35, pp. 39-48). London: The Geological Society.

Gale, A. S. (1995). Cyclostratigraphy and correlation of the Cenomanian Stage in Western Europe. In M. R. House & A. S. Gale (Eds.), *Orbital Forcing Timescales and Cyclostratigraphy* (Vol. 85, pp. 177-197). London: The Geological Society.

Garrels, R. M., & Lerman, A. (1981). Phanerozoic cycles of sedimentary carbon and sulfur. *Proc Natl Acad Sci U S A, 78*, 4652-4656.

Garrels, R. M., & Lerman, A. (1984). Coupling of the sedimentary sulfur and carbon cycles - an improved model. *American Journal of Science, 294*, 989-1007.

Gartner, S. (1980). Calcareous nannofossils, Deep Sea Drilling Project Holes 417D, 418A, and 418B. In T. Donnelly, J. Francheteau, W. Bryan, P. Robinson, M. Flower, M. Salisbury, & e. al. (Eds.), *Initial Reports of the Deep Sea Drilling Project* (Vol. 51, 52, 53, pp. 815-821). Washington: US Government Printing Office.

Ghatak, A., & Basu, A. R. (2011). Vestiges of the Kerguelen plume in the Sylhet Traps, northeastern India. *Earth and Planetary Science Letters, 308*(1-2), 52-64.

Gibson, S. A., Thompson, R. N., & Day, J. A. (2006). Timescales and mechanisms of plume–lithosphere interactions: $^{40}Ar/^{39}Ar$ geochronology and geochemistry of alkaline igneous rocks from the Paraná–Etendeka large igneous province. *Earth and Planetary Science Letters, 251*(1-2), 1-17.

Gislason, S. R., Oelkers, E. H., & Snorrason, A. (2006). Role of river-suspended material in the global carbon cycle. *Geology, 34*, 49-52.

Gohl, K., Uenzelmann-Neben, G., & Grobys, N. (2011). Growth and dispersal of a Southeast African large igeneous province. *South African Journal of Geology, 114*, 379-386.

Gomes, M. L., & Hurtgen, M. T. (2013). Sulfur isotope systematics of a euxinic, low-sulfate lake: Evaluating the importance of the reservoir effect in modern and ancient oceans. *Geology, 41*(6), 663-666.

Gomes, M. L., Hurtgen, M. T., & Sageman, B. B. (2016). Biogeochemical sulfur cycling during Cretaceous oceanic anoxic events: A comparison of OAE1a and OAE2. *Paleoceanography, 31*, 233-251. doi:10.1002/2015PA002869

Gothmann, A. M., Stolarski, J., Adkins, J. F., Schoene, B., Dennis, K. J., Schrag, D. P., Mazur, M., & Bender, M. L. (2015). Fossil corals as an archive of secular variations in seawater chemistry since the Mesozoic. *Geochimica et Cosmochimica Acta, 160*, 188-208.

Gradstein, F., Ogg, J., & Smith, A. (Eds.). (2004). *A Geologic TIme Scale 2004*. New York: Cambridge University Press.

Gradstein, F., Ogg, J. G., Schmitz, M. D., & Ogg, G. M. (Eds.). (2012). *The Geologic Time Scale 2012*. New York: Elsevier.

Gradstein, F. M., Agterberg, F. P., Ogg, J. G., Hardenbol, J., van Veen, P., Thierry, J., & Huang, Z. (1995). A Triassic, Jurassic and Cretaceous time scale. In W. A. Berggren, D. V. Kent, M.-P. Aubry, & J. Hardenbol (Eds.), *Geochronology Time Scales and Global Stratigraphic Correlation* (Vol. 54, pp. 95--126). Tulsa, OK: SEPM.

Graf, H. F., Langmann, B., & Feichter, J. (1998). The contribution of Earth degassing to the atmospheric sulfur budget. *Chemical Geology, 147*, 131-145.

Grantz, A., Hart, P. E., & Childers, V. A. (2011). Geology and tectionic development of the Amerasia and Canada Basins, Arctic Ocean. In A. M. Spencer, A. F. Embry, D. L. Gautier, A. V. Stoupakova, & K. Sorensen (Eds.), *Arctic Petroleum Geology* (Vol. 35, pp. 771-800). London: The Geological Society.

Graziano, R., & Raspini, A. (2015). Long- and short-term hydroclimatic variabilities in the Aptian Tethys: Clues from the orbital chronostratigraphy of evaporite-rich beds in the Apennine carbonate platform (Mt. Faito, southern Italy). *Palaeogeography, Palaeoclimatology, Palaeoecology, 418*, 319-343.

Greinert, J., Bollwerk, S. M., Derkachev, A., Bohrmann, G., & Suess, E. (2002). Massive barite deposits and carbonate mineralization in the Derugin Basin, Sea of Okhotsk: precipitation processes at cold seep sites. *Earth and Planetary Science Letters, 203*, 165-180.

Grenne, T., & Slack, J. F. (2003). Paleozoic and Mesozoic silica-rich seawater: Evidence from hematitic chert (jasper) deposits. *Geology, 31*, 319-322.

Greselle, B., & Pittet, B. (2010). Sea-level reconstructions from the Peri-Vocontian zone (southeast France) point to Valanginian glacioeustasy. *Sedimentology, 57*, 1640-1684.

Greselle, B., Pittet, B., Mattioli, E., Joachimski, M., Barbarin, N., Riquier, L., Reboulet, S., & Puceat, E. (2011). The Valanginian isotope event: a complex suite of palaeoenvironmental perturbations. *Palaeogeography, Palaeoclimatology, Palaeoecology, 306*, 41-57.

Grippo, A., Fischer, A. G., Hinnov, L. A., Herbert, T. D., & Premoli Silva, I. (2004). Cyclostratigraphy and chronology of the Albian Stage (Piobbico core, Italy). In B. D'Argenio, A. G. Fischer, I. Premoli Silva, H. Weissert, & V. Ferreri (Eds.), *Cyclostratigraphy: Approaches and Case Histories* (Vol. 81, pp. 57-81). Tulsa, OK: SEPM.

Grocke, D. R., Price, G. D., Robinson, S. A., Baraboshkin, E. Y., Mutterlose, J., & Ruffell, A. H. (2005). The Upper Valanginian (Early Cretaceous) positive carbon-isotope event recorded in terrestrial plants. *Earth and Planetary Science Letters, 240*, 495-509.

Habicht, K. S., Gade, M., Thamdrup, B., Berg, P., & Canfield, D. E. (2002). Calibration of sulfate levels in the Archean ocean. *Science, 298*, 2372-2374.

Haig, D. W. (1992). Aptian-Albian Foraminifers from site 766, Cuvier Abyssal Plain, and comparison with coeval faunas from the Australian region. In F. M. Gradstein, J. N. Ludden, & e. al. (Eds.), *Proceedings of the Ocean Drilling Program, Scientific Results* (Vol. 123, pp. 271-297). College Station, TX: ODP.

Halevy, I., Peters, S. E., & Fischer, W. W. (2012). Sulfate burial constraints on the Phanerozoic sulfur cycle. *Science, 337*(6092), 331-334. doi:10.1126/science.1220224

Halmer, M. M., Schmincke, H. U., & Graf, H. F. (2002). The annual volcanic gas input into the atmosphere, in particular into the stratosphere: a global data set for the past 100 years. *Journal of Volcanology and Geothermal Research, 115*, 511-528.

Hansen, K. W., & Wallmann, K. (2003). Cretaceous and Cenozoic evolution of seawater composition, atmospheric O_2 and CO_2: A model perspective. *American Journal of Science, 303*, 94-148.

Haq, B. U. (2014). Cretaceous eustasy revisited. *Global and Planetary Change, 113*, 44-58.

Harland, W. B. (1997). *The Geology of Svalbard* (Vol. 17). London: The Geological Society.

Hay, W. W. (2008). Evolving ideas about the Cretaceous climate and ocean circulation. *Cretaceous Research, 29*(5-6), 725-753.

Hay, W. W. (2009). Cretaceous oceans and ocean modeling. In X. Hu, C. Wang, R. W. Scott, M. Wagreich, & L. Jansa (Eds.), *Cretaceous Oceanic Red Beds: Stratigraphy, Composition, Origins, and Paleoceanographic and Paleoclimatic Significance* (Vol. 91, pp. 243-271). Tulsa, OK: SEPM.

Hay, W. W., Migdisov, A., Balukhovsky, A. N., Wold, C. N., Flögel, S., & Söding, E. (2006). Evaporites and the salinity of the ocean during the Phanerozoic: Implications for climate, ocean circulation and life. *Palaeogeography, Palaeoclimatology, Palaeoecology, 240*(1-2), 3-46.

Hein, J. R., Zierenberg, R. A., Maynard, J. B., & Hannington, M. D. (2007). Barite-forming environments along a rifted continental margin, Southern California Borderland. *Deep Sea Research Part II: Topical Studies in Oceanography, 54*(11-13), 1327-1349.

Hennig, S., Weissert, H., & Bulot, L. G. (1999). C-isotope stratigraphy, a calibration tool between ammonite- and magnetostratigraphy: The Valanginian-Hauterivian transition. *Geologica Carpathica, 50*, 91-96.

Herman, F., Seward, D., Valla, P. G., Carter, A., Kohn, B., Willett, S. D., & Ehlers, T. A. (2013). Worldwide acceleration of mountain erosion under a cooling climate. *Nature, 504*, 423-426.

Herrle, J. O., & Mutterlose, J. (2003). Calcareous nannofossils from the Aptian-Lower Albian of southeast Fracne: palaeoecological and biostratigraphic implications. *Cretaceous Research, 24*, 1-22.

Herrle, J. O., Schroder-Adams, C. J., Davis, W., Pugh, A. T., Galloway, J. M., & Fath, J. (2015). Mid-Cretaceous High Arctic stratigraphy, climate, and Oceanic Anoxic Events. *Geology, 43*, 403-406.

Herzig, P. M., Hannington, M. D., & Arribas, A. (1998). Sulfur isotopic composition of hydrothermal precipitates from the Lau back-arc: implications for magmatic contributions to seafloor hydrothermal systems. *Mineralium Deposita, 33*, 226-237.

Hicks, J. F., Obradovich, J. D., & Tauxe, L. (1995). A New Calibration Point for the Late Cretaceous Time Scale: The $^{40}Ar/^{39}Ar$ Isotopic Age of the C33r/C33n Geomagnetic Reversal from the Judith River Formation (Upper Creataceous), Elk Basin, Wyoming, USA. *The Journal of Geology, 103*(3), 243-256.

Hicks, J. F., Obradovich, J. D., & Tauxe, L. (1999). Magnetostratigraphy, isotopic age calibration and intercontinental correlation of the Red Bird section of the Pierre Shale, Niobrara County, Wyoming, USA. *Cretaceous Research, 20*, 1-27.

Ho, S. L., & Laepple, T. (2016). Flat meridional temperature gradient in the early Eocene in the subsurface rather than surface ocean. *Nature Geoscience, 9*, 606-610.

Hochmuth, K., Gohl, K., & Uenzelmann-Neben, G. (2015). Playing jigsaw with large igneous provinces - A plate tectonic reconstruction of Ontong Java Nui, West Pacific. *Geochemistry Geophysics Geosystems, 16*, 3789-3807. doi:10.1002/2015GC006036

Hodell, D. A., Mead, G. A., & Mueller, P. A. (1990). Variation in the strontium isotopic composition of seawater (8 Ma to present): Implications for chemical weathering rates and dissolved fluxes to the oceans. *Chemical Geology, 80*, 291-307.

Hodell, D. A., Mueller, P. A., McKenzie, J. A., & Mead, G. A. (1989). Strontium isotope stratigraphy and geochemistry of the late Neogene ocean. *Earth and Planetary Science Letters, 92*, 165-178.

Hoernle, K., Hauff, F., van den Bogaard, P., Werner, R., Mortimer, N., Geldmacher, J., . . . Davy, B. (2010). Age and geochemistry of volcanic rocks from the Hikurangi and Manihiki oceanic Plateaus. *Geochimica et Cosmochimica Acta, 74*(24), 7196-7219.

Holser, W. T., Maynard, J. B., & Cruikshank, K. M. (1989). Modelling the natural cycle of sulphur through Phanerozoic time. In P. Brimblecombe & A. Y. Lein (Eds.), *Evolution of the Global Biogeochemical Sulphur Cycle* (pp. 21-56). New York: John Wiley & Sons Ltd.

Holser, W. T., Schidlowski, M., Mackenzie, F. T., & Maynard, J. B. (1988). Geochemical cycles of carbon and sulfur. In C. B. Gregor, R. M. Garrels, F. T. Mackenzie, & J. B. Maynard (Eds.), *Chemical Cycles in the Evolution of the Earth* (pp. 105-173). New York: Wiley.

Horita, J., Zimmermann, H., & Holland, H. D. (2002). Chemical evolution of seawater during the Phanerozoic: Implications from the record of marine evaporites. *Geochimica et Cosmochimica Acta, 66*, 3733-3756.

Hotinski, R. M., & Toggweiler, J. R. (2003). Impact of a Tethyan circumglobal passage on ocean heat transport and "equable" climates. *Paleoceanography, 18*(1), 1007. doi:10.1029/2001pa000730

Huang, C., Hinnov, L., Fischer, A. G., Grippo, A., & Herbert, T. (2010). Astronomical tuning of the Aptian Stage from Italian reference sections. *Geology, 38*(10), 899-902.

Huang, W., van Hinsbergen, D. J. J., Dekkers, M. J., Garzanti, E., Dupont-Nivet, G., Lippert, P. C., Li, X., Maffione, M., Langereis, C. G., Hu, X., Guo, Z., & Kapp, P. (2015). Paleolatitudes of the Tibetan Himalaya from primary and secondary magnetizations of Jurassic to Lower Cretaceous sedimentary rocks. *Geochemistry, Geophysics, Geosystems, 16*, 77-100.

Huber, B. T., & Leckie, R. M. (2011). Planktonic foraminiferal species turnover across deep-sea Aptian/Albian boundary sections. *Journal of Foraminiferal Research, 41*, 53-95.

Huber, B. T., MacLeod, J. G., & Tur, N. A. (2008). Chronostratigraphic framework for Upper Campanian-Maastrichtian sediments on the Blake Nose (subtropical North Atlantic). *Journal of Foraminiferal Research, 38*, 162-182.

Hurtgen, M. T., Pruss, S. B., & Knoll, A. H. (2009). Evaluating the relationship between the carbon and sulfur cycles in the later Cambrian ocean: An example from the Port au Port Group, western Newfoundland, Canada. *Earth and Planetary Science Letters, 281*(3-4), 288-297.

Huston, D. L., Brauhart, C. W., Drieberg, S. L., Davidson, G. J., & Groves, D. I. (2001). Metal leaching and inorganic sulfate reduction in volcanic-hosted massive sulfide mineral systems: Evidence from the paleo-Archean Panorama district, Western Australia. *Geology, 29*, 6870690.

Huston, D. L., & Logan, G. A. (2004). Barite, BIFs and bugs: evidence for the evolution of the Earth's early hydrosphere. *Earth and Planetary Science Letters, 220*, 41-55.

Huston, D. L., Pehrrson, S., Eglington, B. M., & Zaw, K. (2010). The geology and metallogeny of volcanic-hosted massive sulfide deposits: Variation through geologic time and with tectonic setting. *Economic Geology, 105*, 571-591.

Immenhauser, A., & Scott, R. W. (1999). Global correlation of middle Cretaceous sea-level events. *Geology, 27*(6), 551.

Ingle, S., Scoates, J. S., Weis, D., Brügmann, G., & Kent, R. W. (2004). Origin of Cretaceous continental tholeiites in southwestern Australia and eastern India: insights from Hf and Os isotopes. *Chemical Geology, 209*(1-2), 83-106.

Ingle, S. P., Weis, D., Scoates, J. S., & Frey, F. A. (2002). Relationship between the early Kerguelen plume and continental flood basalts of the paleo-Eastern Gondwanan margins. *Earth and Planetary Science Letters, 197*, 35-50.

Janasi, V. d. A., de Freitas, V. A., & Heaman, L. H. (2011). The onset of flood basalt volcanism, Northern Paraná Basin, Brazil: A precise U–Pb baddeleyite/zircon age for a Chapecó-type dacite. *Earth and Planetary Science Letters, 302*(1-2), 147-153.

Jeandel, C., & Oelkers, E. H. (2015). The influence of terrigenous particulate material dissolution on ocean chemistry and global element cycles. *Chemical Geology, 395*, 50-66.

Jenkyns, H. C. (1995). Carbon-isotope stratigraphy and paleoceanographic significance of the Lower Cretaceous shallow-water carbonates of Resolution Guyot, Mid-Pacific Mountains. In E. L. Winterer, W. W. Sager, J. V. Firth, & J. M. Sinton (Eds.), *Proceedings of the Ocean Drilling Program, Scientific Results* (Vol. 143, pp. 99-104). College Station, Texas: Ocean Drilling Program.

Jenkyns, H. C. (2010). Geochemistry of oceanic anoxic events. *Geochemistry Geophysics Geosystesm, 11*, Q03004, doi:03010.01029/02009GC002788.

Jenkyns, H. C., Paull, C. K., Cummins, D. I., & Fullagar, P. D. (1995). Strontium-isotope stratigraphy of Lower Cretaceous atoll carbonates in the Mid-Pacific Mountains. In E. L. Winterer, W. W. Sager, J. V. Firth, & J. M. Sinton (Eds.), *Proceedings of the Ocean Drilling Program, Scientific Results* (Vol. 143, pp. 89-97). College Station, Texas: Ocean Drilling Program.

Johnson, C. A., Emsbo, P., Poole, F. G., & Rye, R. O. (2009). Sulfur- and oxygen-isotopes in sediment-hosted stratiform barite deposits. *Geochimica et Cosmochimica Acta, 73*(1), 133-147.

Jones, C. E., & Jenkyns, H. C. (2001). Seawater strontium isotopes, oceanic anoxic events, and seafloor hydrothermal activity in the Jurassic and Cretaceous. *American Journal of Science, 301*, 112-149.

Jones, M. T., Pearce, C. R., & Oelkers, E. H. (2012a). An experimental study of the interaction of basaltic riverine particulate material and seawater. *Geochimica et Cosmochimica Acta, 77*, 108-120.

Jones, M. T., Pearce, C. R., Jeandel, C., Gislason, S. R., Eiriksdottir, E. S., Mavromatis, V., & Oelkers, E. H. (2012b). Riverine particulate material dissolution as a significant flux of strontium to the oceans. *Earth and Planetary Science Letters, 355-356*, 51-59.

Jorgensen, B. B. (1982). Mineralization of organic matter in the sea bed - the role of sulphate reduction. *Nature, 296*, 643-645.

Kah, L. C., Lyons, T. W., & Chesley, J. T. (2001). Geochemistry of a 1.2 Ga carbonate-evaporite succession, northern Baffin and Bylot Islands: implications for Mesoproterozoic marine evolution. *Precambrian Research, 111*, 203-234.

Kah, L. C., Lyons, T. W., & Frank, T. D. (2004). Low marine sulphate and protracted oxygenation of the Proterozoic biosphere *Natrue, 431*, 834-838.

Kaminski, M. A., Baumgartner, P. O., Bown, P. R., Haig, D. W., McMinn, A., Moran, M. J., Mutterlose, J., & Ogg, J. G. (1992). Magnetobiostratigraphic synthesis of Leg 123: Sites 765 and 766 (Argo Abyssal Plain and Lower Exmouth Plateau). In F. M. Gradstein, J. N. Ludden, & e. al. (Eds.), *Proceedings of the Ocean Drilling Program, Scientific Results* (Vol. 123, pp. 717-737). College Station, TX: ODP

Kampschulte, A., & Strauss, H. (2004). The sulfur isotopic evolution of Phanerozoic seawater based on the analysis of structurally substituted sulfate in carbonates. *Chemical Geology, 204*, 255-286.

Karim, A., & Veizer, J. (2000). Weathering processes in the Indus River Basin: implications from riverine carbon, sulfur, oxygen, and strontium isotopes. *Chemical Geology, 170*, 153-177.

Kauffman, E. G. (1977). Geological and biological overview: Western Interior Cretaceous Basin. *The Mountain Geologist, 14*, 75-99.

Kauffman, E. G., & Caldwell, W. G. E. (1993). The Western Interior Basin in space and time. In W. G. E. Caldwell & E. G. Kauffman (Eds.), *Evolution of the Western Interior Basin* (Vol. 39, pp. 1-30). Ottawa: Geological Association of Canada.

Kennedy, W. J., Gale, A. S., Bown, P. R., Caron, M., Davey, R. J., Gröcke, D., & Wray, D. S. (2000). Integrated stratigraphy across the Aptian-Albian boundary in the Marnes Bleues, at the Col de Pré-Guittard, Arnayon (Drôme), and at Tartonne (Alpes-de-Haute-Provence), France: a candidate Global Boundary Stratotype Section and Boundary Point for the base of the Albian Stage. *Cretaceous Research, 21*(5), 591-720.

Kennedy, W. J., Gale, A. S., Huber, B. T., Petrizzo, M. R., Bown, P., Barchetta, A., & Jenkyns, H. C. (2014). Integrated stratigraphy across the Aptian/Albian boundary at Col de Pré-Guittard (southeast France): A candidate Global Boundary Stratotype Section. *Cretaceous Research, 51*, 248-259.

Kent, R. W., Pringle, M. S., Muller, R. D., Saunders, A. D., & Ghose, N. C. (2002). $^{40}Ar/^{39}Ar$ geochronology of the Rajmahal Basalts, India and their relationship to the Kerguelen Plateau. *Journal of Petrology, 43*, 1141-1153.

Kessels, K., Mutterlose, J., & Michalzik, D. (2006). Early Cretaceous (Valanginian-Hauterivian) calcareous nannofossils and isotopes of the northern hemisphere: proxies for the understanding of Cretaceous climate. *Lethaia, 39*, 157-172.

Konhauser, K. O., Lalonde, S. V., Amskold, L., & Holland, H. D. (2007). Was there really an Archean phosphate crisis? *Science, 315*, 1234.

Konig, M., & Jokat, W. (2010). Advanced insights into magmatism and volcanism of the Mozambique Ridge and Mozambique Basin in the view of new potential field data. *Geophysical Journal International, 180*, 158-180.

Korte, C., & Hesselbo, S. P. (2011). Shallow marine carbon and oxygen isotope and elemental records indicate icehouse-greenhouse cycles during Early Jurassic. *Paleoceanography, 26*, PA4219. doi:10.1029/2011PA002160.

Koutsoukos, E. A. M. (1992). Late Aptian to Maastrichtian foraminiferal biogeography and palaeoceanography of the Sergipe Basin, Brazil. *Palaeogeography, Palaeoclimatology, Palaeoecology, 92*, 295-324.

Krabbenhoft, A., Eisenhauer, A., Bohm, F., Vollstaedt, H., Fietzke, J., Liebetrau, V., Augustin, N., Peucker-Ehrenbrink, B., Muller, M. N., Horn, C., Hansen, B. T., Nolte, N., & Wallmann, K. (2010). Constraining the marine strontium budget with natural strontium isotope fractions ($^{87}Sr/^{86}Sr^*$, $\delta^{88/86}Sr$) of carbonates, hydrothermal solutions, and river waters. *Geochimica et Cosmochimica Acta, 74*, 4097-4109.

Krabbenhoft, A., Fietzke, J., Eisenhauer, A., Liebetrau, V., Bohm, F., & Vollstaedt, H. (2009). Determination of radiogenic and stable strontium isotope ratios ($^{87}Sr/^{86}Sr$; $\delta^{88/86}Sr$) by thermal ionization mass spectrometry applying an $^{87}Sr/^{84}Sr$ double spike. *Journal of Analytical Atomic Spectrometry, 24*, 1267-1271.

Kuiper, K. F., Deino, A., Hilgen, F. J., Krijgsman, W., Renne, P. R., & Wijbrans, J. R. (2008). Synchronizing rock clocks of Earth history. *Science, 320*(5875), 500-504.

Kujau, A., Heimhofer, U., Ostertag-Henning, C., Greselle, B., & Mutterlose, J. (2012). No evidence for anoxia during the Valanginian carbon isotope event - an organic-geochemical study from the Vocontian Basin, SE France. *Global and Planetary Change, 92-93*, 92-104.

Kump, L. R. (1989). Alternative modeling approaches to the geochemical cycles of carbon, sulfur and strontium isotopes. *American Journal of Science, 289*, 390-410.

Kump, L. R., & Garrels, R. M. (1986). Modeling atmospheric O_2 in the global sedimentary redox cycle. *American Journal of Science, 286*, 337-360.

Kump, L. R., & Seyfried, W. E. (2005). Hydrothermal Fe fluxes during the Precambrian: Effect of low oceanic sulfate concentrations and low hydrostatic pressure on the composition of black smokers. *Earth and Planetary Science Letters, 235*(3-4), 654-662.

Kurtz, A. C., Kump, L. R., Arthur, M. A., Zachos, J. C., & Paytan, A. (2003). Early Cenozoic decoupling of the global carbon and sulfur cycles. *Paleoceanography, 18*, 1090, doi:1010.1029/2003PA000908.

Larson, R. L. (1991). Latest pulse of Earth: Evidence for a mid-Cretaceous superplume. *Geology, 19*, 547-550.

Leavitt, W. D., Halevy, I., Bradley, A. S., & Johnston, D. T. (2013). Influence of sulfate reduction rates on the Phanerozoic sulfur isotope record. *Proc Natl Acad Sci U S A, 110*, 11244-11249.

Leckie, R. M., Bralower, T. J., & Cashman, R. (2002). Oceanic anoxic events and plankton evolution: Biotic response to tectonic forcing during the mid-Cretaceous. *Paleoceanography, 17*, 10.1029/2001PA000623.

Leinweber, V. T., & Jokat, W. (2011). Is there continental crust underneath the northern Natal Valley and the Mozambique Coastal Plains? *Geophysical Research Letters, 38*, L14303.

Li, X.-D., Liu, C.-Q., Liu, X.-L., & Bao, L.-R. (2011). Identification of dissolved sulfate sources and the role of sulfuric acid in carbonate weathering using dual-isotopic data from the Jialing River, Southwest China. *Journal of Asian Earth Sciences, 42*(3), 370-380.

Li, Y.-X., Bralower, T. J., Montañez, I. P., Osleger, D. A., Arthur, M. A., Bice, D. M., Herbert, T. D., Erba, E., & Premoli Silva, I. (2008). Toward an orbital chronology for the early Aptian Oceanic Anoxic Event (OAE1a, ~120 Ma). *Earth and Planetary Science Letters, 271*(1-4), 88-100.

Li, Z. X., & Powell, C. M. (2001). An outline of the palaeogeographic evolution of the Australasian region since the beginning of the Neoproterozoic. *Earth-Science Reviews, 53*, 237-277.

Lin, S., & Morse, J. W. (1991). Sulfate reduction and iron sulfide mineral formation in Gulf of Mexico anoxic sediments. *American Journal of Science, 291*, 55-89.

Lini, A., Weissert, H., & Erba, E. (1992). The Valanginian carbon isotope event: a first episode of greenhouse climate conditions during theCretaceous. *Terra Nova, 4*, 374-384.

Lowenstein, T. K., Hardie, L. A., Timofeeff, M. N., & Demicco, R. V. (2003). Secular variation in seawater chemistry and the origin of calcium chloride basinal brines. *Geology, 31*, 857-860.

Luo, C., Zheng, H., Tada, R., Wu, W., Irino, T., Yang, S., & Saito, K. (2014). Tracing Sr isotopic composition in space and time across the Yangtze River basin. *Chemical Geology, 388*, 59-70.

Luterbacher, H. (1975). Early Cretaceous foraminifera from the Northwestern Pacific: Leg 32 of the Deep Sea Drilling Project. In R. L. Larson, R. Moberly, & e. al. (Eds.), *Initial Reports of the Deep Sea Drilling Project* (Vol. 32, pp. 703-718). Washington, DC: US Government Printing Office.

Maher, H. D. (2001). Manifestations of the Cretaceous High Arctic Large Igneous Province in Svalbard. *The Journal of Geology, 109*, 91-104.

Maher, H. D., Hays, T., Shuster, R., & Mutrux, J. (2004). Petrography of Lower Cretaceous sandstones of Spitsbergen. *Polar Research, 23*, 147-165.

Mahoney, J., Storey, M., Duncan, R. A., Spencer, K., & Pringle, M. (1993). Geochemistry and age of Ontong-Java Plateu. In M. Pringle, W. Sliter, & S. Stein (Eds.), *The Mesozoic Pacific: geology tectonics and volcanism* (pp. 233-262). Washington, D.C.: AGU.

Mahoney, J. J., Duncan, R. A., Tejada, M. L. G., Sager, W. W., & Bralower, T. J. (2005). Jurassic-Cretaceous boundary age and mid-ocean-ridge–type mantle source for Shatsky Rise. *Geology, 33*(3), 185.

Malinverno, A., Erba, E., & Herbert, T. D. (2010). Orbital tuning as an inverse problem: Chronology of the early Aptian oceanic anoxic event 1a (Selli Level) in the Cismon APTICORE. *Paleoceanography, 25*. doi:doi:10.1029/2009PA001769

Marsagila, K. M. (2005). Sedimentology, petrology, and volcanology of the Lower Aptian Oceanic Anoxic Event (OAE1a), Shatsky Rise, North-Central Pacific Ocean. In T. J. Bralower, I. Premoli Silva, & M. J. Malone (Eds.), *Proceedings of the Ocean Drilling Program, Scientific Results* (Vol. 198, pp. 1-31). College Station, TX: ODP.

Martinez, M., Deconinck, J.-F., Pellenard, P., Reboulet, S., & Riquier, L. (2013). Astrochronlogy of the Valanginian Stage from reference sections (Vocontian Basin, France) and palaeoenvironmental implications for the Weissert Event. *Palaeogeography, Palaeoclimatology, Palaeoecology, 376*, 91-102.

Martinez, M., Pellenard, P., Deconinck, J.-F., Monna, F., Riquier, L., Boulila, S., Moiroud, M., & Company, M. (2012). An orbital floating time scale of the Hauterivian/Barremian GSSP from a magnetic susceptibility signal (Río Argos, Spain). *Cretaceous Research, 36*, 106-115.

Maynard, J. B., & Okita, P. M. (1991). Bedded barite deposits int he United States, Canada, Germany, and China: Two major types based on tectonic setting. *Economic Geology, 86*, 364-376.

Mazumdar, A., Peketi, A., Joao, H., Dewangan, P., Borole, D. V., & Kocherla, M. (2012). Sulfidization in a shallow coastal depositional setting: Diagenetic and palaeoclimatic implications. *Chemical Geology, 322-323*, 68-78.

McAnena, A., Flogel, S., Hofmann, P., Herrle, J. O., Griesand, A., Pross, J., Talbot, H. M., Rethemeyer, J., Wallman, K. & Wagner, T. (2013). Atlantic cooling associated with a marine biotic crisis during the mid-Cretaceous period. *Nature Geoscience, 6*, 558-561. doi:10.1038/ngeo1850

McArthur, J. M., Howarth, R. J., & Shields, G. A. (2012). Strontium isotope stratigraphy. In F. M. Gradstein, J. G. Ogg, M. Schmitz, & G. Ogg (Eds.), *The Geologic Time Scale 2012* (pp. 127-144): Elsevier.

McArthur, J. M., Janssen, N. M. M., Reboulet, S., Leng, M. L., Thirlwall, M. F., & van de Schootbrugge, B. (2007). Paleotemperatures, polar ice-volume, and isotope stratigraphy (Mg/Ca, $\delta^{18}O$, $\delta^{13}C$, $^{87}Sr/^{86}Sr$): The Early Cretaceous (Berriasian, Valanginian, Hauterivian). *Palaeogeography, Palaeoclimatology, Palaeoecology, 248*, 391-430.

McArthur, J. M., Mutterlose, J., Price, G. D., Rawson, P. F., Ruffell, A., & Thirlwall, M. F. (2004). Belemnites of Valanginian, Hauterivian and Barremian age: Sr-isotope stratigraphy, composition ($^{87}Sr/^{86}Sr$, $\delta^{13}C$, $\delta^{18}O$, Na, Sr, Mg) and palaeo-oceanography. *Palaeogeography, Palaeoclimatology, Palaeoecology, 202*, 253-272.

McKenzie, N. R., Horton, B. K., Loomis, S. E., Stockli, D. F., Planavsky, N. J., & Lee, C.-T. A. (2016). Continental arc volcanism as the principal driver of icehouse-greenhouse variability. *Science, 352*, 444-447.

Mearon, S., Paytan, A., & Bralower, T. J. (2003). Cretaceous strontium isotope stratigraphy using marine barite. *Geology, 31*, 15-18.

Menegatti, A. P., Weissert, H., Brown, R. S., Tyson, R. V., Farrimond, P., Strasser, A., & Caron, M. (1998). High-resolution $d^{13}C$ stratigraphy through the early Aptian "Livello Selli" of the Alpine Tethys. *Paleoceanography, 13*(5), 530-545.

Meybeck, M., Laroche, L., Durr, H. H., & Syvitski, J. P. M. (2003). Global variability of daily total suspended solids and their fluxes in rivers. *Global and Planetary Change, 39*, 65-93.

Meyer, K. M., Ridgwell, A., & Payne, J. L. (2016). The influence of the biological pump on ocean chemistry: implications for long-term trends in marine redox chemistry, the global carbon cycle, and marine animal ecosystems. *Geobiology, 14*(3), 207-219.

Meyers, S. R. (2007). Production and preservation of organic matter: The significance of iron. *Paleoceanography, 22*. doi:10.1029/2006PA001332

Meyers, S. R., Siewert, S. E., Singer, B. S., Sageman, B. B., Condon, D. J., Obradovich, J. D., Jicha, B. R., & Sawyer, D. A. (2012). Intercalibration of radioisotopic and astrochronologic time scales for the Cenomanian-Turonian boundary interval, Western Interior Basin, USA. *Geology, 40*(1), 7-10. doi:10.1130/g32261.1

Miles, G. A., & Orr, W. N. (1980). Planktonic foraminifers from the Bermuda Rise, Deep Sea Drilling Porject Legs 51, 52, and 53. In T. Donnelly, J. Francheteau, W. Bryan, P. Robinson, M. Flower, M. Salisbury, & e. al. (Eds.), *Initial Reports of the Deep Sea Drilling Project* (Vol. 51, 52, 53 Part 2, pp. 791-813). Washington: US Government Printing Office.

Milliman, J. D., & Farnsworth, K. L. (2011). *River Discharge to the Coastal Ocean: A Global Synthesis*. New York: Cambridge University Press.

Millot, R., Gaillardet, J., Dupre, B., & Allegre, C. J. (2002). The global control of silicate weathering rates and the coupling with physical erosion: new insights from rivers of the Canadian Shield. *Earth and Planetary Science Letters, 196*, 83-98.

Mills, J., Gomes, M. L., Sageman, B. B., Jacobson, A. D., & Hurtgen, M. T. (2013). Reinterpreting the Early Cretaceous sulfur isotope records: Implications for the evolution of seawater chemistry. *American Geophysical Union Fall Meeting*, Abstract PP33B-1925.

Moberly, R., & Jenkyns, H. C. (1981). Cretaceous volcanogenic sediments of the Nauru Basin, Deep Sea Drilling Project Leg 61. In R. L. Larson, S. O. Schlanger, & R. E. Boyce (Eds.), *Initial Reports of the Deep Sea Drilling Project* (Vol. 61, pp. 533-548). Washington, DC: US Government Printing Office.

Mochizuki, K., Coffin, M. F., Eldholm, O., & Taira, A. (2005). Massive Early Cretaceous volcanic activity in the Nauru Basin related to emplacement of the Ontong Java Plateau. *Geochemistry, Geophysics, Geosystems, 6*(10), Q10003. doi:10.1029/2004gc000867

Modica, C. J., & Brush, E. R. (2004). Postrift sequence stratigraphy, paleogeography, and fill history of the deep-water Santos Basin, offshore southeast Brazil. *AAPG Bulletin, 88*(7), 923-945.

Mokadem, F., Parkinson, I. J., Hathorne, E. C., Anand, P., Allen, J. T., & Burton, K. W. (2015). High precision radiogenic strontium isotope measurements of the modern and glacial ocean: Limits on glacial-interglacial variations in continental weathering. *Earth and Planetary Science Letters, 415*, 111-120.

Molenaar, C. M. (1983). Depositional relations of Cretaceous and Lower Tertiary Rocks, Northeastern Alaska. *AAPG Bulletin, 67*, 1066-1080.

Moran, M. J. (1992). Biostratigraphy of Upper Cretaceous and Paleogene calcareous nannofossils from Leg 123, Northeastern Indian Ocean. In F. M. Gradstein, J. N. Ludden, & e. al. (Eds.), *Proceedings of the Ocean Drilling Program, Scientific Results* (Vol. 123, pp. 381-405). College Station, TX: ODP.

Moulin, M., Aslanian, D., & Unternehr, P. (2010). A new starting point for the South and Equatorial Atlantic Ocean. *Earth-Science Reviews, 98*(1-2), 1-37.

Mutterlose, J. (1992). Lower Cretaceous nannofossil biostratigraphy off Northwestern Australia (Leg 123). In F. M. Gradstein, J. N. Ludden, & e. al. (Eds.), *Proceedings of the Ocean Drilling Program, Scientific Results* (Vol. 123, pp. 343-368). College Station, TX: Ocean Drilling Program.

Mutterlose, J., Autrun, G., Baraboschkin, E. J., Cecca, F., Erba, E., Gardin, S., Herngreen, W., Hoedemaeker, Ph. J., Kakabadze, M., Klein, J., Leereveld, H., Rawson, P. F., Ropolo, P., Vasicek, Z., & von Salis, K. (1996). The Hauterivan Stage. *Bulletin de l'Institut Royal des Sciences Naturelles de Belgique, Sciences de la Terre, 66 (Suppl.)*, 19-24.

Mutterlose, J., Pauly, S., & Steuber, T. (2009). Temperature controlled deposition of early Cretaceous (Barremian-early Aptian) black shales in an epicontinental sea. *Palaeogeography, Palaeoclimatology, Palaeoecology, 273*, 330-345.

Nakanishi, M., Tamaki, K., & Kobayashi, K. (1992). A new Mesozoic isochron chart of the northwestern Pacific Ocean: Paleomagnetic and tectonic implications. *Geophysical Research Letters, 19*, 693-696.

Nakanishi, M., & Winterer, E. L. (1998). Tectonic history of the Pacific-Farallon-Phoenix triple junction from Late Jurassic to Early Cretaceous: An abandoned Mesozoic spreading system in the Central Pacific Basin. *Journal of Geophysical Research, 103*, 12,453-412,468.

Nejbert, K., Krajewski, K. P., Dubinska, E., & Pécskay, Z. (2011). Dolerites of Svalbard, north-west Barents Sea Shelf: age, tectonic setting and significance for geotectonic interpretation of the High-Arctic Large Igneous Province. *Polar Research, 30*, 7306. 10.3402/polar.v30i0.7306

Newton, R. J., Reeves, E. P., Kafousia, N., Wignall, P. B., Bottrell, S. H., & Sha, J. G. (2010). Low marine sulfate concentrations and the isolation of the European epicontinental sea during the Early Jurassic. *Geology, 39*(1), 7-10.

Obradovich, J. D. (1993). A Cretaceous time scale. In W. G. E. Caldwell & E. G. Kauffman (Eds.), *Evolution of the Western Interior Basin* (Vol. 39, pp. 379-396): Geological Association of Canada.

Obradovich, J. D., Tatsuro Matsumoto, M. J. A., Nishida, T., & Inoue, Y. (2002). Integrated biostratigraphic and radiometric study on the Lower Cenomanian (Cretaceous) of Hokkaido, Japan. *Proceedings of Japan Academy, 78*, 149-153.

Ogg, J. G. (2012). Geomagnetic Polarity Time Scale. In F. M. Gradstein, J. G. Ogg, M. Schmitz, & G. Ogg (Eds.), *The Geologic Time Scale 2012* (Vol. 1, pp. 85-113): Elsevier.

Ogg, J. G., Agterberg, F. P., & Gradstein, F. (2004). The Cretaceous Period. In F. Gradstein, J. Ogg, & A. Smith (Eds.), *A Geologic Time Scale 2004* (pp. 344-383). New York: Cambridge University Press.

Ogg, J. G., & Hinnov, L. A. (2012). Cretaceous. In F. M. Gradstein, J. G. Ogg, M. Schmitz, & G. Ogg (Eds.), *The Geologic Time Scale 2012* (Vol. 2, pp. 793-853): Elsevier.

Ono, S., Shanks, W. C., Rouxel, O. J., & Rumble, D. (2007). S-33 constraints on the seawater sulfate contribution in modern seafloor hydrothermal vent sulfides. *Geochimica et Cosmochimica Acta, 71*, 1170-1182.

Ozima, M., Saito, K., & Takigami, Y. (1981). ^{40}Ar-^{39}Ar geochronological studies on rocks drilled at holes 462 and 462A, Deep Sea Drilling Project Leg 61. In R. L. Larson, S. O. Schlanger, & R. E. Boyce (Eds.), *Initial Reports of Deep See Drilling Project* (Vol. 61, pp. 701-703). Washington, DC: US Government Printing Office.

Palmer, M. R., & Edmond, J. M. (1989). The strontium isotope budget of the modern ocean. *Earth and Planetary Science Letters, 92*, 11-26.

Parsiegla, N., Gohl, K., & Uenzelmann-Neben, G. (2008). The Agulhas Plateau: structure and evolution of a Large Igneous Province. *Geophysical Journal International, 174*(1), 336-350.

Paytan, A., & Kastner, M. (1996). Benthic Ba fluxes in the central equatorial Pacific, implications for the oceanic Ba cycle. *Earth and Planetary Science Letters, 142*, 439-450.

Paytan, A., Kastner, M., Campbell, D., & Thiemens, M. H. (1998). Sulfur isotopic composition of Cenozoic seawater sulfate. *Science, 282*, 1459-1462.

Paytan, A., Kastner, M., Campbell, D., & Thiemens, M. H. (2004). Seawater sulfur isotope fluctuations in the Cretaceous. *Science, 304*, 1663-1665.

Paytan, A., Kastner, M., Martin, E. E., Macdougall, J. D., & Herbert, T. (1993). Marine barite as a monitor of seawater stronium isotope composition. *Nature, 366*, 445-449.

Paytan, A., Mearon, S., Cobb, K., & Kastner, M. (2002). Origin of marine barite deposits: Sr and S isotope characterization. *Geology, 30*, 747-750.

Pearce, C. R., Parkinson, I. J., Gaillardet, J., Charlier, B. L. A., Mokadem, F., & Burton, K. W. (2015). Reassessing the stable ($\delta^{88/86}$Sr) and radiogenic (^{87}Sr/^{86}Sr) strontium isotopic composition of marine inputs. *Geochimica et Cosmochimica Acta, 157*, 125-146.

Peate, D. W. (2009). Global dispersal of Pb by large-volume silicic eruptions in the Parana-Etendeka large igneous province. *Geology, 37*, 1071-1074.

Peate, D. W., Hawkesworth, C. J., Mantovani, M. S. M., & Shukowsky, W. (1990). Mantle plumes and flood-basalt stratigraphy in the Parana, South America. *Geology, 18*, 1223-1226.

Peters, M., Strauss, H., Farquhar, J., Ockert, C., Eickmann, B., & Jost, C. L. (2010). Sulfur cycling at the Mid-Atlantic Ridge: A multiple sulfur isotope approach. *Chemical Geology, 269*(3-4), 180-196.

Petrizzo, M. R., & Huber, B. T. (2006). On the phylogeny of the Late Albian genus *Planomalina*. *Journal of Foraminiferal Research, 36*, 233-240.

Petrizzo, M. R., Huber, B. T., Gale, A. S., Barchetta, A., & Jenkyns, H. C. (2012). Abrupt planktic foraminiferal turnover across the Niveau Kilian at Col de Pré-Guittard (Vocontian Basin, southeast France): new criteria for defining the Aptian/Albian boundary. *Newsletters on Stratigraphy, 45*(1), 55-74.

Petrizzo, M. R., Huber, B. T., Gale, A. S., Barchetta, A., & Jenkyns, H. C. (2013). Erratum. *Newsletters on Stratigraphy, 46*(1), 93-93.

Peucker-Ehrenbrink, B., Miller, M. W., Arsouze, T., & Jeandel, C. (2010). Continental bedrock and riverine fluxes of strontium and neodymium isotopes to the oceans. *Geochemistry Geophysics Geosystems, 11*(3), Q03016. doi:10.1029/2009GC002869

Pilson, M. E. Q. (1998). *An Introduction to the Chemistry of the Sea*. Upper Saddle River, NJ: Prentice Hall.

Pinto, V. M., Hartmann, L. A., Santos, J. O. S., McNaughton, N. J., & Wildner, W. (2011). Zircon U–Pb geochronology from the Paraná bimodal volcanic province support a brief eruptive cycle at ~135Ma. *Chemical Geology, 281*(1-2), 93-102.

Pirrie, D., Doyle, P., Marshall, J. D., & Ellis, G. (1995). Cool Cretaceous climates: new data from the Albian of Western Australia. *Journal of the Geological Society of London, 152*, 739-742.

Pogge von Strandmann, P. A. E., Jenkyns, H. C., & Woodfine, R. G. (2013). Lithium isotope evidence for enhanced weathering during Oceanic Anoxic Event 2. *Nature Geosciences, 6*, 668-672.

Portenga, E. W., & Bierman, P. R. (2011). Understanding Earth's eroding surface with ^{10}Be. *GSA Today, 21*(8), 4-10.

Poulsen, C. J., Barron, E. J., Arthur, M. A., & Peterson, W. H. (2001). Response of the mid-Cretaceous global oceanic circulation to tectonic and CO_2 forcings. *Paleoceanography, 16*, 576-592.

Poulsen, C. J., Gendaszek, A. S., & Jacob, R. L. (2003). Did the rifting of the Atlantic Ocean cause the Cretaceous thermal maximum? *Geology, 31*(2), 115.

Price, G. D., & Nunn, E. V. (2010). Valanginian isotope variation in glendonites and belemnites from Arctic Svalbard: Transient glacial termperatures during the Cretaceous greenhouse. *Geology, 38*, 251-254.

Price, G. D., & Passey, B. H. (2013). Dynamic polar climates in a greenhouse world: Evidence from clumped isotope thermometry of Early Cretaceous belemnites. *Geology, 41*, 923-926.

Price, G. D., Ruffell, A. H., Jones, C. E., Kalin, R. M., & Mutterlose, J. (2000). Isotopic evidence for temperature variation during the early Cretaceous (late Ryazanian-mid-Hauterivian). *Journal of the Geological Society of London, 157*, 335-343.

Price, G. D., Williamson, T., Henderson, R. A., & Gagan, M. K. (2012). Barremian-Cenomanian palaeotemperatures for Australian seas based on new oxygen-isotope data from belemnite rostra. *Palaeogeography, Palaeoclimatology, Palaeoecology, 358*, 27-39.

Pringle, M. S. (1992). Radiometric ages of basaltic basement recovered at Sites 800, 801, and 802, Leg 129, Western Pacific Ocean. In R. L. Larson, Y. Lancelot, & e. al. (Eds.), *Proceedings of the Ocean Drilling Program, Scientific Results* (Vol. 129, pp. 389-404). College Station, TX: ODP.

Pringle, M. S., & Duncan, R. A. (1995). Radiometric ages of basaltic lavas recovered at sites 865, 866, and 869. In E. L. Winterer, W. W. Sager, J. V. Firth, & J. M. Sinton (Eds.), *Proceedings of the Ocean Drilling Program, Scientific Results* (Vol. 143, pp. 277-283). College Station, TX: ODP.

Raab, M., & Spiro, B. (1991). Sulfur isotopic variations during seawater evaporation with fractional crystallization. *Chemical Geology, 86*, 323-333.

Raven, M. R., Adkins, J. F., Werne, J. P., Lyons, T. W., & Sessions, A. L. (2015). Sulfur isotopic composition of individual organic compounds from Cariaco Basin sediments. *Organic Geochemistry, 80*, 53-59.

Raven, M. R., Sessions, A. L., Adkins, J. F., & Thunell, R. C. (2016). Rapid organic matter sulfurization in sinking particles from the Cariaco Basin water column. *Geochimica et Cosmochimica Acta, 190*, 175-190.

Raven, M. R., Sessions, A. L., Fischer, W. W., & Adkins, J. F. (2016). Sedimentary pyrite $\delta^{34}S$ differs from porewater sulfide in Santa Barbara Basin: Proposed role of organic sulfur. *Geochimica et Cosmochimica Acta, 186*, 120-134.

Ray, J. S., Pattanayak, S. K., & Pande, K. (2005). Rapid emplacement of the Kerguelen plume–related Sylhet Traps, eastern India: Evidence from40Ar-39Ar geochronology. *Geophysical Research Letters, 32*(10), L10303. doi:10.1029/2005gl022586

Reboulet, S., Szives, O., Aguirre-Urreta, B., Barragán, R., Company, M., Idakieva, V., Ivanov, M., Kakabadze, M. V., Moreno-Bedmar, J. A., Sandoval, J., Baraboshkin, E. J., Caglar, M. K., Fozy, I., Gonzalez-Arreoloa, C., Kenjo, S., Lukeneder, A., Raisossadat, S. N., Rawson, P. F., & Tavera, J. M. (2014). Report on the 5th International Meeting of the IUGS Lower Cretaceous Ammonite Working Group, the Kilian Group (Ankara, Turkey, 31st August 2013). *Cretaceous Research, 50*, 126-137.

Renne, P. R., Balco, G., Ludwig, K. R., Mundil, R., & Min, K. (2011). Response to the comment by W.H. Schwarz et al. on "Joint determination of ^{40}K decay constants and $^{40}Ar^{*}/^{40}K$ for the Fish Canyon sanidine standard, and improved accuracy for $^{40}Ar/^{39}Ar$ geochronology" by P.R. Renne et al. (2010). *Geochimica et Cosmochimica Acta, 75*(17), 5097-5100.

Renne, P. R., Mundil, R., Balco, G., Min, K., & Ludwig, K. R. (2010). Joint determination of ^{40}K decay constants and $^{40}Ar^{*}/^{40}K$ for the Fish Canyon sanidine standard, and improved accuracy for $^{40}Ar/^{39}Ar$ geochronology. *Geochimica et Cosmochimica Acta, 74*(18), 5349-5367.

Renne, P. R., Swisher, C. C., Deino, A. L., Karner, D. B., Owens, T. L., & DePaolo, D. J. (1998). Intercalibration of standards, absolute ages and uncertainties in $^{40}Ar/^{39}Ar$ dating. *Chemical Geology, 145*, 117-152.

Richter, F. M., & Liang, Y. (1993). The rate and consequences of Sr diagenesis in deep-sea carbonates. *Earth and Planetary Science Letters, 117*, 553-565.

Richter, F. M., & Turekian, K. K. (1993). Simple models for the geochemical response of the ocean to climatic and tectonic forcing. *Earth and Planetary Science Letters, 119*, 121-131.

Rowley, D. B. (2002). Rate of plate creation and destruction: 180 Ma to present. *GSA Bulletin, 114*, 927-933.

Sageman, B. B., Meyers, S. R., & Arthur, M. A. (2006). Orbital time scale and new C-isotope record for Cenomanian-Turonian boundary stratotype. *Geology, 34*(2), 125.

Saltus, R. W., Miller, E. L., Gaina, C., & Brown, P. J. (2011). Regional magnetic domains of the Circum-Arctic: a framework for geodynamic interpretation. In A. M. Spencer, A. F. Embry, D. L. Gautier, A. V. Stoupakova, & K. Sorensen (Eds.), *Arctic Petroleum Geology* (Vol. 35, pp. 49-60). London: The Geological Society.

Saltus, R. W., & Oakey, G. N. (2015). Magnetic subdomains of the High Arctic Magnetic High: Speculations and implications for understanding of the High Arctic Large Igneous Province and related tectonics. *AGU Fall Meeting 2015*, T51B-2877.

Sander, S. G., & Koschinsky, A. (2011). Metal flux from hydrothermal vents increased by organic complexation. *Nature Geoscience, 4*(3), 145-150.

Selby, D., Mutterlose, J., & Condon, D. J. (2009). U–Pb and Re–Os geochronology of the Aptian/Albian and Cenomanian/Turonian stage boundaries: Implications for timescale calibration, osmium isotope seawater composition and Re–Os systematics in organic-rich sediments. *Chemical Geology, 265*(3-4), 394-409.

Seton, M., Gaina, C., Muller, R. D., & Heine, C. (2009). Mid-Cretaceous seafloor spreading pulse: Fact or Fiction? *Geology, 37*, 687-690.

Seton, M., Muller, R. D., Zahirovic, S., Gaina, C., Torsvik, T., Shephard, G., Talsma, A., Gurnis, M., Turner, M., Maus, S., & Chandler, M. (2012). Global continental and ocean basin reconstructions since 200 Ma. *Earth-Science Reviews, 113*, 212-270.

Shanks, W. C. (2001). Stable isotopes in seafloor hydrothermal systesm: Vent fluids, hydrothermal deposits, hydrothermal alteration, and microbial processes. In J. W. Valley & D. R. Cole (Eds.), *Stable Isotope Geochemistry* (Vol. 43, pp. 469-525). Washington, DC: The Mineralogical Society of America.

Shen, Y., & Buick, R. (2004). The antiquity of microbial sulfate reduction. *Earth-Science Reviews, 64*, 243-272.

Shen, Y., Farquhar, J., Masterson, A., Kaufman, A. J., & Buick, R. (2009). Evaluating the role of microbial sulfate reduction in the early Archean using quadruple isotope systematics. *Earth and Planetary Science Letters, 279*(3-4), 383-391.

Shimokawa, A. (2010). *Zircon U-Pb Geochronology of the Great Valley Group: Recalibrating the Lower Cretaceous Time Scale.* (Masters), University of North Carolina Chapel Hill, Chapel Hill, NC.

Shipilov, E. V., & Karyakin, Y. V. (2011). The barents sea magmatic province: Geological-geophysical evidence and new $^{40}Ar/^{39}Ar$ dates. *Doklady Earth Sciences, 439*(1), 955-960.

Sikora, P. J., & Bergen, J. A. (2004). Lower Cretaceous planktonic foraminiferal and nannofossil biostratigraphy of Ontong Java Plateau sites from DSDP Leg 30 and ODP Leg 192. In J. G. Fitton, J. J. Mahoney, P. J. Wallace, & A. D. Saunders (Eds.), *Origin and Evolution of the Ontong Java Plateau* (Vol. 229, pp. 83-112). London: The Geological Society.

Silantyev, S. A., Bogdanovskii, O. G., Fedorov, P. I., Karpenko, S. F., & Kostitsyn, Y. A. (2004). Intraplate magmatism of the De Long Islands: A response to the propogation of the ultraslow-spreading Gakkel Ridge into the passive continental margin in the Laptev Sea. *Russian Journal of Earth Sciences, 6*, 153-158.

Sim, M. S., Bosak, T., & Ono, S. (2011a). Large sulfur isotope fractionation does not require disproportionation. *Science, 333*, 74-77.

Sim, M. S., Ono, S., Donovan, K., Templer, S. P., & Bosak, T. (2011b). Effect of electron donors on the fractionation of sulfur isotopes by a marine *Desulfovibrio* sp. *Geochimica et Cosmochimica Acta, 75*, 4244-4259.

Spence, J., & Telmer, K. (2005). The role of sulfur in chemical weathering and atmospheric CO2 fluxes: Evidence from major ions, $\delta^{13}C_{DIC}$, and $\delta^{34}S_{SO4}$ in rivers of the Canadian Cordillera. *Geochimica et Cosmochimica Acta, 69*(23), 5441-5458.

Sprovieri, M., Coccioni, R., Lirer, F., Pelosi, N., & Lozar, F. (2006). Orbital tuning of a lower Cretaceous composite record (Maiolica Formation, central Italy). *Paleoceanography, 21*(4), PA4212. doi:10.1029/2005pa001224

SSP Leg 32. (1975). Site 305: Shatsky Rise. In R. L. Larson, R. Moberly, & e. al. (Eds.), *Initial Reports of the Deep Sea Drilling Project* (Vol. 32, pp. 75-158). Washington: US Government Printing Office.

SSP Legs 51-53. (1980a). Site 417. In T. Donnelly, J. Francheteau, W. Bryan, P. Robinson, M. Flower, M. Salisbury, & e. al. (Eds.), *Initial Reports of the Deep Sea Drilling Project* (Vol. 51, 52, 53 Part 1, pp. 23-350). Washington: US Government Printing Office.

SSP Legs 51-53. (1980b). Site 418. In T. Donnelly, J. Francheteau, W. Bryan, P. Robinson, M. Flower, M. Salisbury, & e. al. (Eds.), *Initial Reports of the Deep Sea Drilling Project* (Vol. 51, 52, 53 Part 1, pp. 351-626). Washington: US Government Printing Office.

SSP Leg 80. (1985). Site 551. In P. C. de Graciansky & C. W. Poag (Eds.), *Initial Reports of the Deep Sea Drilling Project* (Vol. 80, pp. 357-385). Washington: US Governmental Printing Office.

SSP Leg 123. (1990a). Site 765. In J. N. Ludden & F. M. Gradstein (Eds.), *Proceedings of the Ocean Drilling Program, Initia Results* (Vol. 123, pp. 63-267). College Station, TX: ODP.

SSP Leg 123. (1990b). Site 766. In J. N. Ludden, F. M. Gradstein, & e. al. (Eds.), *Proceedings of the Ocean Drilling Program, Initial Reports* (Vol. 123, pp. 269-352). College Station, TX: ODP.

SSP Leg 143. (1993). Site 866. In W. W. Sager, E. L. Winterer, J. V. Firth, & e. al. (Eds.), *Proceedings of the Ocean Drilling Program, Initial Reports* (Vol. 143, pp. 181-271). College Station, Texas: ODP.

SSP Leg 171B. (1998). Site 1049. In R. D. Norris, D. Kroon, & A. Klaus (Eds.), *Proceedings of the Ocean Drilling Program, Initial Reports* (Vol. 171B, pp. 47-91). College Station, TX: ODP.

SSP Leg 198. (2002a). 1207. In T. J. Bralower, I. Premoli Silva, & M. J. Malone (Eds.), *Proceedings of the Ocean Drilling Program, Initial Reports* (Vol. 198, pp. 1-140). College Station, TX: ODP.

SSP Leg 198. (2002b). Site 1213. In T. J. Bralower, I. Premoli Silva, & M. J. Malone (Eds.), *Proceedings of the Ocean Drilling Program, Initial Reports* (Vol. 198, pp. 1-110). College Station, TX: ODP.

Stewart, K., Turner, S., Kelley, S., Hawkesworth, C. J., Kirstein, L., & Mantovani, M. S. M. (1996). 3-D, ^{40}Ar-^{39}Ar geochronolgy in the Parana continental flood basalt province. *Earth and Planetary Science Letters, 143*, 95-109.

Strauss, H. (1997). The isotopic composition of sedimentary sulfur through time. *Palaeogeography, Palaeoclimatology, Palaeoecology, 132*, 97-118.

Strauss, H. (1999). Geological evolution from isotope proxy signals - sulfur. *Chemical Geology, 161*, 89-101.

Strauss, H., Banerjee, D. M., & Kumar, V. (2001). The sulfur isotopic composition of Neoproterozoic to early Cambrian seawater - evidence from the cyclic Hanseran evaporites, NW India. *Chemical Geology, 175*, 17-28.

Syvitski, J. P. M., Peckham, S. D., Hilberman, R., & Mulder, T. (2003). Predicting the terrestrial flux of sediment to the global ocean: a planetary perspective. *Sedimentary Geology, 162*, 5-24.

Takashima, R., Nishi, H., Huber, B. T., & Leckie, R. M. (2006). Greenhouse world and the Mesozoic ocean. *Oceanography, 19*, 64-74.

Takigami, Y., Amari, S., Ozima, M., & Moberly, R. (1986). $^{40}Ar/^{39}Ar$ geochronological studies of basalts from hole 462A, Nauru Basin, Deep Sea Drilling Project Leg 89. In R. Moberly, S. O. Schlanger, & e. al. (Eds.), *Initial Reports of the Deep Sea Drilling Project* (Vol. 89, pp. 519-521). Washington, DC: US Government Printing Office.

Tarduno, J. A., Sager, W. W., & Nogi, Y. (1995). Early Cretaceous magnetostratigraphy and paleolatitudes from the Mid-Pacific Mountains: preliminary results bearing on guyot formaiton and Pacific Plate translation. In E. L. Winterer, W. W. Sager, J. V. Firth, & J. M. Sinton (Eds.), *Proceedings of the Ocean Drilling Program, Scientific Results* (Vol. 143, pp. 395-398). College Station, Texas: ODP.

Taylor, A., & Blum, J. D. (1995). Relation between soil age and silicate weathering rates determined from the chemical evolution of a glacial chronosequence. *Geology, 23*(979-982).

Taylor, B. (2006). The single largest oceanic plateau: Ontong Java–Manihiki–Hikurangi. *Earth and Planetary Science Letters, 241*(3-4), 372-380.

Tegner, C., Storey, M., Holm, P. M., Thorarinsson, S. B., Zhao, X., Lo, C.-H., & Knudsen, M. F. (2011). Magmatism and Eurekan deformation in the High Arctic large Igneous Province: 40Ar-39Ar age of Kap Washington Group volcanics, North Greenland. *Earth and Planetary Science Letters, 303*, 203-214.

Tejada, M. L. G., Mahoney, J. J., Castillo, P. R., Ingle, S. P., Sheth, H. C., & Weis, D. (2004). Pin-pricking the elephant: evidence on the origin of the Ontong Java Plateau from Pb-Sr-Hf-Nd isotopic characteristics of ODP Leg 192 basalts. In J. G. Fitton, J. J. Mahoney, P. J. Wallace, & A. D. Saunders (Eds.), *Origin and Evolution of the Ontong Java Plateau* (Vol. 229, pp. 133-150). London: The Geological Society.

Tejada, M. L. G., Mahoney, J. J., Duncan, R. A., & Hawkins, M. P. (1996). Age and geochemistry of basement and alkalic rocks of Malaita and Santa Isabel, Solomon Islands, southern margin of Ontong Java Plateau. *Journal of Petrology, 37*, 361-394.

Tejada, M. L. G., Mahoney, J. J., Neal, C. R., Duncan, R. A., & Petterson, M. G. (2002). Basement geochemistry and geochronology of Central Malaita, Solomon Islands, with implications for the origin and evolution of the Ontong Java Plateau *Journal of Petrology, 43*, 449-484.

Tejada, M. L. G., Suzuki, K., Kuroda, J., Coccioni, R., Mahoney, J. J., Ohkouchi, N., Sakamoto, T., & Tatsumi, Y. (2009). Ontong Java Plateau eruption as a trigger for the early Aptian oceanic anoxic event. *Geology, 37*(9), 855-858.

Thiede, D. S., & Vasconcelos, P. M. (2010). Parana flood basalts: Rapid extrusion hypothesis confirmed by new 40Ar/39Ar results. *Geology, 38*(8), 747-750.

Timm, C., Hoernle, K., Werner, R., Hauff, F., den Bogaard, P. v., Michael, P., Coffin, M. F., & Koppers, A. (2011). Age and geochemistry of the oceanic Manihiki Plateau, SW Pacific: New evidence for a plume origin. *Earth and Planetary Science Letters, 304*(1-2), 135-146.

Tokuyama, H., & Batiza, R. (1981). Chemical composition of igneous rocks and origin of the sill and pillow-basalt complex of Nauru Basin, Southwest Pacific. In R. L. Larson, S. O.

Schlanger, & R. E. Boyce (Eds.), *Initial Reports of Deep See Drilling Project* (Vol. 61, pp. 673-687). Washington, DC: US Government Printing Office.

Toner, B. M., Fakra, S. C., Manganini, S. J., Santelli, C. M., Marcus, M. A., Moffett, J. W., Rouxel, O., German, C. R., & Edwards, K. J. (2009). Preservation of iron(II) by carbon-rich matrices in a hydrothermal plume. *Nature Geoscience, 2*(3), 197-201. doi:10.1038/ngeo433

Torssander, P. (1989). Sulfur isotope ratios of Icelandic rocks. *Contributions to Mineralogy and Petrology, 102*, 18-23.

Torsvik, T. H., Rousse, S., Labails, C., & Smethurst, M. A. (2009). A new scheme for the opening of the South Atlantic Ocean and the dissection of an Aptian salt basin. *Geophysical Journal International, 177*(3), 1315-1333.

Trabucho Alexandre, J., Tuenter, E., Henstra, G. A., van der Zwan, K. J., van de Wal, R. S. W., Dijkstra, H. A., & de Boer, P. L. (2010). The mid-Cretaceous North Atlantic nutrient trap: Black shales and OAEs. *Paleoceanography, 25*(4), PA4201. doi:10.1029/2010pa001925

Trabucho Alexandre, J., Van Gilst, R. I., RodrÍGuez-LÓPez, J. P., & De Boer, P. L. (2011). The sedimentary expression of oceanic anoxic event 1b in the North Atlantic. *Sedimentology, 58*(5), 1217-1246.

Tremolada, F., & Erba, E. (2002). Morphometric analyses of Aptian Assiperta infracretacea and Rucinolithus terebrodentarius nannoliths: implications for taxonomy, biostratigraphy, and paleoceanography. *Marine Micropaleontology, 44*, 77-92.

Tucker, R. T., Roberts, E. M., Henderson, R. A., & Kemp, A. I. S. (2016). Large igneous province or long-lived magmatic arc along the eastern margin of Australia during the Cretaceous? Insights from the sedimentary record. *Geological Society of America Bulletin, 128*(9-10), 1461-1480.

Turchyn, A. V. (2005). *Oxygen isotopes in marine sulfate and the sulfur cycle over the past 140 million years.* (Ph.D.), Harvard University, Cambridge.

Turchyn, A. V., & Schrag, D. P. (2004). Oxygen isotope constraints on the sulfur cycle over the past 10 million years. *Science, 303*(5666), 2004-2007.

Turchyn, A. V., & Schrag, D. P. (2006). Cenozoic evolution of the sulfur cycle: Insight from oxygen isotopes in marine sulfate. *Earth and Planetary Science Letters, 241*, 763-779.

Turchyn, A. V., Schrag, D. P., Coccioni, R., & Montanari, A. (2009). Stable isotope analysis of the Cretaceous sulfur cycle. *Earth and Planetary Science Letters, 285*(1-2), 115-123.

Turner, S., Regelous, M., Kelley, S., Hawkesworth, C. J., & Mantovani, M. S. M. (1994). Magmatism and continental break-up in the South Atlantic: high precision ^{40}Ar-^{39}Ar geochronolgy. *Earth and Planetary Science Letters, 121*, 333-348.

Ueda, A., & Saki, H. (1984). Sulfur isotope study of Quaternary volcanic rocks from the Japanese Islands Arc. *Geochimica et Cosmochimica Acta, 48*, 1837-1848.

van Cappellen, P., & Ingall, E. D. (1994). Benthic phosphorus regeneration, net primary production, and ocean anoxia: A model of the coupled marine biogeochemical cycles of carbon and phosphorus. *Paleoceanography, 9*(5), 677-692.

van Cappellen, P., & Ingall, E. D. (1996). Redox stabilization of the atmosphere and oceans by phosphorus-limited marine productivity. *Science, 271*, 493-496.

van de Schootbrugge, B., Follmi, K. B., Bulot, L. G., & Burns, S. J. (2000). Paleoceanographic changes during the early Cretaceous (Valanginian-Hauterivian): evidence from oxygen and carbon stable isotopes. *Earth and Planetary Science Letters, 181*, 15-31.

Vance, D., Teagle, D. A. H., & Foster, G. L. (2009). Variable Quaternary chemical weathering fluxes and imbalance in marine geochemical budgets. *Nature, 458*, 493--496.

Verga, D., & Premoli Silva, I. (2003). Early Cretaceous planktonic foraminifera from the Tethys: the small, few-chambered representatives of the genus *Globigerinelloides*. *Cretaceous Research, 24*, 305-334.

Villeneuve, M., & Williamson, M.-C. (2006). *^{40}Ar-$^{39}Ar dating of mafic magmatism from the Sverdrup Basin Magmatic Province*. Paper presented at the Proceedings of the Fourth International Conference on Arctic Margins, Dartmouth, Nova Scotia, Canada.

Voigt, S., Gale, A. S., Jung, C., & Jenkyns, H. C. (2012). Global correlation of Upper Campanian – Maastrichtian successions using carbon-isotope stratigraphy: development of a new Maastrichtian timescale. *Newsletters on Stratigraphy, 45*(1), 25-53.

Vollstaedt, H., Eisenhauer, A., Wallmann, K., Bohm, F., Fietzke, J., Liebetrau, V., Krabbenhoft, A., Farkas, J., Tomasovych, A., Raddatz, J., & Veizer, J. (2014). The Phanerozoic $\delta^{88/86}Sr$ record of seawater: New constraints on past changes in oceanic carbonate fluxes. *Geochimica et Cosmochimica Acta, 128*, 249-265.

von Blanckenburg, F., Bouchez, J., Ibarra, D. E., & Maher, K. (2015). Stable runoff and weathering fluxes into the oceans over Quaternary climate cycles. *Nature Geosciences, 8*, 538-543.

Voss, B. M., Peucker-Ehrenbrink, B., Eglinton, T. I., Fiske, G., Wang, Z. A., Hoering, K. A., Montlucon, D. B., LeCroy, C., Pal, S., Marsh, S., Gillies, S. L., Janmaat, A., Bennett, M., Downey, B., Fanslau, J., Fraser, H., Macklam-Harron, G., Martinec, M., & Wiebe, B. (2014). Tracing river chemistry in space and time: Dissolved inorganic constituents of the Fraser River, Canada. *Geochimica et Cosmochimica Acta, 124*, 283-308.

Wagner, T., Wallmann, K., Herrle, J. O., Hofmann, P., & Stuesser, I. (2007). Consequences of ~moderate ~25,000 yr lasting emission of light CO^2 into the mid-Cretaceous ocean. *Earth and Planetary Science Letters, 259*(1-2), 200-211.

Wallmann, K. (2001). Controls on the Cretaceous and Cenozoic evolution of seawater composition, atmospheric CO_2 and climate. *Geochimica et Cosmochimica Acta, 65*, 3005-3025.

Wallmann, K. (2004). Impact of atmospheric CO_2 and galactic cosmic radiation on Phanerozoic climate change and the marine $\delta^{18}O$ record. *Geochemistry Geophysics Geosystems, 5*(6). doi:10.1029/2003GC000683

Waltham, D., & Grocke, D. R. (2006). Non-uniqueness and interpretation of the seawater $^{87}Sr/^{86}Sr$ curve. *Geochimica et Cosmochimica Acta, 70*, 384-394.

Wang, P., Chen, C., & Liu, H. (2016). Aptian giant explosive volcanic eruptions in the Songliao Basin and northeast Asia: A possible cause for global climate change and OAE-1a. *Cretaceous Research, 62*, 98-108.

Warren, J. K. (2010). Evaporites through time: Tectonic, climatic and eustatic controls in marine and nonmarine deposits. *Earth-Science Reviews, 98*(3-4), 217-268.

Wei, G., Ma, J., Liu, Y., Xie, L., Lu, W., Deng, W., Ren, Z., Zeng, T., & Yang, Y. (2013). Seasonal changes in the radiogenic and stable strontium isotopic composition of Xijiang River water: Implications for chemical weathering. *Chemical Geology, 343*, 67-75.

Weissert, H., & Erba, E. (2004). Volcanism, CO_2 and palaeoclimate: a Late Jurassic-Early Cretaceous carbon and oxygen isotope record. *Journal of the Geological Society of London, 161*, 695-702.

Westermann, S., Follmi, K. B., Adatte, T., Matera, V., Schnyder, J., Fleitmann, D., . . . Duchamp-Alphonse, S. (2010). The Valanginian $\delta^{13}C$ excursion may not be an expression of a global oceanic anoxic event. *Earth and Planetary Science Letters, 290*, 118-131.

White, A. F., & Brantley, S. L. (2003). The effect of time on the weathering of silicate minerals: why do weathering rates differ in the laboratory and field. *Chemical Geology, 202*, 479-506.

Wigand, M., Schmitt, A. K., Trumbull, R. B., Villa, I. M., & Emmermann, R. (2004). Short-lived magmatic activity in an anorogenic subvolcanic complex: $^{40}Ar/^{39}Ar$ and ion microprobe U-Pb zircon dating of Erongo, Dmaraland, Namibia. *Journal of Volcanology and Geothermal Research, 130*, 285-305.

Wing, B. A., & Halevy, I. (2014). Intracellular metabolite levels shape sulfur isotope fractionation during microbial sulfate respiration. *Proc Natl Acad Sci U S A, 111*(51), 18116-18125. doi:10.1073/pnas.1407502111

Woodhead, J. D., Harmon, R. S., & Fraser, D. G. (1987). O, S, Sr, and Pb isotope variations in volcanic rocks from the Northern Mariana Islands: implications for crustal recycling in intra-oceanic arcs. *Earth and Planetary Science Letters, 83*, 39-52.

Wortmann, U. G., & Chernyavsky, B. M. (2007). Effect of evaportie deposition on Early Cretaceous carbon and sulfur cycling. *Nature, 446*, 654-656.

Wortmann, U. G., & Paytan, A. (2012). Rapid variability of seawater chemistry over the past 130 million years. *Science, 337*(6092), 334-336. doi:10.1126/science.1220656

Wu, N., Farquhar, J., Strauss, H., Kim, S.-T., & Canfield, D. E. (2010). Evaluating the S-isotope fractionation associated with Phanerozoic pyrite burial. *Geochimica et Cosmochimica Acta, 74*(7), 2053-2071.

Young, J. R., Bown, P. R., & Lees, J. A. (2014). Nannotax3 website. from International Nannoplankton Association http://ina.tmsoc.org/Nannotax3/index.html

Young, S. A., Saltzman, M. R., Foland, K. A., Linder, J. S., & Kump, L. R. (2009). A major drop in seawater $^{87}Sr/^{86}Sr$ during the Middle Ordovician (Darriwilian): Links to volcanism and climate. *Geology, 37*, 951-954.

Yuan, F., & Mayer, B. (2012). Chemical and isotopic evaluation of sulfur sources and cycling in the Pecos River, New Mexico, USA. *Chemical Geology, 291*, 13-22.

Zhou, X., Chen, D., Dong, S., Zhang, Y., Guo, Z., Wei, H., & Yu, H. (2015). Diagenetic barite deposits in the Yurtus Formation in Tarim Basin, NW China: Implications for barium and sulfur cycling in the earliest Cambrian. *Precambrian Research, 263*, 79-87.

Zhu, D. C., Chung, S. L., Mo, X. X., Zhao, Z. D., Niu, Y., Song, B., & Yang, Y. H. (2009). The 132 Ma Comei-Bunbury large igneous province: Remnants identified in present-day southeastern Tibet and southwestern Australia. *Geology, 37*(7), 583-586.

Appendix I – Published radiometric dates for Cretaceous LIPs

Table A1-1. Published radioisotopic ages for Early Cretaceous Parana-Etendeka LIP

Method	Ref.	Sample ID	Age	Notes
EXTRUSIVES				
Laser incremental heating $^{40}Ar/^{39}Ar$ plateau ages	1	PAR-1	134.8 ± 0.7 Ma MSWD 1.28	Redated oldest(1) & youngest(2) samples from Turner et al., 1994 & Stewart et al., 1996; FC 28.201 Ma
		DSM05A	134.2 ± 0.8 Ma MSWD 1.61	
		DSM23	134.6 ±1.1 Ma MSWD 0.74	
		Total	134.6 ± 0.6 Ma MSWD 1.15	
	2	PR93-35	131.5 ± 0.2 Ma	High-Ti basalts Northern Parana basin; updated to FC 28.201 Ma by Janasi et al., 2011
		PR93-37A	131.9 ± 0.2 Ma	
		PR93-41	133.6 ± 0.8 Ma	
	3	CV190WR	134.2 ± 0.3 Ma	Low-Ti basalts Gramado type southeastern basin; Updated to FC 28.201 Ma by Janasi et al., 2011
		CV231P	134.5 ± 1.1 Ma	
		TA-137C	134.2 ± 0.3 Ma	
		GB-40cWR	134.1 ± 0.7 Ma	
		SM-278P	134.6 ± 0.6 Ma	
U-Pb baddeleyite & zircon	4	OU-09	134.3 ± 0.8 Ma MSWD 0.3	Chapeco-type dacites Ourinhos region Northern Parana overlain by main package of high-Ti basalts
	5	VIF	134.4 ± 1.1 Ma MSWD 0.48	Basalt, rhyodacite, quartz latite (2)
		WWP	134.6 ± 1.4 Ma MSWD 0.80	
		WW-254	134.8 ± 1.4 Ma MSWD 0.70	
		WW-255	135.6 ± 1.8 Ma MSWD 2.40	
	6	467 zircon	131.8 ± 1.0 Ma MSWD 0.6	Erongrorus rhyodacite
		469 zircon	132.6 ± 4.2 Ma MSWD 3.0	Ekuta rhyolite
$^{187}Re/^{188}Os$ vs $^{187}Os/^{188}Os$ isochron	7		131.6±2.3 Ma MSWD 4.5	N=6 low Ti basalts (South), N=5 high Ti basalts (North)

Table A1-1. Continued

Method	Ref.	Sample ID	Age	Notes
INTRUSIVES				
Laser incremental heating $^{40}Ar/^{39}Ar$ plateau ages	8	PR93-17B	132.9 ± 0.5 Ma	Ponta Grossa Dike Swarm, plagioclase separates, updated to FC 28.201 Ma by Janasi et al., 2011
		PR93-18	132.1 ± 0.4 Ma	
		PR93-19	132.1 ± 0.6 Ma	
		PR93-22A	131.8 ± 0.4 Ma	
		PR93-23	132.0 ± 0.4 Ma	
		PR93-24	130.8 ± 0.4 Ma	
		PR93-25	132.5 ± 0.4 Ma	
		PR93-26	132.5 ± 0.4 Ma	
		PR93-27	131.9 ± 0.4 Ma	
		PR93-30	132.7 ± 0.5 Ma	
		PR93-32	127.4 ± 0.6 Ma	
		PR93-33A	133.1 ± 0.5 Ma	
		PA-1	133.0 ± 0.3 Ma	
		PA-2	132.4 ± 0.9 Ma	
		PA-5	131.8 ± 0.4 Ma	
		PA-7	122.2 ± 1.3 Ma	
		FL-6	122.3 ± 0.7 Ma	
	9	RJ-7546	131.4 ± 0.6 Ma	Santos-Rio de Janeiro Dike Swarm plagioclase separates, updated to FC 28.201 Ma by Janasi et al., 2011
		RJ-7549	132.2 ± 0.4 Ma	
		RJ-7551	132.1 ± 0.4 Ma	
		RJ-7556	132.0 ± 0.4 Ma	
	10	RE-II-10	145.7 ± 0.2 Ma	Santos-Rio de Janeiro Dike Swarm, updated to FC 28.201 Ma by Janasi et al., 2011
		BP-M-127c	135.1 ± 0.5 Ma	
		VR-288	134.1 ± 0.3 Ma	
		BAN-351	135.3 ± 0.8 Ma	
	11	FL-13	123.8 ± 0.4 Ma	Florianopolis Dike Swarm plagioclase separates, updated to FC 28.201 Ma by Janasi et al., 2011
		FL-28	129.9 ± 0.5 Ma	
		FL-30	120.5 ± 0.7 Ma	
		FL-81	128.9 ± 0.5 Ma	
		FL-82	127.4 ± 0.5 Ma	
		FL-90	123.0 ± 0.5 Ma	
	6	212 biotite	133.1 ± 1.1 Ma	Erongo granite, hornblende MMhb-1 520.4 Ma
		454 biotite	133.3 ± 1.1 Ma	
		391 biotite	132.6 ± 1.0 Ma	Ombu granodiorite MMhb-1 520.4 Ma
		432 phlogopite	130.8 ± 1.0 Ma	Foidite plug, hornblend MMhb-1 520.4 Ma
		435 kaersutite	132.0 ± 1.0 Ma	
U-Pb zircons		460 zircon	132.3 ± 1.9 Ma MSWD 1.5	Ombu granodiorite
		454 zircon	130.3 ± 1.4 Ma MSWD 0.7	Erongo granite

References: 1 – Thiede & Vasconcelos, 2010; 2 – Ernesto et al., 1999; 3 – Renne et al., 1992; 4 – Janasi et al., 2011; 5 – Pinto et al., 2011; 6 – Wigand et al., 2004; 7 – Rocha-Junor et al., 2012; 8 – Renne et al., 1996; 9 – Deckart et al., 1998; 10 – Guedes et al., 2005; 11 – Raposo et al., 1998

Table A1-2. Published radioisotopic ages for Early-Mid Cretaceous High Arctic LIP

Method	Ref.	Sample ID	Age	Notes
EXTRUSIVES				
U-Pb zircon	1	DH3-CO2	123.3 ± 0.2 Ma MSWD 1.9	Felsic bentonite Helvetiafjellet Formation from drill core Svalbard
K-Ar whole rock	2	BF-833	109 Ma	Mg-alkaline basalts, Bennett Island, De Long Islands, Russia
		BF-834	110 Ma	
		BF-835	124 Ma	
		5-83	106 Ma	Alkaline basalt, Bennett Island
Laser incremental heating $^{40}Ar/^{39}Ar$ plateau ages	3		95.3 ± 0.2 Ma	Upper flow Strand Fiord Formation, Axel Heiberg Island, whole rock, FC 28.03 Ma
	4	AX85-75	92.3 ± 1.1 Ma	Artharber Creek Section, Strand Fiord Fm., Axel Heiberg Island, tholeiitic lava whole rock, FC 28.03 Ma
Laser incremental heating $^{40}Ar/^{39}Ar$ inverse isochron		AX85-97	96.1 ± 1.9 Ma	
INTRUSIVES				
Laser incremental heating $^{40}Ar/^{39}Ar$ plateau ages	4	AX85-37	128.2 ± 2.1 Ma	Lightfoot River dyke, Axel Heiberg Island, Canadian Arctic, FC 28.03 Ma
		BL Sill plag	129 ± 2 Ma	Buchanan Lake, Axel Heiberg Island Canadian Arctic, Williamson 1988 Ph.D. thesis, updated to FC 28.03 Ma
		BL Sill biot	126 ± 2 Ma	
		BL dyke wr	113 ± 6 Ma	
		EL84-50	97.2 ± 1.4 Ma	Piper Pass, Ellesmere Island, Canadian Arctic, FC 28.03 Ma
	5	HI 65-3	134.0 ± 3.4 Ma	Heiss Island, Franz Josef Land, dykes, plagioclase separates
		HI 74-2	134.0 ± 4.6 Ma	
		HI 79-4	138.0 ± 3.0 Ma	
		HI 40-1	125.2 ± 5.5 Ma	
		HI 80-3	125.9 ± 2.8 Ma	Heiss Island, Franz Josef Land, sills plagioclase separates
		HI 81-2	131.1 ± 2.4 Ma	
U-Pb zircons	1	1AX	124.5 ± 0.2 Ma MSWD 2.5	Mafic sills Svalbard
		7A	124.7 ± 0.3 Ma MSWD 2.4	
		1895, 1902	122.7 ± 0.3 Ma MSWD 1.3	Mafic sill Franz Josef Land
K-Ar whole rock	6	ES-1	102.1 ± 3.6 Ma	Dolerite sills and dykes, Eastern Svalbard Dolerite Belt
		ES-2	112.9 ± 3.5 Ma	
		ES-3	109.4 ± 3.4 Ma	
		ES-4	116.6 ± 3.7 Ma	
		ES-5	114.8 ± 3.7 Ma	
		ES-6	98.8 ± 3.1 Ma	
		ES-7	125.5 ± 3.6 Ma	
		ES-8	100.6 ± 3.2 Ma	
		ES-9	111.9 ± 3.5 Ma	
		ES-11	115.8 ± 3.7 Ma	
		ES-12	103.5 ± 3.0 Ma	
		ES-13	99.6 ± 3.2 Ma	
		ES-14	78.3 ± 2.6 Ma	
		ES-15	119.8 ± 3.8 Ma	
		ES-16	113.5 ± 3.8 Ma	
		ES-17	110.2 ± 3.9 Ma	
		ES-29	112.1 ± 3.7 Ma	

Table A1-2. Continued

Method	Ref.	Sample ID	Age	Notes
K-Ar whole rock	6	ES-30	99.4 ± 3.2 Ma	Dolerite sills and dykes, Eastern Svalbard Dolerite Belt
		ES-31	115.4 ± 3.9 Ma	
		ES-33	106.4 ± 3.3 Ma	
		ES-34	108.1 ± 3.6 Ma	
		ES-35	124.3 ± 4.0 Ma	
		CS-18	110.1 ± 3.6 Ma	Dolerite sills, Central Spitsbergen Dolerite Centre, Svalbard
		CS-21	104.9 ± 3.5 Ma	
		CS-22	93.9 ± 3.3 Ma	
		CS-23	118.7 ± 4.1 Ma	
		CS-26	118.6 ± 3.9 Ma	
		BH-3C	119.6 ± 3.9 Ma	
		S-32	117.8 ± 3.6 Ma	Dolerite sill, eastern Spitsbergen

References: 1 – Corfu et al., 2013; 2 – Silantyev et al., 2004; 3 – Tarduno et al., 1998; 4 – Villeneuve and Williamson, 2006; 5 – Shipilov and Karyakin, 2011; 6 – Nejbert et al., 2011;

Table A1-3. Published radioisotopic ages for Early Cretaceous Ontong Java-Manihiki-Hikurangi Plateau, Nauru Basin flood basalts, and East Mariana Basin flood basalts

Method	Ref.	Sample ID	Age	Notes
Laser incremental heating $^{40}Ar/^{39}Ar$ plateau ages	1	SG7	123.1 ± 2.1 Ma	Malaita, Solomon Islands Ontong Java, whole rock FCT-3 27.55 Ma
		SGB25	128.2 ± 8.5 Ma	
		ML475	123.2 ± 3.0	
		KF36	120.7 ± 3.2 Ma	
		KF53	124.9 ± 3.8 Ma	
	2	Malaita P43	121.8 ± 2.9 Ma	Malaita, Solomon Islands Ontong Java, whole rock Mmhb-1 513.9 Ma
		Malaita 8374	120.8 ± 2.4 Ma	
		Ramos I221	119.6 ± 1.6 Ma	Solomon Islands, Ontong Java FCT-3 biotite 27.7 Ma
		Sigana I2169	122.9 ± 1.5 Ma	
	3	DR52-2 IFM-GEOMAR	126.0 ± 1.5 Ma MSWD 1.02	Manihiki basement weighted mean 2 separate glass runs, TCR-2 27.87 Ma
		DR52-2 UO	123.8 ± 0.8 Ma	
		DR18-4B	125.2 ± 8.3 Ma MSWD 1.06	Manihiki basement, feldspar separates, TCR-2 27.87 Ma
		DR46-1	125.0 ± 2.1 Ma MSWD 2.10	
		DR26-1	124.5 ± 1.5 Ma MSWD 1.50	Manihiki basement, glass, TCR-2 27.87 Ma
		DR26-7	122.9 ± 1.6 Ma MSWD 0.57	
	4	DSDP 462A 109R1 106-108	129.7 ± 4.6 Ma	Nauru Basin, phyric basalt, whole rock, "plateau-like" JG-1 90.8 Ma
	5	DSDP 317 32R-2 54-62	116.8 ± 3.7 Ma MSWD 0.03	Manhihiki, basalts, TCR-2 27.87 Ma
		DSDP 317 34R-4 125-135	116.4 ± 5.1 Ma MSWD 0.08	
$^{40}Ar/^{39}Ar$ laser fusion of single feldspar crystals		SO168-34-4, 16 crystals	118.4 ± 4.0 Ma MSWD 1.18	Hikurangi basement Rapuhia Scarp, basalt, TCR-2 27.87 Ma
		SO168-34-11, 12 crystals	108.0 ± 0.7 Ma MSWD 1.36	Hikurangi basement Rapuhia Scarp, gabbro, TCR-2 27.87 Ma
		SO168-34-9, 10 crystals	110.8 ± 2.7 Ma MSWD 1.30	Hikurangi basement Rapuhia Scarp, dolerite, TCR-2 27.87 Ma
		SO168-38-3, 9 crystals	96.3 ± 3.8 Ma MSWD 1.30	Hikurangi basement Rapuhia Scarp, dolerite-gabbro, TCR-2 27.87 Ma
	6	ODP 1184 subunit IIE cores 40-45	123.54 ± 1.79 Ma MSWD 0.20	Ontong Java volcaniclastic sediment, weighted average 6 fusions, FCT 28.02 Ma
Laser incremental heating $^{40}Ar/^{39}Ar$ inverse isochron	7	ODP 807C 75R-2 129-131	121.7 ± 3.6 Ma SUMS(N-2) 0.08	Ontong Java whole rock, Mmhb-1 520.4 Ma, $^{40}Ar/^{36}Ar$ 297.3±11.0
		ODP 807C 78R-1 67-69	124.0 ± 2.5 Ma SUMS(N-2) 0.40	Ontong Java whole rock, Mmhb-1 520.4 Ma, $^{40}Ar/^{36}Ar$ 294.0±3.3
		ODP 807C 80R-1 52-55	122.4 ± 4.0 Ma SUMS(N-2) 1.22	Ontong Java whole rock, Mmhb-1 520.4 Ma, $^{40}Ar/^{36}Ar$ 290.5±4.9
		ODP 807C 84R-6 0-3	122.6 ± 1.7 Ma SUMS(N-2) 0.05	Ontong Java whole rock, Mmhb-1 520.4 Ma, $^{40}Ar/^{36}Ar$ 292.6±17.5
		ODP 807C 90R-1 38-41	119.5 ± 9.9 Ma SUMS(N-2) 0.28	Ontong Java whole rock, Mmhb-1 520.4 Ma, $^{40}Ar/^{36}Ar$ 307.6±29.9
		ODP 807C 93R-3 15-18	126.0 ± 4.8 Ma SUMS(N-2) 0.30	Ontong Java whole rock, Mmhb-1 520.4 Ma, $^{40}Ar/^{36}Ar$ 294.0±3.0

Table A1-3. Continued

Method	Ref.	Sample ID	Age	Notes
Laser incremental heating $^{40}Ar/^{39}Ar$ inverse isochron	7	DSDP 289 132R4 122-125	122.7 ± 2.2 Ma SUMS(N-2) 0.22	Ontong Java whole rock, Mmhb-1 520.4 Ma, $^{40}Ar/^{36}Ar$ 297.3±11.0
		DSDP 289 132R4 79-81	128.5 ± 2.6 Ma SUMS(N-2) 0.53	Ontong Java whole rock, Mmhb-1 520.4 Ma, $^{40}Ar/^{36}Ar$ 288.8±4.1, plateau age 121.7 ± 2.7 Ma
	8	ODP 802A 62R2 45-50	116.8 ± 4.8 Ma SUMS(N-2) 2.12	East Mariana, whole rock, Mmhb-1 514.0 Ma, $^{40}Ar/^{36}Ar$ 303.2±39.4
		ODP 802A 62R2 45-50 dup	112.5 ± 4.6 Ma SUMS(N-2) 0.40	East Mariana, whole rock, Mmhb-1 514.0 Ma, $^{40}Ar/^{36}Ar$ 306.0±24.5
		ODP 802A 62R3 4-12	116.0 ± 13.1 Ma SUMS(N-2) 0.97	East Mariana, whole rock, Mmhb-1 514.0 Ma, $^{40}Ar/^{36}Ar$ 294.4±38.3
	9	DSDP 462A 106R2 54-61	111.6 ± 1.5 Ma 109.9 ± 1.4 Ma	Nauru Basin, tholeiites, whole rock, duplicate runs, Mmhb-1 514.0 Ma
		DSDP 462A 108R2 4-9	113.6 ± 4.5 Ma 100.5 ± 24.1 Ma	
	10	DSDP 462A 32R-1 46-49	110 ± 3 Ma SUMS(N-2) 2.86	Nauru Basin, aphyric basalt/dolerite sill, whole rock
Incremental heating $^{40}Ar/^{39}Ar$ total fusion age		DSDP 462A 50R-3 130-134	130.6 ± 15 Ma	Nauru Basin, dolerite sill, whole rock, ragged age spectrum, isochron age not calculated

References: 1 – Tejada et al., 2002; 2 – Tejada et al., 1996; 3 – Timm et al., 2011; 4 – Takigami et al., 1986; 5 – Hoernle et al., 2010; 6 – Chambers et al., 2004; 7 – Mahoney et al., 1992; 8 – Pringle, 1992; 9 – Castillo et al., 1994; 10 – Ozima et al., 1981

Table A1-4. Published radioisotopic ages for Early Cretaceous Comie-Bunbury LIP

Method	Ref.	Sample ID	Age	Notes
EXTRUSIVES				
Laser incremental heating $^{40}Ar/^{39}Ar$ plateau ages	1	BB-3	130.6 ± 2.1 Ma	Casuarina lava type Bunbury basalts, whole rock, FCT-3 27.7 ± 0.2 Ma
		BB-4	129.2 ± 1.8 Ma	
	2	BB-1	132.2 ± 0.3 Ma MSWD 0.36	Casuarina lava type Bunbury basalt, plagioclase separate, USGS sandine 85G003 28.34 Ma
U-Pb zircons	3	08JBT04	131 ± 5 Ma MSWD 0.1	Comei dacites, Sangxiu Formation
		SX(10)-1	133.0 ± 3.0 Ma	
INTRUSIVES				
U-Pb zircons	3	DL06-1	129.5 ± 1.3 Ma MSWD 0.69	Comei diabasic dikes
		08DL01	133 ± 2 Ma MSWD 0.2	
		08JBT01	132 ± 2 Ma MSWD 0.4	
		CM2-1	130.8 ± 2.0 Ma MSWD 1.94	
		QG3-2	132.1 ± 1.0 Ma MSWD 1.13	
		YM04-1	134.1 ± 2.0 Ma	
		YM04-4	133.4 + 1.6 Ma	
		DJ3-4	129.7 ± 1.4 Ma MSWD 1.07	Comei gabbros
		08JBT03	132 ± 3 Ma MSWD 0.2	
		08CM8-1	131 ± 1 Ma MSWD 0.2	
		08ZG02-4	132 ± 1 Ma MSWD 0.4	
		CN20-2	131.1 ± 6.1 Ma	
		ZG5-1	130.0 ± 2.0 Ma MSWD 1.08	Comei pyroxenite

References: 1 – Frey et al., 1996; 2 – Coffin et al., 2002; 3 – Zhu et al., 2009

Table A1-5. Published radioisotopic ages for Kerguelen Plateau-Broken Ridge and Rajmahal-Bengal-Sylhet Traps

Method	Ref.	Sample ID	Age	Notes
EXTRUSIVES				
Laser incremental heating $^{40}Ar/^{39}Ar$ plateau ages	1	ODP 750B 16R2 102-108	112.4 ± 0.4 Ma MSWD 0.42	Southern Kerguelen Plateau plagioclase separate USGS sandine 85G003 28.34 Ma
		KP-7	118.1 ± 0.3 Ma MSWD 0.08	Rajmahal basalts plagioclase separate USGS sandine 85G003 28.34 Ma
	2	ODP 1136A 16R1 84-89	118.99 ± 2.11 Ma MSWD 1.11	Southern Kerguelen Plateau plagioclase separate FCT-3 28.04 Ma
		ODP 1136A 18R2 83-84	118.73 ± 2.11 Ma MSWD 0.19	
		ODP1137A 32R7 52-59	107.07 ± 1.27 Ma MSWD 1.79	Elan Bank plagioclase separate FCT-3 28.04 Ma
		ODP 1138A 80R2 126-134	100.83 ± 2.94 Ma MSWD 0.23	Central Kerguelen Plateau plagioclase separate FCT-3 28.04 Ma
		ODP 1138A 80R2 126-134	100.24 ± 1.09 Ma MSWD 2.22	Central Kerguelen Plateau whole rock FCT-3 28.04 Ma
		ODP 1138A 84R5 88-93	100.51 ± 1.00 Ma MSWD 1.82	Central Kerguelen Plateau whole rock FCT-3 28.04 Ma
		ODP 1141A 22R3 143-150	95.17 ± 0.77 Ma MSWD 0.76	Broken Ridge whole rock FCT-3 28.04 Ma
		ODP 1142A 6R1 12-16	94.18 ± 0.83 Ma MSWD 2.22	
		ODP 1142A 9R3 91-94	94.88 ± 0.90 Ma MSWD 2.11	
	3	RJ 1-30-4	117.9 ± 0.4 Ma MSWD 1.30	Rajmahal quartz tholeiite group I lava, TCR sandine 85G003 28.34 MA
		A-531	117.5 ± 0.5 Ma	Rajmahal quartz tholeiite group I lava, FCT-3 27.95 Ma
		Galsi	117.3 ± 1.0 Ma 117.1 ± 0.3 Ma	Bengal Traps borehole alkali basalt, splits done twice, FCT-3 27.95 Ma
	4	ST94-1	116.1 ± 4.2 Ma MSWD 0.67	Sylhet Traps, flux monitor Minnesota Hornblende (MMhb-1) 523.2 Ma
		ST94-2	115.6 ± 5.4 Ma MSWD 0.36	
INTRUSIVES				
S.A.	5	RJ 1-13-2	115.3 ± 0.4 Ma MSWD 0.88	Rajmahal quartz tholeiite group II dyke, TCR sandine 85G003 28.34 Ma

References: 1 – Coffin et al., 2002; 2 – Duncan, 2002; 3 – Kent et al., 2002; 4 – Ray et al., 2005; S.A. – Same as above

Appendix II – GTS2012 ages and S isotope data

Table A2-1. ODP Hole 1213B samples, GTS2012 age assignment, and S isotope data

Sample	Depth (mbsf)	GTS2012 age (Ma)	$\delta^{34}S_{Ba}$ (‰ VCDT)	$\delta^{34}S_{py}$ (‰ VCDT)	$\Delta^{34}S$ (‰ VCDT)
9R-1 12-15 cm	266.535	126.38 ± 0.63	NA	-51.08	NA
9R-1 29-32 cm	266.705	126.40 ± 0.64	16.41 ± 0.45 (n=3)	-52.56	-68.97
9R-1 46-49 cm	266.875	133.81 ± 1.31	NA	-54.47	NA
14R-1 6-10 cm	313.18	136.50 ± 1.06	NA	-51.80	NA
14R-1 27-30 cm	314.385	136.54 ± 1.06	NA	-49.90	NA
14R-1 37-40 cm	314.485	136.54 ± 1.06	NA	-47.88 ± 0.89	NA
14R-1 53-57 cm	314.65	136.55 ± 1.06	NA	-50.93 ± 0.40	NA
14R-1 60-63 cm	314.715	136.56 ± 1.06	NA	-50.53	NA
15R-1 26-28 cm	324.07	137.09 ± 1.02	NA	-51.26	NA
15R-1 33-36 cm	324.145	137.10 ± 1.02	NA	-50.43 ± 0.48	NA
19R-1 7-10 cm	362.285	139.29 ± 0.93	NA	-46.83	NA
19R-1 20-23 cm	362.415	139.30 ± 0.93	NA	-44.36	NA
19R-1 104-106 cm	363.25	139.35 ± 0.93	21.24 ± 0.47 (n=6)*	-44.48	-65.72
20R-1 20-24 cm	372.025	139.85 ± 0.93	NA	-46.72 ± 0.26	NA
20R-1 48-50 cm	372.29	139.87 ± 0.93	NA	-46.04	NA
20R-1 71-73 cm	372.52	139.88 ± 0.93	NA	-45.17	NA
21R-1 26-28 cm	381.67	140.40 ± 0.93	21.16 ± 0.60 (n=5)*	-51.02	-72.18
21R-1 63-65 cm	382.04	140.43 ± 0.93	NA	-48.80 ± 1.59	NA
22R-1 22-24 cm	391.33	140.96 ± 0.95	NA	-50.23	NA
22R-1 37-41 cm	391.49	140.97 ± 0.95	NA	-47.81	NA
22R-1 66-68 cm	391.77	140.99 ± 0.95	18.12 ± 0.07 (n=3)	-48.98	-67.10
22R-1 90-93 cm	392.015	141.00 ± 0.95	NA	-47.28 ± 0.56	NA
23R-1 13-16 cm	400.845	141.51 ± 0.96	NA	-47.58	NA
23R-1 30-33 cm	401.015	141.52 ± 0.97	NA	-51.28	NA
23R-1 54-56 cm	401.255	141.53 ± 0.97	NA	-42.94	NA
24R-1 4-7 cm	410.355	142.05 ± 0.99	NA	-52.71	NA
24R-1 25-28 cm	410.565	142.07 ± 0.99	NA	-51.02	NA
24R-1 115-117 cm	411.46	142.12 ± 0.99	NA	-50.26 ± 0.74	NA
25R-1 21-23 cm	420.12	142.61 ± 1.03	NA	-44.63	NA
26R-1 14-17 cm	429.255	143.14 ± 1.06	NA	-43.05	NA

Table A2-2. ODP Hole 1207B samples, GTS2012 age assignment, and S isotope data

Sample	Depth (mbsf)	GTS2012 age (Ma)	$\delta^{34}S_{Ba}$ (‰ VCDT)	$\delta^{34}S_{py}$ (‰ VCDT)	$\Delta^{34}S$ (‰ VCDT)
40R-CC 17-19 cm	526.68	120.55 ± 1.68	NA	-46.46	NA
40R-CC 27-29 cm	526.78	120.56 ± 1.68	NA	-45.38	NA
43R-1 16-18 cm	555.57	123.29 ± 1.51	16.86 ± 0.28 (n=2)*	NA	NA
43R-1 56-58 cm	555.97	123.33 ± 1.52	NE	NA	NA
43R-1 63-65 cm	556.04	123.33 ± 1.52	NA	-37.10 ± 0.24	NA
43R-1 68-70 cm	556.09	123.34 ± 1.52	15.91 ± 0.34 (n=4)*	NA	NA
43R-1 73-75 cm	556.14	123.34 ± 1.52	NA	NA	NA
43R-1 78-80 cm	556.19	123.35 ± 1.52	NE	NA	NA
43R-1 87-89 cm	556.28	123.36 ± 1.52	NA	-32.73	NA
43R-1 103-105 cm	556.44	123.37 ± 1.52	NA	-34.18	NA
43R-1 112-114 cm	556.53	123.38 ± 1.52	NA	-34.65 ± 0.03	NA
43R-1 122-124 cm	556.63	123.39 ± 1.53	NA	-34.93	NA
44R-1 40-43 cm	565.415	124.22 ± 1.68	PD/NE	-52.94	NA
44R-1 49-52 cm	565.505	124.23 ± 1.68	NE	-35.84	NA
44R-1 132-135 cm	566.335	125.44 ± 0.98	NA	-33.81 ± 0.25	NA
44R-2 13-16 cm	566.575	125.46 ± 0.98	NA	-42.20 ± 0.78	NA
46R-1 14-17 cm	584.355	127.50 ± 0.86	NA	-53.26	NA
46R-1 49-52 cm	584.705	127.54 ± 0.86	18.29 ± 0.33 (n=3)	-50.44	-68.73
46R-1 81-84 cm	585.025	127.58 ± 0.86	19.68 ± 0.27 (n=2)	-51.52 ± 1.51	-71.20 ± 1.53
46R-1 97-100 cm	585.185	127.59 ± 0.86	19.32 ± 0.23 (n=3)	-51.06 ± 0.50	-70.38 ± 0.55
46R-2 34-36 cm	586.05	127.69 ± 0.86	NA	-43.65	NA
47R-1 15-18 cm	593.965	128.60 ± 0.86	NA	-38.54 ± 0.71	NA
47R-1 36-38 cm	594.17	128.62 ± 0.86	NA	-40.01	NA
47R-1 76-78 cm	594.57	128.67 ± 0.86	NE	-45.04	NA
47R-2 10-13 cm	595.415	128.77 ± 0.86	NE	-32.83	NA
47R-2 73-75 cm	596.04	128.84 ± 0.86	NA	-42.23	NA
47R-3 45-48 cm	597.265	128.98 ± 0.86	NE	-36.28	NA
48R-1 28-30 cm	603.79	129.72 ± 0.89	NA	-45.35 ± 1.42	NA
48R-1 94-96 cm	604.45	129.80 ± 0.90	18.23 ± 0.79 (n=3)	-26.34	-44.57 ± 0.79
49R-1 20-23 cm	613.415	130.83 ± 0.97	NA	-30.62 ± 0.77	NA
49R-1 50-53 cm	613.715	130.86 ± 0.97	NE	-30.92 ± 1.62	NA
49R-116-119 cm	614.375	130.94 ± 0.98	NA	-25.59 ± 3.79	NA

Table A2-3. ODP Hole 766A samples, GTS2012 age assignment and S isotope data

Sample	Depth (mbsf)	GTS2012 age (Ma)	$\delta^{34}S_{Ba}$ (‰ VCDT)	$\delta^{34}S_{py}$ (‰ VCDT)	$\Delta^{34}S$ (‰ VCDT)
15R-3 32-35 cm	136.535	100.00 ± 0.73	16.91 ± 0.17 (n=2)	NA	NA
15R-3 72-77.5 cm	136.95	100.05 ± 0.72	16.35 ± 0.57 (n=3)	NA	NA
15R-4 9-13 cm	137.81	100.15 ± 0.69	17.42 ± 0.03 (n=2)	NA	NA
15R-4 89-93 cm	138.61	100.25 ± 0.67	17.17 ± 0.01 (n=2)	NA	NA
15R-4 144.5-146.5 cm	139.155	100.31 ± 0.65	17.57 ± 0.03 (n=2)	NA	NA
15R-5 25-29 cm	139.47	100.35 ± 0.65	17.08 ± 0.79 (n=3)	NA	NA
15R-5 75-79 cm	139.97	100.41 ± 0.63	17.15	NA	NA
15R-5 140-144 cm	140.62	100.49 ± 0.62	17.18 ± 0.06 (n=2)	NA	NA
15R-6 51-55 cm	141.23	100.56 ± 0.60	16.91 ± 0.35 (n=2)	NA	NA
16R-1 32-36 cm	143.24	100.80 ± 0.55	17.10 ± 0.11 (n=3)	NA	NA
16R-1 100-104 cm	143.92	100.88 ± 0.54	16.92 ± 0.11 (n=3)	NA	NA
16R-2 8-12 cm	144.5	100.95 ± 0.53	16.32 ± 0.21 (n=3)	NA	NA
16R-2 50-54 cm	144.92	101.00 ± 0.52	17.13 ± 0.11 (n=3)	NA	NA
17R-6 25-28 cm	160.265	102.80 ± 0.63	14.75 ± 0.07 (n=3)	NA	NA
17R-7 16-20 cm	161.68	103.04 ± 0.63	14.31 ± 0.10 (n=3)	NA	NA
17R-7 61-65 cm	162.13	103.11 ± 0.63	15.06	NA	NA
25R-1 26-29 cm	229.875	118.06 ± 0.60	15.00 ± 0.47	NA	NA
26R-2 46.5-50.5 cm	241.285	125.27 ± 1.06	15.92 ± 0.02 (n=2)	NA	NA
26R-3 40.5-44.5 cm	242.725	125.50 ± 1.03	15.99	NA	NA
27R-2 110.5-114.5 cm	251.525	126.88 ± 0.91	16.89 ± 0.14 (n=2)	-36.20	-53.09 ± 0.14
27R-3 5-9 cm	251.97	126.95 ± 0.91	17.00	-43.55 ± 0.98 (n=2)	-60.55 ± 0.98
28R-1 10-14 cm	258.72	128.00 ± 0.84	16.78 ± 0.21 (n=3)	52.62 ± 0.00 (n=2)	-69.40 ± 0.21
28R-1 98-102 cm	259.6	128.14 ± 0.84	16.68	-46.73	-63.41
28R-2 31-35 cm	260.43	128.27 ± 0.83	17.04 ± 0.59 (n=2)	-50.65 ± 0.73 (n=2)	-67.69 ± 0.94
29R-1 35-39 cm	268.67	129.56 ± 0.80	16.74 ± 0.35 (n=2)	-51.19	-67.93 ± 0.35
29R-1 105-109 cm	269.37	129.67 ± 0.80	16.60	-49.24 ± 0.08 (n=2)	-65.84 ± 0.08
29R-3 86-89 cm	272.175	130.11 ± 0.80	17.54 ± 0.01 (n=2)	-48.73 ± 0.86 (n=2)	-66.27 ± 0.86
29R-4 105-108 cm	273.865	130.38 ± 0.80	17.60 ± 0.34 (n=3)	-51.42 ± 1.66 (n=2)	-69.02 ± 1.69

Table A2-4. ODP Hole 866A samples, GTS2012 age assignment, and pyrite S isotope data. Barremian-Albian data from Mills et al. (2013) and Hautervian data from current study. Samples with error estimate are standard deviation from replicate analyses (n=2).

Sample	Depth (mbsf)	GTS2012 age (Ma)	$\delta^{34}S_{py}$ (‰ VCDT)
51R-1 22-28 cm	463.62	115.54 ± 0.69	-42.62
53R-1 45-53 cm	483.15	116.47 ± 0.66	-34.01
54R-1 47-54 cm	492.77	116.93 ± 0.65	-41.93
56R-1 24-33 cm	511.84	117.84 ± 0.64	-40.96
57R-1 10-17 cm	521.4	118.29 ± 0.64	-42.36
57R-1 92-98 cm	522.22	118.33 ± 0.64	-46.02
58R-1 54-60 cm	531.54	118.77 ± 0.65	-40.99
59R-1 51-56 cm	541.21	119.23 ± 0.65	-42.70
61R-1 116-126 cm	561.06	120.18 ± 0.67	-37.55
62R-1 41-51 cm	570.01	120.61 ± 0.69	-39.22
63R-1 95-105 cm	580.25	121.09 ± 0.70	-37.59
63R-2 95-105 cm	581.75	121.16 ± 0.71	-41.95
64R-1 87-97 cm	589.87	121.55 ± 0.72	-31.28
64R-2 60-70 cm	591.1	121.61 ± 0.73	-41.07
65R-1 70-80 cm	599.3	122.00 ± 0.50	-40.66
66R-1 89-96 cm	609.19	122.15 ± 0.62	-41.95
67R-1 34-44 cm	618.34	122.28 ± 0.59	-41.96
70R-1 25-35 cm	647.15	122.71 ± 0.57	-41.15
70R-2 43-53 cm	648.14	122.73 ± 0.57	-43.02
71R-2 38-48 cm	658.16	122.88 ± 0.59	-43.02
72R-1 62-69 cm	666.82	123.01 ± 0.62	-39.34
74R-2 75-85 cm	687.53	124.71 ± 0.56	-42.44
74R-3 25-35 cm	688.24	124.71 ± 0.56	-40.03
75R-2 55-65 cm	696.8	124.76 ± 0.55	-43.83
75R-4 38-48 cm	699.24	124.77 ± 0.54	-39.71
76R-2 115-125 cm	707.35	124.81 ± 0.53	-37.89
88R-1 70-80 cm	821.6	125.43 ± 0.64	-35.67
89R-2 15-25 cm	832.25	125.57 ± 0.63	-36.51
91R-1 17-27 cm	849.67	125.79 ± 0.61	-43.05
97R-1 45-55 cm	907.85	126.53 ± 0.58	-47.51
98R-1 35-45 cm	917.35	126.65 ± 0.57	-41.84
98R-2 20-30 cm	918.7	126.67 ± 0.57	-40.52
99R-1 10-20 cm	924	126.74 ± 0.57	-34.05
100R-1 10-20 cm	933.5	126.86 ± 0.57	-38.62
101R-1 3-13 cm	943.13	126.98 ± 0.56	-38.15
103R-1 43-47 cm	962.83	127.23 ± 0.56	-37.75
104R-1 63-67 cm	972.33	127.36 ± 0.56	-44.63
105R-1 43-47 cm	981.73	127.47 ± 0.56	-32.81
107R-1 15-19 cm	1000.65	127.72 ± 0.57	-38.96
108R-1 73-77 cm	1010.93	127.85 ± 0.57	-38.14
109R-1 65-69 cm	1020.55	127.97 ± 0.57	-39.65
110R-1 15-19 cm	1029.75	128.09 ± 0.57	-39.52
111R-1 95-99 cm	1040.25	128.22 ± 0.58	-36.94
113R-CC 20-27 cm	1058.7	128.46 ± 0.61	-40.53
114R-1 70-77 cm	1068.9	128.59 ± 0.60	-38.90

Table A2-4. Continued

Sample	Depth (mbsf)	GTS2012 age (Ma)	$\delta^{34}S_{py}$ (‰ VCDT)
115R-1 23-30 cm	1078.13	128.72 ± 0.60	-36.89
116R-1 48-55 cm	1087.98	128.85 ± 0.59	-36.74
118R-1 40-47 cm	1107.2	129.10 ± 0.59	-32.97
119R-1 23-30 cm	1116.73	129.23 ± 0.59	-37.41
120R-1 40-47 cm	1126.5	129.36 ± 0.59	-45.77
122R-1 35-42 cm	1145.75	129.61 ± 0.60	-41.73
125R-1 27-34 cm	1174.67	129.99 ± 0.61	-39.17
125R-3 110-117 cm	1178.43	130.04 ± 0.62	-38.77
127R-1 25-32 cm	1193.75	130.25 ± 0.63	-37.12
149R-1 5.5-9 cm	1405.4725	132.865 ± 0.642	-39.97 ± 0.02
149R-1 23-25 cm	1405.64	132.866 ± 0.642	-40.17
149R-1 76-79 cm	1406.175	132.869 ± 0.641	-40.05 ± 0.09
149R-1 128-131 cm	1406.695	132.871 ± 0.640	-39.89
149R-2 0-4 cm	1406.92	132.873 ± 0.639	-38.86 ± 0.90
149R-2 43-46 cm	1407.345	132.875 ± 0.638	-39.21
149R-2 66-69 cm	1407.575	132.876 ± 0.638	-39.90
150R-1 8-11 cm	1415.195	132.915 ± 0.623	-42.23 ± 0.51
150R-1 27.5-31.5 cm	1415.395	132.916 ± 0.623	-43.90 ± 0.26
150R-1 77-78 cm	1415.875	132.919 ± 0.622	-41.37 ± 0.21
150R-1 122-125 cm	1416.335	132.921 ± 0.621	-40.31
150R-2 12-15 cm	1416.735	132.923 ± 0.620	-42.49 ± 0.25
150R-2 36-39 cm	1416.975	132.924 ± 0.620	-41.76 ± 0.83
150R-2 85-89 cm	1417.47	132.927 ± 0.619	-42.66
150R-2 105-108 cm	1417.665	132.928 ± 0.619	-41.33
150R-3 13-15 cm	1418.24	132.931 ± 0.618	-39.57
150R-3 36.5-39 cm	1418.4775	132.932 ± 0.618	-39.89 ± 0.31
150R-3 60-63 cm	1418.715	132.933 ± 0.617	-40.94
150R-3 111-114 cm	1419.225	132.936 ± 0.616	-41.88 ± 0.88
150R-3 139-142 cm	1419.505	132.937 ± 0.616	-42.89
150R-4 8-11 cm	1419.695	132.938 ± 0.616	-42.97 ± 0.52
150R-4 25-28 cm	1419.865	132.939 ± 0.616	-40.29 ± 0.32
150R-4 41-44 cm	1420.025	132.940 ± 0.615	-41.05 ± 0.13
150R-4 67-71 cm	1420.29	132.941 ± 0.615	-42.54
150R-4 87-89 cm	1420.485	132.942 ± 0.615	-40.49 ± 0.11
150R-4 94-97 cm	1420.555	132.943 ± 0.615	-42.29
152R-1 23-25 cm	1434.745	133.016 ± 0.602	-40.56 ± 0.05
152R-1 57-60.5 cm	1435.085	133.018 ± 0.601	-41.92
152R-1 78-81 cm	1435.29	133.019 ± 0.601	-41.75 ± 0.04
152R-2 25-28 cm	1436.27	133.024 ± 0.601	-41.16
152R-2 125-128 cm	1437.27	133.029 ± 0.601	-41.34
158R-2 32-34 cm	1494.33	133.393 ± 0.790	-39.07
167R-1 102-104 cm	1581.43	133.816 ± 0.806	-42.34 ± 0.27
167R-1 139-142 cm	1581.805	133.818 ± 0.807	-40.48
167R-2 25-28 cm	1582.165	133.820 ± 0.808	-41.59
169R-2 126-128 cm	1602.57	133.919 ± 0.603	-38.43 ± 0.26
169R-3 12-14 cm	1602.93	133.921 ± 0.603	-39.27
170R-1 27-30 cm	1609.685	133.954 ± 0.610	-39.05 ± 0.90
170R-1 75-79 cm	1610.17	133.956 ± 0.610	-38.31 ± 0.51
170R-1 116-119 cm	1610.575	133.958 ± 0.611	-38.39

Appendix Table A2-4. Continued

Sample	Depth (mbsf)	GTS2012 age (Ma)	$\delta^{34}S_{py}$ (‰ VCDT)
170R-2 17-20 cm	1611.085	133.961 ± 0.612	-40.06
170R-2 92-95 cm	1611.835	133.964 ± 0.613	-37.74 ± 0.84
170R-2 131-135 cm	1612.23	133.966 ± 0.613	-37.16
170R-3 52-55 cm	1612.935	133.970 ± 0.614	-38.47
170R-3 97-101 cm	1613.39	133.972 ± 0.615	-37.85
170R-3 137-141 cm	1613.79	133.974 ± 0.616	-37.11
170R-4 85-88 cm	1614.765	133.979 ± 0.617	-38.98
170R-4 123-126 cm	1615.145	133.980 ± 0.618	-40.36

Appendix III - Carbonate associated sulfate S isotope data from ODP Hole 866A Resolution Guyot and DSDP Hole 511 Falkland Plateau

A3.1 Carbonate-Associated Sulfate (CAS) extraction

CAS was extracted from carbonate rich ODP and DSDP samples following standard techniques based on Wotte et al. (2012). Three rounds of suspension of the powdered samples within a 10% NaCl solution were used to dissolve and remove surface bound non-CAS S phases. After filtering from the final NaCl suspension, the samples were rinsed thoroughly with deionized water. The samples were then dissolved with 4N acetic acid while being constantly stirred. After allowing some time for settling the insoluble residue was filtered within 4 hours of acidification. A saturated $BaCl_2$ solution was added to the filtrate to facilitate precipitation of $BaSO_4$ overnight. The $BaSO_4$ was filtered, dried and then weighed to estimate CAS concentrations gravimetrically. The $BaSO_4$ was then used for S isotope analysis.

A3.2 DSDP Leg 71 Hole 511 Falkland Plateau age model

DSDP Hole 511 is an intermediate depth drill hole located on the eastern extension of the Falkland Plateau east of Argentina and the Falkland Islands in the South Atlantic/Southern Ocean [Wise, 1983]. Key biostratigraphic data used to constrain the Aptian-Albian boundary and determine sedimentation rates within the Mid Cretaceous are presented in Table A3-1 with their core depth and GTS2012 age assignments [Wise, 1983; Huber and Leckie, 2011]. The Late Aptian marks a major lithologic change within Hole 511 from black shales and nannofossil mudstones to claystones, nannofossil claystones, and muddy nannofossil chalk as this region transitioned to a much more open marine environment with the opening of the South Atlantic

Ocean [SSP IR Ch2, 1983; Robert and Maillot, 1983; Torsvik et al., 2009; Moulin et al., 2010; Chaboureau et al., 2013]. Despite extensive black shale deposition during the Jurassic and Early Cretaceous on the Falkland Plateau there is no lithologic indication for the Jacob, Killan, or Paquier/Urbino black shales associated with OAE 1b in Hole 511 [SSP IR Ch2, 1983]. High resolution planktonic foraminifera analysis by Huber and Leckie (2011) identified the Aptian-Albian boundary in Hole 511 with the LO *Paraticinella eubejaouaensis* (= *P. rohri*, Ando et al., 2013) (Table A3-1). The recently proposed GSSP for the Aptian-Albian boundary (AAB) by Kennedy et al. (2014), however, uses the FO *Microhedbergella renilaevis* as the marker for the AAB. In Hole 511 the FO *M. renilaevis* occurs approximately 1 m above the LO *P. eubejaouaensis* (Table A3-1) [Huber and Leckie, 2011]. The LO of planktonic foraminifera

Table A3-1. GTS2012 age assignments of select key biostratrigraphic data for Aptian-Albain from DSDP Hole 511. Data from Wise (1983) and Huber and Leckie (2011). The age assignment location (listed below sample depth) is the midpoint between the sample containing FO or LO and the next sample analyzed where the organism is absent.

Sample	mbsf	Biostratigraphic data	Age Assignment	Comments
50R-1 100 cm	433.5 (433.95 ± 0.45)	FO *Eiffellithus turriseiffelii*	103.13 ± 0.5	Late Albian CC9 base GTS2012 103.13 Ma
51R-2 135 cm	444.85	LO *Sollasites falklandensis*		Middle Albian 107.59 Ma Nannotx3
51R-CC	450.90 (452.24 ± 1.34)	FO *Tranolithus orionatus*	110.73 ± 0.5	Middle Albian GTS2012 110.73 Ma
52R-3 25-27 cm	454.75	FO *Ticinella yezoana*		
55R-3 32 cm	483.32	FO *Seribiscutum primitivum* FO *Sollasites falklandensis*		Nannotax3 NC8a Early Albian 112.95 Ma
55R-4 24-26 cm	484.75	FO *Microhedbergella rischi*		
55R-4 60-61 cm	485.11	FO *Microhedbergella renilaevis*		Kennedy et al., 2014 marker for AAB proposed GSSP
55R-5 24-26 cm	485.95	LO *Hedbergella praelippa*		
55R-5 43-44 cm	486.14	LO *Paraticinella eubejaouaensis*		Late Aptian – Huber & Leckie, 2011 marker for AAB; = *P. rohri* see Ando et al., 2013
55R-5 99-100 cm	486.70	FO *Microhedbergella miniglobularis*		Late Aptian – GTS2012 & Kennedy et al., 2014 after LO P. eubejaouaensis but Huber & Leckie, 2011 slight overlap

Hedbergella praelippa within this interval along with the Early Albian FO of calcareous nannofossil *Seribiscutum primitivum* and *Sollasites falklandensis* occurring above the FO *M. renilaevis* further supports the reassignment of the AAB (Table A3-1) [Wise, 1983; Huber and Leckie, 2011; Kennedy et al., 2014]. Therefore, the AAB within DSDP Hole 511 is assigned to the midpoint between the FO *M. renilaevis* and the sample below (485.28 ± 0.15 mbsf) with the GTS2012 age of 113 ± 0.4 Ma. Calcareous nannofossils provide the remaining Albian tie points in Hole 511 with the FO *Tranolithus orionatus* constraining the Early to Middle Albian and FO *Eiffellithus turriseiffelii* defining the Late Albian (Table A3-1) [Wise, 1983]. The sedimentation rate calculated for the Early to Middle Albian (AAB to FO *T. orionatus*) is ~6 times higher than the sedimentation rate estimated for the Middle to Late Albian (FO T. orionatus to FO *E. turriseiffelii*). These two sedimentation rates were used to determine the age estimate for samples in cores 55 through 52 and core 51, respectively. The age estimates for samples in core 51 are in line with the Middle Albian LO *Sollasites falklandensis* (Table A3-1) supporting the drastic change in calculated sedimentation rates during the Middle Albian.

A3.3. Results

The CAS S isotope ($\delta^{34}S_{CAS}$) records from ODP Hole 866 and DSDP Hole 511 are presented in Figure A3-1 and listed in Tables A3-2 and A3-3. While the range of $\delta^{34}S_{CAS}$ values from the Barremian-Albian section of ODP Hole 866 is similar to that of the Early Cretaceous $\delta^{34}S_{Ba}$ record the values from DSDP Hole 511 and the Hauterivian section of ODP Hole 866 differ significantly (Figs. 4-6 and A3-1). Despite significant scatter during the Barremian and an earlier return to more ^{34}S enriched values the general structure of the $\delta^{34}S_{CAS}$ record from ODP Hole 866 during the Aptian is similar to the composite $\delta^{34}S_{Ba}$ record (Figs. 4-6 and A3-1).

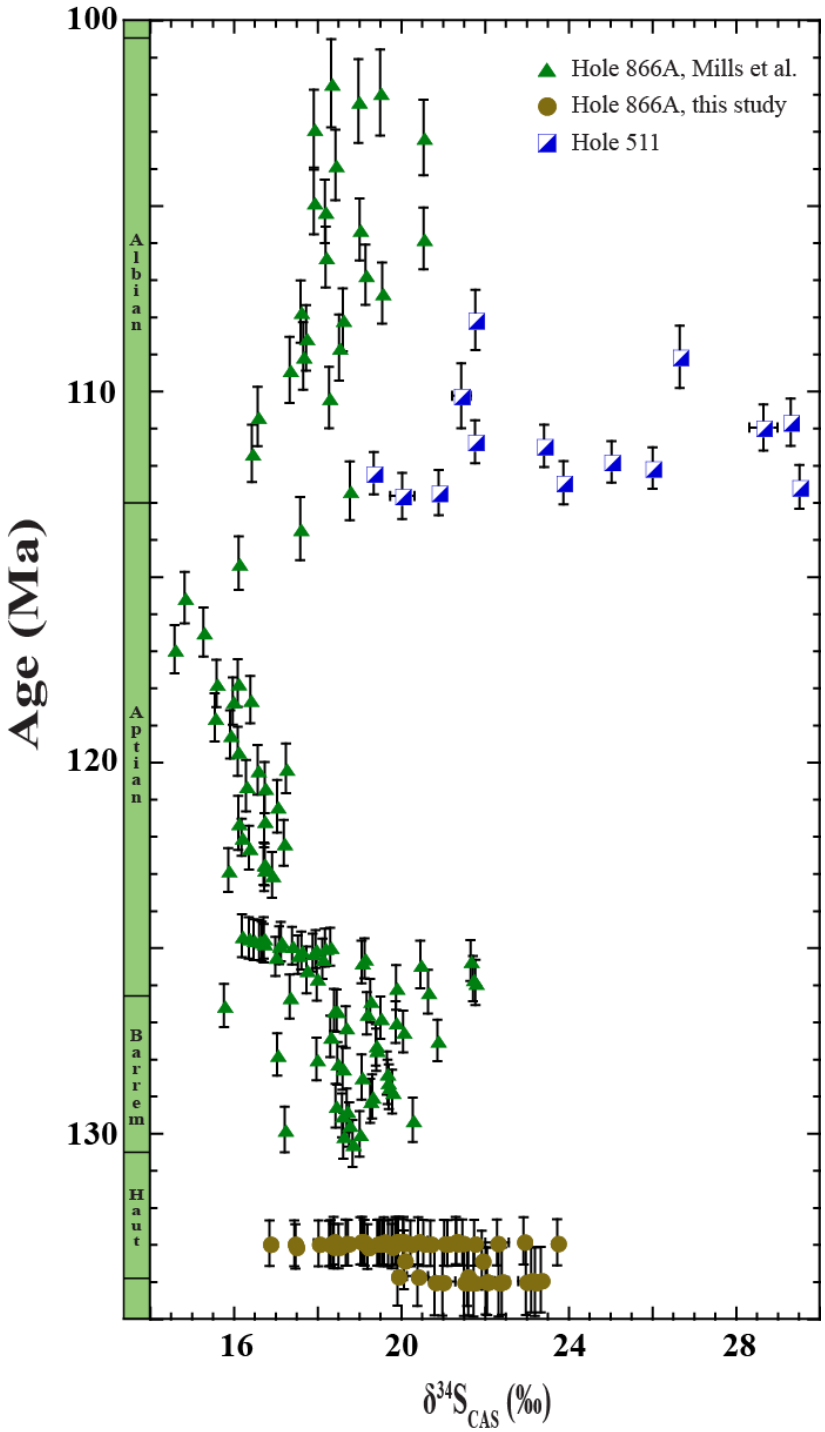

Figure A3-1 Early Cretaceous CAS S isotope data

Early Cretaceous $\delta^{34}S_{CAS}$ data from this study and Mills et al. (2013) with GTS2012 age assignments. Data listed in Tables A3-2 and A3-3.

Table A3-2. DSDP Hole 511 samples, GTS2012 age assignment, and S isotope data

Sample	Depth (mbsf)	GTS2012 age (Ma)	$\delta^{34}S_{CAS}$ (‰ VCDT)
51R-3 80-84 cm	445.82	108.06 ± 0.81	21.76
51R-5 17-21 cm	448.19	109.05 ± 0.84	26.64
51R-6 120-124 cm	450.72	110.10 ± 0.88	21.42 ± 0.22
52R-2 36-40 cm	453.38	110.81 ± 0.64	29.29
52R-3 105-108 cm	455.565	110.96 ± 0.62	28.64 ± 0.34
52R-7 56-60 cm	461.08	111.34 ± 0.58	21.75
53R-2 16-20 cm	462.68	111.45 ± 0.57	23.40 ± 0.03
53R-6 42-46 cm	468.94	111.88 ± 0.56	25.01
54R-1 88-92 cm	471.4	112.05 ± 0.56	25.99
54R-2 140-144 cm	473.42	112.19 ± 0.57	19.33 ± 0.10
54R-5 65-69 cm	477.17	112.44 ± 0.58	23.86
54R-6 85-89 cm	478.87	112.56 ± 0.59	29.50 ± 0.05
55R-1 98-102 cm	481.00	112.71 ± 0.61	20.88
55R-2 79-83 cm	482.31	112.80 ± 0.62	20.01 ± 0.29

Table A3-3. ODP Hole 866A samples, GTS2012 age assignment and CAS S isotope data. Barremian-Albian data from Mills et al. (2013) and Hauterivian data from current study. Samples with error estimate is standard deviation from replicate analyses (n=2).

Sample	Depth (mbsf)	GTS2012 age (Ma)	$\delta^{34}S_{CAS}$ (‰ VCDT)
6R-CC 1-20 cm	38.41	101.68 ± 1.19	18.31
7R-CC 30-35 cm	48.1	101.93 ± 1.16	19.48
8R-CC 8-20 cm	57.38	102.16 ± 1.13	18.96
11R-CC 1-10 cm	86.51	102.90 ± 1.05	17.90
12R-CC 1-9 cm	96.11	103.14 ± 1.02	20.52
15R-CC 8-15 cm	125.08	103.88 ± 0.95	18.41
19R-CC 4-10 cm	164.84	104.88 ± 0.87	17.90
20R-CC 3-9 cm	174.53	105.13 ± 0.86	18.16
22R-CC 5-12 cm	193.85	105.62 ± 0.84	18.99
23R-CC 0-5 cm	203.4	105.86 ± 0.83	20.52
25R-1 50-55 cm	223.2	106.36 ± 0.82	18.18
27R-CC 3-10 cm	242.03	106.84 ± 0.81	19.13
29R-CC 3-7 cm	261.33	107.33 ± 0.82	19.53
31R-1 55-60 cm	281.15	107.83 ± 0.84	17.58
32R-CC 20-25 cm	290.1	108.05 ± 0.85	18.59
34R-CC 5-10 cm	309.25	108.54 ± 0.88	17.71
35R-1 45-53 cm	319.35	108.80 ± 0.89	18.50
36R-1 28-35 cm	328.78	109.03 ± 0.91	17.64
38R-1 55-60 cm	343.25	109.40 ± 0.89	17.32
40R-CC 30-42 cm	357.6	110.15 ± 0.83	18.26
41R-1 34-40 cm	367.34	110.66 ± 0.80	16.55
43R-CC 10-15 cm	386.4	111.65 ± 0.77	16.42
45R-CC 23-27 cm	405.83	112.66 ± 0.79	18.76
47R-1 64-73 cm	425.34	113.68 ± 0.85	17.57
49R-CC 15-23 cm	444.15	114.61 ± 0.72	16.10
51R-1 22-28 cm	463.62	115.54 ± 0.69	14.81
53R-1 45-53 cm	483.15	116.47 ± 0.66	15.26
54R-1 47-54 cm	492.77	116.93 ± 0.65	14.57
56R-1 24-33 cm	511.84	117.84 ± 0.64	16.08
56R-1 52-60 cm	512.12	117.85 ± 0.64	15.57
57R-1 10-17 cm	521.4	118.29 ± 0.64	16.38
57R-1 92-98 cm	522.22	118.33 ± 0.64	15.96
58R-1 54-60 cm	531.54	118.77 ± 0.65	15.53
59R-1 51-56 cm	541.21	119.23 ± 0.65	15.90
60R-1 22-31 cm	550.52	119.68 ± 0.66	16.08
61R-1 32-41 cm	560.22	120.14 ± 0.67	17.23
61R-1 116-126 cm	561.06	120.18 ± 0.67	16.55
62R-1 41-51 cm	570.01	120.61 ± 0.69	16.28
62R-2 5-15 cm	571.15	120.66 ± 0.69	16.72
63R-2 95-105 cm	581.75	121.16 ± 0.71	17.02
64R-1 87-97 cm	589.87	121.55 ± 0.72	16.71
64R-2 60-70 cm	591.1	121.61 ± 0.73	16.09
65R-1 70-80 cm	599.3	122.00 ± 0.50	16.17
66R-1 89-96 cm	609.19	122.15 ± 0.62	17.18
67R-1 34-44 cm	618.34	122.28 ± 0.59	16.35

Table A3-3. Continued

Sample	Depth (mbsf)	GTS2012 age (Ma)	$\delta^{34}S_{CAS}$ (‰ VCDT)
70R-1 25-35 cm	647.15	122.71 ± 0.57	16.70
70R-2 43-53 cm	648.14	122.73 ± 0.57	16.72
71R-1 88-98 cm	657.38	122.86 ± 0.59	16.71
71R-2 38-48 cm	658.16	122.88 ± 0.59	15.85
72R-1 62-69 cm	666.82	123.01 ± 0.62	16.90
73R-1 95-105 cm	676.75	124.65 ± 0.58	16.18
74R-2 75-85 cm	687.53	124.71 ± 0.56	16.34
74R-3 25-35 cm	688.24	124.71 ± 0.56	16.70
75R-2 55-65 cm	696.8	124.76 ± 0.55	16.46
75R-4 38-48 cm	699.24	124.77 ± 0.54	16.59
76R-1 80-90 cm	705.5	124.80 ± 0.53	16.65
76R-2 115-125 cm	707.35	124.81 ± 0.53	17.11
77R-1 30-40 cm	714.8	124.85 ± 0.52	16.70
78R-1 100-110 cm	725.1	124.91 ± 0.51	17.07
78R-3 85-95 cm	727.84	124.92 ± 0.51	17.38
79R-1 65-75 cm	734.45	124.95 ± 0.51	18.29
79R-3 20-30 cm	736.85	124.97 ± 0.51	18.16
80R-1 65-75 cm	744.15	125.01 ± 0.51	17.94
81R-1 25-35 cm	753.35	125.05 ± 0.51	17.60
82R-1 40-47 cm	763.2	125.11 ± 0.51	17.87
83R-1 15-25 cm	772.65	125.16 ± 0.52	17.52
84R-1 33-40 cm	782.53	125.21 ± 0.53	16.98
85R-1 20-30 cm	792	125.26 ± 0.54	19.11
85R-2 120-130 cm	794.45	125.27 ± 0.54	18.10
86R-2 40-50 cm	803.4	125.32 ± 0.55	21.64
87R-1 51-61 cm	811.71	125.36 ± 0.57	19.04
88R-1 70-80 cm	821.6	125.43 ± 0.64	20.44
89R-2 15-25 cm	832.25	125.57 ± 0.63	17.72
91R-1 17-27 cm	849.67	125.79 ± 0.61	17.97
91R-2 5-15 cm	850.81	125.81 ± 0.61	21.70
92R-1 11-18 cm	859.31	125.91 ± 0.61	21.76
93R-1 20-30 cm	868.9	126.04 ± 0.60	19.86
94R-1 40-50 cm	878.8	126.16 ± 0.59	20.62
95R-1 55-64 cm	888.5	126.29 ± 0.59	17.32
96R-1 5-20 cm	897.75	126.40 ± 0.58	19.24
97R-1 45-55 cm	907.85	126.53 ± 0.58	15.75
98R-1 35-45 cm	917.35	126.65 ± 0.57	18.38
98R-2 20-30 cm	918.7	126.67 ± 0.57	18.44
99R-1 10-20 cm	924	126.74 ± 0.57	19.16
100R-1 10-20 cm	933.5	126.86 ± 0.57	19.49
101R-1 3-13 cm	943.13	126.98 ± 0.56	19.85
102R-1 77-87 cm	953.47	127.11 ± 0.56	18.66
103R-1 43-47 cm	962.83	127.23 ± 0.56	20.03
104R-1 63-67 cm	972.33	127.36 ± 0.56	18.29
105R-1 43-47 cm	981.73	127.47 ± 0.56	20.85
106R-1 12-16 cm	991.02	127.59 ± 0.56	19.38
107R-1 15-19 cm	1000.65	127.72 ± 0.57	19.39
108R-1 73-77 cm	1010.93	127.85 ± 0.57	17.02
109R-1 65-69 cm	1020.55	127.97 ± 0.57	17.96

Table A3-3. Continued

Sample	Depth (mbsf)	GTS2012 age (Ma)	$\delta^{34}S_{CAS}$ (‰ VCDT)
110R-1 15-19 cm	1029.75	128.09 ± 0.57	18.46
111R-1 95-99 cm	1040.25	128.22 ± 0.58	18.58
112R-1 30-41 cm	1050.7	128.35 ± 0.58	19.64
113R-CC 20-27 cm	1058.7	128.46 ± 0.61	19.04
114R-1 70-77 cm	1068.9	128.59 ± 0.60	19.66
115R-1 23-30 cm	1078.13	128.72 ± 0.60	19.69
116R-1 48-55 cm	1087.98	128.85 ± 0.59	19.77
117R-1 65-72 cm	1097.75	128.98 ± 0.59	19.29
118R-1 40-47 cm	1107.2	129.10 ± 0.59	19.24
119R-1 23-30 cm	1116.73	129.23 ± 0.59	18.42
120R-1 40-47 cm	1126.5	129.36 ± 0.59	18.68
121R-1 75-82	1136.45	129.49 ± 0.59	18.57
122R-1 35-42 cm	1145.75	129.61 ± 0.60	20.26
123R-1 20-27 cm	1155.3	129.74 ± 0.60	18.74
124R-1 70-77 cm	1165.5	129.87 ± 0.61	17.20
125R-1 27-34 cm	1174.67	129.99 ± 0.61	18.99
125R-3 110-117 cm	1178.43	130.04 ± 0.62	18.60
127R-1 25-32 cm	1193.75	130.25 ± 0.63	18.82
149R-1 5.5-9 cm	1405.4725	132.865 ± 0.642	19.05
149R-1 23-25 cm	1405.64	132.866 ± 0.642	21.29
149R-1 45-48 cm	1405.865	132.867 ± 0.641	19.91 ± 0.03
149R-1 76-79 cm	1406.175	132.869 ± 0.641	20.04 ± 0.57
149R-1 128-131 cm	1406.695	132.871 ± 0.640	19.85
149R-2 0-4 cm	1406.92	132.873 ± 0.639	18.37
149R-2 29-32 cm	1407.205	132.874 ± 0.638	20.39
149R-2 43-46 cm	1407.345	132.875 ± 0.638	19.01
149R-2 59-62 cm	1407.505	132.876 ± 0.638	22.91
149R-2 66-69 cm	1407.575	132.876 ± 0.638	19.57 ± 0.03
150R-1 8-11 cm	1415.195	132.915 ± 0.623	20.03
150R-1 18-20 cm	1415.29	132.916 ± 0.623	23.71
150R-1 27.5-31.5 cm	1415.395	132.916 ± 0.623	19.78
150R-1 52-54 cm	1415.63	132.917 ± 0.622	22.27 ± 0.28
150R-1 77-78 cm	1415.875	132.919 ± 0.622	19.46 ± 0.10
150R-1 109-111 cm	1416.2	132.920 ± 0.621	21.45
150R-1 122-125 cm	1416.335	132.921 ± 0.621	18.66
150R-1 139-142 cm	1416.505	132.922 ± 0.621	21.30
150R-2 12-15 cm	1416.735	132.923 ± 0.620	19.11
150R-2 36-39 cm	1416.975	132.924 ± 0.620	18.71
150R-2 67-69 cm	1417.28	132.926 ± 0.619	21.01
150R-2 85-89 cm	1417.47	132.927 ± 0.619	19.09
150R-2 105-108 cm	1417.665	132.928 ± 0.619	19.41 ± 0.00
150R-2 132-134 cm	1417.93	132.929 ± 0.618	21.73
150R-3 13-15 cm	1418.24	132.931 ± 0.618	20.51
150R-3 36.5-39 cm	1418.4775	132.932 ± 0.618	19.48
150R-3 60-63 cm	1418.715	132.933 ± 0.617	19.54
150R-3 81-84 cm	1418.925	132.934 ± 0.617	21.09 ± 0.05
150R-3 111-114 cm	1419.225	132.936 ± 0.616	18.30
150R-3 139-142 cm	1419.505	132.937 ± 0.616	20.68

Table A3-3. Continued

Sample	Depth (mbsf)	GTS2012 age (Ma)	$\delta^{34}S_{CAS}$ (‰ VCDT)
150R-4 8-11 cm	1419.695	132.938 ± 0.616	16.84
150R-4 25-28 cm	1419.865	132.939 ± 0.616	20.21
150R-4 41-44 cm	1420.025	132.940 ± 0.615	17.43
150R-4 67-71 cm	1420.29	132.941 ± 0.615	18.01 ± 0.11
150R-4 87-89 cm	1420.485	132.942 ± 0.615	19.67
150R-4 94-97 cm	1420.555	132.943 ± 0.615	18.26
152R-1 23-25 cm	1434.745	133.016 ± 0.602	18.36
152R-1 57-60.5 cm	1435.085	133.018 ± 0.601	18.49
152R-1 78-81 cm	1435.29	133.019 ± 0.601	19.76
152R-2 25-28 cm	1436.27	133.024 ± 0.601	17.46
152R-2 125-128 cm	1437.27	133.029 ± 0.601	19.18
158R-1 114-116 cm	1493.65	133.389 ± 0.791	20.05
158R-2 32-34 cm	1494.33	133.393 ± 0.790	21.91
167R-1 102-104 cm	1581.43	133.816 ± 0.806	19.90 ± 0.07
167R-1 139-142 cm	1581.805	133.818 ± 0.807	21.56
167R-2 25-28 cm	1582.165	133.820 ± 0.808	20.37 ± 0.25
169R-2 126-128 cm	1602.57	133.919 ± 0.603	23.32
169R-3 12-14 cm	1602.93	133.921 ± 0.603	23.09 ± 0.13
170R-1 27-30 cm	1609.685	133.954 ± 0.610	22.00
170R-1 75-79 cm	1610.17	133.956 ± 0.610	22.39 ± 0.17
170R-1 116-119 cm	1610.575	133.958 ± 0.611	22.04
170R-2 17-20 cm	1611.085	133.961 ± 0.612	22.96 ± 0.18
170R-2 92-95 cm	1611.835	133.964 ± 0.613	20.78
170R-2 131-135 cm	1612.23	133.966 ± 0.613	21.59
170R-3 52-55 cm	1612.935	133.970 ± 0.614	20.97 ± 0.31
170R-3 97-101 cm	1613.39	133.972 ± 0.615	23.18 ± 0.00
170R-3 137-141 cm	1613.79	133.974 ± 0.616	21.48
170R-4 85-88 cm	1614.765	133.979 ± 0.617	21.71
170R-4 123-126 cm	1615.145	133.980 ± 0.618	22.31